



**Fluorescent nanodiamonds: bioengineered
functional materials**

Thesis submitted for the degree of Doctor of Philosophy by:

Adam H. Day

School of Chemistry

Cardiff University

September 2019

Abstract

This thesis examines the development of tools which enable the production of functional hybrid materials utilising a synthetic biology derived structural component and a nanoparticle based functional component. These components were designed to be covalently linked with a produced ligase enzyme, Sortase A (SrtA).

The functional component, nanodiamond (ND), a nanoparticle consisting of an sp^3 carbon core and orthogonal surface was subjected to surface functionalisation using dispersions of surface polycarboxylated **ND-COOH** in aqueous and organic media *via* EDC/NHS mediated amidation. Due to the paucity of well-defined and characterised particles in the literature, initial methodology development in the production and characterisation of such surface functionalised species was demonstrated, investigating the functionalisation of **ND-COOH** with synthesised water soluble naphthalimide based and [Ru(bipy)₃] based amine terminated luminophores **Nap-1** and **Ru-1** (respectively) and co-functionalisation of **ND-COOH** with both species (Chapter 2). From this development, ND suspension exhibiting green (**Nap-1**) and red (**Ir-1**, a synthesised iridium organometallic luminophore) emitting species and a SrtA enzyme tag were produced with the **Nap-1**/peptide ND species exhibiting demonstrable activity towards sortase modification. (Chapter 3)

The biological structural component, *E. coli* biofilms presented here chiefly consist of, and rely on for their formation, curli fibrils primarily composed of amyloid structures of the protein CsgA. Through the incorporation of a developed plasmid, PFF753CcsgA (which harbours the *csgA* gene), into an engineered *E. coli* strain MG1655 ompR234 PRO Δ csgA, a system demonstrating tight control (dependent on chemical induction) in CsgA production and biofilm formation was demonstrated. Induction *E. coli* strain carrying this plasmid resulted in a statistically verified increase in biofilm biomass, surface area, and thickness imaged through confocal fluorescence microscopy (CFM). Engineering of the CsgA protein to incorporate a sequence recognisable by the ligase SrtA at the C-terminus through resulted in abrogation of CsgA amyloid mediated biofilm formation. This was partially ameliorated through the incorporation of a flexible linker region between CsgA and the SrtA tag. (Chapter 4)

Finally, from the development of the luminophore **Nap-1** for ND attachment, a set of six bispicolylamine fluorescent ligands and their corresponding *fac*-[Re(CO)₃L^x]BF₄ complexes were synthesised and their photophysical properties characterised. The water-soluble **Nap-1** derived ligand **L⁵** was chosen for further work with the analogous

technetium complex with applications as a bimodal (optical/SPECT) imaging agent (Chapter 5).

Table of contents

ABSTRACT	I
LIST OF FIGURES	VIII
LIST OF TABLES	XVI
LIST OF EQUATIONS	XVIII
LIST OF ABBREVIATIONS	XIX
DEDICATION AND ACKNOWLEDGEMENTS	XXI
CHAPTER 1. INTRODUCTION	1
1.1. Project aims	2
1.1.1. Interest in hybrid functional materials	2
1.1.2. Potential for structurally ordered functional materials through layering	3
1.1.3. Material production from a synthetic biology approach	4
1.1.4. Nanoparticles as functional components	4
1.1.5. Theme of work	5
1.1.5.1. Development of nanodiamond surface functionalisation methodology and characterisation of surface functionalised particles	8
1.1.5.2. Nanodiamond development for use as a functional component in the production of synthetic biology produced functional materials	9
1.1.5.3. Design, production and evaluation of curli based <i>E. coli</i> biofilm materials	10
1.1.5.4. Utilisation of luminescent systems developed for advanced multimodal imaging	10
1.2. Fundamental concepts employed in study	11
1.2.1. Luminescent materials and study thereof	11
1.2.1.1. Photoluminescence	11
1.2.1.2. Examples of fluorescent and phosphorescent luminophores	14
1.2.2. Core techniques in synthetic biology utilised in study	17
1.2.2.1. The genetic makeup of <i>E. coli</i> strains utilised in synthetic biology	17
1.2.2.2. Plasmids as a route to genetically alter <i>E. coli</i>	19
1.2.2.3. Controlling gene expression <i>via</i> operons in plasmid technologies	21
1.2.2.4. Site directed mutagenesis as a tool to alter the genetic code of plasmids	22
CHAPTER 2. SURFACE FUNCTIONALISED NANODIAMOND: METHODOLOGY DEVELOPMENT	26
2.1. Chapter aims	27
2.2. Introduction	30
2.2.1. Nanodiamond as a highly modifiable, inert nanoparticle	30
2.2.1.1. Nanodiamond composition and structure	30
2.2.1.2. Synthesis of nanoscale diamond: detonation and CVD	31
2.2.1.3. Post-synthesis purification	32
2.2.2. Nanodiamond surface termination	34
2.2.3. Route to carboxylated ND surface functionalisation in aqueous and organic media	35

2.2.4. Applications of nanodiamond particle systems	36
2.2.4.1. Nanodiamond nanocomposites	36
2.2.4.2. Nanodiamond in drug delivery	37
2.2.5. Methods used to characterise functionalised nanodiamond particles	39
2.2.5.1. Colloidal stability (DLS/NTA/ZP)	40
2.2.5.2. Surface chemical environment (XPS)	42
2.2.5.3. Photoluminescent characterisation	45
2.2.5.4. Particle morphology and purity (TEM)	46
2.3. Results and discussion	48
2.3.1. Production and characterisation of luminescent nanodiamond species Nap-1@ND in buffered aqueous media and acetonitrile	48
2.3.1.1. Synthesis of the 4-amino-1,8-naphthalimide derivative Nap-1	49
2.3.1.2. Colloidal properties	52
2.3.1.3. X-Ray photoelectron spectroscopy	54
2.3.1.4. Photophysical properties of Nap-1@ND	58
2.3.1.5. Transmission electron microscopy	59
2.3.2. Production and characterisation of Ru-1@ND , and the co-functionalised, dual emissive nanodiamond probe Nap-1/Ru-1@ND	60
2.3.2.1. Particle size and colloidal stability	61
2.3.2.2. X-ray photoelectron spectroscopy	62
2.3.2.4. Transmission electron spectroscopy	64
2.3.3. Attempting to control colloidal stability of Nap-1 functionalised aqueous ND suspensions through co-functionalisation with Taurine	66
2.3.3.1. Confirmation of incremental Nap-1 functionalisation <i>via</i> UV-Visible spectroscopy	67
2.3.3.2. Particle size and Colloidal stability	68
2.4. Chapter conclusion	72
2.5. Experimental	74
2.5.1. General considerations and measurement parameters	74
2.5.1.1. General reagents	74
2.5.1.2. Nanodiamond dispersions	74
2.5.1.3. X-ray photoelectron spectroscopy	74
2.5.1.4. Particle size and zeta potential measurements	75
2.5.1.5. Optical spectroscopy	75
2.5.2. Synthetic methods	75
2.5.2.1. Synthesis routes in the surface functionalisation of ND	75
2.5.2.2. Synthesis of Nap-1 from 4-chloro-1,8-naphthalic anhydride	76
<u>CHAPTER 3. DEVELOPMENT OF SORTASE ACTIVE FUNCTIONAL NANODIAMOND PARTICLES</u>	79
3.1. Chapter Aims	80
3.2. Introduction	81
3.2.1. Sortases: a group of cell membrane associated enzymes critical for attachment of proteins to the peptidylglycan cell wall	81
3.2.2. Mechanism of <i>S.aureus</i> SrtA transpeptidation	82
3.2.3. Development of <i>S.aureus</i> SrtA in protein modification technologies	85
3.2.4. Utilisation of SrtA in chemical biology	86
3.2.4.1. Labelling of proteins	86
3.2.4.2. Attachment of proteins to abiotic planar and particle surfaces	87
3.2.4.3. Cell surface modification	88
3.3. Results and discussion	90
3.3.1. Expression of <i>S.aureus</i> Sortase A from <i>E. coli</i>	90

3.3.2. Confirmation of SrtA(7M) activity towards TTLPYTGG and GGGGTTTT peptides	91
3.3.3. Synthesis of red luminescent organometallic iridium (III) complex, Ir-1 suitable for ND attachment.	94
3.3.3.1. Optical properties of Ir-1	97
3.3.4. Development of enzyme labile peptide luminophore co-functionalised ND suspensions suitable for surface modification by Sortase A Nap-1/Srtpep1@ND and Ir-1/Srtpep1@ND	98
3.3.4.1. Evaluating optical properties of protected and deprotected suspensions of Nap-1/Srtpep1@ND and Ir-1/Srtpep1@ND	100
3.3.4.2. Size distribution analysis of Nap-1/Srtpep1@ND and Ir-1/Srtpep1@ND	103
3.3.4.3. XPS analysis of Nap-1/Srtpep1@ND and Ir-1/Srtpep1@ND	104
3.3.5. Evaluating the ability to modify luminophore/SrtPep-1 co-functionalised ND suspensions with SrtA using bespoke, synthesised peptide	107
3.3.5.1. Development of [Ru(bipy)₂L₁]-LPYTGG , a luminescent peptide conjugate suitable for Sortase A ligation with a polyglycine expressing peptide.	107
3.3.5.2. Sortase A mediated ligation of [Ru(Bipy)₂L₁]-Srtpep2 to surface functionalised ND dispersions	111
3.4. Chapter conclusions	114
3.5. Experimental	115
3.5.1. General reagents	115
3.5.2. Expression of <i>S. aureus</i> SrtA	115
3.5.3. Surface cofunctionalisation of ND-COOH with Nap-1/Ir-1 and SrtPep 1	116
3.5.4. Sortase ligation assay with TTLPYTGG and GGGGTTTT	117
3.5.5. Sortase ligation with Nap-1/Srtpep1@ND and Ir-1/Srtpep1@ND and crude [Ru(Bipy)₂L₁]-Srtpep2	117
3.5.6. Synthesis of compounds	118
3.5.6.1. Ir-1	118
3.5.6.2. [Ru(Bipy)₂L₁]-LPYTGG	121
3.5.7. Analytical techniques employed	121
3.5.8. Buffers and reagents for biochemical protocols	122

CHAPTER 4. DEVELOPMENT OF CONTROLLABLE, ENGINEERED CURLI MEDIATED *E. COLI* BIOFILMS

4.1. Introduction	126
4.1.1. Chapter aims	126
4.1.2. Role of curli amyloid in the biofilm environment of <i>Escherichia coli</i>	127
4.1.3. Amyloids as functional biofilm components	128
4.1.4. Curli biosynthesis in <i>Escherichia coli</i>	129
4.1.5. Design of <i>E. coli</i> strain demonstrating controllable curli production	132
4.1.6. Overview of methods employed in biofilm analysis	133
4.1.6.1. Biofilm culture methods	133
4.1.6.2. Overview of methods employed in biofilm analysis	136
4.1.6.2.1. Congo Red binding	138
4.1.6.2.2. Crystal violet assay	138
4.1.6.2.3. Fluorescence microscopy and confocal fluorescence microscopy	139
4.1.7. Background to <i>Escherichia coli</i> strains employed in the present study	139
4.2. Results and discussion	141
4.2.1. Plasmid and strain construction	141
4.2.1.1. PFF753CcsgA	141
4.2.1.2. PFF753CcsgASau	142
4.2.1.3. PFF753CcsgASauGGS	142

4.2.2. Inspection of curli ECM production by <i>E. coli</i> MG1655 ompR234 PRO ΔcsgA :: pFF753CcsG	142
4.2.3. Evaluation of curli production by reference strains and MG1655ompR234ΔcsgA::PFF753CCsgA in static culture over 72h	146
4.2.3.1. Morphology and distribution of biofilm at the coupon surface	146
4.2.3.2. COMSTAT 2 quantification of biofilm properties	152
4.2.3.3. Statistical verification of COMSTAT 2 results	154
4.2.3.4. Significance of results obtained for 72h static biofilm experiments	157
4.2.4. Evaluation of curli production MG1655 ompR234 ΔCsgA :: PFF753CCsgA in flow culture over 24h	159
4.2.4.1 Morphology and distribution of biofilm at the coupon surface	159
4.2.4.2. COMSTAT 2 quantification of biofilms	163
4.2.4.3. Statistical verification of COMSTAT quantification	166
4.2.4.4. Significance of results for 24h flow biofilm experiments	167
4.2.5. Evaluation of curli production MG1655 ompR234 ΔCsgA :: PFF753CCsgASau and PFF753CcsGASauGGS in flow culture over 24h	168
4.2.5.1. Morphology and distribution of biofilm at the coupon surface	168
4.2.5.2. COMSTAT 2 quantification of biofilm properties	171
4.2.5.3. Statistical verification of COMSTAT quantification	173
4.2.5.4. Significance of results of 24h flow biofilms produced by <i>E. coli</i> producing engineered mutants of CsgA incorporating the SrtA tag	175
4.3. Chapter conclusion	177
4.4. Experimental	179
4.4.1. Plasmid constructs used in this study	179
4.4.1.1. Design of PFF753csgA(proto)	179
4.4.1.2. PFF753BcsgA(proto)	179
4.4.1.3. PFF753CCsgA(proto)	179
4.4.1.4. PFF753CcsG and PFF753CcsGASau	180
4.4.2. <i>Escherichia coli</i> strains used in this study	181
4.4.2.1. MG1655 ompR234 PRO ΔcsgA	181
4.4.2.2. W3110	181
4.4.2.3. BL21-DE3 RP codonplus	182
4.4.2.4. XL-1 Blue	182
4.4.3. Control of curli biofilm formation by <i>Escherichia coli</i> with plasmid PFF753CcsG	182
4.4.3.1. Growth of curli biofilm on polypropylene coupons in CDC bioreactor ®	182
4.4.3.2. Confocal fluorescence microscopy	184
4.4.3.3. COMSTAT 2 analyses Z-series of the stained biofilm	185
4.4.3.4. Scanning electron microscopy	187
4.4.4. General biochemical protocols	188
4.4.4.1. PCR with PrimeSTAR® HS DNA polymerase	188
4.4.4.2. Site directed mutagenesis	188
4.4.4.3. Transformation of supercompetent <i>E. coli</i> cell stocks with plasmid DNA	191
4.4.4.4. Miniprep plasmid isolation	191
4.4.4.5. Preparation of glycerol stocks of <i>E. coli</i> strains	191
4.4.4.6. Poly agarose gel electrophoresis	192
4.4.5. Buffers and reagents	192
CHAPTER 5. DEVELOPMENT OF LUMINESCENT NAPHTHALIMIDE CONJUGATED RE(I) AND TC(I) COMPLEXES	195
5.1. Chapter aims	196
5.2. Introduction	199
5.2.1. General characteristics of an ideal bioimaging probe	199

5.2.1.1. Toxicity	199
5.2.1.2. Metabolic stability	199
5.2.1.3. Permeability and solubility	200
5.2.2. Re(I) and Tc(I) coordination complexes in bioimaging	200
5.2.2.1. Cationic <i>fac</i> -{M(CO) ₃ } based Re(I) and Tc(I) complexes utilised in bioimaging	201
5.2.2.2. Other Re(I) and Tc(I) coordination modes utilised in bioimaging	202
5.2.3. Mitochondrial targeting in bioimaging	203
5.2.3.1. Mitochondrial membrane potential dependant uptake	204
5.3. Results and discussion	205
5.3.1. Synthesis of ligands L ¹ -L ⁶	205
5.3.2. Synthesis of rhenium complexes <i>fac</i> -[Re(CO) ₃ (L ^x)]BF ₄	207
5.3.3. Optical properties of ligands L ¹ -L ⁶ and corresponding <i>fac</i> -[Re(CO) ₃ (L ⁶)]BF ₄ complexes	210
5.3.3.1. UV-Visible absorption spectra	211
5.3.3.2. Luminescence emission properties of ligands L ¹ -L ⁶ and their corresponding [Re(CO) ₃ (L ^x)]BF ₄ complexes	212
5.3.3.3. Optical properties summary	215
5.3.4. Radiolabelling of L ⁵ with technetium-99m	216
5.3.5. <i>In-vitro</i> assessment of properties relevant to biodistribution and stability	218
5.3.6. Bioimaging studies with <i>fac</i> -[M(CO) ₃ (L ₅)]BF ₄ (M = Re, ^{99m} Tc)	219
5.3.6.1. Cell viability	219
5.3.6.2. <i>In-vitro</i> mitochondrial uptake studies of <i>fac</i> -[^{99m} Tc(CO) ₃ (L ₅)]BF ₄	220
5.3.6.3. <i>In-vitro</i> imaging of human breast cancer cells (MCF-7) and rat cardiomyocytes (H9c2), mitochondrial localisation studies	221
5.3.6.4. <i>In-vivo</i> imaging	222
5.2.4. Chapter conclusion	224
5.4. Experimental	226
5.4.1. General considerations	226
5.4.2. Radiolabelling of ligand L1-L6 with ^{99m} Tc	226
5.4.3. Lipophilicity measurements	226
5.4.4. Serum stability	227
5.4.5. <i>In-vivo</i> SPECT imaging and stability	227
5.4.6. <i>In vitro</i> analysis	227
5.4.6.1. Cell culture	227
5.4.6.2. Toxicity	227
5.4.6.3. Flow cytometry	228
5.4.6.4. Confocal microscopy	228
5.4.7. Synthesis of compounds	229
5.4.7.1. Ligands and precursors	229
5.4.7.2. <i>fac</i> -[Re(CO) ₃ L ^x]]BF ₄ complexes	243
THESIS SUMMARY	249
BIBLIOGRAPHY	251

List of figures

Chapter 1:

- Figure 1.1:** Schematic showing the production of hybrid materials through incorporation of a functional component within/on a structural component. 2
- Figure 1.2:** Schematic showing the production of a polyfunctional hybrid material incorporating functional components through structural layering. 4
- Figure 1.3:** Structure of curli amyloid fibrils expressed by *E. coli* imaged by electron microscopy. 6
- Figure 1.4:** Designed synthetic biology approach to produce hybrid functional materials based on a biological (curli biofilm) material component and surface functionalised ND component. 7
- Figure 1.5:** Potential to develop layered materials based on the curli biofilm structural matrix (blue sheets) and orthogonally functionalised ND structural elements. 8
- Figure 1.6:** Schematic showing surface functionalisation of ND *via* proposed strategy. 9
- Figure 1.7:** Schematic showing designed route to SrtA mediated incorporation of the appropriately functionalised ND functional component to the curli biological matrix. 10
- Figure 1.8:** Structure of L_5 , the luminescent ligand suitable for chelation of *fac-tricarbonyl* Re(I) and ^{99m}Tc . 11
- Figure 1.9:** Example of a Jablonskii diagram 12
- Figure 1.10:** Demonstration of an absorption and emission spectrum of a luminophore, 13
- Figure 1.11:** Structures and photophysical parameters of selected linear chromophoric and polyaromatic fluorescent species 15
- Figure 1.12:** Examples of luminescent octahedral low-spin d^6 complexes 16
- Figure 1.13:** The overall structure of the *E. coli* genome. 17
- Figure 1.14:** Plasmid map representation of pET30b plasmid 20
- Figure 1.15:** Selected parts of the *lac* operon showing the promoter sequence 21
- Figure 1.16:** Schematic of a single cycle in the PCR reaction 24
- Figure 1.17:** Schematic of mismatched PCR primer design to yield a mutated (deletion mutation) product by PCR. 25

Chapter 2:

Figure 2.1: Route to covalently attached, surface functionalised ND suspensions exhibiting orthogonal fluorescent substrates 1 and 2, and co-functionalisation with both substrates.	27
Figure 2.2: Structures of luminophores Nap-1 and Ru-1 utilised in this chapter as substrates for ND functionalisation.	28
Figure 2.3: Representation of ND structure, showing core sp^3 hybridised carbon core (grey lattice), and mixture of surface graphitic and oxidised carbon species.	30
Figure 2.4: Raman spectra of UD98 and UD90 ND samples prior to and following oxidation at 425 °C for 5 hours.	33
Figure 2.5: Routes to surface terminations from oxidized ND from references. HMP denotes Hydrogen microwave plasma.	34
Figure 2.6: Surface functionalisation of carboxylated nanodiamond through the activation by EDC to form the NHS ester intermediate.	35
Figure 2.7: Carbodiimide activation of carboxylic acids to form metastable NHS esters.	35
Figure 2.8: Nucleophilic substitution of NHS ester.	36
Figure 2.9: Depiction of method in which doxorubicin can be incorporated into ND aggregates through addition of salt.	38
Figure 2.10: HeLa cells demonstrating uptake of 35 nm luminescent ND's	39
Figure 2.11: Schematic diagram of the NTA setup.	41
Figure 2.12: Diagram describing the photoelectric ejection of a core 1s electron from a solid carbon sample through irradiation with an X-ray source.	43
Figure 2.13: Example of a deconvoluted XPS trace.	45
Figure 2.14: TEM image of c.a. 50 nm in diameter ND particles.	47
Figure 2.15: Schematic representation of functionalisation and co-functionalisation of ND suspensions with Nap-1, Ru-1 and Taurine yielding multiple species of functionalised species.	48
Figure 2.16: Synthesis of 4-amino-1,8-naphthalimide Nap-1 from 4-chloro-1,8-naphthalic anhydride.	49
Figure 2.17: UV-Visible absorbance and luminescence emission spectra of Nap-1 in aqueous solution.	51
Figure 2.18: Particle sizes of dispersions of ND-COOH , Nap-1 @NDa , Nap-1 @NDb and Nap-1 @NDc in H ₂ O measured by DLS and NTA.	53
Figure 2.19: Deconvoluted C(1s) region of the XPS spectrum of ND-COOH .	56
Figure 2.20: Deconvoluted XPS C(1s) traces of Nap-COOH , Nap-1 @NDa , Nap-1 @NDb and Nap-1 @NDc .	

Figure 2.21: UV-visible absorption and normalised luminescence emission spectra of Nap-1 and Nap-1@ND .	57
Figure 2.22: TEM images of ND-COOH from dispersions prepared in H ₂ O and MeCN and Nap-1@ND dispersions once purified.	59
Figure 2.23: Structure of luminescent ruthenium complex Ru-1 .	60
Figure 2.24: Size distribution analysis by DLS and NTA of surface functionalised nanodiamond dispersions Ru-1@ND and Ru-1/Nap-1@ND measured immediately following final purification.	61
Figure 2.25: Deconvoluted XPS C(1s)/Ru(3d) traces of Nap-1@ND and Nap1/Tau@ND1-3 .	62
Figure 2.26: UV-Visible absorption and luminescence emission spectra of Ru-1 and functionalised ND suspensions Ru-1@ND and Ru-1/Nap-1@ND in aqueous solution.	63
Figure 2.27: TEM images of Ru-1@ND and Ru-1/Nap-1@ND .	64
Figure 2.28: UV-Visible absorption of Nap-1 in H ₂ O and Nap-1/Tau@ND suspensions.	65
Figure 2.29: Absorbance at 445 nm as a function of concentration ratio of Nap-1 and taurine in the functionalisation reaction.	67
Figure 2.30: Size distribution analysis by DLS (blue bars) and NTA (black solid line) of surface functionalised nanodiamond dispersions prepared by method 1.	68
Figure 2.30: Size distribution analysis by DLS (blue bars) and NTA (black solid line) of surface functionalised nanodiamond dispersions prepared by method 2.	70
Chapter 3:	70
Figure 3.1: Route to enzyme modified nanodiamond embedded curli biofilm materials	81
Figure 3.2: Residue preference of SrtA	83
Figure 3.3: Structure of SrtA	84
Figure 3.4: Active site of SrtA	84
Figure 3.5: Reverse protonation mechanism purported for SrtA	84
Figure 3.6: Orthogonal SrtA modification of IFN α 2 by <i>S. aureus</i> (SrtA _{staph}) and <i>S. pyogenes</i> (SrtA _{strep}) sortases to yield a variety of products.	86
Figure 3.7: Demonstration of the ability to attach species to a polystyrene surface <i>via</i> SrtA transpeptidation	88
Figure 3.8: SDS PAGE of SrtA.	89
Figure 3.9: Mass spectrum of SrtA	91
	92

Figure 3.10: Mass spectra of TTLPYTGGGGTTTT and TTLPYTGG detected at ~8.7 and 8.3 minutes respectively	93
Figure 3.11: Measurement of SrtA activity as a product formation ratio from chromatogram integrals.	94
Figure 3.12: Structures of Nap-1 and Ir-1 luminophores	95
Figure 3.13: Synthetic route to the organometallic Ir(III) based complex, Ir-1 .	96
Figure 3.14.: Aromatic region of the ¹ H NMR spectrum of Ir-1 .	97
Figure 3.15: UV-Visible absorption spectrum and luminescence emission spectrum of Ir-1 in water.	99
Figure 3.16: Schematic showing method of incorporation of SrtA recognition peptide and luminophore.	99
Figure 3.17: Structure of Srt pep 1 .	100
Figure 3.18: UV-visible absorption spectra of Nap-1/Srtpep1@ND and Ir-1/Srtpep1@ND .	101
Figure 3.19: Luminescence emission spectra of Nap-1/Srtpep1@ND prior to and following deprotection.	102
Figure 3.20: Luminescence emission spectra of Ir-1/Srtpep1@ND prior to (left) and following (right) deprotection	103
Figure 3.21: Particle sizes of dispersions of Nap-1/Srtpep1@ND and Ir-1/Srtpep1@ND in H ₂ O measured by DLS and NTA.	104
Figure 3.23: Depiction of functionalisation of Nap-1/Srtpep1@ND and Ir-1/Srtpep1@ND by Sortase A using the synthetic conjugate peptide [Ru(bipy)₂L₁]-Srtpep2 .	108
Figure 3.24: Structure of [Ru(Bipy)₂L₁] .	109
Figure 3.25: Structure of the Sortase Active [Ru(Bipy)L₁]-Srtpep2 .	109
Figure 3.26: Comparison of the obtained isotope pattern of [Ru(bipy)₂L₁]-Srtpep2 with a theoretical pattern of ruthenium.	110
Figure 3.27: Top: LCMS chromatogram (TIC MS detection) of crude [Ru(bipy)₂L₁]-Srtpep2 .	111
Figure 3.28: UV-Visible absorption and emission spectra of [Ru(bipy)₂L₁]-Srtpep2 .	112
Figure 2.29: Left - Luminescence excitation and emission spectra of Nap-1/Srtpep1@ND following treatment with [Ru(Bipy)₂L₁]-Srtpep2 either with 10 molar % of SrtA and without SrtA.	113

Figure 2.30: Luminescence excitation and emission spectra of Ir-1/Srtpep1@ND following treatment with [Ru(Bipy)₂L₁]-Srtpep2 either with 10 molar % of <i>S.aureus</i> SrtA or without SrtA.	114
Chapter 4	
Figure 4.1: Schematic representation of project aims. Use of chemistry in the surface functionalisation of ND and synthetic biology in the production of the genetic circuit controllably producing structural protein together to (poly)functional bioengineered materials.	127
Figure 4.2: Electron micrograph of <i>E. coli</i> K12 BW25113 grown on a low-salt agar plate at 26°C, showing amyloid fibrils produced by cells, creating a cell-cell adhesive environment.	129
Figure 4.3: CsgA Sequence and contact predictions from multiple sequence alignment. Left- β -Sheet predicted structures of CsgA in solution.	130
Figure 4.4: CR indicator agar demonstrating interbacterial complementation between <i>csgA</i> ⁻ and <i>CsgB</i> ⁻ strains of <i>E. coli</i> .	131
Figure 4.5: Mechanism of export of CsgA and CsgB <i>via</i> accessory proteins CsgE, CsgG and CsgF.	133
Figure 4.6: Route to engineered curli production under the control of an inducible promoter.	133
Figure 4.7: CDC bioreactor ® used in this study.	136
Figure 4.8: Left- structure of CR. Right- CR indicator plate showing the effect of deletion of curli specific genes A, F and E from the genome of <i>E. coli</i> MC4100.	139
Figure 4.9: Plasmid map of PFF753CcsG.	142
Figure 4.10: Representation of relevant sections of plasmids PFF753CcsG, PFF753CcsGASau and PFF753CcsGASauGGS and their translated products showing the engineering of the C-terminal end of the produced CsgA protein.	143
Figure 4.11: SEM micrographs of deposited <i>E. coli</i> MG1655 ompR234 PRO Δ csgA :: PFF753CcsG without aTC induction from a liquid culture.	145
Figure 4.12: SEM micrographs of deposited networks of <i>E. coli</i> MG1655 ompR234 PRO Δ csgA :: PFF753CcsG with aTC induction from a liquid culture.	146
Figure 4.13: Maximum projection images of propidium iodide stained 72h static biofilms formed on a polycarbonate coupon surface by <i>E. coli</i> BL21-DE3.	148
Figure 4.14: 3D projection image of propidium iodide stained 72h static biofilm formed on polycarbonate coupon surface by <i>E. coli</i> BL21-DE3.	148
Figure 4.15: Maximum projection images of propidium iodide stained 72h static biofilms formed on polycarbonate coupon surface by <i>E. coli</i> W3110.	149

- Figure 4.16:** 3D projection image of PI stained 72h static biofilm formed on polycarbonate coupon surface by *E. coli* W3110. 149
- Figure 4.17:** Maximum projection images of propidium iodide stained 72h static biofilms formed on polycarbonate coupon surface by *E. coli* MG1655 ompR234 PRO Δ csgA 150
- Figure 4.18:** 3D projection image of PI stained 72h static biofilm formed on polycarbonate coupon surface by *E. coli* MG1655 ompR234 Δ csgA. 150
- Figure 4.19:** Maximum projection images of propidium iodide stained 72h static biofilms formed on polycarbonate coupon surface by *E. coli* MG1655 ompR234 PRO Δ csgA :: PFF753CcsgA without induction with aTC 151
- Figure 4.20:** 3D projection image of PI stained 72h static biofilm formed on polycarbonate coupon surface by *E. coli* MG1655 ompR234 PRO Δ csgA :: PFF753CcsgA without induction with aTC. 151
- Figure 4.21:** Maximum projection images of propidium iodide stained 72h static biofilms formed on polycarbonate coupon surface by *E. coli* MG1655 ompR234 PRO Δ csgA :: PFF753CcsgA with induction with 200 ng mL⁻¹ aTC 152
- Figure 4.22:** 3D projection image of propidium iodide stained 72h static biofilm formed on polycarbonate coupon surface by *E. coli* MG1655 ompR234 PRO Δ csgA :: PFF753CcsgA with induction with 200 ng mL⁻¹ aTC. 152
- Figure 4.23:** COMSTAT quantification results illustrating biofilm biomass, average thickness of biofilm, average thickness in entire area, surface roughness, surface area and surface area to biovolume ratio. 154
- Figure 4.24:** Maximum projection images of propidium iodide stained 24h flow system biofilms formed on polycarbonate coupon surface by *E. coli* MG1655 ompR234 PRO Δ csgA :: PFF753CcsgA without induction with 200 ng mL⁻¹ aTC. 160
- Figure 4.25:** 3D projection image of PI stained 24h flow system biofilm formed on polycarbonate coupon surface by *E. coli* MG1655 ompR234 PRO Δ csgA :: PFF753CcsgA without induction with aTC 161
- Figure 3.26:** Maximum projection images of propidium iodide stained 24h flow system biofilms formed on polycarbonate coupon surface by *E. coli* MG1655 ompR234 PRO Δ csgA :: PFF753CcsgA with induction with 200 ng mL⁻¹ aTC. 162
- Figure 3.27:** 3D projection image of PI stained 24h flow system biofilm formed on polycarbonate coupon surface by *E. coli* MG1655 ompR234 PRO Δ csgA :: PFF753CcsgA without induction with aTC. 163
- Figure 4.28:** Comstat analysis results from 24h flow biofilms describing biofilm biomass, average thickness of biomass. average thickness in entire area, surface roughness, surface area and surface area to biovolume ratio. 165
- Figure 4.29:** Maximum projection images of propidium iodide stained 24h flow system biofilms formed on polycarbonate coupon surface by *E. coli* MG1655 ompR234 PRO Δ csgA :: PFF753CcsgASau with induction with 200 ng mL⁻¹ aTC. 170

- Figure 4.30:** 3D projection image of PI stained 24h flow system biofilm formed on polycarbonate coupon surface by *E. coli* MG1655 ompR234 PRO Δ csgA :: PFF753CcsgASau with induction with aTC. 170
- Figure 4.31:** Maximum projection images of propidium iodide stained 24h flow system biofilms formed on polycarbonate coupon surface by *E. coli* MG1655 ompR234 PRO Δ csgA :: PFF753CcsgASauGGS with induction with 200 ng mL⁻¹ aTC. 171
- Figure 4.32:** 3D projection image of PI stained 24h flow system biofilm formed on polycarbonate coupon surface by *E. coli* MG1655 ompR234 PRO Δ csgA :: PFF753CcsgASauGGS with induction with aTC. 171
- Figure 4.33:** Comstat analysis results from 24h flow biofilms with no c-terminal tag, with a C-terminal SrtA tag and a C-terminal SrtA tag with a mediating flexible GGS linker region describing biofilm biomass, average thickness of biomass, average thickness in entire area, surface roughness, surface area and surface area to biovolume ratio. 173
- Figure 4.34:** Structural alignments of proteins CsgA, CsgASau and CsgASauGGS in line with the calculated β -barrel structure identified by Tian et al. 177
- Figure 4.35:** Diagram showing flow biofilm culture apparatus set up. Light yellow represents sterile media whilst darker yellow represents inoculum. 185
- Figure 4.36:** Example of thresholding in COMSTAT 2 of a single slice in a z-series image of a biofilm produced by *E. coli* (from this work). 187
- Figure 4.37:** Design of semi-overlapping primers for point, deletion and insertion mutations. 190
- Chapter 5:**
- Figure 5.1:** Structure development of ligands **L^x** for coordination to M = Re(I) and ^{99m}Tc(I) from amine terminated 4-amino-1,8-naphthalimides **N^x**. 197
- Figure 5.2:** Examples of cationic M= Re(I)/ ^{99m}Tc(I) complexes exhibiting *fac*-{M(CO)₃} geometry employed in bioimaging. 202
- Figure 5.3:** Left: structure of ELJ-*fac*[Re(CO)₃(L²)]BF₄, previously employed in *in-vitro* studies. Right: imaging of osteoarthritic cells undergoing apoptosis showing staining of mitochondrial membranes by ELJ-*fac*[Re(CO)₃(L²)]BF₄ using fluorescence from ELJ-*fac*[Re(CO)₃(L²)]BF₄ and transmitted light. 203
- Figure 5.4:** Neutral dirhenium pyridazine (left) and *fac*-[Re(CO)₃(N^N)Cl] luminescent complexes utilised in bioimaging. 204
- Figure 5.5:** Synthetic routes to ligands **L¹-L⁶** from commercially available 4-chloro-1,8-naphthalic anhydride. 207
- Figure 5.6:** Chelation of rhenium by the dipicolylamine chelating units present in **L¹-L⁶** (R group represents linker and naphthalimide) through substitution of the labile acetonitrile ligands in the precursor. 208
- Figure 5.7:** ¹H NMR spectrum of *fac*-[Re(CO)₃(L⁵)]BF₄ (structure top left) with diastereotopic methyl resonances starred at around 5.2 ppm and 4.4 ppm. 208

- 209
Figure 5.8: Selected region of ^{13}C NMR spectrum of for ***fac*-[Re(CO)₃(L⁵)]BF₄** showing metal carbonyl resonance c.f. 195 ppm and naphthalimide resonances c.f. 165 ppm.
- 210
Figure 5.9: UV-Visible absorption spectra of selected ligands and complexes in this study.
- 213
Figure 5.10: Normalised emission spectra of ligands **L⁴** and **L⁵** and their corresponding **[Re(CO)₃(L^x)]BF₄** complexes.
- 214
Figure 5.11: Radiolabelling of **L⁵** with ***fac*-[^{99m}Tc(CO)₃(H₂O)₃]⁺** to give complex ***fac*-[^{99m}Tc(CO)₃(L⁵)]⁺**.
- 217
Figure 5.12: Cell viability (MTS) assay for U-87 cells incubated with differing concentrations of ***fac*-[Re(CO)₃(L₅)]BF₄**.
- 221
Figure 5.13: Mitochondrial uptake of ***fac*-[^{99m}Tc(CO)₃(L₅)]⁺** both with and without CCCP membrane depolarisation.
- 222
Figure 5.13: Maximum projection representations of confocal fluorescence microscopy studies of MCF-7 cells incubated with ***fac*-[Re(CO)₃(L₅)]BF₄** and MDR and the overlay of both images.
- 223
Figure 5.14: SPECT and CT overlaid images with SPECT images acquired using the radiotracer ***fac*-[^{99m}Tc(CO)₃(L₅)]⁺**.
- 224

List of tables

Chapter 1:

Table 1.1: <i>E. coli</i> strains employed in study and their genotypes.	19
---	----

Chapter 2:

Table 2.1: Summary of surface functionalised ND particles produced in this section	49
Table 2.2: Optical absorption and emission properties of Nap-1 in water. Molar absorptivity (ϵ) shown of lowest energy absorption (bold)	50
Table 2.3: Colloidal properties of aqueous suspensions of ND-COOH and surface functionalised ND samples Nap-1@NDa-c .	52
Table 2.4: Normalised atomic composition as evaluated by XPS of Nap-1@NDa-c and ND-COOH .	55
Table 2.5: Optical characteristics of Nap-1@ND in comparison with Nap-1 .	58
Table 2.6: Particle size and zeta potential measurements of ND-COOH surface functionalised nanodiamond samples Ru-1@ND and Ru1-Nap-1@ND .	61
Table 2.7: Normalised atomic percentages found from processed XPS spectra of Ru-1@ND and Ru-1/Nap-1@ND .	62
Table 2.8: Concentrations of substrates in surface functionalisation of ND.	66
Table 2.9: Particle size and zeta potential measurements of surface functionalised nanodiamond samples ND1-4 and ND-COOH following purification.	69

Chapter 3:

Table 3.1: Summary of optical absorption and emission properties of luminophores Nap-1 and Ir-1 recorded in aerated water.	98
Table 3.2: Summary of optical properties of Nap-1/Srtpep1@ND and Ir-1/Srtpep1@ND .	103
Table 3.3: Size distribution analysis of aqueous suspensions of ND-COOH and surface functionalised ND samples Nap-1/Srtpep1@ND , Ir-1/Srtpep1@ND and Nap-1@NDc .	104
Table 3.4: Normalised atomic percentages of carbon, nitrogen and oxygen in Nap-1/Srtpep1 and Ir-1/Srtpep1 .	106

Chapter 4:

Table 4.1: Selected analytical techniques employed in biofilm analyses.	138
Table 4.2: Comstat evaluation of biofilms produced by <i>E. coli</i> strains over 72h in a static culture.	153
Table 4.3: Critical values from one-way ANOVA analysis of data described in Table 4.2 and Figure 4.23.	157

Table 4.4: Groupings from post-hoc Tukey-Kramer analysis.	158
Table 4.5: Comstat evaluation of biofilms produced by <i>E. coli</i> strains over 24h in a flow culture with (+aTC) and without (-aTC) induction with 200 ng mL ⁻¹ aTC.	164
Table 4.6: Critical values from one-way ANOVA analysis of data described in Table 3.5 and Figure 3.23.	168
Table 4.6: Comstat evaluation of biofilms produced by <i>E. coli</i> strains over 24h in a static culture.	172
Table 4.7: Critical values from one-way ANOVA analysis of data described in Table 4.6 and Figure 4.33.	175
Table 4.8: Groupings from post-hoc Tukey-Kramer analysis of the no tag, SrtA tag and SrtA tag with linker conditions.	176
Table 4.9: Antibiotic concentrations used.	180
Table 4.10: Overview of <i>E. coli</i> strains employed in study.	182
Table 4.11: Composition of PCR mixture employed in this project.	189
Table 4.12: Thermocycling conditions used for PCR reactions in this study	189
Table 4.13: Primers employed in this study.	191
<u>Chapter 5:</u>	
Table 5.1: Structures of ligands L ₁ -L ₆ .	199
Table 5.2: Metal carbonyl CO stretches observed for rhenium complexes fac-[Re(CO)₃(L^x)]BF₄ .	211
Table 5.3: Lowest energy UV-visible absorption maxima recorded for ligands L ₁ -L ₆ and for the corresponding [Re(CO)₃(L¹)]BF₄ complexes in acetonitrile, chloroform and water.	212
Table 5.4: Summary of luminescence emission properties of L ¹ -L ⁶ and corresponding [Re(CO)₃(L^x)]BF₄ complexes.	215
Table 5.5: Radiochemical yields for the formation of fac-[^{99m}Tc(CO)₃(L⁵)]⁺ at 70 °C in PBS buffer with respect to L ⁵ concentration.	

List of equations**Chapter 1:**

Equation 1.1: Beer Lambert law defining how the optical absorbance (A) of a compound in solution is dependent on the molar extinction coefficient (ϵ , $\text{dm}^3\text{mol}^{-1}\text{cm}^{-1}$), the compound concentration (c , $\text{dm}^3\text{mol}^{-1}$) and the pathlength of light (l , cm).

14

Chapter 2:

Equation 2.1: Equilibrium between CO and $\text{CO}_2 / C_{(\text{S})}$ at the shockwave cross-section.

31

Equation 2.2: Relationship between hydrodynamic radius (r_k), temperature (T) and translational diffusion coefficient (D). (k is Boltzmann's constant, and η is solvent viscosity).

41

Equation 2.3: Energy of photoemitted electron with energy E described by kinetic energy, binding energy and workfunction components.

43

Equation 2.4: Determination of binding energy (B.E.) from energy of incident X-rays, kinetic energy of emitted photoelectron (K.E.) and the spectrometer workfunction.

43

Equation 2.5: Description of final emitted intensity of photoelectrons I_s as a function of initial emission intensity (I_0), depth in sample (d) and mean inelastic free path of electrons (λ_i).

44

Chapter 5:

Equation 5.1: Determination of the partition coefficient, P , for a particular chemical species.

219

Equation 5.2: Determination of the distribution coefficient, D , at pH 7.4 for a particular chemical species.

219

List of abbreviations

Analytical methods

ELIZA	Enzyme linked immunosorbent assay
SERS	Surface enhanced raman scattering
CLM	Confocal luminescence microscopy
PCR	Polymerase chain reaction
SDM	Site directed mutagenesis
DLS	Dynamic light scattering
NTA	Nanoparticle tracking analysis
ZP	Zeta potential
XPS	X-ray photoelectron spectroscopy
TEM	Transmission electron microscopy
HPHT	High-pressure-high-temperature
LRMS	Low resolution mass spectrometry
HRMS	High resolution mass spectrometry
NMR	Nuclear magnetic resonance
MP-AES	Microwave plasma atomic absorption spectroscopy
SS-NMR	Solid state nuclear magnetic resonance
EM	Electron microscopy
SEM	Scanning electron microscopy

General terms

AuNP	Gold nanoparticle
AgNP	Silver Nanoparticle
SPIONS	Superparamagnetic iron oxide nanoparticles
ND	Nanodiamond
SrtA	Sortase A
fac	Facial (in terms of coordination geometry)
MO	Molecular orbital
UV	Ultraviolet
NIR	Near infra-red
ICT	Intramolecular charge transfer
MLCT	Metal to ligand charge transfer
HOMO	Highest occupied molecular orbital
LUMO	Lowest unoccupied to molecular orbital
FRET	Forster resonance energy transfer
GMO	Genetically modified organism
UDD	Ultradispersed nanodiamond
DND	Detonation nanodiamond
UCND	Ultrananocrystalline diamond
CVD	Chemical vapour deposition
DFT	Density functional theory
TGA	Thermogravimetric analysis
NV	Nitrogen vacancy
SiV	Silicon vacancy
IR	Infra-red
QD	Quantum dots
CCD	Charge coupled device
B.E.	Binding energy
K.E.	Kinetic energy

EWG Electron withdrawing group
SnAr Nucleophilic aromatic substitution
PDI Polydispersity index
mwco molecular weight cut-off
HDD hydrodynamic diameter
LC-MS Liquid chromatography with mass spectrometry detection
EPS Extracellular polymeric matrix

Chemical abbreviations

EDC 1-Ethyl-3-(3-dimethylaminopropyl)carbodiimide
NHS n-hydroxysuccinimide
DNA Deoxyribonucleic acid
RNA Ribonucleic acid
dNTP Deoxynucleoside triphosphate
MeCN Acetonitrile
TNT Trinitrotoluene
RDX cyclotrimethylenetrinitramine (Royal detonation explosive)
MTT 3-(4,5-dimethylthiazol-2-yl)-2,5-diphenyltetrazolium bromide
Dox Doxorubicin
Dex Dexamethasone
4-OHT 4-Hydroxytamoxifen
DMSO Dimethylsulfoxide
CHES N-Cyclohexyl-2-aminoethanesulfonic acid
Boc tert-Butoxycarbonyl
Fmoc 9-fluorenylmethyloxycarbonyl
TFA Trifluoroacetic acid
DIPEA diisopropylethylamine
NMP n-methylpyrrolidone
HBTU (2-(1H-benzotriazol-1-yl)-1,1,3,3-tetramethyluronium hexafluorophosphate
HoBt hydroxybenzotriazole
XDR X-ray diffraction
CR Congo Red
CV Crystal Violet
PI Propidium iodide
MTS (3-(4,5-dimethylthiazol-2-yl)-5-(3-carboxymethoxyphenyl)-2-(4-sulfophenyl)-2H-tetrazolium)
TMRE Tetramethylrhodamine ethyl ester
CCCP Carbonyl cyanide m-chlorophenyl hydrazone
BODIPY Boron-dipyrromethene

Dedication and Acknowledgements

This thesis is dedicated to the memory of Mr Reginald James Edward Spaak, a man whom, throughout my entire career of study and life provided no end of wit, reason and quiet encouragement. I will always owe you a debt of gratitude and hold you in the highest of regards.

I would like to first thank primary supervisor Professor Simon Pope. Your constant support, direction and mentorship was without doubt above and beyond what one could expect. Furthermore, I would like to extend a great deal of thanks to Dr Ian Fallis, whose input on a scientific and personal level was invaluable to this myself and this work. I would also like to thank Dr Robert Mart for his support particularly in aiding the development of the chemical biological techniques and skills necessary for this work, Professor David Williams for his guidance in biofilm studies and writing, and Dr Joel Loveridge who whilst he is no longer with us (and now in Swansea) has been of great help in the design and execution of this project. Also, thank you to Dr Samuel Adams for his help and collaboration throughout my PhD studentship.

In addition, I would like to thank the entire technical services team at the School of Chemistry in Cardiff University, who keep the wheels turning in the department, with particular thanks to Dr Rob Jenkins and Mr Thomas Williams for their input in the NMR and LC-MS help.

A big thank you to all my labmates past and present: Kait, Stokes, Lara, Ella, Chris, Sion, Andy, Yashar, Ben, Darren, Luke, Bria, Rob, Mark S, Mark D, Mauro, Gez, for keeping me at least partially sane throughout this degree.

I would like to express an enormous amount of gratitude towards all my family, particularly my Mum and Dad. Without your support and guidance, I would've been in no way able to even start this work, yet alone get through it. Finally, to my long-suffering girlfriend, Liz, who I met whilst studying chemistry nearly 8 years ago, throughout the bad and the good you have always been there for me and I am incredibly thankful. I could not have done this without you.

Chapter 1. Introduction

1.1. Project aims

In this thesis the feasibility of using synthetic biology to produce semi-synthetic functional materials incorporating a functional aspect is examined, demonstrating several novel tools to address this aim. Synthetic biology is the redesign of existing biomechanics and metabolic functions to yield unnatural but highly utilisable products, ¹ applies the ideas of chemical science and engineering in a biological context. The potential of synthetic biology to produce specific, novel materials has been identified as an extremely valuable route to new materials. ^{2,3}

The ease in which genetic material may be manipulated renders biological materials, particularly those based on proteins provide uniquely attractive aspects in their potential for customisability and design. Microorganisms can be manipulated *via* recoding to produce a range of materials which exhibit structures, reactivity and functions alien to natural products. Novel material design and synthesis through synthetic biology therefore allows for materials to be produced following design and coding of the genetic code of a microorganism exhibiting specific properties utilisable to produce hybrid-functional material composites, such as incorporation of specific chemical tags for functional component incorporation. Furthermore, biological materials have been consistently identified to exhibit extremely well regulated and designed architectures, lending them particularly suited to the production of layered polyfunctional hybrid materials.

1.1.1. Interest in hybrid functional materials

The development of functional, hybrid materials is of fundamental academic interest. In the development of such materials, functional characteristics and material properties can theoretically be tuned independent of one-another. As such, a *viable* route in the production of these materials is to incorporate within the structural matrix a functional component (for example nanoparticles, proteins or other chemical species) (Figure 1.1). Functional characteristics include (but are not limited to) an optical or magnetic (or a combination thereof) response or chemical lability for specific substrates.

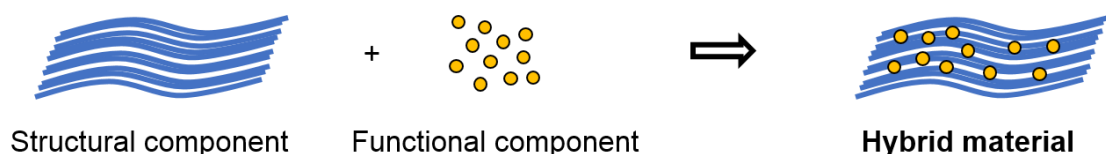


Figure 1.1: Schematic showing the production of hybrid materials through incorporation of a functional component within/on a structural component.

Specific material properties can be achieved through identification of the ideal material for an application area. Functional components similarly be attuned to a general interest area, for example in optically or magnetically responsive materials. In separating the functional and structural elements, a high degree of orthogonal control over the two properties can be achieved, giving way to the production of highly attuned specific advanced materials to address a particular application area.

A wide array of materials incorporating an exogenous structural element have been produced to enhance or impart a particular function on a material spanning several research areas. Incorporation of nanoparticles on/in polymeric materials provides a route in developing such materials to elicit an enhanced or novel response. Materials following this concept include: a silver nanoparticle/photosensitiser conjugated cellulose based material generating a material with photo responsive antimicrobial activity, ⁴ embedded antimony nanoparticle graphene oxide material demonstrating sodium ion storage capability, ⁵ poly(4-methyl-2-pentyne) based materials incorporating silica nanoparticles enhancing permeability and substrate selectivity. ⁶

The incorporation/immobilisation of proteins/antibodies on surfaces is a commonly employed strategy in bioassay/bioreactor development. A wide array of materials employed in bioassays have been commercially developed and are now available, including: antibody-labelled gold surfaces in extremely sensitive SPR antigen detection, ⁷ enzyme-linked immunosorbent assays (ELISA's) ⁸ and immobilised enzyme reactor systems utilised in enzymatic modification/generation of substrates *in-vitro*. ⁹

1.1.2. Potential for structurally ordered functional materials through layering

Polyfunctional materials are achievable through this strategy in through layering of the structural matrix component and subsequent incorporation of distinct functional components (Figure 1.2). In producing polyfunctional materials in this methodology, a degree of hierarchical structural control is possible through layering of materials with specific ordering of functional (and structural) elements.

Whilst multiple examples of hybrid functional materials demonstrating a single functional component have been described (Section 1.1.1), very little precedent exists in the production of layered materials which exhibit multiple functional components in a structurally organised fashion. A huge array of possible materials presents themselves, from artificial polymeric substances, naturally occurring surfaces and fibres as well as novel biologically inspired materials produced by genetically modified organisms.

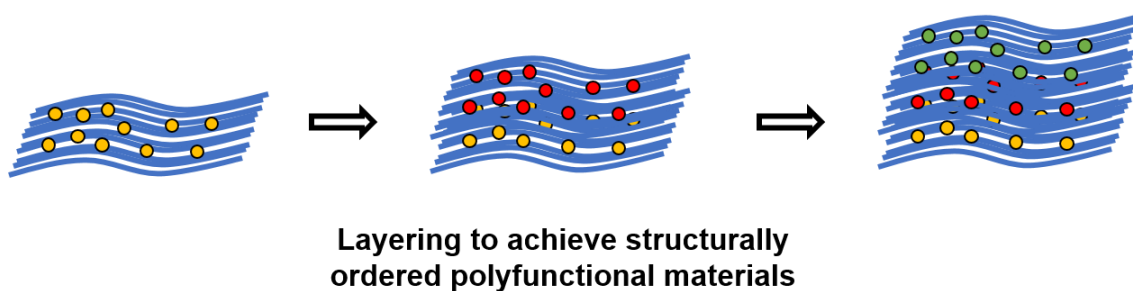


Figure 1.2: Schematic showing the production of a polyfunctional hybrid material incorporating functional components through structural layering.

1.1.3. Material production from a synthetic biology approach

Synthetic biology, the redesign of existing biomechanics and metabolic functions to yield unnatural but highly utilisable products, ¹ applies the ideas of chemical science and engineering in a biological context. The potential of synthetic biology to produce specific, novel materials has been identified as an extremely valuable forefront of modern scientific research. ^{2,3}

Biological materials, particularly those based on proteins provide uniquely attractive aspects in their potential for customisability and design, as the genetic code is now more accessibly altered providing theoretically inexhaustible routes to produce novel materials. Through the relative ease of genetic code modification through a plethora of techniques, microorganisms can be ‘hacked’, recoded to produce a huge potential range of materials which exhibit structures, reactivity and functions alien to natural products. Material production through synthetic biology therefore allows for materials to be produced following design and coding of the genetic code of a microorganism exhibiting specific properties utilisable for the production of hybrid-functional material composites, such as incorporation of specific chemical tags for functional component incorporation. Furthermore, biological materials have been consistently identified to exhibit extremely well regulated and designed architectures, lending them particularly suited to the production of layered polyfunctional hybrid materials.

1.1.4. Nanoparticles as functional components

Nanoparticles (NP’s), chemical species/structures existing in the ‘nano’ domain (relative to size, i.e. of the order of $\sim 10^{-9}$ m in size), present as ideal functional components in the production of hybrid functional materials through the strategy laid out in sections 1.1.1 and 1.1.2. NP’s can have a variety of compositions, including purely metal based examples (i.e. gold and silver nanoparticles, AuNPs and AgNPs

respectively), semiconductors (such as quantum dots), metal oxides (FeO particles) and main-group non-metallic elements such as silicon and carbon. Elemental arrays in the form of nanoparticles often exhibit broadly unique features and characteristics not seen for comparable macro-materials. For example, whilst gold is a relatively inert metal, very infrequently found as an adduct in nature, gold nanoparticles exhibit a high degree of chemical reactivity and have been widely employed as catalysts for a range of applications.¹⁰ Changes in optical and magnetic characteristics are also widely described, such as in superparamagnetism in iron oxide nanoparticles (SPIONS),¹¹ particle size and morphology dependent surface enhanced raman scattering (SERS) of gold nanoparticles,¹² particle size dependant absorption and luminescent properties of quantum dots.¹³

The core features and surface termination environments of nanoparticles dictate their key parameters (thermal/mechanostability, chemical reactivity and dispersibility in solvent). It is possible to alter the surface chemistry through a variety of methods, such as coating/functionalisation *via* electrostatic or covalent approaches. Their novel, exciting and highly tuneable properties present them as an ideal tool as functional components in hybrid materials. The availability of their surfaces to further modify them to be chemically active towards attachment to a functional matrix also provides a route whereby their core function can be maintained throughout attachment/incorporation within a material.

1.1.5. Theme of work

The desired properties of the biologically generated material component included the following:

- i- Self-assembly and structural control onto an abiotic surface from monomeric units
- ii- Chemical and mechanical resistance to exogenous stresses
- iii- Expression of a tag enabling a strong, covalent attachment of the functional component
- iv- Optical transparency/translucency, enabling for detection of optically active functional components

The proteinaceous material, amyloid, has the potential fulfil these criteria. Amyloids are fibrillar, highly ordered structures of protein consisting predominantly of a cross β -sheet structure¹⁴⁻¹⁷ formed through aggregation of one or more component proteins. Amyloids exhibit a generally unbranched fibrillar morphology, with fibre widths of

between 9-30 nm, which exhibit very strong mechanical properties, comparable to silk.¹⁸ In achieving the ability to produce a material able to self-assemble onto a surface, the amyloid based material curli was selected. Curli (Figure 1.3) is an adhesin amyloid structure produced by *Escherichia coli* (*E. coli*) in the interbacterial complementation and surface adhesion during biofilm development.^{16,19} Briefly, the protein component of curli is dominated by a single component protein, CsgA, which under extremely tight regulation by a series of dedicated chaperone, export and nucleator proteins aggregates to form extracellular amyloid fibrils. Biofilm development is highly dependent on curli production, and the extracellular matrix it assumed to contain a large quantity of the amyloid material, making the biofilm an ideal structural component for the desired hybrid material. Through incorporation of an enzyme tag at the C-terminal end of CsgA, it is possible to engineer an *E. coli* biofilm which can be covalently modified to incorporate an exogenous element, i.e. the functional component. Extended introduction into the biogenesis of curli, and the design of the controllable engineered curli producing strains is given in Section 4.1.

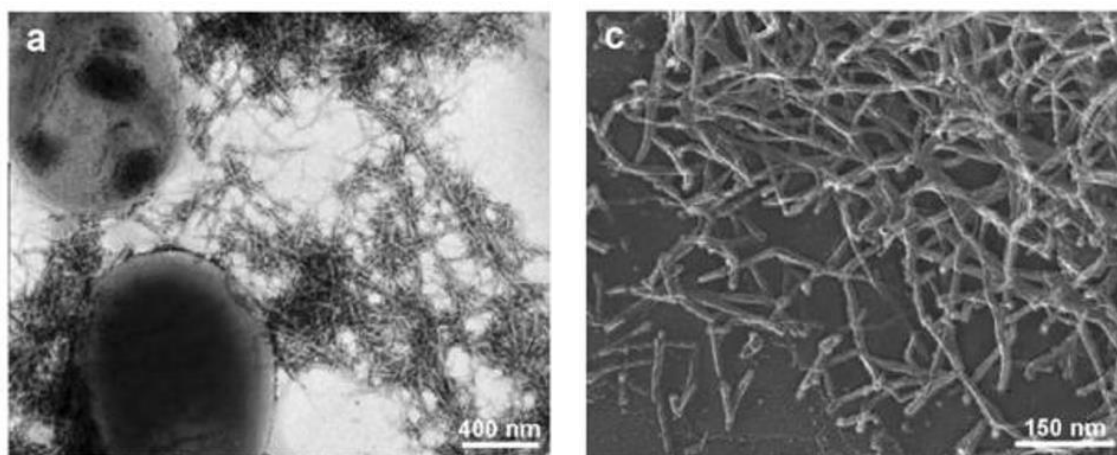


Figure 1.3: Structure of curli amyloid fibrils expressed by *E. coli* imaged by electron microscopy. Figure adapted from reference 16.

Several potential nanoparticle species present themselves as targets for functional components to incorporate into the curli biofilm of *E. coli*. In determining the ideal functional component, several ideal characteristics were identified:

- i- Robust stability towards chemical processing and temperature cycling
- ii- Available facile routes to surface functionalisation
- iii- Ability to impart a range of functionalities (such as optical response) and ligation tags to immobilise particle on the biofilm surface

- iv- Potential to include an innate (core) functionality distinct to its surface environment

Nanodiamond (ND), a nanoparticle material based on a core sp^3 hybridised carbon structure was identified as an ideal material satisfying these criteria. ND as a material retains some properties of macroscale diamond such as excellent resistance to mechanical and thermal stresses, whilst exhibiting unique characteristics due to its high surface to area ratio.²⁰ The surface of ND is highly modifiable through processing, and can yield a great degree reactive surface terminations such as carboxylates (-COOH).²¹ Polycarboxylated ND (**ND-COOH**) provides a particularly useful basis for development of ND probes providing a variety of functionalities which can be incorporated into the *E. coli* material matrix. Finally, defect sites in the core sp^3 lattice of nanodiamond, present from impurities during synthesis or induced by ion irradiation present potentially advantageous optical properties.²² A detailed introduction into the structure, synthesis and properties of nanodiamond is given in Chapter 2 of this thesis.

This study addresses the feasibility of produce a system whereby functionalised ND is to be incorporated into a controllably produced *E. coli* biofilm dominated by engineered curli fibrils. The model system designed (Figure 1.4) involves the design and production of an engineered *E. coli* strain able to controllably produce biofilm. Through production of an engineered structural protein which expressing an enzyme ligation tag, the biological material was designed to accept a specifically tagged substrate, the functional component. The ND functional component was produced through the covalent attachment of photoluminescent entities and the corresponding enzyme ligation tag to ND. By enzyme ligation, the two component ligation tags would be covalently linked, achieving the desired material.

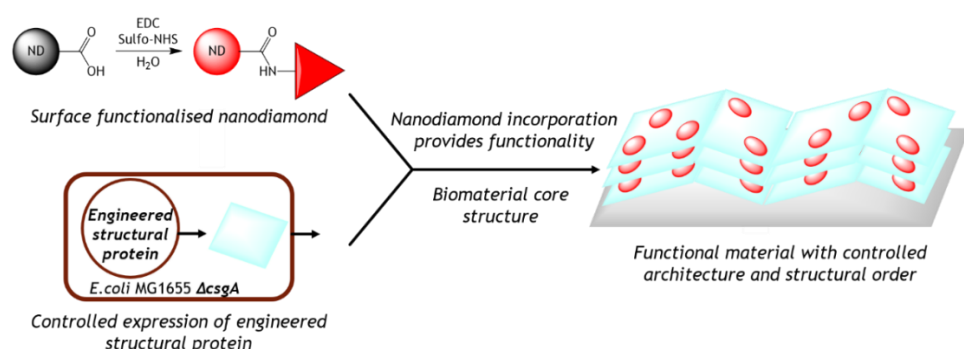


Figure 1.4: Designed synthetic biology approach to produce hybrid functional materials based on a biological (curli biofilm) material component and surface functionalised ND component.

The adhesive nature of curli fibres is well-suited to the development layered materials, with the target of incorporating different ND structural elements in distinct layers. Through subsequent biofilm formation and ND attachment steps utilising orthogonally functionalised ND species) a layered material consisting of the two elements is possible (Figure 1.5).

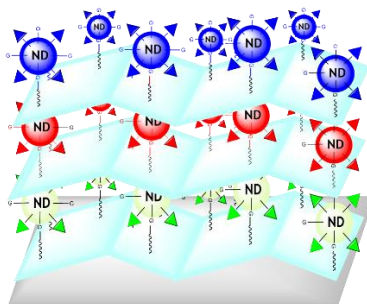


Figure 1.5: Potential to develop layered materials based on the curli biofilm structural matrix (blue sheets) and orthogonally functionalised ND structural elements.

Sections 1.1.5.1 – 1.1.5.4 give specific outlines of results chapters 2-5 of this thesis respectively, defining how they were designed to address the theme of this work.

1.1.5.1. Development of nanodiamond surface functionalisation methodology and characterisation of surface functionalised particles

Chapter 2 of this thesis addresses the synthesis of bespoke luminophores suitable for the attachment to ND and the development of reproducible methodologies in ND surface functionalisation, including comprehensive characterisation of surface functionalised species.

Whilst numerous examples in the literature exist of utilisation of surface functionalised ND species in an array of applications, established protocols to comprehensively and convincingly characterise the resulting particles are not well reported in the literature, and are therefore explored in detail.

ND (as solvent suspended particles) was developed as a functional component through attachment of functional species at the particle surface from the carboxyl-terminated form **ND-COOH**. Attachment of amine-bearing substrates was designed through EDC/NHS mediated amidation (Figure 1.6). Co-functionalisation of ND with two substrates was investigated, providing a platform for incorporation of functionality onto ND (from the first attached substrate) in conjunction with the enzyme ligation tag necessary for incorporation into the structural biofilm matrix.

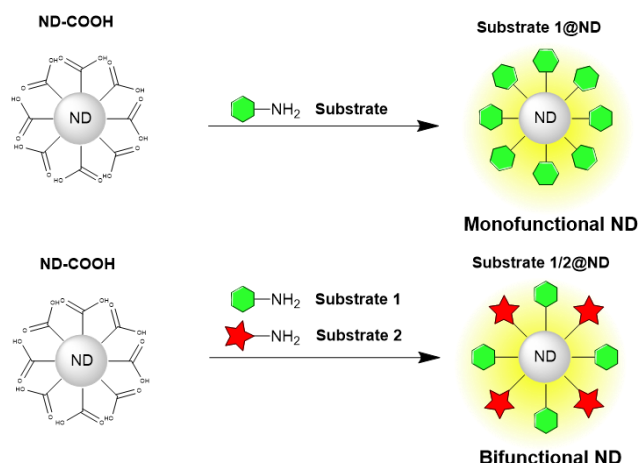


Figure 1.6: Schematic showing surface functionalisation of ND *via* proposed strategy.

Luminescent compounds (luminophores, introduced in Section 1.2.1) were chosen as ideal functional species to provide functionality onto ND, owing to the facile mode of detection. Several novel luminophores were synthesised for attachment to ND, including examples derived from organic species and metal coordination complexes.

1.1.5.2. Nanodiamond development for use as a functional component in the production of synthetic biology produced functional materials

Chapter 3 of this thesis addresses: the synthesis and characterisation of luminophore/enzyme tag co-functionalised ND particles through methods described in Chapter 2 and demonstrates the ability of Sortases (i.e. SrtA) to covalently modify the surface of the tagged ND particles through a model reaction utilising the synthesised Sortase Active peptide conjugate **[Ru(bipy)₂(L)]-LPYTGG**.

The enzyme ligation methodology based on SrtA from *S. aureus* was employed, which relies on enzymatic ligation of two component peptide motifs: LPXTG (where X is any amino acid) and (G)₄-NH₂ (detailed introduction of SrtA ligation technology is given in (Section 3.1)). Recombinant SrtA was recombinantly expressed in *E. coli*, isolated and stored at frozen aliquots. The two component peptide motifs were incorporated into the sequence of CsgA (the core structural protein of curli) and attached to the surface of ND respectively. Enzymatic ligation using SrtA should, in theory, result in a surface attached biofilm which incorporates the functional component (ND) in a covalent manner (Figure 1.7).

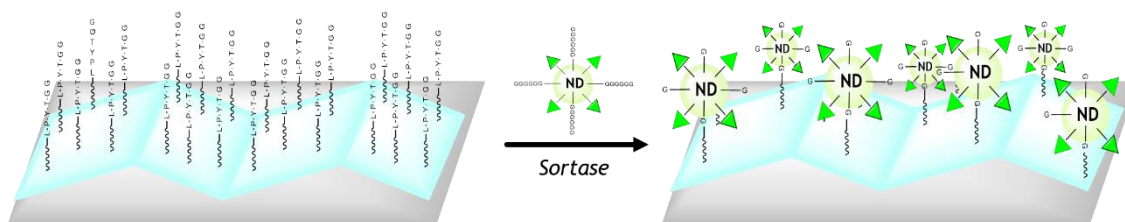


Figure 1.7: Schematic showing designed route to SrtA mediated incorporation of the appropriately functionalised ND functional component to the curli biological matrix.

1.1.5.3. Design, production and evaluation of curli based *E. coli* biofilm materials

Chapter 4 of this thesis addresses the development of a synthetic biology circuits suitable for the controllable expression of *E. coli* biofilms based on controlling curli expression. Briefly, the plasmid PFF753C was designed and produced through subsequent steps, containing the *csgA* gene under an inducible promoter. Engineered strains of the plasmid PFF753C which upon expression yield CsgA incorporating a C-terminal SrtA LPYTGG tag, both with and without a linker region between the wild-type protein and the SrtA tag.

Biofilm growth experiments were undertaken over different time periods and media flow conditions, and methodologies in reproducibly characterising biofilms by confocal fluorescence microscopy (CFM) were developed and utilised. Utilisation of a binary sorting biofilm quantification program, COMSTAT 2, yielded an array of quantified parameters relevant to biofilm formation, which were then statistically verified.

1.1.5.4. Utilisation of luminescent systems developed for advanced multimodal imaging

To complement work addressing the production of *E. coli* biofilm-based materials incorporating ND as a functional component, further work employing novel luminescent molecules based on those developed for surface functionalisation of ND were further developed to incorporate a dipicolylamine metal chelating unit.

This is addressed in chapter 5, a set of six ligands, with varied linker regions between the fluorescent and chelating units termed **L₁-L₆** (given in chapter 5) were produced and coordinated to rhenium (I), producing the corresponding *fac*-**[Re(CO)₃(L^X)]⁺** complexes. The photophysical properties of the developed ligands and corresponding complexes were evaluated. From its excellent water solubility, **L₅** (Figure 1.8) was identified as an ideal candidate for complexation with technetium to yield the corresponding bimodal (luminescent and radiological) probe, *fac*-**[^{99m}Tc(CO)₃(L⁵)]⁺**.

The rhenium and technetium complexes of L_5 were subject to extensive investigation in *in-vitro* and *in-vivo* imaging respectively, investigating their cell penetrating capabilities, cytotoxicities and *in-vivo* clearance routes.

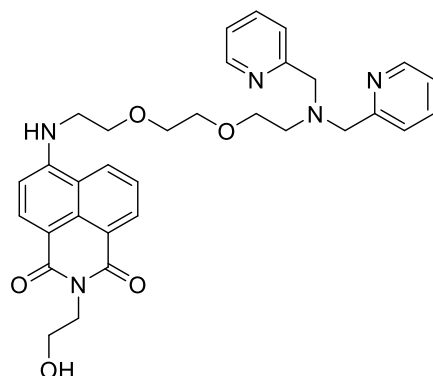


Figure 1.8: Structure of L_5 , the luminescent ligand suitable for chelation of *fac*-tricarbonyl $Re(I)$ and ^{99m}Tc .

1.2. Fundamental concepts employed in study

1.2.1. Luminescent materials and study thereof

Luminescent materials (luminophores) are compounds which exhibit emission of a quanta of light (photons) following excitation by a stimulus. Excitation of such materials can be achieved through a variety of conduits: absorption of light (photoluminescence), mechanical stimulation (mechanoluminescence), chemical reaction (chemiluminescence) and absorption of ionising radiations (radioluminescence). This study solely utilises photoluminescent materials, and as such luminescence is only discussed in this context, therefore luminophores or luminescent materials herein refers only to photoluminescent compounds.

1.2.1.1. Photoluminescence

Photoluminescence is, briefly, the process whereby a molecule absorbs light in the form of discrete packets of energy producing an excited state. This process is described by a Jablonski diagram (Figure 1.9).

The electronic (singlet) ground state (S_0) is excited to the singlet excited energy level (S_1 , S_2 and so on) *via* the absorption process. The Frank-Condon principle dictates that an electronic transition (in this case following photon absorption) occurs on such a short timescale ($\sim 10^{-15}$ s) compared with nuclear motion (i.e. vibration), it therefore occurs without change to the positions of nuclei in a particular molecular entity.²³ Therefore the absorption transition is 'vertical' (with respect to the inharmonic oscillator model of atomic/molecular energy levels). For this reason, the most probable absorption

transitions involve excitation to higher vibrational energy levels of the excited S_1 and S_2 electronic states, with the most probable transition being between the lowest vibronic energy level of S_0 to the first vibrational energy level of S_1 .²³

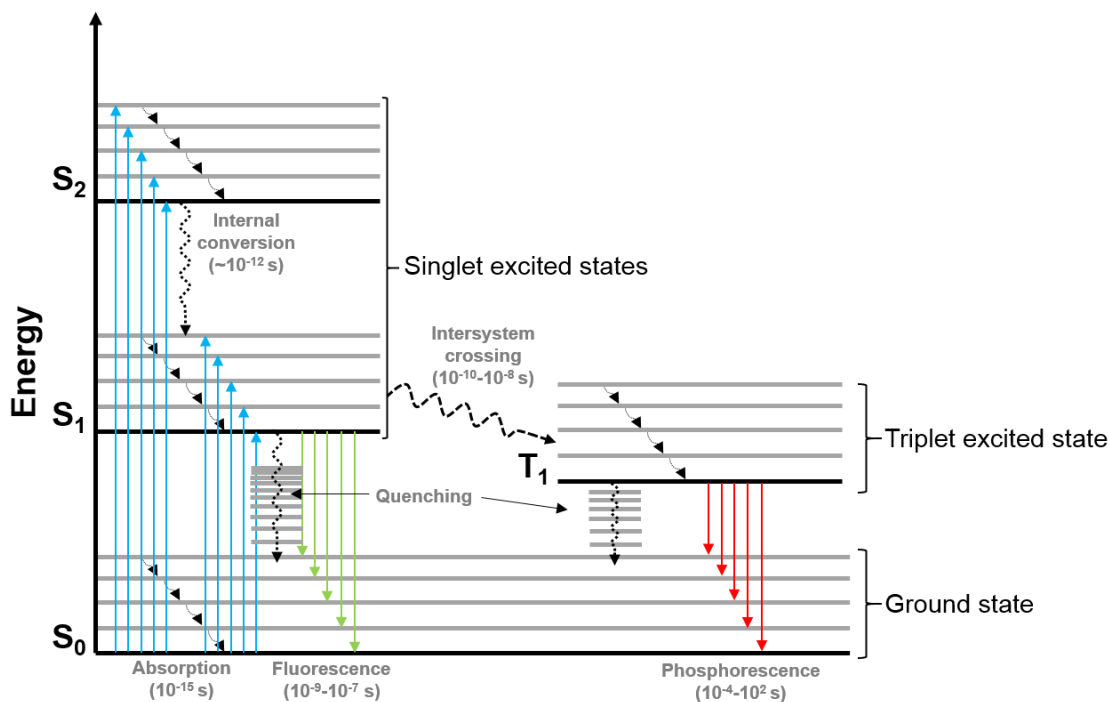


Figure 1.9: Example of a Jablonskii diagram showing radiative (solid straight lines) and non-radiative (undulating dotted lines) processes, including absorption (blue arrows), fluorescent emission (green arrows), phosphorescent emission (red arrows), internal conversion, intersystem crossing and non-radiative quenching.

Following excitation, the higher energy state of the molecule returns to the ground state through a variety of radiative (i.e. fluorescence) and non-radiative processes.

Fluorescence is formally emission from a singlet (S_1) excited state, typically occurring on a timescale between 10^{-9} - 10^{-7} s). Kasha's rule dictates that in most cases rapid (on the scale of 10^{-12} s) relaxation to the lowest vibronic energy level of the lowest electronic excited state of a given multiplicity (i.e. S_1 , a process termed internal conversion) prior to radiative fluorescent emission (on a slower timescale). Therefore, luminescent emission is typically independent of the excitation energy. Non-radiative complete relaxation (quenching) can occur through avenues such as vibronic relaxation, if the bandgap between the lowest vibronic energy level of S_1 and the higher vibronic levels of S_0 allows (not the case in luminescent materials). Again, the radiative emission process of fluorescence occurs such that return to ground state occurs to a variety of vibronic excited states of the ground (S_0) state.²³

Fluorescent emission typically results in emission of electromagnetic radiation at a lower energy with respect to that absorbed, giving a shift in wavelength of light absorbed and emitted in by luminophores. The difference in energies of the most probable (i.e. most intense) absorption and emission transitions is termed the Stokes shift. (Figure 1.10). Due to the mixing of vibronic and electronic energy levels, an array of absorption and emission transitions of different energies (corresponding to the energy difference between the two levels) occur, with different probabilities thereof, giving absorption and emission spectra respectively, characteristic of the particular luminophore. In certain cases, vibronic structure in the electronic spectra of luminophores can be identified through distinctive peaks.

Because of similar spacing of vibronic energy levels in the ground (S_0) and excited (S_1) excited states, absorption and emission spectra are commonly mirror images of one another (Figure 1.10).

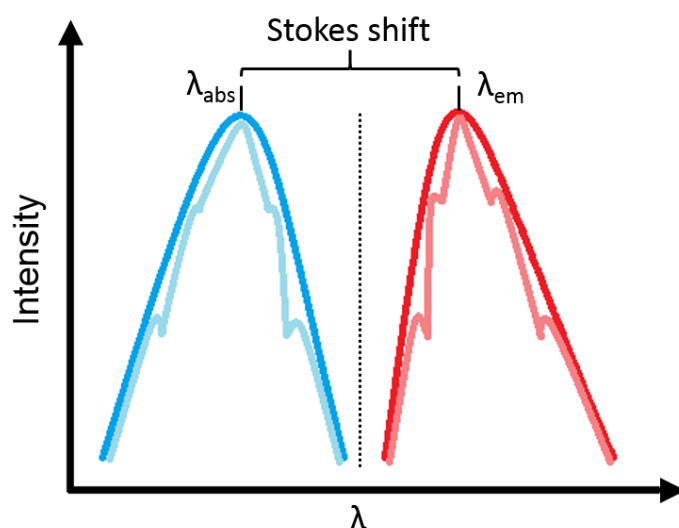


Figure 1.10: Demonstration of an absorption (blue) and emission (red) spectrum of a luminophore, with an example of vibronic structures (light blue and red) which can be observed.

A second radiative route to ground state emission is phosphorescence, the emission from a triplet excited state (i.e. T_1), following intersystem crossing from the singlet (S_1) excited state to the triplet excited state. Phosphorescent emission is generally of lower energy in comparison to fluorescence (due to a lower-lying T_1 excited state) and generally occurs at a much slower rate due to the spin forbidden nature of the intersystem crossing and emissive relaxation from the triplet (T_1) excited state to the singlet (S_0) ground state. Phosphorescent emission typically occurs in luminescent molecules

containing heavy atoms, which facilitate intersystem crossing *via* increase spin-orbit coupling. ²⁴

Several parameters detail key characteristics of a photoluminescent system. Maximal absorption ($\lambda_{\text{max}}/\lambda_{\text{abs}}$) and emission (λ_{em}) wavelengths detail the specific energies of associated transitions. The luminescent lifetime, denoted by τ_{obs} represents the time spent of the luminophore in the electronically excited state, and is a function of all kinetic parameters of the associated radiative and non-radiative processes involved. Finally, quantum yield (Φ_{obs}) is the overall efficiency of the photoluminescent process, depending on the relative probabilities of radiative and non-radiative processes, in effect the ratio of absorbed and emitted photons, given as a percentage.

1.2.1.2. Examples of fluorescent and phosphorescent luminophores

Luminescent species are those which contain appropriately spaced molecular orbitals (MO's) allowing for electronic excitation and radiative emission from absorption of light in the ultraviolet (UV), visible and near infra-red (NIR) of the electromagnetic spectrum. Therefore, luminescent properties are highly sensitive to the intermolecular chemical bonding environment and intramolecular interactions which perturb MO energies. Molecular species containing structures which effect efficient absorption characteristics in the appropriate energy range are termed as chromophores. Chromophores are typically extended π conjugated systems in organic molecules, and transition metal species exhibiting appropriate ligand field splitting parameters. Not all chromophores are luminescent in nature, as many are effectively non-emitting due to efficient quenching of the excited state by non-radiative means. Chromophores can exhibit one or multiple distinct absorption transitions, depending on the composition of the chromophore. The intensity to which a chromophore absorbs light in solution at a given wavelength is given by the Beer-Lambert law (Equation 1.1) and is dependent on the concentration of the chromophoric substance, path length of the sample and the molar extinction coefficient (ϵ). The molar extinction coefficient is dependent on the probability of that transition (or transitions) occurring and is a measure of the degree to which the chromophore absorbs light.

$$A = \epsilon c l$$

Equation 1.1: Beer lambert law defining how the optical absorbance (A) of a compound in solution is dependent on the molar extinction coefficient (ϵ , $\text{dm}^3\text{mol}^{-1}\text{cm}^{-1}$), the compound concentration (c, $\text{dm}^3\text{mol}^{-1}$) and the pathlength of light (l, cm).

Organic chromophores contain extended regions of π delocalisation; either as an alternating double bond motif (such as beta-carotene) or a (poly)aromatic system (naphthalene and anthracene Figure 1.11). Absorption in these chromophore species typically involves excitation to the π^* MO. Increased conjugation areas typically result in a lower energy π^* orbital, resulting in a reduced energy absorption (thus higher wavelength). Linearly conjugated species such as beta-carotene are typically not efficiently luminescent at room temperature, owing to the high degree of freedom for rotational and vibrational non-radiative emission. Polyaromatic species such as anthracene and naphthalene generally exhibit fluorescent emission following excitation.

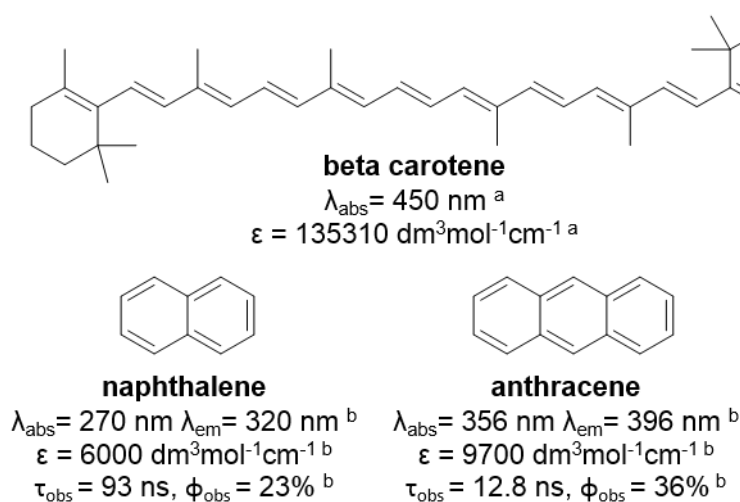


Figure 1.11: Structures and photophysical parameters of selected linear chromophoric and polyaromatic fluorescent species. ^a In acetone ²⁵. ^b In cyclohexane. ^{26,27}

A wide variety of substituent and solvent effects can interplay on the photophysical properties of solutions of aromatic luminophores. Solvatochromism is the effect where solvent identity (usually through polarity) modulates the spectral properties of a luminophore, through (de)stabilisation of the ground or excited states. Substituent effects include the modulation of existing (with respect to the unsubstituted species) transitions, or through the naissance of new transitions, due to now present MOs in the appropriate energy range (i.e. lone pair O/N nonbonding orbitals). A distinct transition, in select cases, occurs through intramolecular charge transfer (ICT) where an aromatic luminophore possesses both an electron withdrawing and electron donating substituent, for example in 4-amino-1,8-naphthalamide derivatives.

Phosphorescence at room temperature in solution typically involves inorganic complexes based around heavy transition metals, such as in octahedrally coordinate

compounds containing low-spin d^6 ligand field systems such as Re(I), Ru(II) and Ir(III) (Figure 1.12).

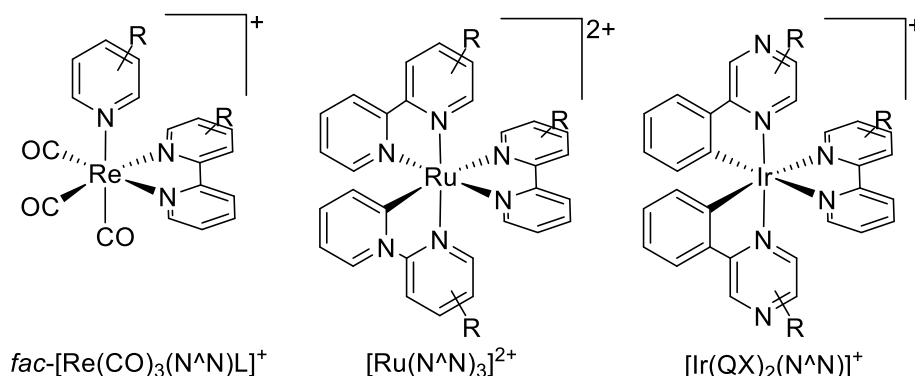


Figure 1.12: Examples of luminescent octahedral low-spin d^6 complexes of Re(I), Ru(II) and Ir(III). N^N = bipyridyl derivative ligand, QX = cyclometallating quinoxaline ligand, L = ancillary pyridyl based ligand.

In conjunction with higher energy ligand centred absorptions, the lowest energy absorption transitions from transition metal complexes such as the examples in Figure 1.12 occurs through metal to ligand charge transfer (MLCT). MLCT absorption in this case arises from the highest occupied molecular orbital (HOMO, in this case the metal centred t_{2g} MO from the ligand field splitting of the frontier d orbitals) to the lowest unoccupied molecular orbital (LUMO) centred around the ligand, a singlet excited state.

Intersystem crossing is facilitated through spin-orbit coupling with the heavy metal atom, followed by phosphorescent emission from the consequential triplet excited state. Ligand substituent effects, solvatochromism, metal oxidation state and availability of molecular oxygen (O_2) are all key parameters in the absorption and phosphorescent emission of these compounds. Molecular oxygen is of triplet spin multiplicity, and thus provides an efficient deactivation route of the triplet excited state producing singlet oxygen as a by-product, reducing phosphorescence quantum yield.

The luminescence of both organic and inorganic molecules is highly sensitive to their environment, making them ideal probes in a huge variety of functions. Their functionality is versatile, and a huge variety of luminescent systems have been applied in the probing of pH²⁸ and intramolecular distance (Förster resonance energy transfer, FRET),²⁹ detection of intramolecular interactions with macromolecular species (such as DNA³⁰ and proteins³¹) and in reductive/oxidative (redox) environment sensing.³²

1.2.2. Core techniques in synthetic biology utilised in study

Synthetic biology provides a tool in which the redesign of natural systems such as protein expression in bacteria can provide avenues to novel, engineered materials such as the sortase-tagged engineered curli biofilm designed in this project. A wide variety of techniques, stemming from molecular/chemical-biological and synthetic chemical techniques are applied, in order to achieve artificial genetic 'circuits' which produce a material utilisable in some fashion. This section aims to set out core techniques employed in this study, centred around plasmid-based routes to alter the normal function of *E. coli*

1.2.2.1. The genetic makeup of *E. coli* strains utilised in synthetic biology

E. coli is a rod-shaped, gram negative species of bacteria. ³³ A huge variety of genetic substructures exist ³⁴, including (non-pathogenic) commensal ³⁵ and pathogenic ³⁶ strains. Non-pathogenic strains have been developed for use in molecular/chemical biology research, almost entirely derived from the K-12 strain (isolated in 1922) ³⁷ or the B strain (isolated in 1945) ³⁸. The genome of *E. coli* K-12 MG1655 (Figure 1.13) was among the first genomes to be entirely sequenced in 1997. ³⁹

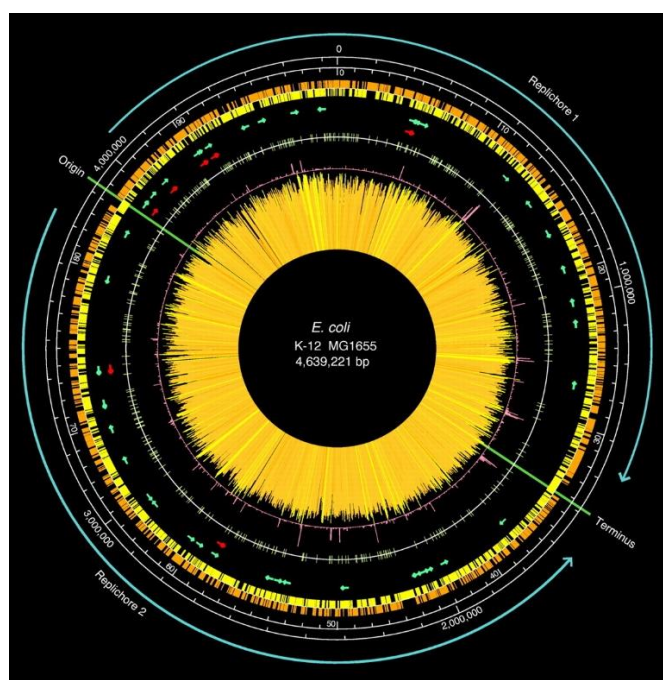


Figure 1.13: The overall structure of the *E. coli* genome. The origin and terminus of replication shown as green lines. Scales indicated coordinates in base pairs (outer) and centisomes (inner). Yellow and orange boxes indicate distribution of genes. Red and green arrows represent rRNA and tRNA encoding genes, from reference 39.

Where *E. coli* K-12 and some strains of this lineage (MG1655 and W3110 for example) are capable of recombinational genomic DNA incorporation, several *E. coli* strains have further been developed such as XL-1 blue and DH5 α containing mutations in the *recA* gene (giving the *recA1* gene) rendering them immune to genomic recombination.⁴⁰ Use of such strains for DNA cloning reduces risk of laboratory strains incorporating virulence factors from a variety of possible sources, as well as in keeping the genome (relatively) consistent across successive colonies and generations. A second gene, *endA* is also often mutated (*endA1*), inactivating the expression product, an endonuclease which is associated with the degradation of plasmid DNA.⁴¹ Therefore these strains are often employed as 'cloning' strains, facilitating the incorporation of exogenous DNA in the form of plasmids when manipulating the plasmid genomes.

E. coli BL21 (and derivatives thereof) derive from the B strain of *E. coli* and contain mutations in the *lon* and *ompT* genes, silencing protease enzymes and are typically employed in protein overexpression studies. MG1655 and its derivatives (including W3110) are more closely related to the parent K-12 strain (in comparison with XL-1 blue) and have precedent in biofilm studies with *e. coli*. A table of genomes of *E. coli* strains of relevance to this study is given in Table 1.1. A key derivative of BL21 is BL21-DE3, containing the λ DE3 lysogen which carries the gene for T7 polymerase under the control of the lac UV5 promoter.

In all cases, gene mutations yield strains of the *E. coli* bacterium which are vastly inferior in terms of growth rate and colonisation relative to wild-type strains, rendering them unlikely to cause a significant infection in users or equipment. This is critical in the employment of *e. coli* in genetic modification studies to prevent release of genetic material important in the responsible development of GMO technologies.

Table 1.1: *E. coli* strains employed in study and their genotypes.

Strain	Genotype ⁴²⁻⁴⁴
W3110	<i>F- LAM- IN(rrnD-rrnE)1</i> <i>rph-1</i>
BL21-DE3	<i>fhuA2 [lon] ompT gal (λ</i> <i>DE3) [dcm] ΔhsdS λ DE3 =</i> <i>λ sBamHlo ΔEcoRI-B</i> <i>int::(lacI::PlacUV5::T7</i> <i>gene1) i21 Δnin5</i>
XL-1 Blue	<i>recA1 endA1 gyrA96 thi-</i> <i>1 hsdR17 supE44 relA1 lac</i>
MG1655 <i>ompR234 PRO ΔcsgA</i>	<i>F- LAM- rph-1 ompR234</i> <i>PRO ΔcsgA</i>

1.2.2.2. Plasmids as a route to genetically alter *E. coli*

Plasmids are a small (in comparison with the genomic DNA component) circular loops of DNA which can be taken up by bacteria such as *E. coli* (Figure 1.14). Plasmids offer an ideal tool as a vector to genetically modify organisms such as *E. coli*, providing a facile route to include extraneous genetic constructs which relate to the expression of unnatural genes. ⁴⁵ Plasmids can be incorporated into *E. coli* through a transformation process with specifically prepared ('competent') bacterial stocks, most commonly through electroporation or chemical transformation (*via* heat-shock). ⁴⁶ Plasmid DNA can be isolated from *E. coli* separate from the genomic DNA component through procedures such as the 'miniprep', making them a valuable tool in which DNA can be inserted and retrieved from the bacterium with relative ease. ⁴⁷

Plasmids for use as gene vectors in *E. coli* require several components in order for reproduction and gene expression function, such as origins of replication (such as ColE1) and a promoter system. Promotor regions of DNA allow for the binding of RNA polymerase, necessary for the transcription process of the coding strand. Promoters can be inducible (requiring a specific event for transcription of a gene to occur) or constitutive (always allowing a level of transcription), and are not created equal in that a variety of promoters allowing for differing 'strengths' of transcription exist. ^{48,49} Inducible promoters are particularly useful when regulation of gene expression is desired (such as in the case of this study) and typically involve an operonic sequence such as a form of the *lac* operon

(Section 1.2.2.3). Finally, an antibiotic resistant gene acting as a selection marker is required for identification of colonies incorporating the plasmid through growth in selective media or on selective agar containing the antibiotic (through positive selection).

A huge variety of plasmids containing genes encoding for utilisable product, such as proteins not normally produced by *E. coli*, and empty vectors which provide the ability to insert an appropriate gene into the plasmid sequence through restriction enzyme ligation⁵⁰ or more advanced methods such as golden gate/ Gibson assembly.^{51,52}

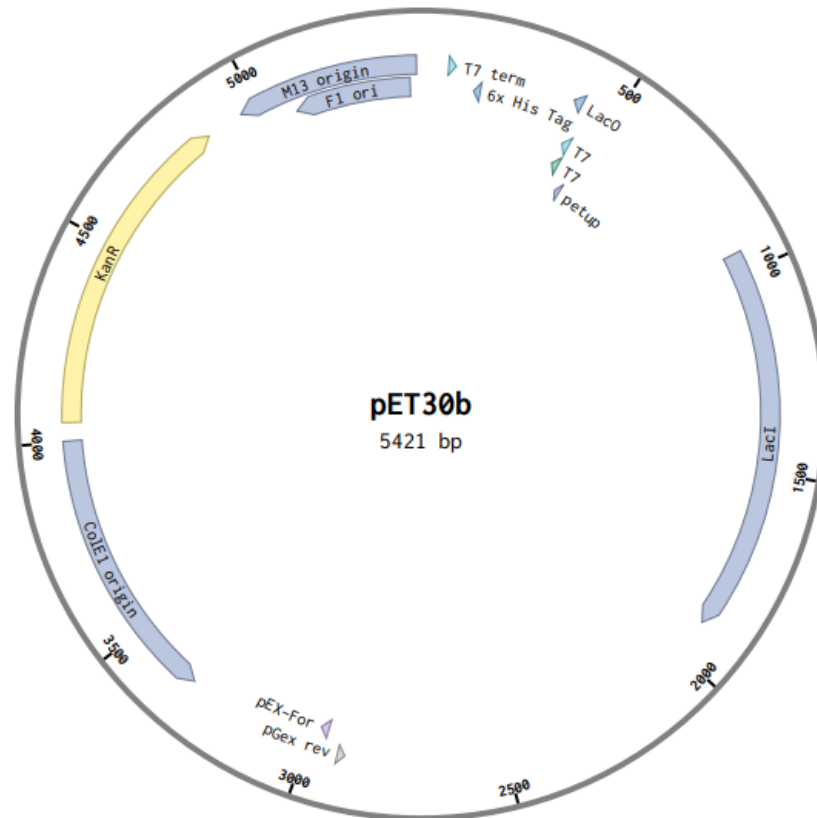


Figure 1.14: Plasmid map representation of pET30b plasmid utilised as an expression vector for genetic manipulation of *E. coli*. Plasmid map shows DNA sequences (and directions) for the origin or replication (CoIE1), a gene conferring resistance to kanamycin (KanR), the gene expressing the LacI repressor protein (LacI), and the inducible T7 promoter. Restriction enzymes HindIII, XhoI and XbaI allow for the incorporation of a gene fragment following the inducible T7 promoter.

Through the employment of plasmid technologies, the genetic makeup of *E. coli* can be easily altered, to perform such functions as gene overexpression to yield protein materials for use in studies. Through the employment of modified polymerase chain reaction (PCR) technologies, the gene sequence of plasmids can be altered to yield

multiple libraries of mutant proteins for a variety of uses, such as the elucidation of structure/function relationships in protein sequences.⁵³

1.2.2.3. Controlling gene expression *via* operons in plasmid technologies

Inducible promoter systems are commonly employed to achieve control over gene expression. Promoter systems based on the *lac* operon consist of the promoter sequence (binding RNA polymerase), an operator sequence followed by the gene sequence, often followed by a terminator sequence where RNA polymerase detaches, and the transcription process is ceased (Figure 1.15). The operator sequence is bound in the repressed state by a repressor protein (the repressor-operator complex), the complex of which arrests the ability of RNA polymerase to continue transcription and thus gene expression is halted. In the activated state, an activator co-factor binds the repressor protein in an allosteric site causing the repressor-operator complex to dissociate, enabling RNA polymerase to continue transcription and thus, the gene (or genes) are expressed.^{45,54}

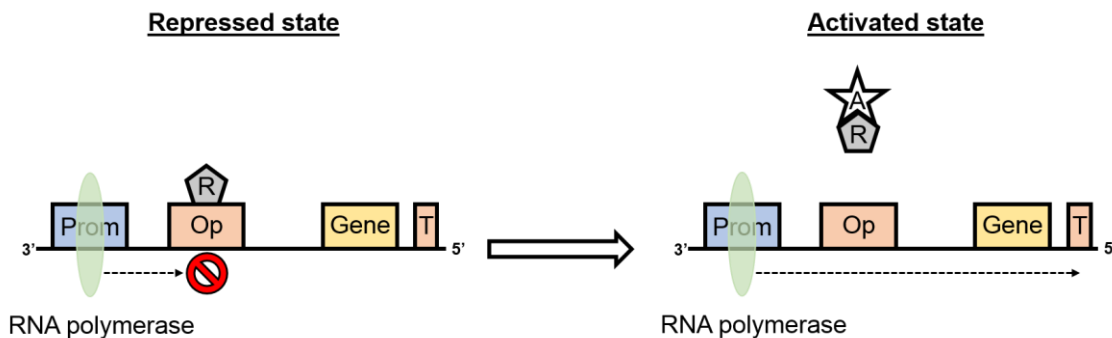


Figure 1.15: Selected parts of the *lac* operon showing the promoter sequence (blue box, Prom), operator sequence (orange box, Op), repressor protein (grey pentangle R), the representative gene and the terminator sequence (T). In the repressed state (right) RNA polymerase (green ellipsoid) is unable to complete 3'-5' transcription due to the repressor-operator complex. Binding of the activator molecule (i.e. lactose) causes the dissociation of the repressor-operator complex allowing for transcriptional activation (left).

In nature, the *lac* operon consists (most importantly) of the promoter sequence, the *lacO* sequence (operator) which is bound by the LacI protein (repressor protein, encoded by the *lacI* gene upstream to the *lacO* sequence) in its repressed state. Genes *lacZ* *lacY* and *lacA* are located downstream of the *lacO* sequence express the β -galactosidase and associated permease and galactosidde acetyltransferase enzymes essential for the processing of lactose as a food source for the prokaryote.⁵⁴ This confers the function to

the prokaryote of only utilizing energy sources to express the necessary proteins when the specific substrate (lactose) is present.

Operonic promoter systems such as T7, P_{TetO} and P_{ara}bad based on this concept have been developed, recognising different activator substrates with varied response levels and specificities.^{55,56} The T7 promoter system derives from the T7 bacteriophage, utilising T7 RNA polymerase (a more active polymerase) recognising the T7 promoter which through molecular biology techniques has been developed in to a *lac* operon analogous system recognising Isopropyl β- d-1-thiogalactopyranoside (IPTG), a non-metabolizable lactose mimic, as the activating co-factor.⁵⁶ The T7 promoter system is applied in all pET plasmid vectors. There is evidence suggesting a strong level of basal expression using the T7 promoter system, with regulatory ranges around 600 fold comparing expression in repressed and activated states often requiring high (1mM) concentrations of IPTG.⁵⁵

Lutz and Bujard derived the P_LTetO promoter system, which exhibits very tight transcriptional control of gene expression in comparison with that of the T7 promoter system. Derived the Tn10-derived *tet* resistance operon from certain strains of *E. coli* (normally controlling genes conferring tetracycline derivative based resistance where the antibiotics are present). Construction of the P_LTetO promoter system was derived from the P_L promoter which is in nature tightly repressed by *cl* (the lambda repressor). Through replacing the *cl* binding sites with those of the tetO operator sequences (binding the TetR repressor protein, with an allosteric site for tetracyclines), a promoter system recognising tetracycline was developed. Use of anhydrotetracycline (aTC) is preferred given its poor antibiotic activity and very low concentrations required (~100 ng/mL) to result in >5000 fold regulatory ranges.

This study employed both the T7 and P_LTetO promoter systems, depending on the desired level of transcriptional control. Where protein expression was desired for the isolation and utilisation of an enzyme species (i.e. SrtA), a pET vector containing the IPTG inducible T7 promoter system was employed as tight regulation was not a priority. Biofilm production controlled by curli (CsgA) production was desired to be tightly regulated, thus the plasmid conferring *csgA* expression contained the gene under P_LTetO control.

1.2.2.4. Site directed mutagenesis as a tool to alter the genetic code of plasmids

Site directed mutagenesis (SDM) is a tool based on PCR for effecting small-scale insertion, deletion and substitution mutations on either linear or plasmid DNA sequences.

PCR utilises a highly-thermally resistant DNA polymerase which recognises doubly stranded regions of DNA.

In the PCR reaction (Figure 1.16) the template DNA is denatured at high (~98 °C) temperatures, followed by reduction in temperature (~60 °C) to allow specific short single stranded DNA sequences (primers) to bind to complementary regions of the 3' and 5' strands. The double stranded regions are bound by the DNA polymerase at 72 °C which then allows for DNA polymerisation with single dNTP's in a complementary fashion in the 3'-5' directions to yield two new doubly stranded regions identical to that of the template DNA (a process termed extension). Through thermocycling between each temperature at individual steps, exponential amplification of DNA sequences is achieved.

Thermally resistant DNA polymerases such as *Taq* (from the extremophile *Thermus aquaticus*), *Pfu* (from the extremophile *Pyrococcus furiosus*) and primeSTAR™ (a proprietary enzyme from TaKaRa Bio Inc.) are utilised, able to both resist the extreme temperatures required for DNA denaturation and requiring high (>70 °C) temperatures in order to operate.⁵⁷⁻⁵⁹ PrimeSTAR™ was employed for all PCR reactions in this study, owing to its vastly reduced error rate and high efficiency in amplification.⁵⁹

Site directed mutagenesis is a form of the PCR reaction whereby PCR primers with a partial DNA mismatch to the DNA template strand (the plasmid) which can encode for the desired mutation. The mismatched DNA primers result in amplification of the mutated sequence. The mutated plasmid can then be transformed into *E. coli* where any 'nicks' in the sequence can be repaired following the plasmid DNA replication processes.

For example, a plasmid in this study (PFF753C(proto)) which carried the gene *csgA-LPYTG* expressing the protein CsgA with a C-terminal LPYTG tag was altered to yield the deletion mutant, the wild type *csgA* gene without the LPYTG tag (Figure 1.17). Through design of partially overlapping primer sequences the deletion product was achieved. This provides a tool whereby a library of similar, altered forms of plasmid encoding mutated proteins can be achieved.

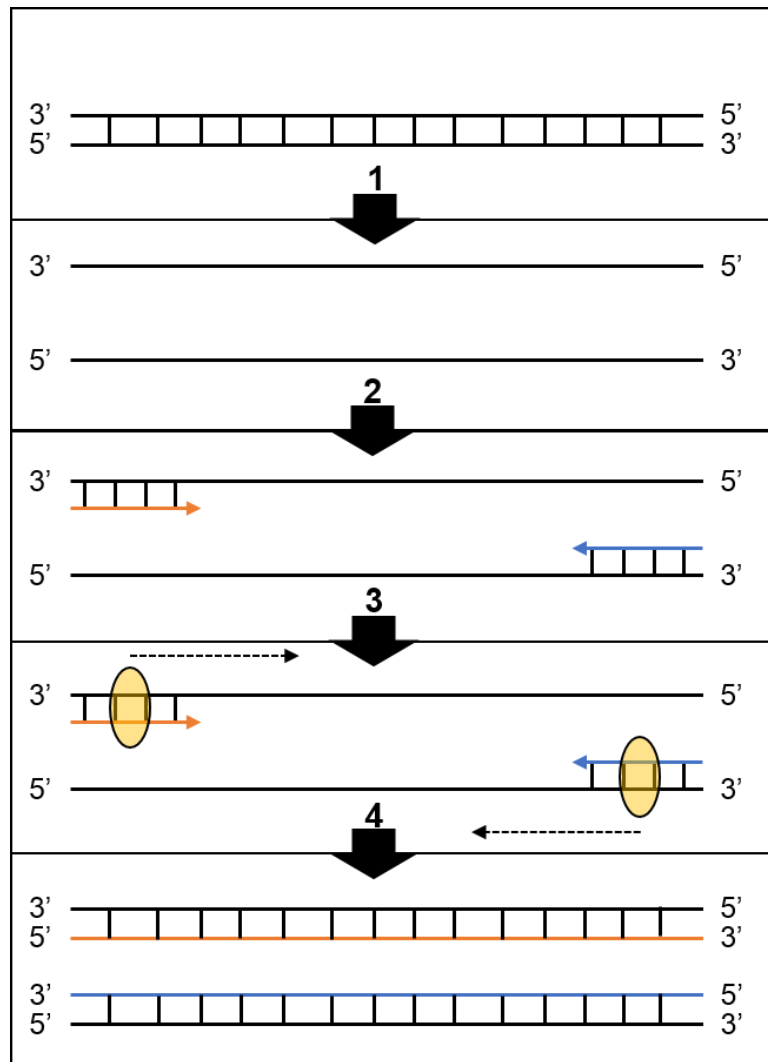


Figure 1.16: Schematic of a single cycle in the PCR reaction. **1:** Thermal denaturing of template DNA to single stranded DNA. **2:** Annealing of PCR primer sequences to DNA strands. **3:** Binding of DNA polymerase (yellow circles) to primer-DNA complex regions. **4:** Extension of DNA from primer annealed regions in the 3'-5' direction to yield two strands identical to the original template strand.

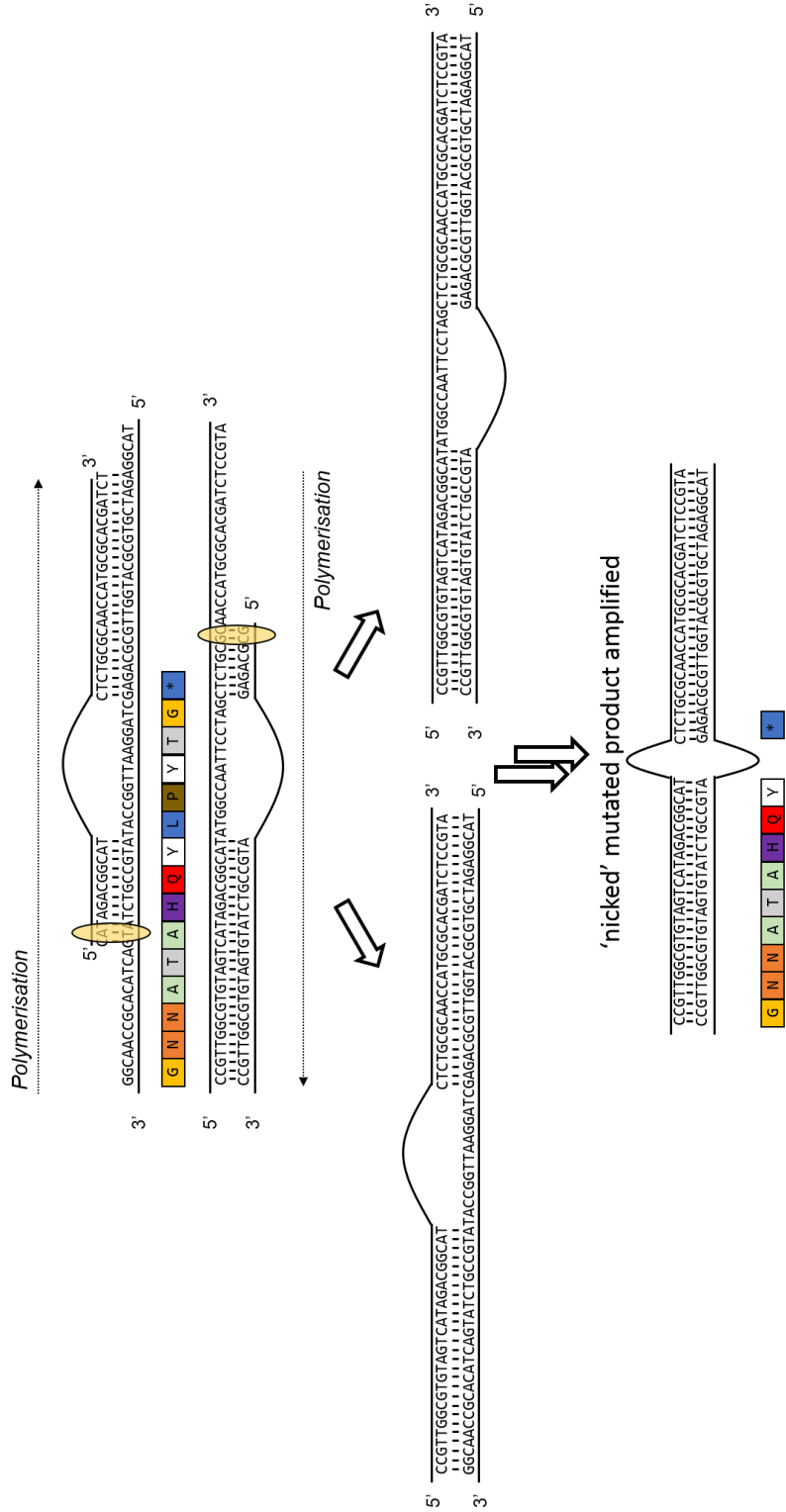


Figure 1.17: Schematic of mismatched PCR primer design to yield a mutated (deletion mutation) product by PCR.

Chapter 2. Surface functionalised nanodiamond: methodology development

2.1. Chapter aims

To provide a broad scope of substrates suitable for functionalisation of nanodiamond (ND), strategies employing organic and aqueous solvent systems are described in this chapter (Figure 2.1). The surface chemistry of ND can vary depending on the synthetic method and post-synthesis processing. Polycarboxylated ND (**ND-COOH**, average diameter *c.a.* 50 nm) was chosen as the ideal format of ND for surface functionalisation, due in part to its good dispersibility in both aqueous and organic (MeCN) based systems, and the facility to covalently attach amine bearing substrates *via* amide coupling. Luminescent materials were chosen as the ideal substrates for ND attachment, owing to the facility to identify successful attachment from evaluation of their photoluminescent properties in purified ND suspensions. Co-functionalisation was also investigated, as poly-functional surface functionalised ND suspensions provide a unique template in the development of functional, covalently immobilised ND based materials as described in Chapter 1.

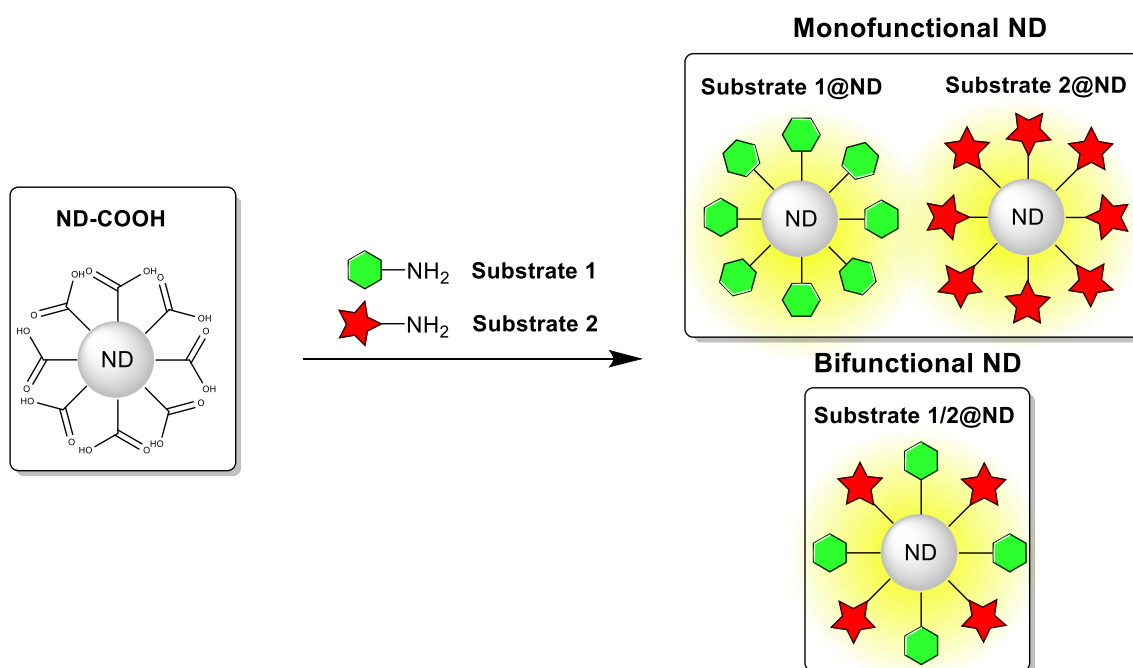


Figure 2.1: Route to covalently attached, surface functionalised ND suspensions exhibiting orthogonal fluorescent substrates 1 and 2, and co-functionalisation with both substrates.

Luminophores **Nap-1** and **Ru-1** (Figure 2.2) were synthesised, yielding amine bearing forms of the commonly employed luminophores suitable for covalent attachment to ND.

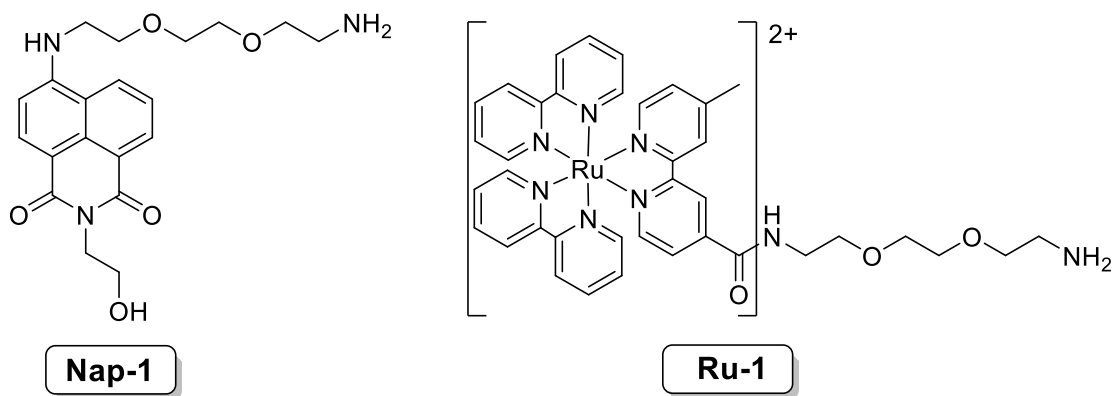


Figure 2.2: Structures of luminophores **Nap-1** and **Ru-1** utilised in this chapter as substrates for ND functionalisation.

Surface modification and functionalisation of ND in a variety of methods is reported in the literature (as outlined in Section 2.1.1), however with a strong focus on the application of dispersions produced. Functionalised ND materials produced in this chapter are produced in a range of systems (aqueous and organic, detailed further in Section 2.3), and comprehensively characterised by a wide range of techniques including:

- i- Evaluation of colloidal properties of resulting dispersions (DLS/NTA/ZP measurements)
- ii- Evaluation of the surface chemical environment of surface functionalised ND particles (XPS)
- iii- Evaluation of particle morphology and crystalline purity (TEM)
- iv- Evaluation of photophysical properties of attached luminescent species.

In producing and developing methodologies for the reproducible surface functionalisation and comprehensive characterisation of surface functionalised ND suspensions in this chapter, the platform for evaluating more advanced, functional ND probes in later studies is outlined. Furthermore, the surface functionalised ND species produced in this chapter have a wide range of applicability in further study, particularly in the development of brightly luminescent nanoparticles exhibiting surface associated luminescent properties orthogonal to an inert particle core. The ability to co-functionalise the surface of ND is of particular interest in the development of advanced polyfunctional ND species suitable for further modification or incorporation into other systems detailed in this overall study.

Further investigation detailed in this chapter addresses the issue of colloidal stability of surface functionalised dispersions. The ability to tune/improve the colloidal parameters of **Nap-1** functionalised ND systems was investigated through co-

functionalisation with taurine (2-aminoethanesulfonic acid), attempting to maintain surface electrostatic properties underpinning the colloidal parameters of the ND dispersions.

The aims of this chapter are therefore to investigate the ability to reproducibly functionalise and co-functionalise the surface of ND with a variety of substrates. Further to this, to develop comprehensive characterisation techniques for later use in production of enzyme labile ND dispersions suitable for incorporation into the biological materials designed for use in this study.

A paper published in the journal *Carbon* in 2019 is included in the appendix of this thesis.

2.2. Introduction

2.2.1. Nanodiamond as a highly modifiable, inert nanoparticle

2.2.1.1. Nanodiamond composition and structure

Nanodiamond is a nanoscale material consisting of sp^3 hybridised carbon, whose primary particle size is generally between 2 – 100 nm in diameter.⁶⁰ Generally termed in the literature as ultradispersed ND (UDD), detonation ND (DND), or occasionally ultrananocrystalline diamond (UNCD, usually specific for particles of less than 10 nm in diameter), ND is generally black or dark grey powder in solid form due to the high degree of light scattering from the small crystal.⁶⁰ Formed through high-pressure-high-temperature (HPHT) treatment of a carbon source either through the detonation of ordinance in a low-oxygen environment or through chemical vapour deposition (CVD),⁶¹ nanodiamond comprises of an sp^3 hybridised carbon core with a graphitic (sp^2) or amorphous carbon shell (Figure 2.3).⁶¹

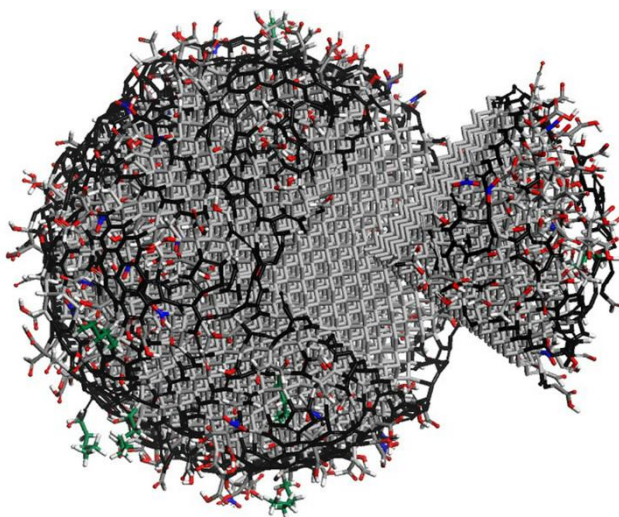


Figure 2.3: Representation of ND structure, showing core sp^3 hybridised carbon core (grey lattice), and mixture of surface graphitic and oxidised carbon species. Adapted from reference 61.

The degree of surface graphitisation is dictated by surface energy and, in turn, particle size. Crystalline sp^3 structures have been determined to be energetically favourable through theoretical studies (DFT) in the case where particle size is above ~1.9 nm in diameter (above 1100 atoms).⁶² sp^2 carbon content in small (< 3 nm in diameter) is also dictated by the particle morphology, with octahedral based structures retaining a larger amount of sp^2 carbon in comparison with cuboidal and cuboctahedral structures⁶³. The decrease in sp^2 carbon with particle size is due to the reduction in surface energy, where increasing particle size lowers the amount of surface atoms with dangling bonds with

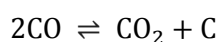
respect to the amount of 'core' atoms with complete hybridization. Calculations have shown that in particles with a diameter lower than 5 nm, surface atom content of nanodiamond structures is almost 20%.⁶⁴ In larger structures, partial surface graphitisation is observed in conjunction with O and N atom containing functional group termination, arising from the composition of explosive used and impurities in the detonation or CVD environment.⁶¹

Given the high surface atom ratio of ND and the large surface area to volume ratio, the surface of ND is remarkably more reactive than other carbon nanoscale materials. In comparison with other nanoparticle dispersions, the core carbon sp³ structure is remarkably inert, and resistant to degradation through thermal and oxidative decomposition.^{60,61,64} Surface modification of ND is, therefore, a key area of interest in producing stable nano-scaffolds for biological, chemical and sensory applications.

2.2.1.2. Synthesis of nanoscale diamond: detonation and CVD

NDs were first discovered from the high temperature, high pressure (HPHT) treatment of graphitic carbon and the detonation of ordinance in oxygen poor conditions.⁶⁵ Oxygen poor conditions are achieved through performing the detonation either under Ar, N₂ or CO₂ gas or in in water/ice, termed 'dry' and 'wet' syntheses, respectively. This results in incomplete oxidation of carbon-based materials. Mixtures of nitrogen containing explosives such as TNT and hexogen (or RDX) are generally used due to their negative oxygen balance which promotes incomplete combustion.⁶⁵⁻⁶⁸

The chemical process at the incredibly high temperatures and pressures experienced at the apex of the shockwave produced upon detonation in which the carbon source forms nanodiamond particles is complex. Calculations by Greiner *et al.* described a model whereby solid carbon is produced by oxygen poor explosives (O:C ratio <1). Detonation produces a mixture of products including N₂, H₂O and CO at the shockwave cross-section. Elemental forms at the shockwave cross-section favours the forward reaction of the equilibrium in Equation 2.1, due to the extremely high temperatures and pressures. For example, upon the detonation of 40% TNT/ 60% RDX mixture, when the rapid increase in temperature and pressure to approximately 2991 K and 26.1 GPa along the cross-section of the detonation shockwave. The same calculations predict elemental carbon is also consumed by the reverse reaction, with products equilibrating during expansion. This is quenched below 2000 K, 'freezing' the reaction products.⁶⁷



Equation 2.1: Equilibrium between CO and CO₂ / C_(s) at the shockwave cross-section.

Elemental carbon produced at the shockwave is predicted to be in the form of liquid carbon clusters (varying in size from 1-2 nm). As the temperature decreases, these clusters coalesce into larger droplets and crystallise into solid carbon. Once the temperature drops below the phase boundary between diamond carbon and graphitic carbon, the nucleation of diamond carbon is replaced by the deposition of graphitic carbon on the surface in addition to resulting in conversion of diamond to graphitic carbon, assuming the conditions are still such that the activation barrier can be surmounted⁶¹. The rate at which temperature and pressure decrease dramatically affects the composition of diamond nanoparticles; slower cooling (or more rapid decrease in pressure) will favour the production of graphite and conversion of diamond to graphitic carbon, whereas rapid cooling with respect to pressure decrease will favour the maintained of diamond phase carbon and reduce the amount of graphitic carbon in the detonation soot.

An alternative method typically employed in smaller scale ND production is chemical vapour deposition with typically hydrogen poor, argon rich CVD atmosphere⁶⁹. Utilising (~7%) methane in argon as the carbon source, nucleation of ND particles occurs on a clean Si/SiO₂ wafer surface, yielding a ND/Si 'film', which upon digestion and purification yields ND particles with narrow size-ranges depending on CVD conditions employed. Advantages of CVD ND synthesis include a greater degree of control over particle size ranges and the ability to incorporate heteroatom defects (such as N, B and Si) through modification of the feedstock gas balance (i.e. use of a small percentage of silane to achieve Si defects in the sp³ carbon lattice).⁷⁰

2.2.1.3. Post-synthesis purification

DND (detonation ND) raw product (the detonation 'soot') contains a large amount of graphitic carbon (25 – 45wt%⁷¹) as well as incombustible impurities such as metal oxides (1 – 8wt%⁷¹) originating from the detonator and walls of the combustion chamber. By comparison ND produced through CVD methods typically contain very little metallic impurities⁶⁶. Metallic impurities can typically be removed through treatment with mineral acids.

Removal of non-diamond carbon, either on the surface of ND or in the general detonation soot can be achieved through strong oxidative treatments, resulting in carboxyl terminations. Use of 'piranha solution'⁷² (sulfuric acid and hydrogen peroxide in a 4:1 ratio respectively), 'aqua regia'⁷³ (nitric and sulfuric acid in a 1:3 ratio) and other mineral acid mixtures have all been reported as 'wet' oxidative protocols, such as perchloric acid and sulfuric acid in a 1:1 ratio.⁷³ Treatment in ozone has also been shown

as a more environmentally friendly route to purify ND on an industrial scale.⁷⁴ However, it has been shown that simple high temperature treatment in air is very efficient in removing a large percentage of non-diamond carbon coating the surface of ND particles. Thermogravimetric analysis (TGA) by Osswald *et al.* described optimal mass loss of commercial ND samples when heating within an optimal temperature range of 400 – 450°C, where lower temperatures exhibit little appreciable oxidation and temperatures above 450°C result in non-selective rapid oxidation of all carbon species. Raman spectra (Figure 2.4) show the dramatic reduction of sp² carbon content of these samples when heating at 425°C for 5 hours, and it was calculated that the resultant samples contained in excess of 96% of sp³ carbon.⁷⁵

Oxidation in air in this matter yields particles with a high degree of surface carboxylate content, which exhibit a high degree of negative surface charge and water solubility. Particles treated in this manner are described as polycarboxylated ND or **ND-COOH** in reference to the carboxylated surface, and present as the starting material in the development of surface functionalised ND particle dispersions.

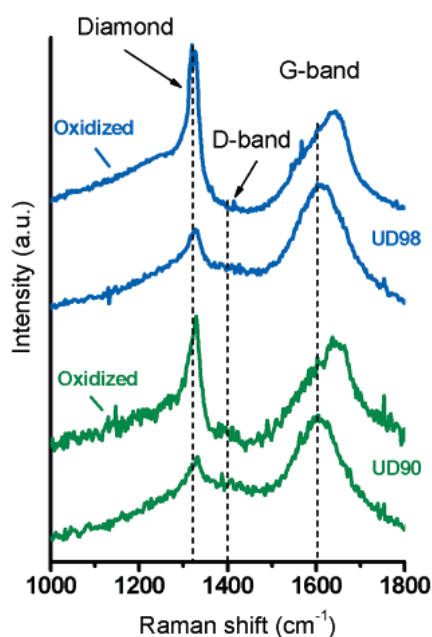


Figure 2.4: Raman spectra of UD98 (blue) and UD90 (green) ND samples prior to (upper) and following oxidation at 425 °C for 5 hours. Adapted from reference 75.

2.2.2. Nanodiamond surface termination

Although the lattice structures of diamond particles formed through detonation or CVD synthesis remain almost identical, the size and surface of the particles produced differs drastically depending on the method of production. Oxygen containing functional groups dominate, arising from the oxidation of amorphous carbon and other impurities from the ND surface during post-synthetic purification with strong acid/oxidising agent mixtures or oxidation in air or ozone.⁷⁶ The oxygen containing groups can consist of carboxylates (COOH/COO⁻), cyclic ketones and hydroxyls.^{77,76} Surface functional group distribution depends largely on the post-synthetic oxidation process: treatment with perchloric acid resulted in a higher density of cyclic-ketone terminations, whereas sulfuric acid treatment resulted in a higher density of carboxylate species.⁷⁶ In addition to oxygen based terminations, residual sp₂ surface carbon can remain after oxidative treatment in with mineral acids, heating in air and ozone, affecting solvent dispersal.^{75,78,79}

The (broadly) polycarboxylated (-CO₂H) surface of ND oxidized in air between 375 and 450 °C can be modified to produce a variety of different surface termination modes (-OH, -NH₂, -X) (Figure 2.5). The ability to produce such a variety of surface chemistries of ND yields particles with different properties in terms of solubility, reactivity and surface electrostatics properties, resulting in the variety of potential applications of ND particles.^{61,77}

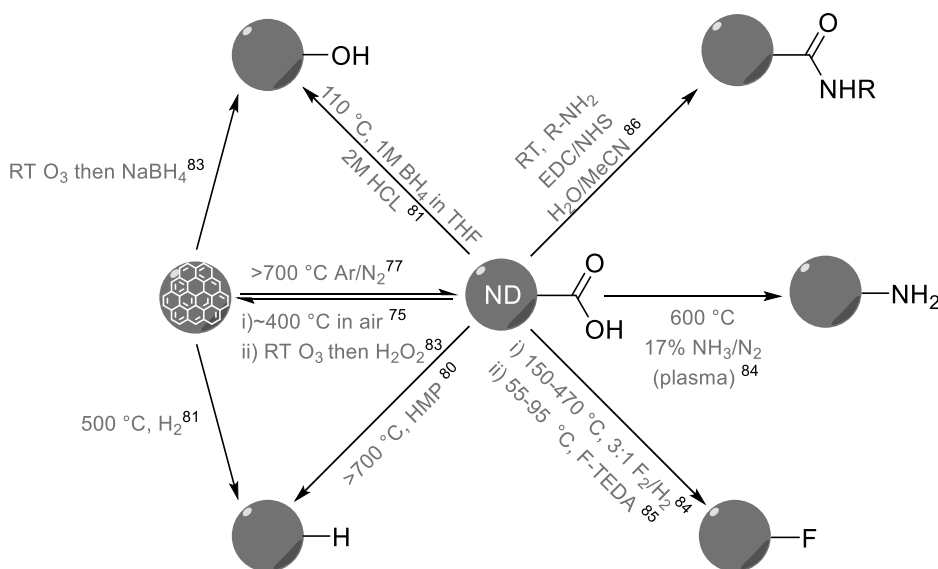


Figure 2.5: Routes to surface terminations from oxidized ND from references. HMP denotes Hydrogen microwave plasma.

2.2.3. Route to carboxylated ND surface functionalisation in aqueous and organic media

Surface functionalisation of carboxylated ND has been demonstrated *via* EDC/sulfo-NHS mediated peptide ligation (Figure 2.6) with an amine species (Gd^{3+} complex) by Shushkov *et al.*,⁸⁶ however no detail on the level of surface loading or functionalisation was reported. This presents an ideal route to ND surface functionalisation

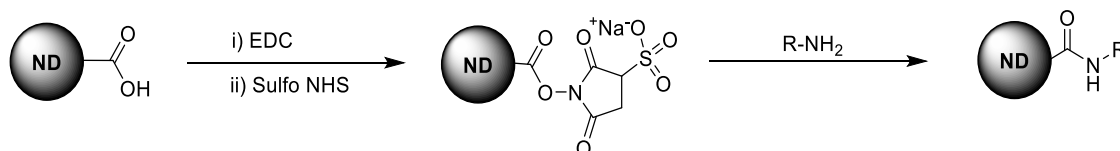


Figure 2.6: Surface functionalisation of carboxylated nanodiamond through the activation by EDC to form the NHS ester intermediate. Like other carbodiimide peptide coupling agents such as HBTU and DCC/DIC, the reaction proceeds *via* activation of the carboxylate moiety through deprotonation and subsequent nucleophilic attack thereof. However, where peptide synthesis often requires the use of large excess of the amine species, this can be avoided through the use of N-hydroxysuccinimide (NHS, or a sulfonate derivative when performed in water), forming a metastable NHS ester (Figure 2.7). This ester remains reactive towards good nucleophiles such as primary (and secondary) amines but is slower to hydrolyse by other less reactive species than the carbodiimide activated intermediate, improving reaction efficiency *via* increasing the lifetime of the activated species.

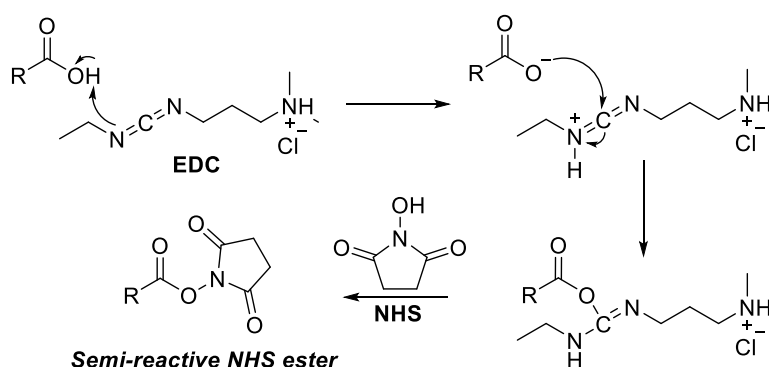


Figure 2.7: Carbodiimide activation of carboxylic acids to form metastable NHS esters.

Following nucleophilic substitution by the amine substrate, NHS is then regenerated, yielding the amide functionalised species (Figure 2.8).

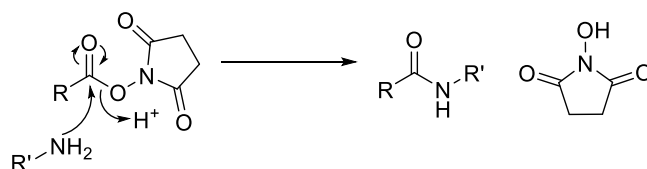


Figure 2.8: Nucleophilic substitution of NHS ester.

Functionalisation of the carboxylated ND surface in this manner presents a simple ‘one-pot’ method to yield covalently functionalised particles. The change in surface charge of the carboxylated ND must be taken into consideration, as not only does the resulting amide species remain neutral across the pH scale, but the intermediate carbodiimide species as well as the NHS-ester capped species can also be considered as neutral. Control of pH in aqueous media throughout the reaction is critical, as an acidic environment would result in inefficient ligation due to protonating the amine species. Elevated pH would not only result in a greater degree of hydrolysis of the NHS ester species, as well as encouraging an intramolecular side reaction by EDC to yield an unreactive by-product.

2.2.4. Applications of nanodiamond particle systems

Since emerging in the wider scientific community, ND’s have been employed in a wide array of applications including (but not limited too); nanocomposites^{87–90} and drug delivery^{91,92}. Nanodiamond particles exhibiting both intrinsic^{68,85,93–95} and surface associated⁹⁶ luminescence centres have been reported and applied in a variety of functions. A vast array of applied nanodiamond particle systems have been produced, covered by several reviews^{60,97,97,98}.

2.2.4.1. Nanodiamond nanocomposites

Nanocomposites based on the incorporation of ND, designed to improve specific properties (hardness and resistance to mechanical stress for example) and to incorporate any innate or imparted functionality on the ND particles. Incorporation of 1-5 wt% of detonation nanodiamond particles (without further purification) into vulcanised SKF-26 based rubber by Dolmatov showed the increase in rupture strength, attrition resistance and tearing.⁸⁹ Incorporation of ND into the polymer was achieved through addition of dispersed ND upon polymerisation, resulting in accelerated polymerisation.

Several other examples of increasing mechanical hardness have been demonstrated,^{99,100} however d’Almeida *et al.* reported the decreased strength following incorporation of ND into an epoxy matrix (10-30 wt%) by adding upon polymerisation. They reported fractures of the micro-surface of the polymer and attributed this effect to

the weak interaction of ND with the epoxy resin and agglomeration of ND during polymerisation producing an ill-distributed hybrid material. This question the applicability of high ND content nanocomposite materials in producing hard, durable materials, owing to the tendency of ND to aggragate during traditional polymer formation procedures.

To overcome this limitation Behler *et al.* reported the production of electrospun poly-acrylonitrile fibrils containing detonation ND with filling up to 60 wt%.⁸⁸ Polymerisation by electrospinning allows for reduced agglomeration, confining the ND particles in the well-defined fibre diameter. The controllable process yielded nanocomposite fibres containing well-distributed ND particles present at the fibre surface. Higher amounts of ND yielded more even distributions at the fibre surface. Transparent materials with ND content below 40 wt% were demonstrated, with a positive correlation in Young's modulus and hardness and ND content observed.

2.2.4.2. Nanodiamond in drug delivery

ND has been identified to exhibit relatively low cytotoxicity,^{61,101,102} advantageous in the development of biologically active ND systems. Owing to the wide array of surface terminations (and properties) and the dispersibility of polycarboxylated ND in water, ND presents a good platform in the development of drug delivery systems. A common theme in utilizing ND in this context is through the electrostatic association of target 'drug' compounds which can be effectively encapsulated in small degree aggregates of particles. In effecting de-agglomeration in response to a stimulus (i.e. pH), the activity of the surface associated drug can be attuned in certain conditions.

Huang *et al.* reported the controllable incorporation of doxorubicin (Dox) into agglomerates of polycarboxylated ND a well-established chemotherapeutic agent in cancer treatment through the addition of NaCl (Figure 2.9).⁹¹ The negatively charged carboxylate ND surface and positively charged doxorubicin is responsible for the surface association, however when in low-salt conditions the high dispersibility of the ND particles results in low adsorption. Through the addition of salt, and resultant 'screening' of both charges, reducing like-for-like charge-based repulsion, thus promoting aggregation. High degrees (~3.0wt%) of Dox incorporation were discovered from the reduction in UV-Visible absorbance around 470 nm (doxorubicin in solution) following the addition of salt. Desalination resulted in the reappearance of high levels of doxorubicin to similar levels prior to ND attachment, thus demonstrating the reversible incorporation process in response to salt content, suitable for drug delivery. Cell viability (measured by MTT assay, see 5.2.3.1) of ND-Dox conjugates was shown to be roughly double that seen for Dox alone, almost of similar level to that of the negative control

currently the imaging applications for ND appear limited. A few examples of intrinsically luminescent ND in imaging have been demonstrated to date.^{104,106}

Fu *et al.* used epifluorescence and brightfield imaging of HeLa cells, demonstrating uptake of 35 nm NV centre containing NDs ($\lambda_{em} = 650-720$ nm, Figure 2.10). General cytoplasmic uptake was observed for the particles. Luminescence intensity was observed to increase over two-fold across the single particle centres, utilising a laser power density of 100 W/cm^2 . Photostability measurements demonstrated particles were photostable at this intensity over 20 minutes.¹⁰⁴

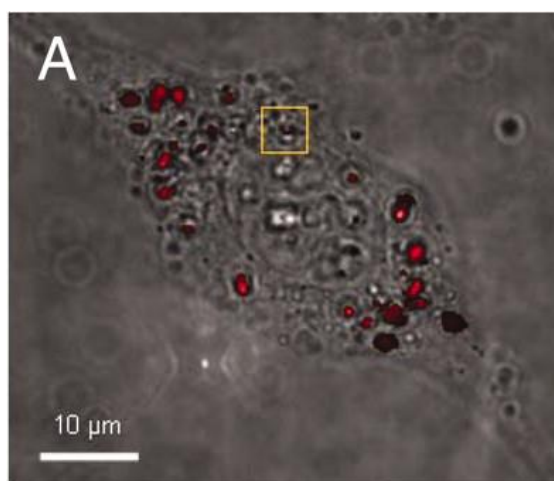


Figure 2.10: HeLa cells demonstrating uptake of 35 nm luminescent ND's. Image is a composite of epifluorescence ($\lambda_{ex} = 532$ nm, $\lambda_{em} = 650-720$ nm) and brightfield acquisitions. Adapted from reference 104.

A great deal of interest instead in fluorescent NDs in molecular probes has been cited in the literature, owing to the magneto-optical coupling of the luminescent NV centre.^{22,86,107} For example, the spin state of a surface attached Gd^{3+} complex was able to be detected through the change in luminescent properties of the innate NV centre.⁸⁶ Whilst these properties of fluorescent ND species present an interesting applicability in the development of advanced probes and materials based on ND, this is less applicable in terms of this study.

2.2.5. Methods used to characterise functionalised nanodiamond particles

Owing to the complex environment in surface functionalised ND particles, an array of characterisation techniques is required to accurately depict the properties of these particles. Whilst the inert sp_3 ND core remains unchanged throughout surface modification, the reactive surface dominates its chemistry. Following any modification or functionalisation, characterisation of the resultant particles through evaluating the

surface environment of ND remains the most informative insight into how particles have been altered.

In evaluating the colloidal stability *via* size determination through dynamic light scattering (DLS) and nanoparticle tracking analysis (NTA) and surface electrostatic properties (Zeta potential, ZP) one can obtain information on the surface environment of the resulting particles, as well as their applicability towards further functionalisation and utilization. X-ray photoelectron spectroscopy (XPS) probes the chemical environment of surface atoms, through measuring core-shell electron binding energy to the nucleus. This allows for distinction of elemental environments and calculation of atomic constitution of the ND surface environment. An advantage of attaching luminescent species onto the surface of ND is that it allows for verification by luminescent spectroscopy. Surface attachment can be confirmed by the presence of similar luminescent properties of attached luminophores. Transmission electron microscopy (TEM) allows for verification that no (or little) non-diamond material is present in samples (verifying purification), as well as investigating particle morphology.

2.2.5.1. Colloidal stability (DLS/NTA/ZP)

Colloidal stability of a nanoparticle dispersion can be measured through determination of average particle size in dispersion and measurement of zeta-potential, a surface electrostatic property.

DLS evaluates the particle size distribution (as the hydrodynamic radius, r_k) through the change in intensity of light scattered at 173° (from the monochromatic incident light source, 633 nm) by particulates in solution as they change position in 3D space according to Brownian motion. Hydrodynamic radius is derived from a reciprocal function of the translation diffusion coefficient (Equation 2.2), measured from the change in scattered light intensity as a function of time (the correlation function). Average particle sizes measured by DLS are often prone to over-estimation, DLS is relatively intolerant of polydisperse samples, as it relies on the Rayleigh scattering of light from particles to directly evaluate particle size. Rayleigh's approximation states that the intensity of scattered light is proportional to the sixth power of the particle diameter, and thus larger sizes will scatter with much greater intensity, giving a false weighting on larger particles when building up a distribution. Estimations can be used to evaluate particle distribution by number (i.e. by number of distinct particles), or by volume (i.e. particle size as a function of volume measured), as opposed to size by intensity, however polydisperse particles or impurities such as dust or air bubbles can severely hamper these

estimations, as the raw information detected by the DLS instrument is still light intensity detected at 173° ¹⁰⁸.

$$r_k = \frac{kT}{6\pi\eta D}$$

Equation 2.2: Relationship between hydrodynamic radius (r_k), temperature (T) and translational diffusion coefficient (D). (k is boltzmann's constant, and η is solvent viscosity).

Where DLS derives hydrodynamic radius directly from changes in light scattering intensity, NTA uses light scattering from particles in solution from a 638nm laser incident light source to project an image of particles in the XY plane, detected through a microscope-attached CCD camera (Figure 2.11). The images built from scattered light do not directly provide size information, but through tracking the movement of projections of individual particles in the XY plane, analysis software can produce an estimate of hydrodynamic radius, again relying it's derived relationship with Brownian motion (or D, the translational diffusion coefficient), shown in equation 1. In addition, given the dimensions of the window in which particles are detected in the XY plane, an estimation in particle concentration (as number of particles against volume) can be derived from the number of detected tracks.

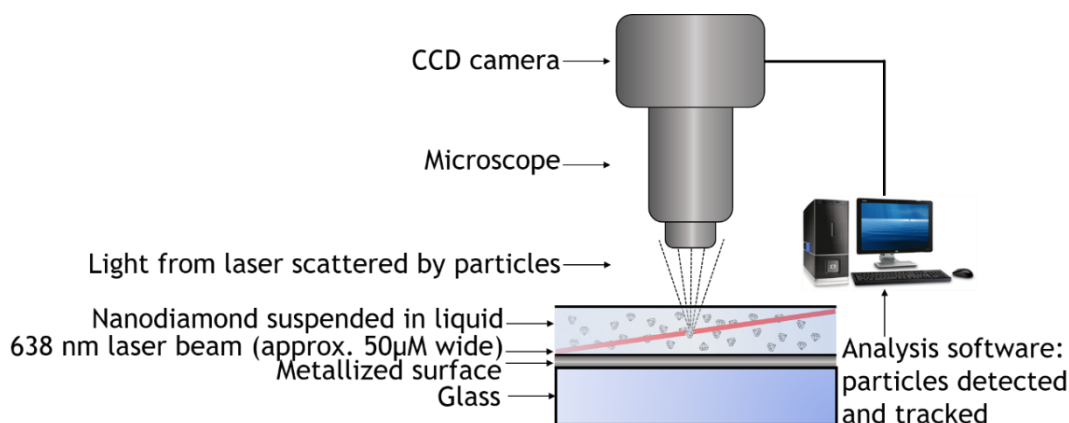


Figure 2.11: Schematic diagram of the NTA setup.

Where both methods derive a hydrodynamic radius distribution from the Brownian motion of particles, NTA does not directly use information from scattering intensity to do so, instead tracking the movement of projections produced from the scattering to evaluate size distributions. Therefore, NTA overcomes problems posed by the much greater scattering of larger samples, and as such allows for more accurate size distribution measurements of polydisperse samples. However, the far reduced scattering intensity

of smaller particles means that particles below ~30 nm in diameter do not project sufficiently well for particle tracking analysis to be undertaken, giving a lower-end size limit of this technique. NTA also infers several other limitations, namely the fact that particles are only projected in the XY plane, and therefore movement in the Z plane is not detected, meaning Brownian motion is not correctly evaluated.

Closely associated with colloidal stability is the ZP of ND particles. ZP is the change in electrostatic potential at the interfacial layer between the nanoparticle and solution, throughout the 'slipping plane', an imaginary layer of the solvent close to the particle, where an accumulation of electrostatic potential of solvent molecules crowding the particle depending on the charge and polarity of both solvent and surface-groups will drop off as you move away from the particle. In the case of the water, a protic, polar solvent, largely positive or negative ζ -potential values confer a stable dispersion, generally more than ± 35 mV. ZP is dependent on pH in aqueous dispersions, as the concentration of charged species (OH^- and H_3O^+) will affect the electrostatic crowding of the particle in dispersion. Changes in surface termination of ND, and functionalisation where a significant change in polarity (or in fact, polarizability) occurs. For example, -COOH terminated ND (from either air oxidation, mineral acid treatment or ozone treatment) are typically highly negative (> -40 mV)⁶⁶, whereas hydroxylated ND typically presents with a positive ZP (~30 mV). ZP measurements provide an informative tool in evaluating the surface environment of ND.

2.2.5.2. Surface chemical environment (XPS)

X-Ray photoelectron spectroscopy (XPS) is a technique whereby core-shell electrons in an atom are ejected in response to excitation with an X-ray source of constant energy, to determine the kinetic energy spectrum of emitted photoelectrons (Figure 2.12) in a vacuum.

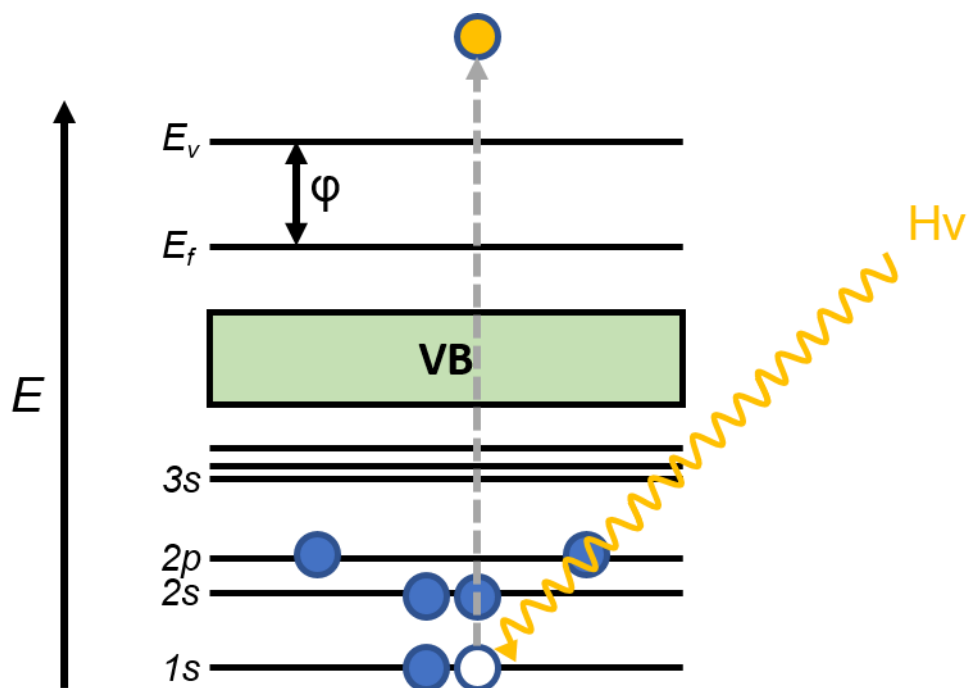


Figure 2.12: Diagram describing the photoelectric ejection of a core 1s electron from a solid carbon sample through irradiation with an X-ray source.

The total energy of a photoemitted electron can be described as a combination of kinetic energy (K.E.), binding energy (B.E.) and workfunction (ϕ) (in solid samples) (Equation 2.3). The workfunction is a property of a solid, describing the minimum energy required to take one electron from the highest occupied level in the valance band (the fermi level E_f) to a point in vacuum close to the solid surface (specific to a bulk solid surface, such as gold-foil commonly employed as a substrate surface for XPS analysis).

$$E = \text{K.E.} + \text{B.E.} + \phi$$

Equation 2.3: Energy of photoemitted electron with energy E described by kinetic energy, binding energy and workfunction components.

The experimentally determined parameter, the binding energy (B.E.) of the core shell electron can be determined from Equation 2.4, where the binding energy is determined by measuring the kinetic energy of the emitted photoelectron as a function of the energy of the incident X-ray source minus the specific spectrometer workfunction (specific to the substrate and spectrometer used).

$$\text{B.E.} = h\nu - \text{K.E.} - \phi_{\text{spectrometer}}$$

Equation 2.4: Determination of binding energy (B.E.) from energy of incident X-rays, kinetic energy of emitted photoelectron (K.E.) and the spectrometer workfunction.

Equipment setup involves mounting of sample onto a conductive surface (in the case of ND dispersions, dropping and drying of particles onto a gold surface), and constant bombardment with a low energy electron gun in order to avoid shifting of binding energy through charging (as electrons removed results in a positively charged substrate). X-Ray source is typically AlK α , with constant energy of $h\nu < 1.5$ keV. Photoelectrons are detected at an angle dependent on the incident angle of X-rays.

Sample depth depends on the mean inelastic free path of electrons (λ_i) in the sampled solid in the range of 0.3-4 nm (depending on the K.E. of photoemitted electrons and sample identity).¹⁰⁹ An electron emitted of intensity I_0 at a depth d in the surface is altered according to the beer-lambert law (Equation 2.5), where in a path length of one λ_i , 63% of emitted photoelectrons are not emitted from the surface. This means that XPS is a typically surface-probing technique, as defined sampling depth in XPS spectroscopy is defined as 3λ (so approximately 3-10 nm).

$$I_s = I_0 e^{-d/\lambda_i}$$

Equation 2.5: Description of final emitted intensity of photoelectrons I_s as a function of initial emission intensity (I_0), depth in sample (d) and mean inelastic free path of electrons (λ_i).

As with other spectroscopic techniques, XPS is capable of determining both elemental identity and chemical shift (change in characteristic properties with respect to elemental level). In XPS, an element exhibits key characteristic binding energies corresponding to different core shell environments (e.g. 1s, 2p, 3d), allowing for identification of elemental composition, for example the C1s environment of diamond (sp^3) carbon typically exhibits a binding energy of around 274.2 eV.¹¹⁰ A chemical shift occurs where the binding energy of the core shell electron is altered due to chemical bonding of that element. Changes in the electrostatic interactions of core shell electrons arise from changes in shielding of the electron towards the effective nuclear charge, such as where the atom is bonded to a more electronegative element resulting in induction of charge away from the nucleus.

Fitting of a global environment (such as total C1s environment) can give information as to what chemical environments that particular atom is present in, such as C=O(NH-C) amide carbon, diamond (sp^3) carbon, graphitic (sp^2) carbon and oxidised C-O species of carbon in a diamond sample. It is imperative that fitting gives an accurate depiction of the total overall core-shell environment, and fitting is based on empirical and experimental data to avoid over-interpretation of results. An example of a deconvoluted C1s environment in the XPS spectrum of graphene oxide is given in Figure 2.13, showing

the sp^2 environment c.a. 284 eV, with progressively more oxidised carbon species at higher binding energies.¹¹¹

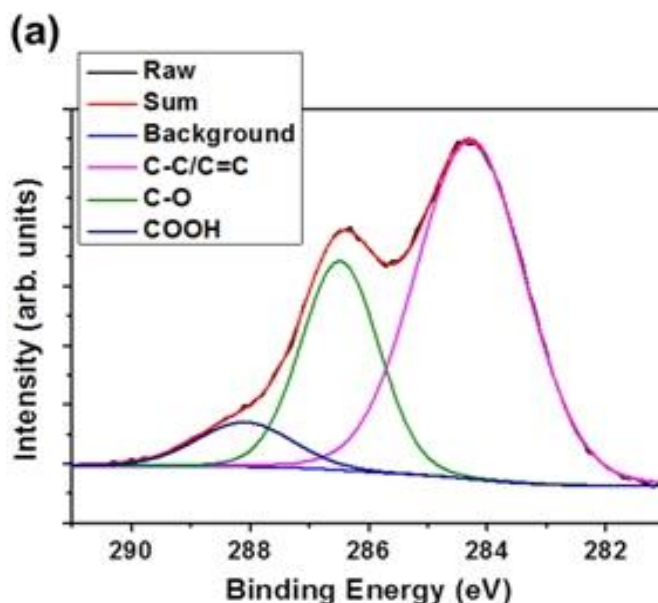


Figure 2.13: Example of a deconvoluted XPS trace. Deconvolution of the raw (black solid line) XPS trace of the C1s environment of a reduced graphene oxide surface to give the fitted trace (red) against a background (blue), showing C-C (magenta), C-O (green) and COOH (navy) components. Adapted reference 111.

Quantification of XPS spectra allows for calculation of the elemental composition in a chemical sample. Specific scanning of individual regions (such as O1s, C1s and N1s), and calculation of the total intensity (as electron counts per second) gives information as to the proportion of different elements present in a sample. Elements and core shell environments of elements are not uniformly sensitive towards quantification by XPS, the relative sensitivity factor (RSF) is a measure (with respect to carbon 1s, with a RSF of 1) of the sensitivity of a particular environment towards quantification (i.e. the amount of photoemitted electrons in samples as a function of sample concentration). In factoring in the RSF of specific chemical environments (which can change depending on the experimental set up), one can determine atomic concentration of different elements in a chemical sample.

2.2.5.3. Photoluminescent characterisation

Attachment of luminescent species to ND allows us to determine attachment (and can give a qualitative measure of attached species) *via* photophysical characterisation of the resulting purified particle dispersions. Optical absorption (UV-Vis/ Excitation PL

spectroscopy), steady state and time dependant emission spectroscopy is covered in detail in Section 1.2

Experimental analysis of nanoparticle dispersions is different in one key aspect (with respect to solution state measurements of small particles), as the large particle diameter (in our case, 50 nm average diameter) results in a large degree of light scattering. Higher energies of incident radiation result in increased scattering, giving an absorption profile dominated by higher absorptions at lower wavelengths. Light scattering is proportional to particle concentration, however it makes direct quantification of attached colour centres impossible (*via* the beer-lambert law), as absorption arises from both absorption by the chromophore and light scatter from particles. However, UV-Vis and excitation photoluminescence spectroscopy is critical in evaluating how the absorption characteristics of luminescent species change (if they do change), providing information on the chemical environment through changes in absorption wavelength.

Emission characteristics of attached probes can be used to evaluate whether attachment of luminescent substrates to the ND surface results in any changes in excited state energy (changes in emission wavelength), or avenues to non-radiative deactivation of said excited state (luminescent lifetime).

2.2.5.4. Particle morphology and purity (TEM)

Transmission electron microscopy (TEM) relies on the transmission of electrons *via* absorption/interaction of substrates with electrons from a high energy electron beam in a vacuum, thus allowing imaging at a very high resolution. Different sample constitutions interact with electrons and produce different levels of contrast. TEM can be employed to image samples of sub-micron diameters (such as ND), all the way up to a few nanometers in size (HR-TEM). Diamond samples should all appear similar in morphology (as they derive in shape from the cubic diamond crystal, and thus TEM can identify where other crystalline (or amorphous) material is present due to differences in shape. Larger (*c.a.* 50 nm in diameter) ND particles similar to those used in this study (Figure 2.14) observed through TEM are described by a broad mixture of particle shapes, with multiple different faceted structures able to be distinguished.

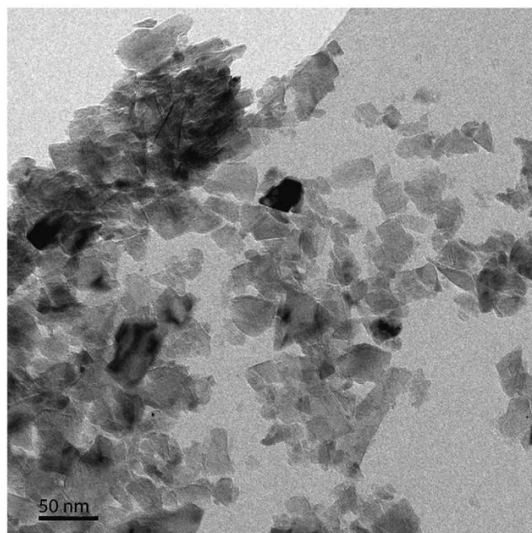


Figure 2.14: TEM image of c.a. 50 nm in diameter ND particles, adapted from reference 81.

2.3. Results and discussion

2.3.1. Production and characterisation of luminescent nanodiamond species **Nap-1@ND** in buffered aqueous media and acetonitrile

Polycarboxylated (air oxidised) ND particles with an average diameter of 50 nm (**ND-COOH**) were provided by Professor Oliver Williams *et al.* (School of physics, Cardiff University) either as solid particles (then dispersed in MeCN) or as aqueous dispersions. Synthesised luminophores **Nap-1** and **Ru-1** were attached through EDC/NHS mediated amide coupling in either aqueous or acetonitrile-based media.

Three methods in the surface functionalisation were employed: in aqueous media (methods **a** and **b**) buffered with CHES (N-Cyclohexyl-2-aminoethanesulfonic acid) and borate systems respectively, and in organic (MeCN) media with a small amount of triethylamine (method **c**) (Figure 2.15).

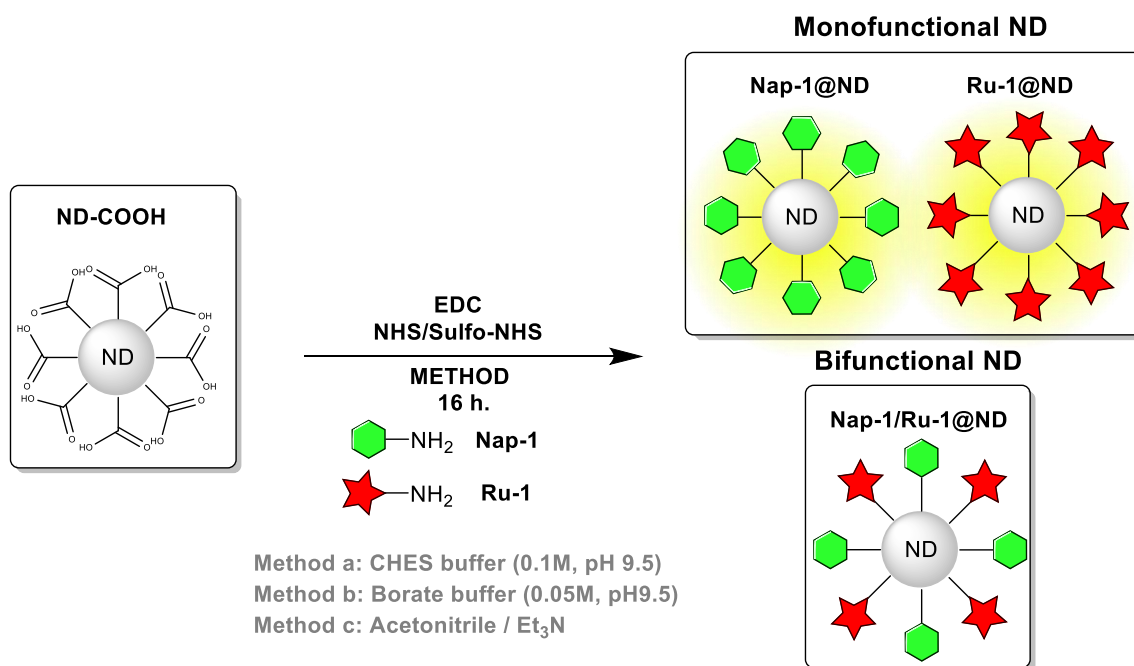


Figure 2.15: Schematic representation of functionalisation and co-functionalisation of ND suspensions with Nap-1, Ru-1 and Taurine yielding multiple species of functionalised species.

Nap-1 exhibited excellent water solubility and the surface functionalisation was investigated and compared *via* methods **a-c** to give surface functionalised ND suspensions **Nap-1@ND_{a-c}** respective of the method used. **Ru-1** was attached to the ND surface *via* method **c** owing to its relatively poor water solubility, giving the surface functionalised ND suspension **Ru-1@ND**. Finally, both **Nap-1** and **Ru-1** in a stoichiometric mixture were attached *via* method **c** to give the co-functionalised particle

dispersion **Nap-1/Ru-1@ND**. A summary of the particles produced, and methods employed in purification is given in Table 2.1.

Table 2.1: Summary of surface functionalised ND particles produced in this section.

	Method used	Purification
Nap-1 @NDa	0.1M CHES (pH 9.0)	Dialysis
Nap-1 @NDb	0.05M borate (pH 9.0)	Dialysis
Nap-1 @NDc	MeCN / Et ₃ N	Washing by centrifugation /redispersal
Ru-1 @ND	MeCN / Et ₃ N	Washing by centrifugation /redispersal
Nap-1/Ru-1 @ND	MeCN / Et ₃ N	Washing by centrifugation /redispersal

2.3.1.1. Synthesis of the 4-amino-1,8-naphthalimide derivative **Nap-1**

Nap-1, a novel compound synthesised as a highly water soluble naphthalimide candidate suitable for attachment to ND, was produced from 4-chloro-1,8-naphthalic anhydride *via* a three-step synthesis: nucleophilic substitution of the anhydride moiety with ethanolamine, followed by the S_NAr reaction step with the protected solubilising linker N-Boc-2,2'-(ethylenedioxy)bis(ethylamine) (**NBoc-EDBE**), (Figure 2.16). Deprotection yielded the primary amine terminated **Nap-1** luminophore.

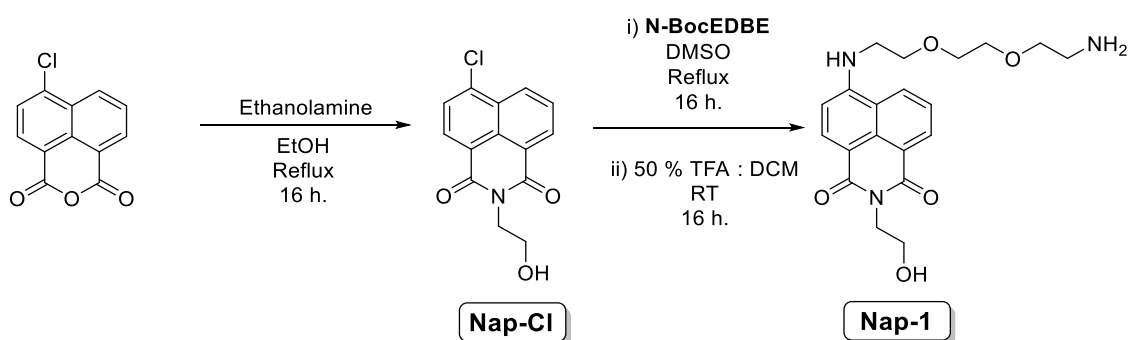


Figure 2.16: Synthesis of 4-amino-1,8-naphthalimide **Nap-1** from 4-chloro-1,8-naphthalic anhydride.

The S_NAr reaction overcomes the limitations of nucleophilic substitution of aromatic species when an electron withdrawing group (EWG) is present (in the case of **Nap-Cl**, the diimide moiety). Despite the activation of aromatic species towards nucleophilic substitution by EWG attachment, nucleophilic substitution through this method requires

a relatively high amount of energy, due to the ‘break’ in aromaticity. Therefore reflux (or near reflux) in a high boiling point solvent such as DMSO¹¹² or 2-methoxyethanol¹¹³ is commonly employed to achieve the substitution.

A significant colour change from light yellow to dark-orange following heating at reflux over 16h. Following the S_NAr substitution of **Nap-CI** with **N-BocEBDE** a mixed product was observed by TLC (2:3 acetone/hexane with 4% triethylamine, approximately $r_f^1 = 0.4$, $r_f^2 = 0.55$), with both spots fluorescing yellow green under illumination 360 nm light. Isolation of the BOC protected precursor to **Nap-1** was achieved through column chromatography, collecting very small (~1 mL) fractions, due to the high likelihood of some co-elution owing to the very close r_f values of the two species. Deprotection with 50% TFA in DCM was achieved without issue to give the final 4-amino-1,8-naphthalimide derived luminophore.

Nap-1 exhibited a very high degree of water solubility, and stock solutions in water of over 0.1 M were prepared for use. The photophysical properties (Table 2.2, Figure 2.17) of **Nap-1** are comparable to similar 4-amino-1,8-naphthalimides described in the literature.^{112,114,115} UV-Visible spectroscopy elucidated a lowest energy absorption corresponding to the intramolecular charge transfer (ICT) transition at 445 nm, absorptions arising from n- π^* and π - π^* transitions. Following excitation at 445 nm, emission from the singlet (as suggested by the short lifetime) excited state is observed giving a broad emission peak centred around 543 nm in water with a high quantum yield comparable to that found in similar literature examples.¹¹⁶

Table 2.2: Optical absorption and emission properties of **Nap-1** in water. Molar absorptivity (ϵ) shown of lowest energy absorption (bold).

Compound	λ_{\max} (UV-Vis) / nm	λ_{em} / nm	$\epsilon_{445 \text{ nm}}$ / $\text{dm}^3\text{mol}^{-1}\text{cm}^{-1}$	Lifetime / ns	Φ / %
Nap-1	258, 283, 445	543	8800	3.9	39

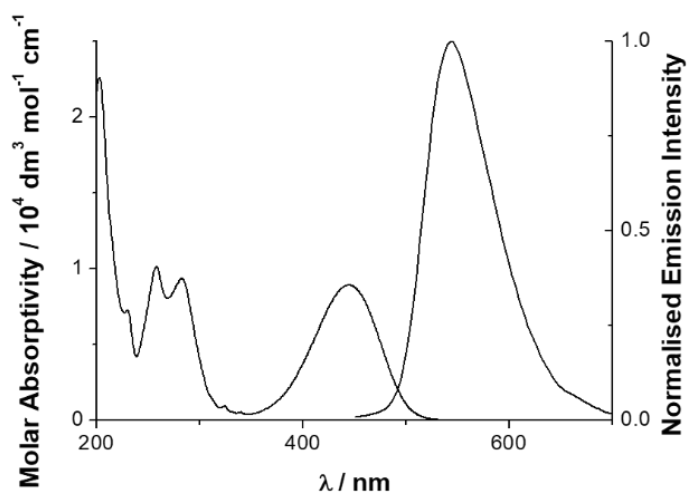


Figure 2.17: UV-Visible absorbance and luminescence emission spectra (slits 4,4 nm) of **Nap-1** in aqueous solution ($[\text{Nap-1}] = 0.1 \times 10^{-5} \text{ M}$).

The water solubility of **Nap-1**, combined with its bright emissive properties and flexible amine terminated hydrophilic linker make it an ideal candidate for the surface functionalisation of ND.

ND-COOH particle dispersions in water and acetonitrile were surface functionalised with **Nap-1** through employing EDC and sulfoNHS mediated amidation. Methods 1 and 2 were performed using 100 mM CHES and 50 mM sodium borate/ boric acid buffered (at ~pH 9.5) aqueous suspensions, utilizing aqueous suspensions of **ND-COOH**. Purification of surface functionalised particles was performed through membrane dialysis using a 3000 mwco cellulose membrane dialysing to purified water in order to remove unattached **Nap-1**, buffer and by-products (synthesis detailed in Section 2.5.2). Particles produced by methods 1 and 2 are termed **Nap-1@NDa** and **Nap-1@NDb**. Method 3 employed EDC/NHS based amidation in acetonitrile. Particles produced through this method were purified through pelleting with centrifugation and redispersal by sonication, a process repeated 3 times finally redispersing in purified water producing **Nap-1@NDc**.

2.3.1.2. Colloidal properties

Zeta potential, PDI (polydispersity index) and average particle sizes (hydrodynamic diameters/HDD) of **Nap1@NDa-c** as measured by NTA and DLS are shown in table 2.3 and figure 2.10 in comparison with **ND-COOH**. **Nap-1@NDa-c** dispersions were all strongly yellow following purification, suggesting surface retention of the yellow **Nap-1** luminophore.

Table 2.3: Colloidal properties of aqueous suspensions of **ND-COOH** and surface functionalised ND samples **Nap-1@NDa-c**.

Sample	pH	Particle Diameter (HDD) / nm		PDI (DLS)	Zeta Potential / mV
		DLS	NTA		
ND-COOH	5.0	62	53±1	0.13	-43.0
Nap-1@NDa	5.4	228	134±3	0.18	-12.8
Nap-1@NDb	4.8	143	146±5	0.39	-24.8
Nap-1@NDc	5.2	182	165±3	0.12	-19.5

Average particle sizes of surface functionalised ND species **Nap-1@NDa-c** are broadly comparable, increased to a degree of between 130 and 170 nm (by NTA) with respect to **ND-COOH**. The polydispersity indices of the functionalised dispersions were comparable to **ND-COOH** with the exception of **Nap-1@NDb**. Where DLS measurements of **ND-COOH**, **Nap-1@NDa** and **Nap-1@NDc** reported larger average particle sizes greater than those seen in the NTA measurement (as predicted by the

overestimation related to the direct measurement of particle scattering by DLS), the DLS HDD value reported for **Nap-1@NDb** was slightly lower than that reported by NTA. This is likely a result of the high degree of polydispersity (PDI = 0.39) of the **Nap-1@NDb** dispersion, making the DLS measurement less reliable on account of its lack of tolerance towards polydisperse samples. The NTA measured size distribution (Figure 18) of **Nap-1@NDb** appears to be in reasonably close agreement of that measured for **Nap-1@NDa** and **Nap-1@NDc**.

Nap-1 functionalised ND suspensions are broadly similar in their colloidal properties, based on identification that NTA is a more representative method of characterising particle dispersions which exhibit a degree of polydispersity. The increase in particle sizes measured in comparison with ND-COOH represents aggregation on a small scale of surface functionalised ND species.

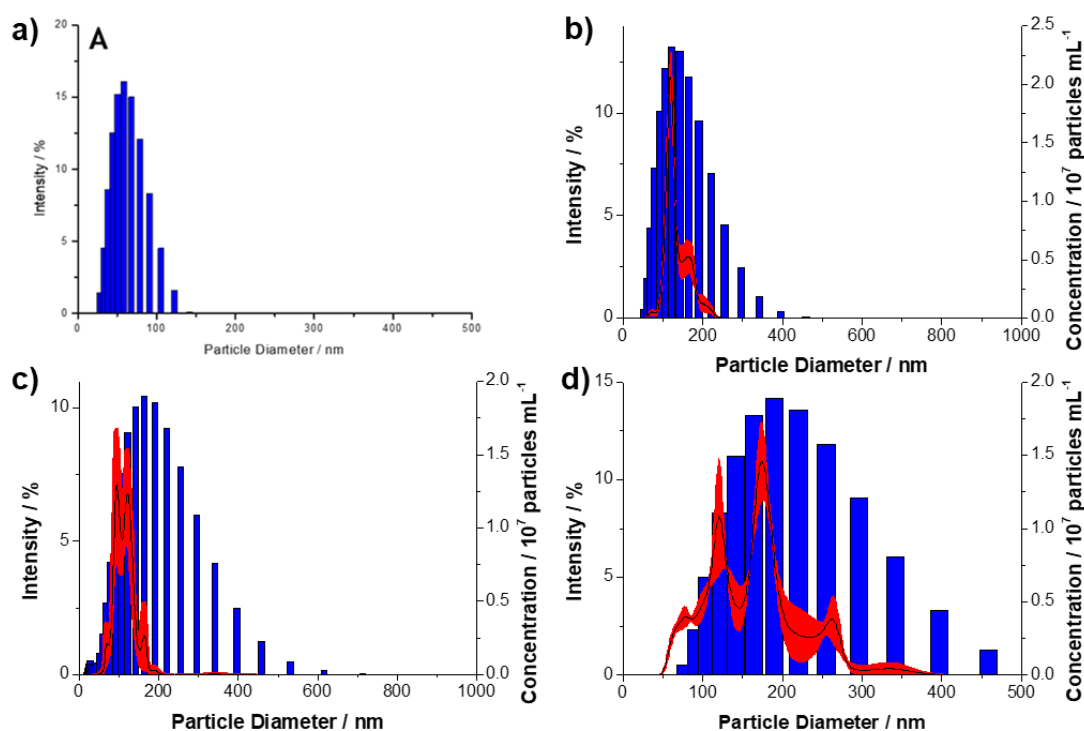


Figure 2.18: Particle size (hydrodynamic diameter) of dispersions of **ND-COOH** (top left), **Nap-1@NDa** (top right), **Nap-1@NDb** (bottom left), **Nap-1@NDc** (bottom right) in H₂O measured by DLS (blue bars) and NTA (black solid line with red error area).

The agglomeration on a small scale of **Nap-1@ND** particles in suspension is in part explained by the reduction in zeta potential of the ND surface from -43.0 mV for **ND-COOH** to between -12 and -28 mV. The reduction in zeta potential is significant, as it suggests the capping of the negatively charged carboxylate ND terminations with the

neutral **Nap-1** luminophore. Zeta potentials are heavily pH dependent with lower pH values associated with increasing 'screening' of the negative polycarboxylated surface by H⁺.

The high zeta potential of **Nap-1@NDb** in respect to the other **Nap-1** functionalised ND samples is therefore difficult to explain; one would expect the lower pH to result in reduced zeta potential. The high polydispersity measured by DLS was not reflected in increased average particle sizes in comparison with other **Nap-1@ND** suspensions, suggesting that although the **Nap-1@NDb** dispersion exhibits a more negative surface environment of ND on average, this is not significant enough to result in aggregation to a lower degree. Reasons for the low zeta potential are difficult to pinpoint, although it would appear logical to suggest that the buffer identity (boric acid/borohydrate) could play a role in surface association, or was not completely removed during sample purification, or resulted in a lower degree of **Nap-1** termination in **Nap-1@NDb** in comparison with other **Nap-1** dispersions.

To summarise, the colloidal properties of **Nap-1** functionalised **ND** suspensions **Nap-1@NDa-c** prepared through methods 1-3 were evaluated. Evidence from NTA and DLS particle size measurements suggests the aggregation of ND when functionalised to small-order aggregates of between 120 and 170 nm in diameter. The reduction in zeta potential seen for all **Nap-1@ND** particles in suspension was identified and correlates with the increased propensity of ND to aggregate, suggesting that the neutral **Nap-1** luminophore was successfully attached to the ND surface *via* the surface functionalisation protocol, reducing the net surface charge distribution.

2.3.1.3. X-Ray photoelectron spectroscopy

Normalised atomic percentages of carbon, nitrogen and present for **ND-COOH**, **Nap-1@ND** and calculated from XPS spectra are shown in Table 2.4. Initial survey spectra revealed elements present prior to a quantitative scan. Survey spectra of **ND-COOH** and **Nap-1@NDa** are given in the supplied appendix for this thesis. Survey scans were not observably different across **Nap-1@ND** suspensions produced by the differing methods, therefore **Nap-1@NDa** was chosen as a representative example.

It is important to note that several impurities were present: mainly calcium (0.07 - 1.07 At%) and sodium (1.26 - 3.73 At%), which likely represent salts present in the ND aqueous dispersions potentially from numerous sources (such as NaOH pH alteration of the concentrated CHES buffer stock). Chlorine was also found to be present albeit in very low (typically >0.2 At%) concentrations. A degree of sulfur content was observed

for **Nap-1@NDa-b** and to a much lower degree in **Nap-1@NDc** which could represent surface associated sulfonates from sulfuric acid used to pH balance the CHES and borate buffers. Importantly, no boron was detected in **Nap-1@NDb**, suggesting that borate was not in fact retained to a detectable degree.

Upon surface functionalisation with **Nap-1**, changes in the atomic composition of the ND particles can be observed: most clearly the increase in nitrogen (from below 0.5 At% to 7.05- 11.00 At%) and oxygen (from 11.80 At% to over 20 At%) in comparison with **ND-COOH**. As the nitrogen and oxygen content increased, respective carbon content decreased from 87.84% to between 60.14 and 62.47 At%. These results suggest the surface association of substrates **Nap-1** and Taurine to ND, although they do not indicate whether this is through electrostatic interactions or by the formation of a covalent peptide bond between the carboxylated surface of **ND-COOH** and the amine containing substrates.

Table 2.4: Normalised atomic composition as evaluated by XPS of **Nap-1@NDa-c** and **ND-COOH**.

Sample	Carbon %	Nitrogen %	Oxygen %
ND-COOH	87.84	0.36	11.80
Nap-1@NDa	62.15	10.51	20.64
Nap-1@NDb	60.14	9.33	22.26
Nap-1@NDc	61.47	11.11	20.15

Deconvolution of the C(1s) peak (Figure 2.19) of **ND-COOH** revealed two major and two minor components: C(1s-1) (B.E. = 283.9 eV), C(1s-2) (B.E. = 284.6 eV), C(1s-3) (B.E. = 285.5) and C(1s-4) (287.2), respectively. C(1s-1) corresponds to core sp³ carbon, in good agreement with Shenderova *et al.* (B.E. = 283.2 eV)⁷⁹ for smaller diameter nanodiamond; C(1s-2) corresponds to other surface located C-H and C-C content. The minor components C(1s-3) and C(1s-4) correlate to oxidized surface carbon species C-O and C=O respectively, in good agreement with Lim *et al.* for air oxidized nanodiamonds of comparable size¹¹⁷. The C(1s) peak of ND-CO₂H is dominated by C(1s-1) and C(1s-2) (48 % and 43 % of total carbon composition), with the minor components, C(1s-3) (7%) and C(1s-4) (2%) representing very small proportions of carbon content in ND-COOH. It is important to note that although we assume the majority of oxidised surface carbon in **ND-COOH** are present as carboxylate moieties, a wide range of other possible species are likely present, and the components identified here are likely made up of

several sub-components, which would be impossible to elucidate through gaussian fitting.

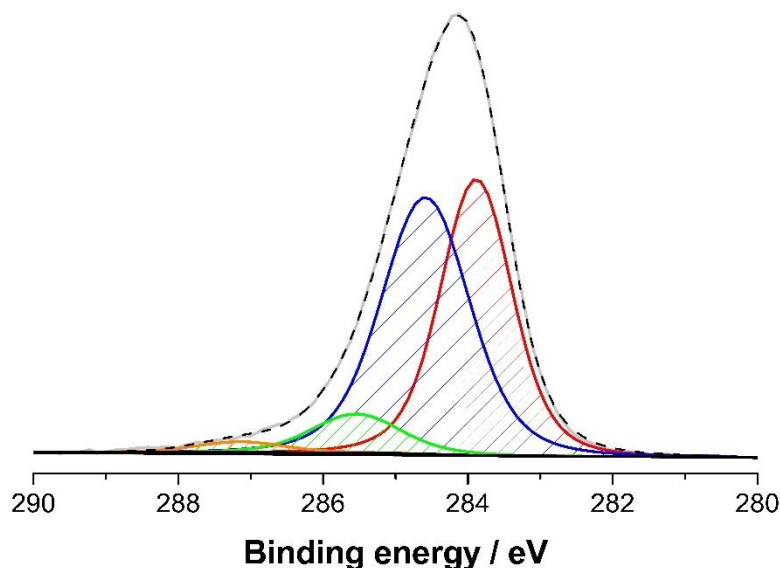


Figure 2.19: Deconvoluted C(1s) region of the XPS spectrum of **ND-COOH**, showing components C1s-1 (red), C1s-2 (blue), C1s-3 (green) and C1s-4 (orange) fitted to the XPS spectral trace (light grey solid line) to give the fitted environment (black dashed line).

The C(1S) peaks of **Nap-1@NDa-c** (Figure 2.20) show a shoulder around 287.3-288.4 eV. Deconvolution of the C(1s) peaks of functionalised ND samples elicit the presence of four components: C1s-1 (B.E. = 283.61 ± 0.28) C1s-2 (B.E. = 284.41 ± 0.33) C1s-3 (B.E. = 285.35 ± 0.33) and C1s-4 (B.E. = 287.42 ± 0.38). Again the major components C1s-1 and C1s-2 represent sp^3 Carbon and surface associated carbon (C-H/ C-C), in close agreement with similar environments in **ND-COOH**. Both the minor components C1s-3 and C1s-4 also fit to similar binding energies to **ND-COOH**, but in surface functionalised ND samples represent a larger component of the C1s peak, giving rise to the shoulder seen.

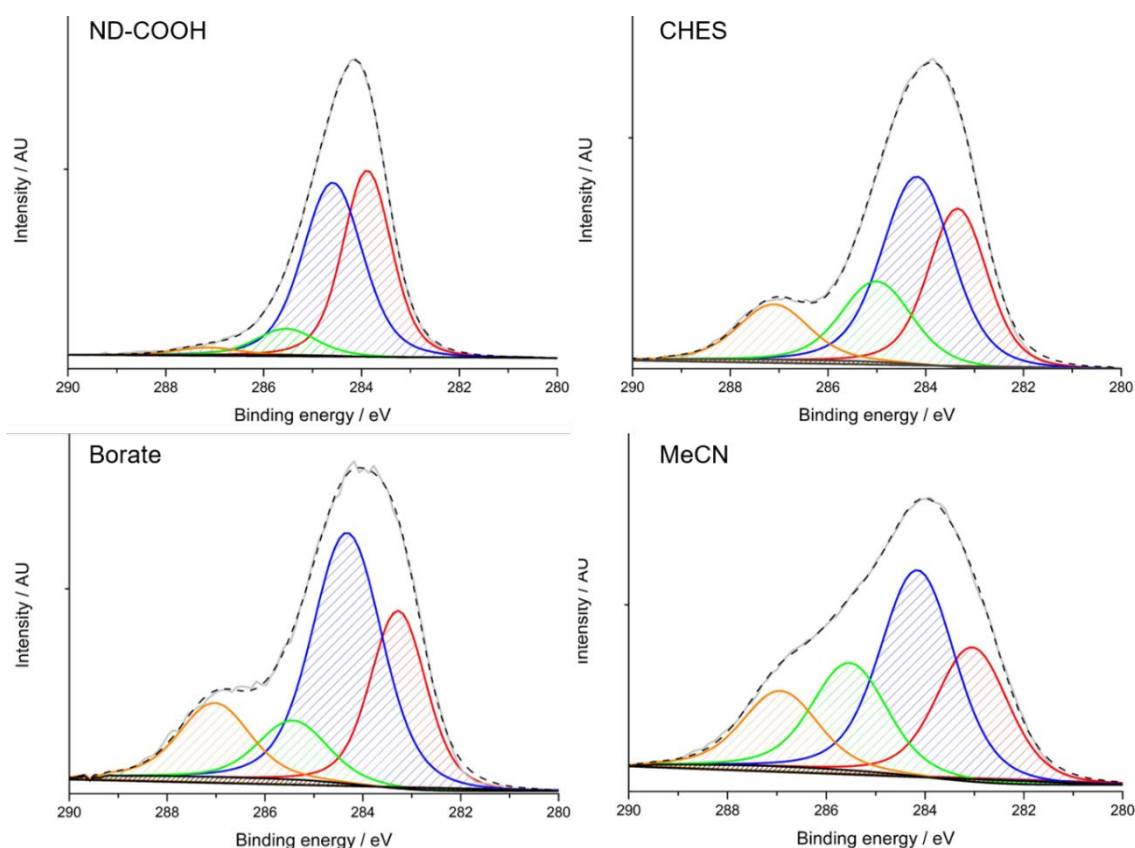


Figure 2.20: Deconvoluted XPS C(1s) traces of **Nap-COOH**, **Nap-1@NDa** (top right), **Nap-1@NDb** and **Nap-1@NDc** showing components C1s-1 (red), C1s-2 (blue), C1s-3 (green) and C1s-4 (orange) fitted to the XPS spectral trace (light grey solid line) to give the fitted environment (black dashed line).

The increase in contribution from C1s-3 and C1s-4 environments represents the increased proportion of oxidised carbon species present at the surface of ND functionalised samples. It is difficult to ascribe the increase in contribution from these components to the overall C(1s) signal, but likely due to the formation of an amide $\text{C}(\text{O})\text{-N}$ environment at the ND surface, in conjunction with contributions from highly oxidised carbon environments (such as imides) on surface attached species.

Ruck-Braun *et al.* described the binding energy of the $\text{C}(\text{O})\text{-N}$ as around 288.90 eV¹¹⁸, found from deconvolution of XPS spectra of amide terminated alkyl monolayers on a silicon (111) surface. Although the systems described in Ruck-Braun *et al.* are vastly different to the surface functionalised ND systems reported here, the amide environments are certainly comparable (amide groups in the Si deposited Si layers at the opposite end of the a C_9 alkyl linker to the Si surface). Identification of this component as the amide environment provides confirmation that (as opposed to electrostatic

association), substrates were covalently attached to the surface of ND through the formation of an amide bond, through treatment of the ND surface.

2.3.1.4. Photophysical properties of **Nap-1@ND**

The photophysical properties of the **Nap-1** functionalised ND particles (**Nap-1@NDa-c**) were determined in aqueous solution, compared to the optical properties of **Nap-1** in aqueous solution (Section 2.2.1). Photophysical properties of **Nap-1** attached to ND in the particles produced by the various methods were shown to be totally indistinct and.

The absorption and emission characteristics (Figure 2.21, Table 2.5) of **Nap-1** is conserved upon attachment to ND, yielding particles with identical luminescent properties to the unattached luminophore, exhibiting: multiple absorptions including the lowest energy absorption from intramolecular charge transfer (455 nm), and broad emission around 540 nm with a short (~5 ns) lifetime ascribed to emission from the singlet excited state. A distinct light scattering profile (increased absorption at lower wavelengths) can be observed in the UV-visible spectrum of **Nap-1@ND**. An apparent small increase in lifetime of aerated ND suspensions (by 1.2 ns) could represent the change in luminophore environment, where attachment to the ND surface and subsequent small-scale agglomeration could affect the relaxation of the excited state.

The ICT absorption of **Nap-1** ($\lambda_{\max} = 445$ nm) does not alter with respect to functionalisation methodology and despite the possible differences in surface environment and colloidal properties, one would not expect other optical characteristics to change depending on functionalisation method.

Table 2.5: Optical characteristics of **Nap-1@ND** in comparison with **Nap-1**. Bold absorption wavelength shows lowest energy absorption used as excitation wavelength for emission spectrum.

	$\lambda_{\text{abs}} / \text{nm}$	$\lambda_{\text{em}} / \text{nm}$	τ / ns
Nap-1	258, 283, 445	543	3.9
Nap-1@ND	288, 445	540	5.1

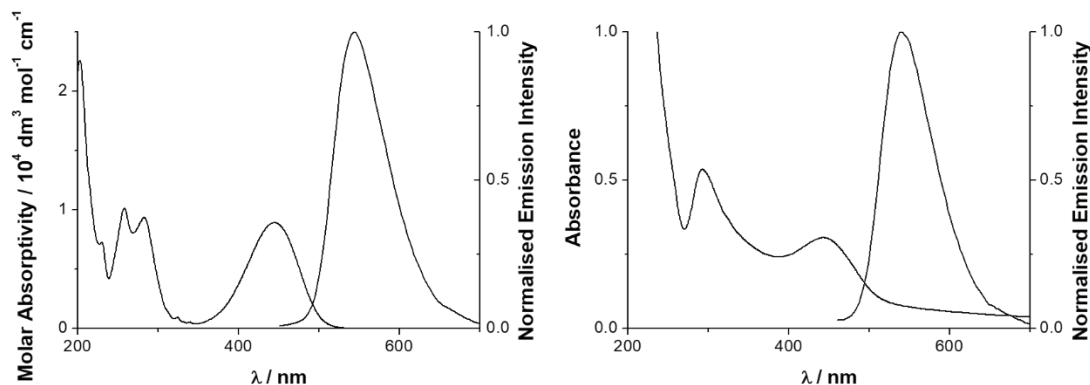


Figure 2.21: UV-visible absorption and normalised luminescence emission spectra of **Nap-1** (left) and **Nap-1@ND** (right).

2.3.1.5. Transmission electron microscopy

TEM samples were prepared by dropcasting 4 μL of sample dispersions onto grids and allowing for the solvent to dry. Images of **ND-COOH** prepared suspensions in H_2O and MeCN are shown as well as surface functionalised **Nap-1@ND** (Figure 2.22).

The crystalline nature of ND particles can clearly be observed in TEM images of **ND-COOH** prepared in both H_2O and MeCN. Images appear consistent with those found for similarly sized, sourced and treated ND dispersions by Gines *et al.* (2015).⁵¹ Particles with an approximate diameter of *ca.* $\sim 50 \text{ nm}$ are clearly visible for **ND-COOH** and **Nap-1@ND** particle dispersions, with little to no other crystalline or amorphous material observed deposited on the grids. A contrast between the sizes of particle agglomerates can be seen, owing to the increased particle concentration in initial **ND-COOH** dispersions, therefore upon drying these agglomerated to a greater degree.

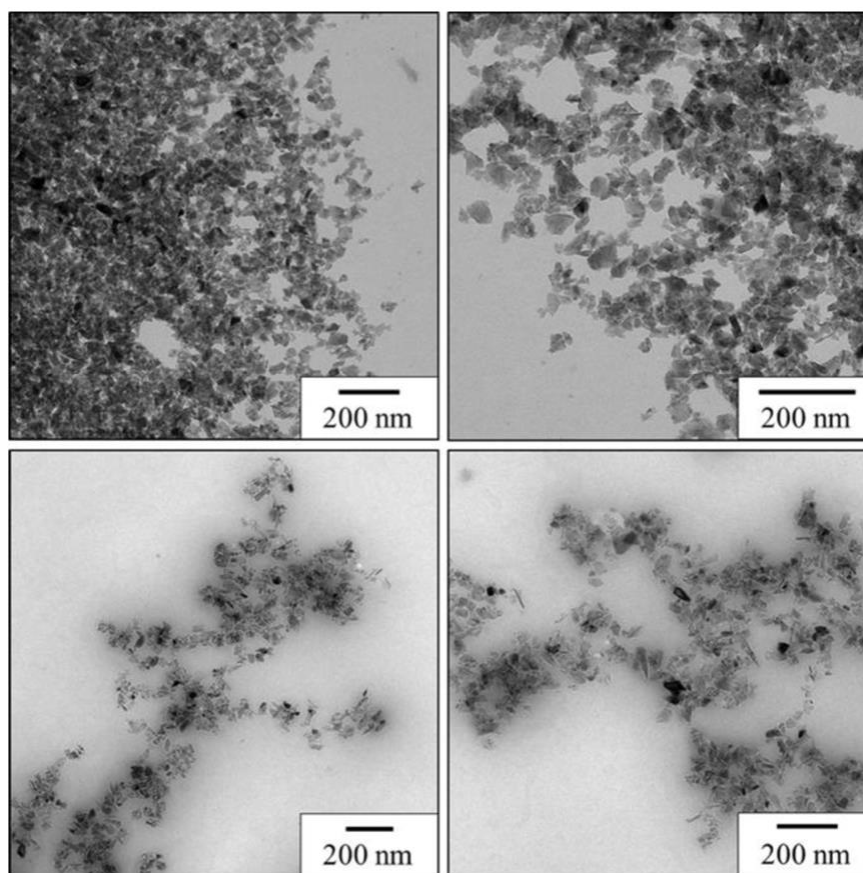


Figure 2.22: TEM images of **ND-COOH** from dispersions prepared in H₂O (top left) and MeCN (top right) and **Nap-1@ND** dispersions once purified (bottom).

2.3.2. Production and characterisation of **Ru-1@ND**, and the co-functionalised, dual emissive nanodiamond probe **Nap-1/Ru-1@ND**

ND-COOH was surface functionalised *via* EDC/NHS mediated amide formation in acetonitrile, as per the method described in Section 2.5.2 with **Ru-1** and a stoichiometric ratio of **Nap-1** and **Ru-1** substrates. Surface functionalised nanodiamond suspensions **Nap-1@ND**, **Ru-1@ND** and **Nap-1/Ru-1@ND**. **Ru-1** (Figure 2.23) was synthesised by Dr Samuel Adams (School of Chemistry, Cardiff University), from [Ru(bipy)Cl₂], and fully characterised (reported in Section 2.5.2) giving the acetonitrile soluble amine terminated luminescent Ru based luminophore suitable for ND attachment.

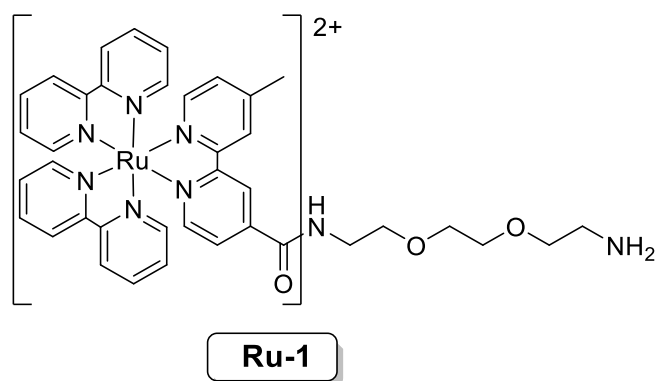


Figure 2.23: Structure of luminescent ruthenium complex **Ru-1**.

2.3.2.1. Particle size and colloidal stability

Measurements by DLS/NTA of hydrodynamic diameter of **Nap-1@ND**, **Ru-1@ND** and **Ru-1/Nap-1@ND** and zeta potential measurements are shown in table 2.6 and Figure 2.24. Aggregation and increase in polydispersity were exhibited by both **Ru-1** functionalised particles. **Ru-1@ND** exhibited a positive zeta potential of +19.0 mV, indicative of a high degree of surface attachment of the positively charged **Ru-1** complex. Co-functionalisation with **Ru-1/Nap-1@ND** yielded particles exhibiting a close to neutral surface zeta potential (-4.5 mV), much lower than **Nap-1@ND** prepared by all methods. This indicates that functionalisation with **Ru-1**, a positively charged substrate results in change in overall surface polarity for **Ru-1@ND**, indicative of extensive surface coverage, which is lesser for co-functionalised **Ru-1/Nap-1@ND**.

Table 2.6: Particle size and zeta potential measurements of **ND-COOH** surface functionalised nanodiamond samples **Ru-1@ND** and **Ru1-Nap-1@ND**.

Sample	pH	Particle Diameter / nm		PDI	Zeta Potential / mV
		DLS	NTA		
ND-COOH	5.0	62	53±1	0.13	-43.0
Nap-1@NDc	5.2	182	165±3	0.12	-19.5
Ru-1@ND	5.5	171	171±8	0.14	+19.0
Ru-1/Nap-1@ND	5.4	151	218±8	0.23	-4.5

The high degree of polydispersity for the **Ru-1/Nap-1@ND** is in agreement with the very low magnitude of the surface zeta potential, whereby the lack of surface charge reduces like-for-like surface charge repulsions leading to more extensive aggregation with respect to the monofunctionalised **Ru-1@ND** and **Nap-1@ND**.

Particle sizes of **Ru-1@ND** and **Ru-1/Nap-1** are of comparable order to **Nap-1@ND** produced by the same method, with the bifunctional **Ru-1/Nap-1@ND** exhibiting more extensive aggregation owing to the more neutral zeta potential, arising from partial coverage of the ND surface by **Ru-1**, a positively charged complex.

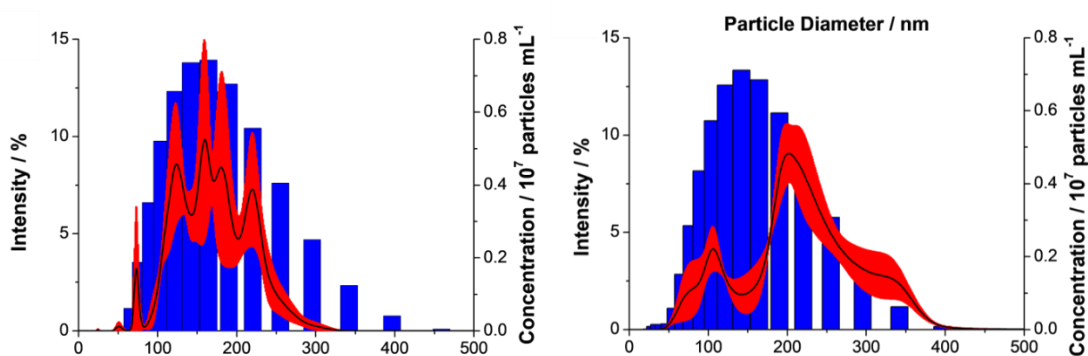


Figure 2.24: Size distribution analysis by DLS (blue bars) and NTA (black solid line) of surface functionalised nanodiamond dispersions **Ru-1@ND** (left) and **Ru-1/Nap-1@ND** measured immediately following final purification.

2.3.2.2. X-ray photoelectron spectroscopy

Initial survey spectra revealed elements present prior to a quantitative scan. Survey spectra of **ND-COOH** and **Nap-1@NDa** are shown in the appendix supplied with this thesis. **Ru-1@ND** and **Ru-1/Nap-1@ND** XPS spectra reveal the elemental composition, identifying the significant carbon (and ruthenium), nitrogen and oxygen components, as well as a level of calcium, sodium, sulfur and silicon impurity.

Normalised atomic % composition of carbon, nitrogen, oxygen and ruthenium are shown in Table 2.7. **Ru-1@ND** exhibits a high level of nitrogen content (~17.5 At%), and a similar level of oxygen content to **Nap-1** functionalised ND samples. (sections 2.2.3.1 - 2.2.3.2). **Ru-1/Nap-1@ND** exhibits nitrogen and oxygen compositions slightly higher to those found for **Nap-1@ND**. The increased nitrogen content agrees with attachment of the trisbipyridyl complex **Ru-1** to the ND surface, with a higher proportion of nitrogen in individual substrate molecules in comparison with **Nap-1**.

Table 2.7: Normalised atomic percentages found from processed XPS spectra of **Ru-1@ND** and **Ru-1/Nap-1@ND**.

Sample	Carbon	Nitrogen	Oxygen	Ruthenium
Ru-1@ND	66.06	17.58	16.12	0.24
Ru-1/Nap-1@ND	70.87	10.77	18.23	0.13

A clear peak at 279.20 eV prior to the C(1s) environment for **Ru-1**, ascribed to the 5/2 component of the Ru(3d) environment can be seen in the C1s acquired regions of the XPS spectra of **Ru-1@ND** and **Ru-1/Nap-1@ND**. Ruthenium content was therefore derived from the combination of 5/2 and 3/2 3d peak fitted from the deconvoluted C(1s) scans of **Ru-1@ND** and **Ru-1/Nap-1@ND** (Figure 2.25).

Deconvolution of this environment showed the comparable 4 components from the C(1s) environment fitted to the spectral trace, C1s-1 (B.E = 283.17 eV), C1s-2 (B.E. 284.07 eV), C1s-3 (B.E. = 285.71 eV) and C1s-4 (B.E. = 286.54) as well as two components of the Ru 3d environment: Ru 3d_{5/2} (B.E. = 279.20) and Ru 3d_{3/2} (B.E. = 283.2 eV). Like **Nap-1** functionalised ND dispersions, the contribution of the higher energy C1s-3 and C1s-4 environments increased upon functionalisation with **Ru-1** and **Nap-1** in this manner, indicative of amide formation at the ND surface.

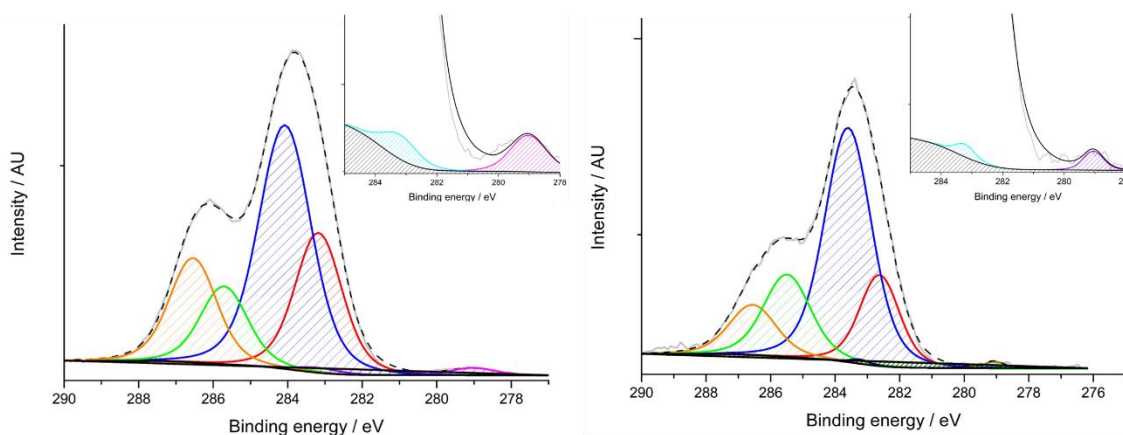


Figure 2.25: Deconvoluted XPS C(1s)/Ru(3d) traces of **Nap-1@ND** and **Nap1/Tau@ND1-3** showing components C1s-1 (red), C1s-2 (blue), C1s-3 (green), C1s-4 (orange) and Ru3d-5/2 (magenta) and fitted to the XPS spectral trace (light grey solid line) to give the fitted environment (black dashed line).

2.3.2.3. Optical characterisation of **Nap-1** and **Ru-1** luminophores attached to the ND surface

Comparison of the optical absorption spectra (Figure 2.24) of **Ru-1** and **Ru-1@ND** show the retention of the lowest energy absorption arising from the metal-to-ligand charge transfer at 458 nm (as well as other ligand-based absorptions below 300 nm). Luminescence emission spectra of **Ru-1@ND** showed a broad emission peak centred around 664 nm ascribed to emission from the ³MLCT excited state (further supported by the exhibited long lifetime of the excited state, 332 ns). An apparent increase in lifetime from 287 ns exhibited by the unattached **Ru-1** luminophore could represent the change

in environment resulting from the small-scale aggregation of the functionalised **Ru-1@ND** particles, resulting in reduced solvent exposure leading to a longer lifetime of the excited state.

The co-functionalised **Ru-1/Nap-1@ND** exhibited an absorption profile dominated by light scatter, making individual absorption bands difficult to distinguish (Figure 2.26). The ligand centred absorption around 300 nm can be distinguished in the UV-Visible spectrum of **Ru-1/Nap-1@ND**. The emission profile of the luminescence spectrum of **Ru-1/Nap-1@ND** is dominated by the peak at 540 nm corresponding to singlet emission from the **Nap-1** excited state (confirmed by the emissive lifetime of 4.8 ns). In the emission peak tail, a distinct peak at 664 nm can be noted (with an emissive lifetime of 328 ns), ascribed to emission from the ³MLCT excited state of the co-attached **Ru-1** luminophore. The disparity in emission intensities is not representative of the degree of functionalisation by each substrate but represents the lower quantum yield of **Ru-1** with respect to **Nap-1**. The lifetimes of the two components are comparable to those seen for the respective mono-functionalised particles, indicating that the chromophores are not within a distance for resonance energy transfer.

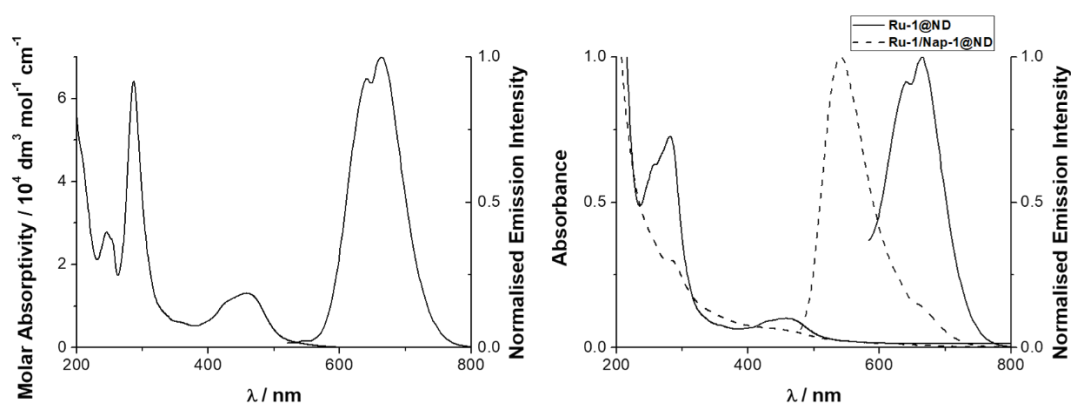


Figure 2.26: UV-Visible absorption and luminescence emission spectra of **Ru-1** (left) and functionalised ND suspensions (right) **Ru-1@ND** (black solid line) and **Ru-1/Nap-1@ND** (black dashed line) in aqueous solution.

2.3.2.4. Transmission electron spectroscopy

TEM images obtained through dropping and evaporation of 4 μL of **Ru-1@ND** and **Ru-1/Nap-1** are shown in Figure 2.27. Again, particles appear to be highly ordered crystals, very similar to those seen for unmodified **ND-COOH** dispersions reported in chapter 2.2.2.4. Little to no other polycrystalline material was observed, confirming the particle dispersions purity. Particle sizes appear to be consistent with that of the primary ND particles (50 nm) agglomerated to an extensive degree following drying of

dispersions on the TEM grid. Where the colloidal parameter measurements (DLS/NTA) describe the particle sizes in suspension, TEM is not representative of this, rather providing confirmation of the agglomerated primary surface functionalised ND particles.

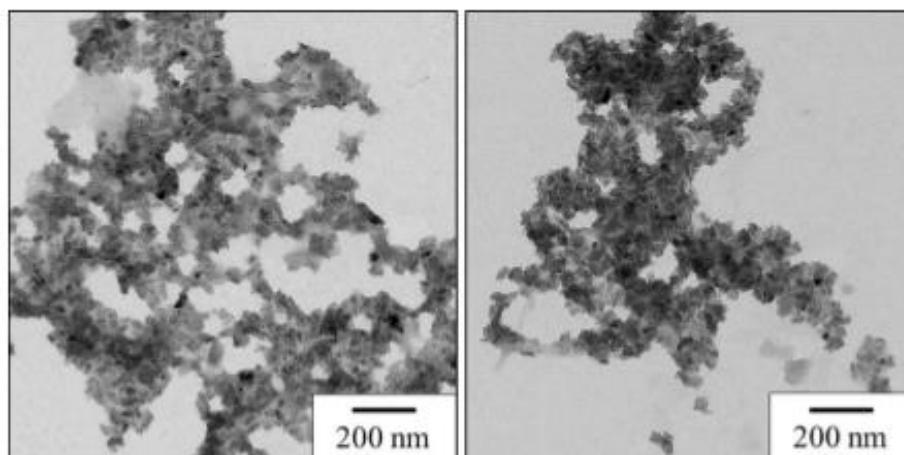


Figure 2.27: TEM images of **Ru-1@ND** (left) and **Ru-1/Nap-1@ND** (right).

2.3.3. Attempting to control colloidal stability of Nap-1 functionalised aqueous ND suspensions through co-functionalisation with Taurine

In the development of the **Nap-1@ND** and **Ru-1@ND** functionalised ND dispersions, it was noted that upon surface functionalisation with neutral and oppositely charged (with respect to the negatively charged polycarboxylate surface) substrates, a small degree of agglomeration was observed in most cases. Whilst this is at a low order (generally below 200 nm from a primary particle diameter of ~50 nm) of aggregation, it was noted that maintenance of a high zeta potential may be advantageous to the stabilisation of primary ND particles.

It was hypothesised therefore, that a more negative surface charge in the production of surface functionalised ND species could result in more favourable colloidal properties of functionalised dispersions. Through co-incorporation of the neutral **Nap-1** luminophore with a negatively charged co-substrate, one could achieve a more negative zeta potential of the resulting dispersions, possibly reducing aggregation. Having established the precedent for co-functionalising the ND surface (Section 2.2.3), taurine (2-aminosulfonic acid) was investigated as a surface additive for ND (Table 2.8).

Table 2.8: Concentrations of substrates in surface functionalisation of ND.

Sample	[Taurine]/ mM	[Nap-1]/ mM	Percentage of taurine upon coupling
Nap-1@ND	0.0	2.0	0%
Nap-1/Tau@ND1	0.5	1.5	25%
Nap-1/Tau@ND2	1.0	1.0	50%
Nap-1/Tau@ND3	1.5	0.5	75%

2.3.3.1. Confirmation of incremental **Nap-1** functionalisation *via* UV-Visible spectroscopy

UV-visible spectra of **Nap-1@ND** and **Nap-1/Tau@ND1-3** (Figure 2.28) show a definite correlation between **Nap-1** concentration upon coupling and the concentration of **Nap-1** attached in the purified surface functionalised ND suspensions. This was indistinctive of the method (**a** or **b**) employed in surface functionalisation.

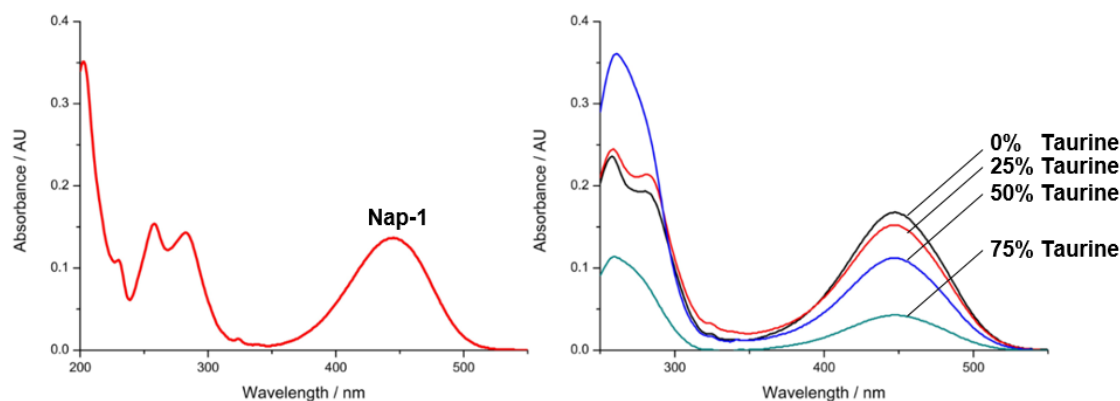


Figure 2.28: UV-Visible absorption of **Nap-1** in H₂O (left, red solid line) and **Nap-1/Tau@ND** suspensions (10x diluted right). **Nap-1@ND1** (black solid line), **Nap-1/Tau@ND1** (red solid line), **Nap-1/Tau@ND2** (blue solid line), **Nap-1/Tau@ND3** (green solid line)

Where the Beer Lambert law would normally permit calculation of concentrations (based on the recorded molar extinction coefficient at 445 nm of **Nap-1** of 8800 dm³ mol⁻¹ cm⁻¹) of **Nap-1** present in surface functionalised particles, here it would be essentially useless. Purification by dialysis results in a small change in volume, which would not necessarily be comparable across all samples, and one cannot be sure that during the purification process the particle concentration remains the same. However, increasing the ratio of **Nap-1** to taurine results in an increased concentration of **Nap-1** in the functionalised **ND** suspensions as measured by the change in absorbance at 445 nm (Figure 2.29).

Figure 2.29: Absorbance at 445 nm as a function of concentration ratio of **Nap-1** and taurine in the functionalisation reaction.

2.3.3.2. Particle size and Colloidal stability

Zeta potential, PDI and average particle sizes (hydrodynamic diameter) of **Nap1@ND** and **Nap1/Tau@ND1-3** prepared through the aqueous CHES buffered method (a) and borate buffered method (b) as measured by NTA and DLS are shown in Table 2.9, with the particle size distributions shown in Figures 2.30 and 2.31 respectively

Table 2.9: Particle size and zeta potential measurements of surface functionalised nanodiamond samples ND1-4 and ND-COOH following purification.

Sample	Buffer	pH	HDD/ nm (DLS)	HDD/ nm (NTA)	ZP / mV	PDI (DLS)
Nap-1 @NDa	CHES	5.4	228	134 ± 2.8	-12.8	0.18
Nap-1/Tau@ND1a	CHES	5.3	187	123 ± 6.3	-14.2	0.25
Nap-1/Tau@ND2a	CHES	5.4	190	118 ± 1.2	-17.9	0.27
Nap-1/Tau@ND3a	CHES	5.2	153	102 ± 3.1	-18.3	0.28
Nap-1 @NDb	Borate	4.8	143	146 ± 5.0	-24.8	0.39
Nap-1/Tau@ND1b	Borate	5.5	190	139 ± 8.2	-21.2	0.50
Nap-1/Tau@ND2b	Borate	5.2	210	109 ± 1.9	-20.9	0.60
Nap-1/Tau@ND3b	Borate	5.1	188	118 ± 4.3	-18.5	0.39

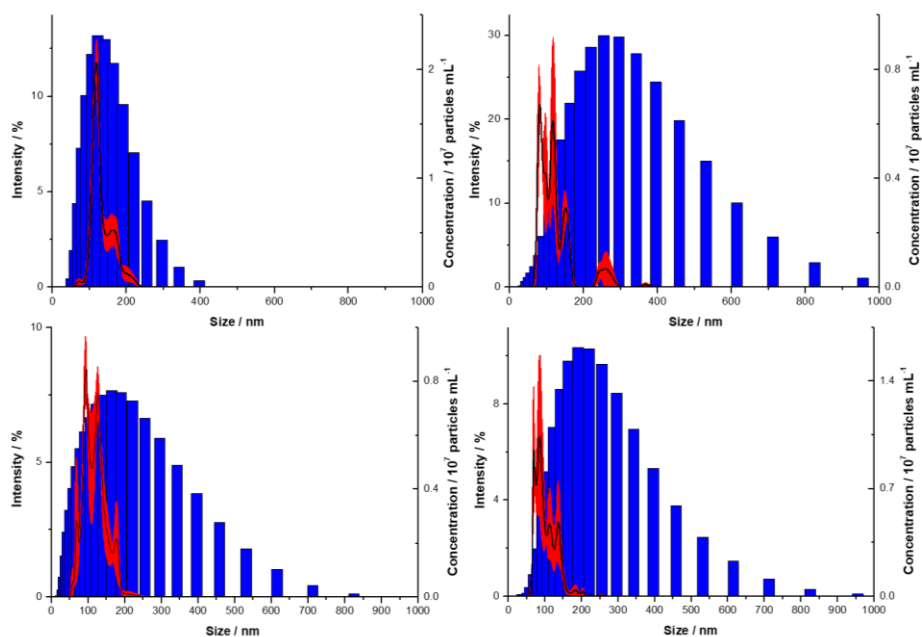


Figure 2.30: Size distribution analysis by DLS (blue bars) and NTA (black solid line) of surface functionalised nanodiamond dispersions **Nap-1@NDa** (top left), **Nap-1/Tau@ND1a** (top right), **Nap-1/Tau@ND2a** (bottom left) and **Nap-1/Tau@ND3a** (bottom right) measured immediately following final purification.

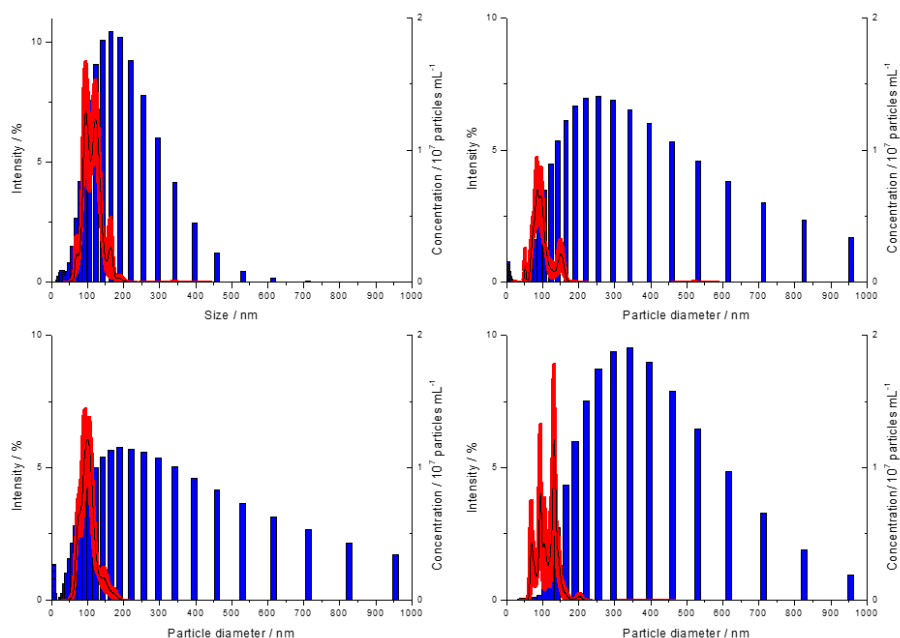


Figure 2.31: Size distribution analysis by DLS (blue bars) and NTA (black solid line) of surface functionalised nanodiamond dispersions **Nap-1@NDb** (top left), **Nap-1/Tau@ND1b** (top right), **Nap-1/Tau@ND2b** (bottom left) and **Nap-1/Tau@ND3b** (bottom right) measured immediately following final purification.

The CHES buffered series (**Nap-1@NDa** and **Nap-1/Tau@ND1-3a**) exhibited an approximate negative trend in particle size measured by both NTA and DLS (Figure 2.28), with respect to taurine content. This was also reflected in the surface zeta potential. Polydispersity was shown, however, to increase with taurine content. The 75% taurine 25% **Nap-1** functionalised dispersion, **Nap-1/Tau@ND3a** appeared to exhibit enhanced colloidal stability, exhibiting particle sizes of around 100 nm (by DLS).

Taurine co-functionalised particles produced in the borate buffered system (**Nap-1@NDb** and **Nap-1/Tau@ND1-3b**) appear to be a great deal more polydisperse, as represented by the increased PDI and very broad distribution found by DLS. NTA results for **Nap-1@NDb** and **Nap-1/Tau@NDb** are not concordant with this result, describing a system whereby little discernible trend can be observed with respect to particle size and composition.

Zeta potential differences in the series of taurine co-functionalised particles were relatively small, exhibiting around a 20 mV reduction in magnitude in comparison with **ND-COOH**. However, ND particles functionalised by **Nap-1** and taurine still display agglomeration in a similar manner to particles functionalised by **Nap-1** alone. The tentative conclusion can be drawn, therefore, that in aqueous buffered systems, co-functionalisation with taurine at the concentrations described here does not result in a significant increase in colloidal stability for the functionalised ND particles.

From the investigations into the colloidal stability of **Nap-1@ND** and **Nap-1/Tau@ND** with respect to taurine concentration, it was unclear whether increasing taurine concentration alters the ratios of **Nap-1** and taurine attached to the ND surface.

Co-functionalisation of **ND-COOH** with taurine and **Nap-1** demonstrated the ability to alter the loading of the **Nap-1** luminophore, evidenced by the decreased absorbance at 445 nm with increasing taurine concentration. It was unclear however whether this results in improved colloidal stability, as size distribution and zeta potential appear to exhibit differing trends depending on the buffer used for the ND functionalisation procedure.

Potential reasons for the lack of correlation between taurine concentration and colloidal stability, may include:

- i) impact of buffer: differing trends in taurine cofunctionalisation were observed dependant on the borate/CHES buffer system. This could indicate that buffer takes part in the reaction or is surface associated to the functionalised particles *via* electrostatic interactions. This could explain the lack of response in zeta potential with respect to taurine concentration.

- ii) non-covalent interactions of taurine: in aqueous media, taurine is a zwitterion, and although at pH 9.5 the proportion of protonated amine is relatively low, a significant component could surface attach to already functionalised areas of ND during the functionalisation reaction leading to unpredictable aggregation behaviours.

2.4. Chapter conclusion

Surface functionalisation of polycarboxylated ND dispersion was achieved through amidation of the ND surface *via* EDC/NHS coupling in both aqueous and organic solvents. Successful attachment was demonstrated through retention of luminescent properties of the novel **Nap-1** luminophore and the **Ru-1** luminophore in surface functionalised ND dispersions **Nap-1@NDa-c** and **Ru-1@ND**.

Surface functionalisation of ND is supported by evidence from DLS and NTA particle size measurements as well as zeta potential measurements. Agglomeration, caused by the drop in surface zeta potential reducing the like-for-like charge based repulsion of primary ND particles, was observed upon surface functionalisation. This agglomeration was shown to be reproducible in order across **Nap-1@ND** dispersions produced across methods a, b and c, and was not shown to exceed 250 nm across all surface functionalised ND dispersions. Functionalisation with **Ru-1** appeared to result in polarity change of the surface zeta potential (-42 mV for **ND-COOH** to +19 mV for **Ru-1@ND**) indicative of extensive surface coverage of the positively charged luminescent **Ru-1** complex. Whilst aggregation occurs, it is of low order and reproducible, indicating that the surface functionalisation of ND in this manner is widely applicable in producing dispersions which can be post-modified to provide further functionality, or be used as sensors in a biological and chemical context.

XPS revealed the clear formation of a shoulder around 288 eV in the C1s peak of surface functionalised ND samples **Nap-1@NDa-c**, **Ru-1@ND** and **Ru-1/Nap-1@ND**, ascribed to the increased highly oxidised C component in the amide environment following surface functionalisation. This is evidence of covalent attachment (as opposed to surface association *via* electrostatic interaction).

TEM imaging revealed purified, monocrystalline ND dispersions in all surface functionalised cases. Particle morphology appear very similar in surface functionalised ND samples in comparison with **ND-COOH**.

In the production and extensive characterisation of bright, luminescent and co-functionalised (in the case of **Ru-1/Nap-1@ND**) ND dispersions, we describe a reproducible system whereby extensive surface functionalisation of ND is achievable through the facile and oft employed route of amidation by EDC/NHS. In demonstrating the applicability of the system across different buffered aqueous media and organic media (MeCN) we open up a huge scope of potential substrates which could be attached to the ND surface. Results detailed here, therefore, describe a very exploitable system

for the production and characterisation of surface functionalised ND. Whilst attempts at controlling surface electrostatic properties with co-functionalisation with taurine were relatively unsuccessful, ND colloidal stability does appear to alter with respect to surface identity. UV-Visible spectroscopic measurements identified the clear negative correlation of **Nap-1** concentration in purified dispersions with taurine concentration upon functionalisation. This identifies a route whereby ratiometric control of multiple substrates in the attachment to ND can be employed.

The outlook from this work involves both the interest in developing surface functionalised ND dispersions which exhibit as close to primary particle size distributions in aqueous media. This could be attained through investigating other co-functionalisation substrates, surface coating with a polyacid (such as oleic acid) or silica or moving towards a negatively charged luminophore.

In further developing surface functionalised ND chemistry, we employed these synthetic routes in the development of enzyme active luminescent ND dispersions, of which it is hoped to attach to the curli biofilm matrix to yield the overarching aim of a hybrid ND-embedded biomaterial.

2.5. Experimental

2.5.1. General considerations and measurement parameters

2.5.1.1. General reagents

Reagents and starting materials were obtained from commercial sources (i.e. Sigma Aldrich, Alfa Aesar, VWR and fluorochem) and used without further purification. Purified water from a Millipore milliQ purification system with an activity of not lower than $15 \text{ m}\Omega\text{cm}^{-3}$ was used.

2.5.1.2. Nanodiamond dispersions

Nanodiamond particles were purchased from either Van Moppes or Microdiamant, with an average particle diameter of 50 nm. Particles were treated with air oxidation at $420 \text{ }^\circ\text{C}$ for 5 hours prior to dispersal.

Aqueous nanodiamond samples were obtained from Professor Oliver Williams as slurries of $\sim 50 \text{ nm}$ d. particles in water at a concentration of 0.5 mg mL^{-1} and used without further treatment in surface functionalisation. ND particles from either Van Moppes or Microdiamant were treated at $\sim 400 \text{ }^\circ\text{C}$ over 5 hours in air prior to suspension in water.

Acetonitrile slurries containing 0.5 mg mL^{-1} oxidised ND were prepared through sonication of particles in the solvent at 30% amplitude over 5 minutes (cycled 5 s on 10 s off). Samples were centrifuged at 4000 rpm over 15 minutes and re-dispersed with sonication. This was repeated 5 times until all particles were well dispersed, followed by centrifugation at 2000 rpm over 15 minutes to remove any titanium particles sheared from the sonication probe.

2.5.1.3. X-ray photoelectron spectroscopy

Nanodiamond dispersions ($20\text{-}100 \text{ }\mu\text{L}$) in water were dropped onto cleaned pure gold foil and dried under laminar flow prior to loading into the Thermo Escalab 250 XPS. Spectroscopy was performed with a monochromated aluminium K-alpha X-ray source, measuring a spot size of $500 \text{ }\mu\text{M}$ with a power of 150 W. Detailed spectra of individual peaks were taken at energy of 20 eV with a step size of 0.1 eV, optimising scan number to give acceptable signal to noise for each measurement. Binding energy was calibrated by setting the Na (1s) peak to 1080 eV. Deconvolution and fitting was performed using Shirley or Linear backgrounds, fitting was performed using mixed Gaussian-Lorentzian fits in CASA XPS. Elemental analysis was derived using relative sensitivity factors from the CASA Scofield library.

2.5.1.4. Particle size and zeta potential measurements

A Malvern Zetasizer Nano ZS (DLS and zeta potential) equipped with a 633 nm laser in backscattering configuration (173 °) and a Malvern Nanosight LM10 equipped with a 635 nm laser (NTA) were employed in particle size measurements. Zeta potential measurements were made in the Malvern Zetasizer Nano ZS. Zeta potentials are reported at a given pH. Particle size distributions by DLS are the average of 100 × 30 s scans and zeta potential of 3 × 100 scans. Particle size measurements by NTA are the result of tracking over 3 × 20 s videos from scattered particles. The pH was measured by a Hanna Instruments HI 2211 pH meter.

2.5.1.5. Optical spectroscopy

UV-Visible spectroscopy was performed in aerated solutions (1×10^{-5} M where applicable) using a Shimadzu UV-1800 spectrophotometer. Photophysical data was obtained on a JobinYvon-Horiba Fluorolog spectrometer fitted with a JY TBX picosecond photodetection module as water solutions. Emission spectra were uncorrected and excitation spectra were instrument corrected. The pulsed source was a Nano-LED configured with for a 295 nm output at 1 MHz. Luminescence lifetimes were obtained using the JobinYvon-Horiba FluoroHub single photon counting module fitting the lifetime data using DAS6 deconvolution software. Quantum yield measurements were obtained on aerated solutions using $[\text{Ru}(\text{bipy})_3](\text{PF}_6)_2$ in aerated MeCN as a standard ($\phi = 0.016$).

119

2.5.2. Synthetic methods

2.5.2.1. Synthesis routes in the surface functionalisation of ND

Method 1

Nap-1 (aq.) was added to aqueous dispersions of ND-CO₂H (0.5 mg mL⁻¹) to give a final concentration of 2 mM in 3 ml. Solutions of N-hydroxysulfosuccinimide (10 mM) and 1-ethyl-3-(3-dimethylaminopropyl)carbodiimide (20 mM) were added, giving a final ND-CO₂H concentration of 0.25 mg mL⁻¹. Dispersions were buffered to pH 9.5 using CHES and stirred at 30°C for 16 hours. Samples were dialysed using a 3 K MWCO cellulose membrane at room temperature into water, sonicated for a total time of 10 minutes at 0°C and treated with another round of dialysis. A 1000-fold dilution was achieved over 12 h of equilibration at room temperature for each round of dialysis, resulting in the assumed dilution of any remaining substrate or coupling reagents or byproducts to 10⁻⁶ of their original concentration. Samples were then passed through a 0.22 μm PES membrane to remove any dust or large aggregates for analysis. Repeat measurements

after 42 days were done with no further purification of filtration, samples were kept sealed in a dark, dry cupboard in the intervening time.

Method 2

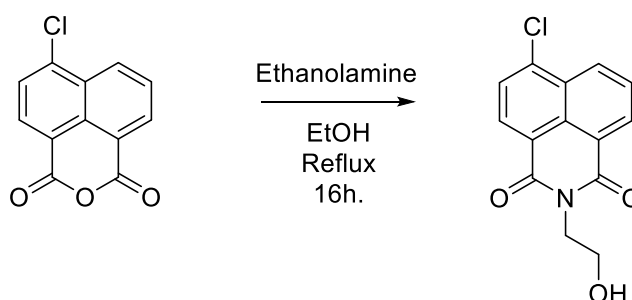
As for Method 1, but using a 50 mM borate buffer system (sodium tetraborate/boric acid) at pH 9.5.

Method 3

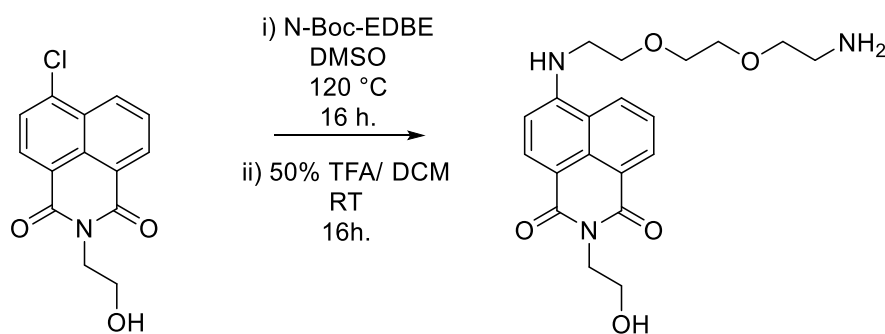
ND-CO₂H was dispersed in acetonitrile (0.25 mg mL⁻¹) and then stirred at room temperature. A 2 mM solution of Nap-1 or Ru-1 was added together with 1-ethyl-3-(3-dimethylaminopropyl)carbodiimide (20 mg mL⁻¹), N-hydroxysuccinimide (20 mg mL⁻¹) and triethylamine (0.5 mL) for 24 hours. In the case of the mixed Ru-1/Nap-1@ND, the concentration of each was 1 mM. The functionalised nanodiamond was pelleted by centrifugation (4400 rpm, 30 minutes, Eppendorf micro-centrifuge), followed by subsequent washing steps in acetonitrile by probe sonication of the sample (30% amplitude, 30 minutes), followed by centrifugation (4400 rpm, 30 minutes) until the supernatant was clear. The nanodiamond material was finally dispersed by probe sonication in water (1 mL, 30% amplitude, 30 minutes), followed by centrifugation (4400 rpm, 5 minutes) to remove residual titanium from the sonicator tip.

2.5.2.2. Synthesis of **Nap-1** from 4-chloro-1,8-naphthalic anhydride

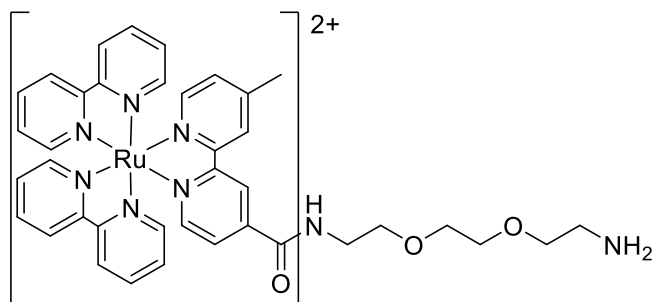
Synthesis of **Nap-Cl** precursor



4-chloro-1,8-naphthalic anhydride (2 g, 8.6 mmol) was dissolved in ethanol (60 mL) and ethanolamine (0.79 mL, 12.9 mmol) was added. The solution was then heated at reflux for 12 hrs under a nitrogen atmosphere. Upon cooling to 0 °C precipitation occurred, and filtration yielded **C¹** as a yellow solid (2.01 g, 85 %). ¹H NMR (400 MHz, CDCl₃): δ_H 8.70 (d, *J* = 6.8 Hz, 1H), 8.64 (d, *J* = 8.4 Hz, 1H), 8.54 (d, *J* = 7.6 Hz, 1H), 7.88 (m, 2H), 4.48 (t, *J* = 4.8 Hz, 2H), 4.01 (t, *J* = 4.8 Hz, 2H) ppm. LRMS ES⁺ found *m/z* = 275.03 [M⁺]

Synthesis of **Nap-1** from **Nap-cl**

C¹ (0.75 g, 2.72 mmol) was dissolved in DMSO (5 mL) and *N*-tert-butyl EBDE (1.4 g, 5.64 mmol) was added and the solution heated at reflux for 16 hours under a nitrogen atmosphere. Upon being allowed to cool the solution was flooded with 30 mL of water and neutralised with 0.1 M HCl. The product was then extracted with dichloromethane (3 x 15 mL) and washed with water (3 x 10 mL) and brine (3 x 10 mL). The crude intermediate product was then purified further through the use of silica gel column chromatography using 3:2 acetone hexane with 4% triethylamine as the eluent. The solvents were then removed under vacuum yielding the intermediate product as a red oil (0.40 g, 30 %). ¹H NMR (300 MHz, CDCl₃): δ_H 8.37 (d, *J* = 6.8 Hz, 1H), 8.28 (d, *J* = 8.4 Hz, 1H), 8.08 (d, *J* = 8.1 Hz, 1H), 7.46 (t, *J* = 7.5 Hz, 1H), 6.53 (d, *J* = 8.4 Hz, 1H), 6.03 (s, 1H), 5.00 (s, 1H), 4.36 (t, *J* = 4.8 Hz, 2H), 3.92 (t, *J* = 4.5 Hz, 2H), 3.82 (t, *J* = 5.1 Hz, 2H), 3.64 (m, 4H), 3.57 – 3.45 (m, 4H), 3.28 (d, *J* = 4.8 Hz, 2H), 1.34 (s, 9H) ppm. LRMS found *m/z* = 389.18 [M+H]⁺. Deprotection of the intermediate product was achieved by stirring in 50% TFA in DCM (10 mL) for 24 hours under a nitrogen atmosphere. The solvents were then removed under vacuum, and the residue dissolved in methanol and the solvent removed again. This was repeated in triplicate to yield **Nap-1** as a red oil (0.29 g, 91 %). ¹H NMR (300 MHz, CD₃OD): δ_H 8.31 – 8.19 (m, 2H), 8.09 (m, 1H), 7.43 (m, 1H), 6.61 (m, 1H), 4.23 (m, 2H), 3.80 (t, *J* = 5.1 Hz, 2H), 3.72 – 3.64 (m, 6H), 3.59 – 3.51 (m, 2H), 3.30 – 3.25 (m, 2H), 3.11 – 3.01 (m, 2H) ppm. ¹³C{¹H} NMR (75 MHz, CD₃OD): δ_C 164.78, 150.78, 149.04, 134.14, 133.04, 130.55, 128.31, 128.01, 127.62, 123.86, 108.00, 103.65, 70.03, 68.62, 66.54, 59.03, 42.69, 39.22 ppm. LRMS found *m/z* = 388.18 [M+H]⁺. HRMS expected *m/z* = 388.1794 for [M+H]⁺, found *m/z* = 388.1857.



2.5.2.3. Characterisation of **Ru-1**

Ru-1 was isolated as a red oil (45 mg, 0.05 mmol). ^1H NMR (400 MHz, CD_3OD) δ_{H} 8.97 (1H, s), 8.58-8.64 (5H, m), 8.54 (1H, s), 7.99-8.09 (5H, m), 7.85 (1H, d, $J = 5.9$ Hz), 7.67-7.77 (6H, m), 7.53 (1H, d, $J = 5.8$ Hz), 7.35-7.43 (5H, m), 7.27 (1H, d, $J = 5.8$ Hz), 3.49-3.66 (8H, m), 3.17-3.22 (2H, m), 2.99-3.06 (2H, m), 2.50 (3H, s) ppm. $^{13}\text{C}\{^1\text{H}\}$ NMR (100 MHz, CD_3OD) δ_{C} 164.6, 161.0, 160.7, 158.1, 157.2, 157.1, 157.0, 156.2, 151.9, 151.3, 151.1, 151.0, 150.4, 142.5, 138.0, 137.9, 128.8, 127.6, 125.5, 124.9, 124.4, 124.3, 121.5, 70.0, 69.9, 69.0, 66.5, 39.7, 39.2, 19.9 ppm. HRMS found $m/z = 379.1133$; calcd. 379.1133 for $[\text{C}_{38}\text{H}_{40}\text{N}_8\text{O}_3\text{Ru}]^{2+}$. UV-vis. λ_{max} (H_2O) / nm ($\epsilon / \text{dm}^3 \text{mol}^{-1} \text{cm}^{-1}$) 246 (27800), 287 (64100), 458 (13100).

Chapter 3. Development of Sortase Active functional nanodiamond particles

3.1. Chapter Aims

The overarching aim of this study (Section 1.1) requires the production of functional ND species that can be used as substrates by appropriate ligase enzymes, in order to be incorporated into the structural biological matrix.

The ability to co-functionalise polycarboxylated ND suspensions has been identified and evaluated in Chapter 2 of this thesis. In continuing from this the aim was to utilise a site-specific transpeptidase enzyme native to the gram-positive *S. aureus* and *S. pyogenes* bacterial species, Sortase A, which recognises and ligates specific peptide motifs to attach functional ND species onto an engineered curli biofilm (Figure 3.1). Thus, in developing dual-functioning ND suspensions, with particles expressing both one component of the Sortase A peptide tag and a functional component (i.e. luminophore), and recombinantly expressing the identified Sortase A enzyme, a system would be produced whereby it is possible to enzymatically modify engineered *E. coli* biofilms with luminescent ND particles.

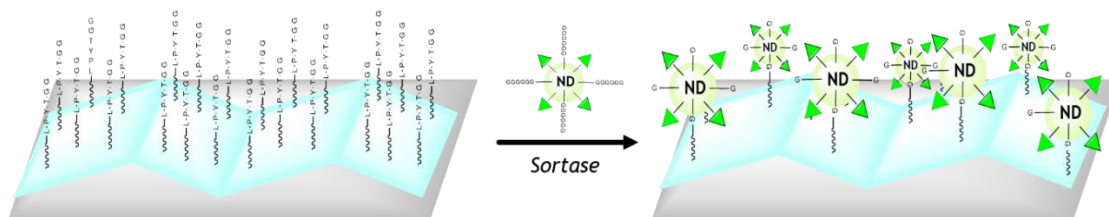


Figure 3.1: Route to enzyme modified nanodiamond embedded curli biofilm materials

This chapter evaluates the following critical aspects of this aim:

- Recombinant expression of Sortase A in *E. coli*
- Confirmation of Sortase A activity through peptide ligation assay
- Synthesis and characterisation of **Ir-1** a red emitting phosphorescent dye suitable for the attachment to ND
- Development of nanodiamond suspensions co-functionalised with orthogonally luminescent species and the Sortase A ligase peptide tag
- Solid phase peptide synthesis of a bespoke luminescent Ru(II) peptide conjugate, **[Ru(Bipy)₂L₁]-LPYTGG**
- Evaluation of the ability to utilise Sortase A to modify the co-functionalised Sortase A active nanodiamond suspensions

In the evaluation of these aspects, this chapter further develops established ND functionalisation technologies for application for the targeted synthetic biological production of novel hybrid materials.

3.2. Introduction

3.2.1. Sortases: a group of cell membrane associated enzymes critical for attachment of proteins to the peptidoglycan cell wall

Sortases are a family of enzymes produced by Gram-positive bacteria, playing a critical role in the development of the peptidoglycan cell wall.¹²⁰ Recognising specific sequence motifs, this group of enzymes 'sort' secreted proteins for covalent attachment to the outer surface of the cell membrane (specifically via attachment to lipid II),¹²¹ or are involved in polymerisation of secreted proteins to form pili.¹²² Sortases have received a great deal of attention in recent literature, due in part to their role in virulence factor display in pathogens such as *S.aureus*,^{123,124} but also due to their applicability in covalently modifying proteins to produce chimeric post-translationally modified proteins.¹²⁵⁻¹²⁷ Different sortases recognise different peptide motifs for transpeptidation, typically with different roles in attachment/pili formation.¹²⁰

Typically more than one sortase is present in an organisms genome, exhibiting differing levels of substrate specificity and function.¹²⁸ One member of the sortase family, Sortase A (SrtA), is commonly termed the 'housekeeping' sortase, attaching a wide variety of protein substrates secreted *via* the *sec* pathway in *S. aureus* and *S. pyogenes*.¹²⁶ SrtA from both organisms attaches a variety of proteins to the cell wall through recognition of the LPXTG (*S.aureus*) or LPXTA (*S.pyogenes*) motif (where X can be any amino acid). Attachment in both cases occurs through transpeptidation with an N-terminal polyglycine entity on the peptidoglycan cell wall. For clarity, SrtA henceforth refers to that found in *S.aureus*, recognising LPXTG motif.

SrtA is highly selective for the LPXTG motif. Experiments by Clancy *et al.* showed that apart from the X position, all amino acid residues were essential to their ability to act as a SrtA substrate (Figure 3.2).¹²⁹

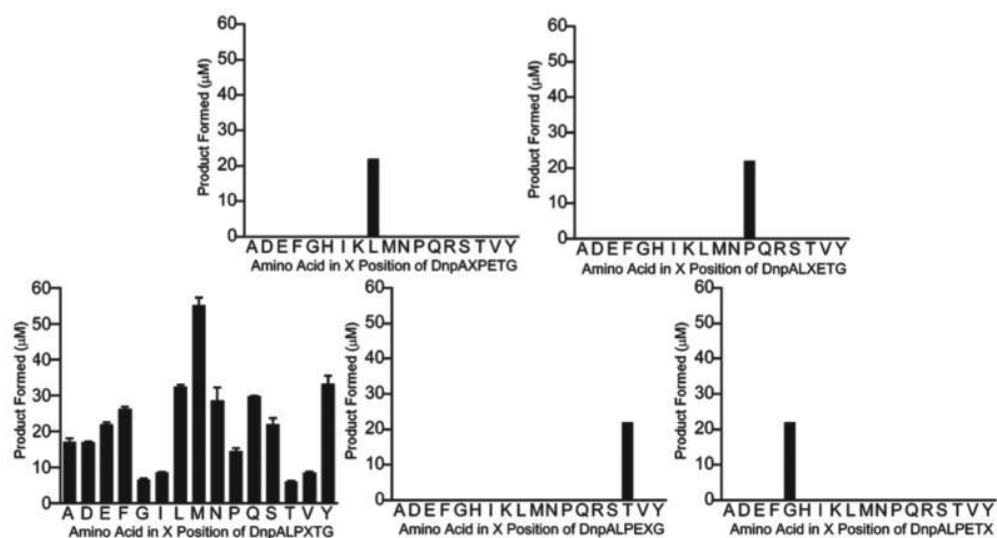


Figure 3.2: Residue preference of SrtA: Libraries of substituted sequences were produced in varying positions of the LPXTG motif, showing that apart from residue X, all other residues are critical in substrate selection by SrtA. Figure adapted from reference 129.

A plethora of methods have available to generate such site-specific protein modifications. They often require the incorporation of large enzymatic domains onto the protein substrate, or are limited in their range of substrates able to be attached.¹²⁶ Transpeptidases such as SrtA provide an efficient, highly selective route to modification, and as such have received a large amount of interest.

In the context of this study, SrtA provides an ideal route to attach ND a biofilm matrix containing an engineered amyloid protein matrix. Through incorporation of the specific LPXTG motif onto the CsgA protein (addressed in Chapter 4), and a $H_2N-(G)_n$ sequence onto the surface of nanodiamond it is hypothesised that sortase will efficiently effect the necessary covalent attachment thus ligating the two components and yielding the functional biofilm matrix.

3.2.2. Mechanism of *S.aureus* SrtA transpeptidation

The structure of Sortase A is dominated by a β -barrel conformation containing 8 β -strands (Figure 3.3). The active site is located within a hydrophobic pocket away from the β -barrel structure (Figure 3.4). In nature the morphology of SrtA is conserved through Ca^{2+} binding adjacent to the active site; Ca^{2+} has been observed to stimulate the activity of SrtA.¹³⁰

SrtA catalyses transpeptidation between the specific LPXTG sequence and N-terminal polyglycine ($NH_2-(G)_n$) sequence. The mechanism of SrtA catalysed transpeptidation is

relies on a catalytic dyad formed by cysteine and histidine residues C184 and H120 in the active site (Figure 3.5). The arginine residue R197 and tryptophan W194 have also been identified to be involved in stabilisation of the enzyme-substrate complex.¹²⁹ C184, and H120 are absolutely critical to SrtA activity,^{131,132} substitution of which abolishes the transpeptidation of SrtA activity.

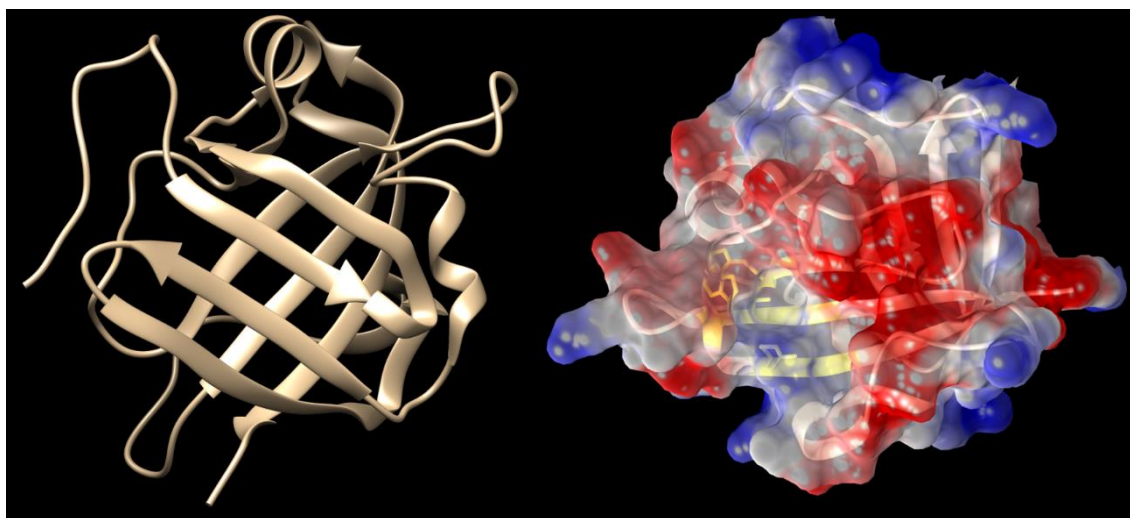


Figure 3.3: Left- β -barrel structure of SrtA from *S.aureus*. Right- structure of SrtA showing the active site (yellow coloured ribbon) in hydrophobic pocket with coulombic surface rendering. Images rendered using UCSF Chimera from PDB 1T2P.¹³³

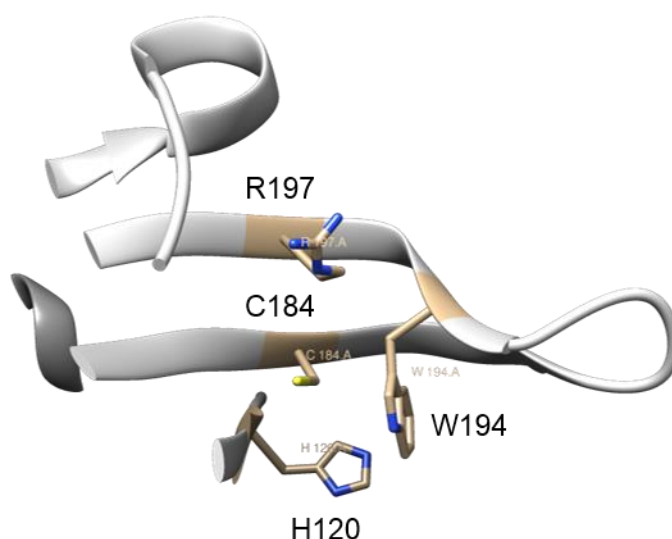


Figure 3.4: Active site of SrtA made up of C184, H120, R197 and W194 residues

The exact mechanism by which SrtA acts has been the subject of discussion in the literature, with several mechanisms suggested. In all cases, transpeptidation is proposed to be mediated through thioesterification of C184 with the threonine residue of the

LPXTG tagged substrate, which is then subjected to substitution *via* nucleophilic attack of the NH₂ terminus on the second, polyglycine tagged substrate. This is aided by proton transfer with the nearby H120 residue.^{129,134,135}

Whilst detailed discussion of all postulated mechanisms for SrtA action is beyond the scope of this study, the most likely mechanism is based around the a ‘ping-pong’ reverse protonation mechanism (Figure 3.5) proposed for similar enzymes.^{136–138} Several supporting factors including data from kinetic isotope effect experiments and inactivation experiments support this mechanism.¹²⁹ SrtA catalyses the hydrolysis of proteins bearing the LPXTG motif in the absence of a polyglycyl nucleophile, with kinetic studies suggesting a rate limiting step in the initial thioesterification event.¹³¹ Importantly, this enzyme relies on the equilibrium between the thiol/imidazole and thiolate/imidazolium forms of C184 and H120, with the latter being the active form. Clearly, the nucleophilicity and basicity of the thiolate form is increased, and thus better able to act in thioesterification, whilst the imidazolium acidity is purported to be key in the non-reversible formation of the thioester intermediate. Therefore, if this mechanism is to be taken as true, at biologically relevant pH, only a small amount (0.06%) of SrtA is available to perform catalysis.¹²⁹

In the ‘reverse-protonation’ mechanism, thioesterification is initiated by nucleophilic attack of the thiolate group from C184 on the amide bond between the threonine and glycine residues of the LPXTG motif. The imidazolium species from the H120 residue acts as a Brønsted acid, promoting the route to thioester formation (as opposed to cleavage of the sulphur-carbon bond). Transpeptidation occurs through nucleophilic attack by the NH₂ terminus of the polyglycine substrate, which following by proton transfer to H120 by the intermediate thioether yields the ligated product.

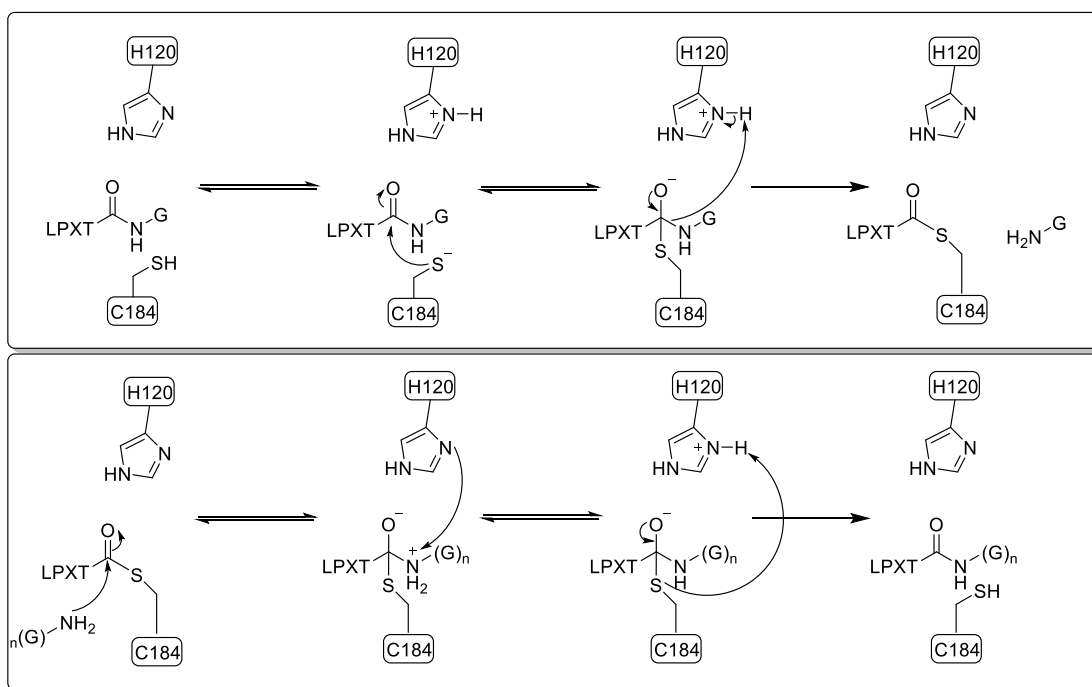


Figure 3.5: Reverse protonation mechanism purported for SrtA

R197 plays a key role in transient state stabilisation through hydrogen bonding with the LPYTG motif. Substitution of R197 with citrulline (a neutral homologue of arginine, capable of hydrogen bonding) showed only a slightly decreased catalytic rate, suggesting its role in enzyme substrate complex stabilisation as opposed to being directly involved as a base.¹³⁹ W194 appears important, as the W194A mutant produced by Ton-That *et al.* exhibited drastically reduced activity, suggesting further stabilisation of a transition state.¹⁴⁰

Transpeptidation is reasonably tolerant of nucleophiles, requiring at least one N-terminal glycine in achieving michaelis constants (K_m) of between 35 – 16 μM for the xenobiotic substrate, Abz-LPXTG-Dpn, translating in identical conditions to turnover rates of around 0.1 $\mu\text{M min}^{-1}$.¹³⁵

3.2.3. Development of *S.aureus* SrtA in protein modification technologies

A variety of SrtA enzymes have been applied in sortase mediated modification of proteins. Wild type SrtA from *S.aureus* has been noted to exhibit poor reaction rates and it's applicability is limited by reliance on binding the Ca^{2+} cofactor.¹⁴¹ Variant forms of this sortase exhibit superior catalytic activity. Chen *et al.* reported a significant improvement over the relevant parameters of the wild type SrtA ($k_{\text{cat}} = 1.5 \text{ s}^{-1}$, K_m LPETG = 7.6 mM,) in utilisation of the pentamutant P94R/D160N/D155A/K190E/K196T variant ($k_{\text{cat}} = 5.4 \text{ s}^{-1}$, K_m LPETG = 0.23 mM), with a 140 fold increase in overall catalytic

efficiency (k_{cat}/K_m LPETG). Incorporation of two further mutations identified to remove dependence on Ca^{2+} (E105K and E108Q) ¹⁴² allowed the generation of a catalytically optimised, calcium independent septamutant SrtA; SrtA(7M), retaining the improved kinetic parameters of the pentamutant form. ¹⁴³ This form of the enzyme is available commercially through plasmid sharing platforms and presents an attractive, easily available optimised form of SrtA to employ for transpeptidation.

Reversibility in SrtA mediated transpeptidation is another important issue, as the -LPXTG- motif containing product formed can present as a target for transpeptidation with the cleaved H_2N -G- unit. Various strategies have been employed to overcome this, through experimental design to yield unattractive H_2N -G- fragments upon initial transpeptidation, complexation of the products with metal ions, and incorporation of WTWTW sequences either side of the ligated peptide motifs, yielding a product exhibiting a β -hairpin unable to be recognised by SrtA. ¹⁴⁴

3.2.4. Utilisation of SrtA in chemical biology

SrtA has been employed in a huge variety of applications to date, including protein and peptide labelling, ^{145–148} attachment of proteins/peptides to abiotic planar ^{127,149,150} and particle surfaces, ^{151,152} and cell surface modification. ^{153–155}

3.2.4.1. Labelling of proteins

Popp *et al.* exploited WT SrtA from both *S. aureus* and *S. pyogenes* in both the circularisation and PEGylation of cytokine proteins such as human interferon alpha (IFN α 2). Two versions of IFN α 2 (a four-helix bundle cytokine) were produced, one containing an N-terminal polyglycine motif and both containing either LPETG/LPETA sortase motifs at the opposing end of the protein (Figure 3.6). Through the orthogonal action of SrtA from *S. aureus* and *S. pyogenes*, a variety of different products could be produced from SrtA transpeptidation, including circularised and PEGylated products (Figure 3.6). The produced protein forms exhibited advantageous properties compared to the unmodified forms, including increased thermal stability of the helix bundles from circularisation and increased *in-vivo* stability of the PEGylated form. ¹⁴⁵

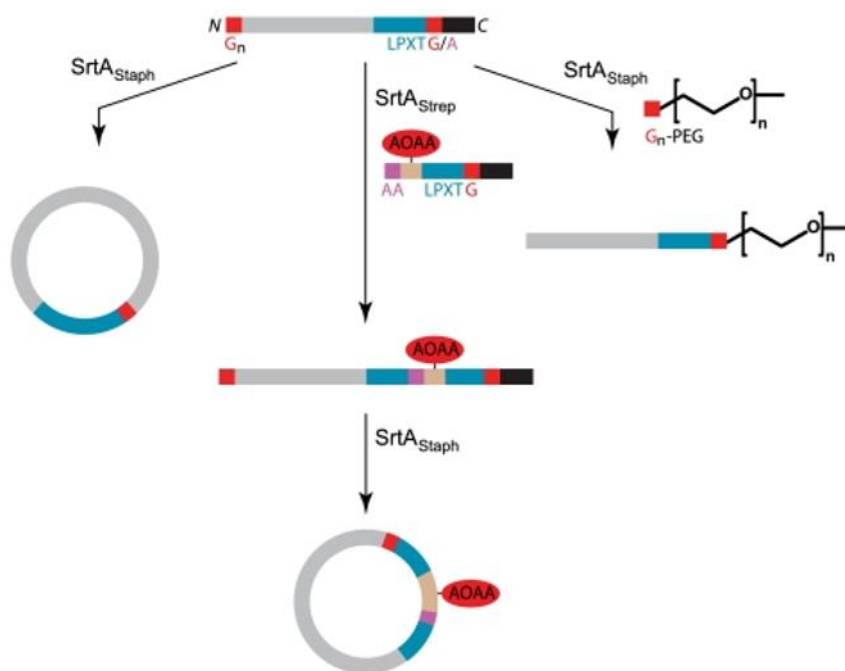


Figure 3.6: Orthogonal SrtA modification of IFN α 2 by *S. aureus* (SrtA_{staph}) and *S. pyogenes* (SrtA_{strep}) sortases to yield a variety of products. Adapted from reference 145.

Antos *et al.* described the C-terminal labelling of protein substrates bearing the LPETG recognition sequence with cholesterol tryglycine derivatives in good (60-90%) yield. Utilising eGFP-LPETG as the protein substrate, lipid modification resulted in a 500-fold enhancement (with respect to the native protein) in fluorescence intensity in HeLa cells, ascribed to their increased ability to interact and cross/interact with the various cellular membranes present.¹⁴⁶

Incorporation of the LPETG motif in the internal crossover loop in the ubiquitin C-terminal hydrolase UCHL3 contributed to the function determination that. Cleavage and transpeptidation at the LPETG site with a polyglycine labelled biotin substrate allowed for labelling of the protein active towards a streptavidin-HRP conjugate. Ubiquitin hydrolysis rates of the engineered strains showed a small degree of reduction in the enzyme function following cleavage, contributing to the conclusion that the crossover loop restrict access of bulky adducts to the active site, rather than a major contribution to maintenance of structure at the active site itself.¹⁴⁸

3.2.4.2. Attachment of proteins to abiotic planar and particle surfaces

Sijbrandij *et al.* utilised SrtA transpeptidation technologies to investigate the ability to prevent biofouling of a surface through attachment of a PEG group. A polystyrene

surface was functionalised with the (G)₅P3 peptide through hydrophobic interaction with the P3 peptide (Figure 3.7). Initial testing with a biotin labelled LPETG surface confirmed the ability of SrtA to covalently link substrates to the surface (*via* evaluation of HRP activity following concurrent interaction with a streptavidin-HRP conjugate). A PEG chain containing the LPETG sequence was then attached, which resulted in a decrease in bacterial binding over 3 hours of around 40% relative to the control polystyrene surface.

127

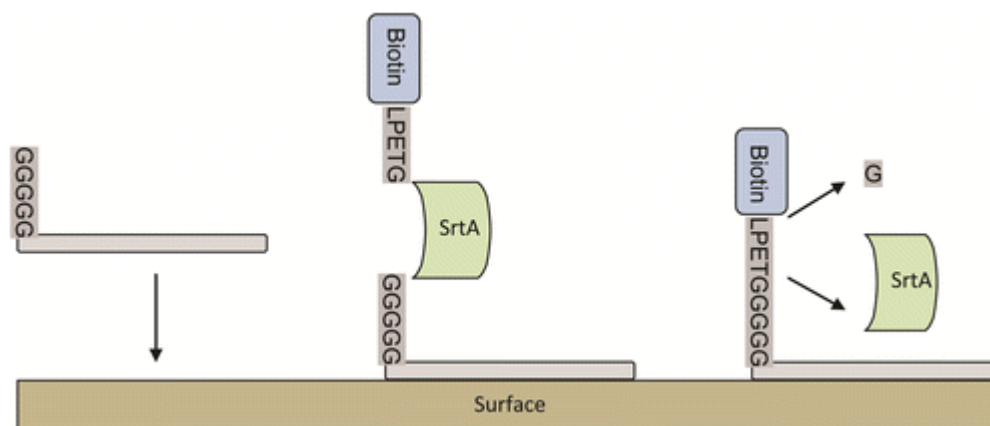


Figure 3.7: Demonstration of the ability to attach species to a polystyrene surface *via* SrtA transpeptidation Adapted from reference 127

Ta *et al.* conjugated the single chain antibody (scFv) to iron oxide particles, for applications in contrast imaging in MRI studied. The LPETG motif was included in the antibody chain and expressed in insect cells. The aminated iron oxide particles were conjugated to a polyglycine motif. Sortase immobilisation of the antibody was then performed yielding the conjugate product. The conjugate product demonstrated the ability to attach to cells expressing the appropriate antigen in *in-vitro* studies, and *in-vivo* MRI imaging demonstrated the ability to utilise the conjugate as a negative contrast agent specific to thrombi in mouse carotid arteries.¹⁵¹

3.2.4.3. Cell surface modification

In utilising the naturally exposed polyglycine residues on the cell surface of the bacterium *Toxoplasma gondii*, CD8 T cells, yeast cells and mouse spenocytes, recombinant proteins were attached to the cell surface *via* expression with C-terminal LPETG sequences and biotin-LPETG. Biotin-LPETG was conjugated *via* SrtA to the surfaces of various microorganisms, which was then subjected to attachment of streptavidin. SDS-PAGE analysis of the unmodified cells showed the successful incorporation of streptavidin. Cellular attachment of single domain antibodies to the toxic

CD8 T cells with a view to induce specificity to leukemic cells was performed, utilising the interaction with antigen labelled GFP. Successful interaction with GFP was identified through flow cytometry, demonstrating the ability to specifically modify the immunoprocessing of specific toxic cell lines.¹⁵⁵

3.3. Results and discussion

3.3.1. Expression of *S.aureus* Sortase A from *E. coli*

SrtA from *S. aureus* was expressed in *E.coli* from a *srtA* gene harboured by a pET30b plasmid *via* the method described in Section 3.5.2. The crude hexa-histidine tagged protein was obtained through purification of the supernatant *via* Ni-NTA affinity chromatography and eluted from the column with sortase elution buffer. SDS-PAGE (Figure 3.8) of fractions from Ni-NTA column confirmed the expression of SrtA, with a band corresponding to ~18 kDa present in all elution fractions (theoretical mass of heptamutant histidine tagged SrtA is 17.85 kDa). The elution fractions were then combined, and dialysed into sortase storage buffer (1000:1 dilution factor, 2 cycles). Analysis by SDS-PAGE of the dialysed protein showed the protein present as a band corresponding to ~18 kDa in very high purity.

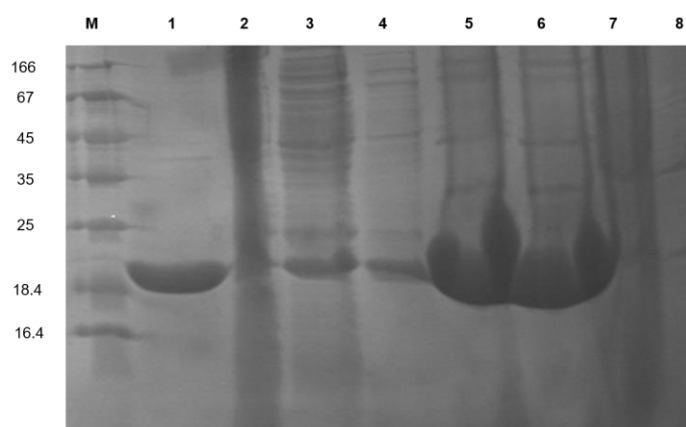


Figure 3.8: SDS PAGE of SrtA. Lane 1- Dialysed protein from combined fractions (diluted by 4), Lane 2- flow through from Ni-NTA column, Lane 3+4- wash fractions from Ni-NTA column, Lane 5+6- Elution fractions from Ni-NTA column.

UV-visible analysis of the protein showed that the combined fractions contained SrtA at a concentration of 0.375 mM (determined from the absorbance at 280 nm, $\epsilon = 14400$ from predicted data).

Production of SrtA was confirmed by charge deconvoluted mass spectrometry, identifying the mass of product at 17853 g mol^{-1} (Figure 3.9), within 0.1% to the theoretical exact mass of 17851 g mol^{-1} , an error associated with the mass deconvolution process.

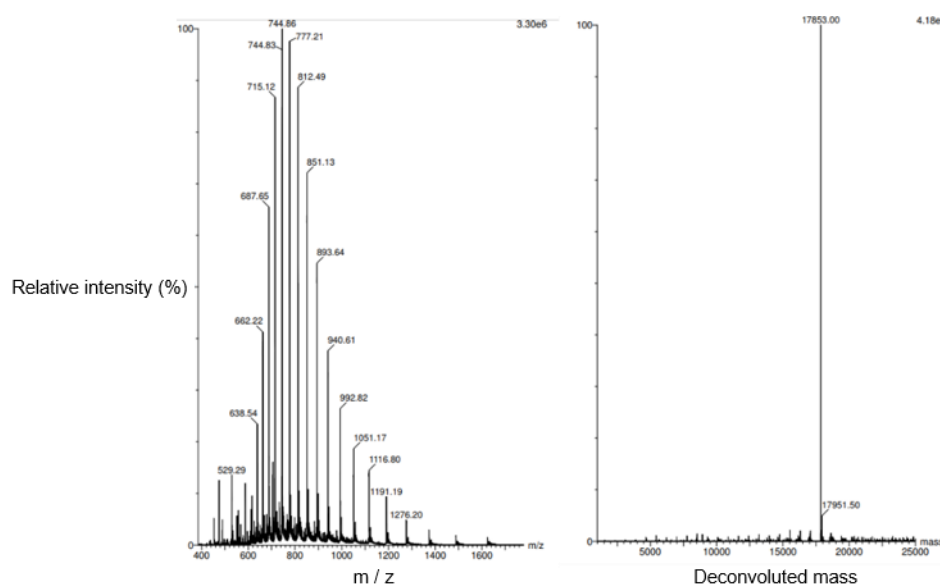


Figure 3.9: Mass spectrum of SrtA produced from the expression of *srtA* in *E. coli* (left), deconvoluted by charge states (right).

3.3.2. Confirmation of SrtA(7M) activity towards TTLPYTGG and GGGGTTTT peptides

In the initial confirmation of SrtA(7M) (sequence given in section 3.5.2) activity, peptides TTLPYTGG and GGGGTTTT were ligated over the course of 24 hours in the appropriate sortase reaction buffer at pH 7.5. Integration of TIC detected chromatogram peaks at ~8.30 and ~8.70 minutes corresponding to the appropriate masses of TTLPYTGG (809.40 for $[M+H]^+$, Figure 3.10) and the product TTLPYTGGGGTTTT (1327.64 for $[M+H]^+$, Figure 3.10) respectively allowed the reaction progress to be followed through aliquot quenching at specific timepoints (Figure 3.11). Although TIC integration cannot be employed in the absolute quantification of product formation, comparison of the integrals for TTLPYTGG and TTLPYTGGGGTTTT can be employed in the relative rate of product formation as a ratio. All chromatograms are reported in the appendix of this thesis.

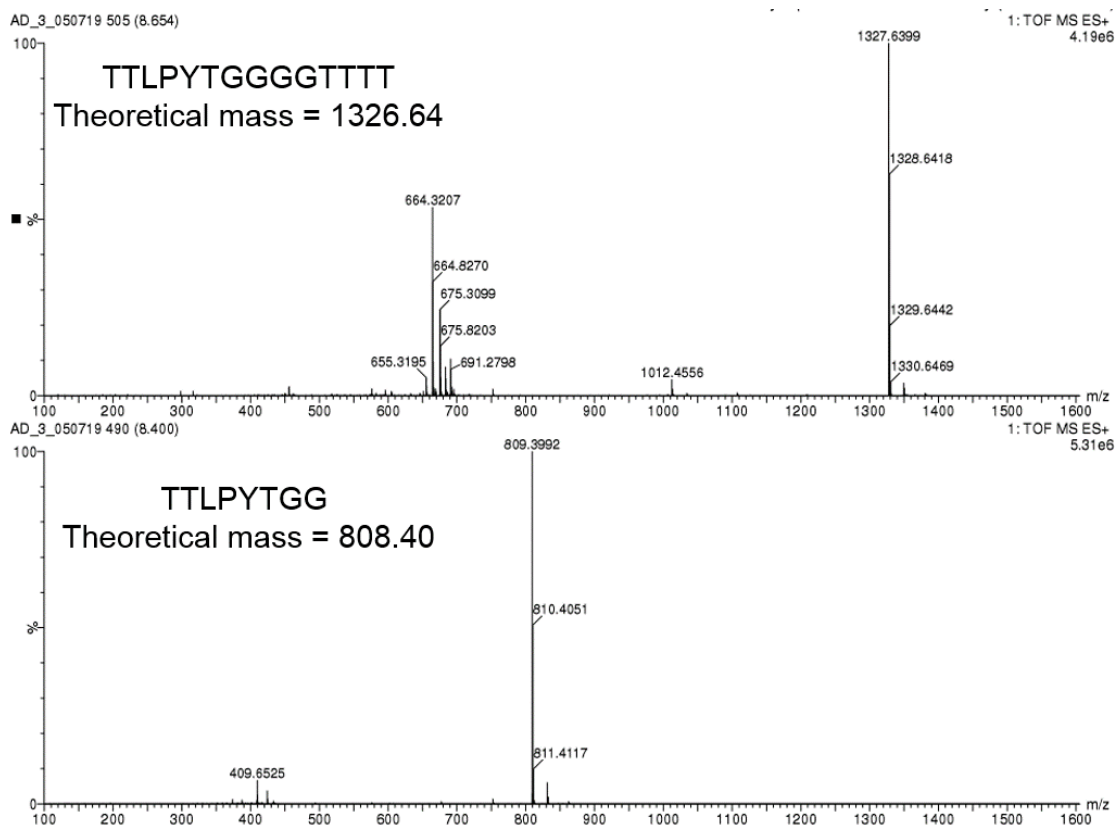


Figure 3.10: Mass spectra of TTLPYTGGGGTTTT (Top) and TTLPYTGG (bottom) detected at ~8.7 and 8.3 minutes respectively

From integral ratios, a rapid initial rate of product formation to almost 50% was observed within the first 20 minutes. This rate appeared to tail off to a lower, linear rate of conversion culminating around 93% product conversion under these conditions. Detailed rate analyses for SrtA (7M) is not relevant to this work, and would require multiple experiments, requiring specially designed peptide conjugates enabling fluorescent monitoring of reaction rate. Given the similarities of the peptides TTLPYTGG and GGGTTTT to the peptides designed for utilisation in covalent ligation of ND particles to the surface, this assay was designed to accurately represent conditions employed in ligating an excess of ND particles to a LPYTGG expressing biofilm surface. Through this assay, it is clear that over 24 hours almost 95% of ligation product was formed from TTLPYTGG and GGGTTTT, indicating that the SrtA is active and suitable for ND attachment.

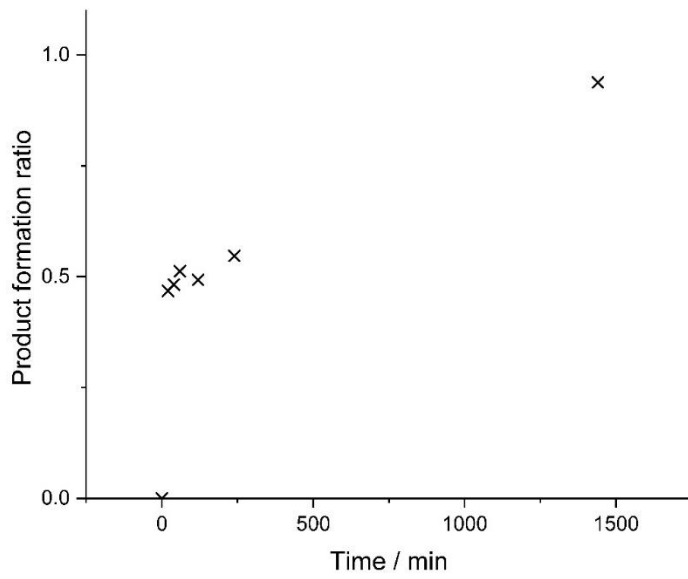


Figure 3.11: Measurement of SrtA activity as a product formation ratio from chromatogram integrals.

3.3.3. Synthesis of red luminescent organometallic iridium (III) complex, **Ir-1** suitable for ND attachment.

Luminophores employed included **Nap-1** (synthesis and characterisation described in Chapter 2), and **Ir-1** (Figure 3.12) to give a broad range of luminescent properties (i.e. modified lifetime and emitting wavelength). Both luminophores contain a terminal primary amine suitable for covalent attachment to nanodiamond through the methods described in Chapter 2.

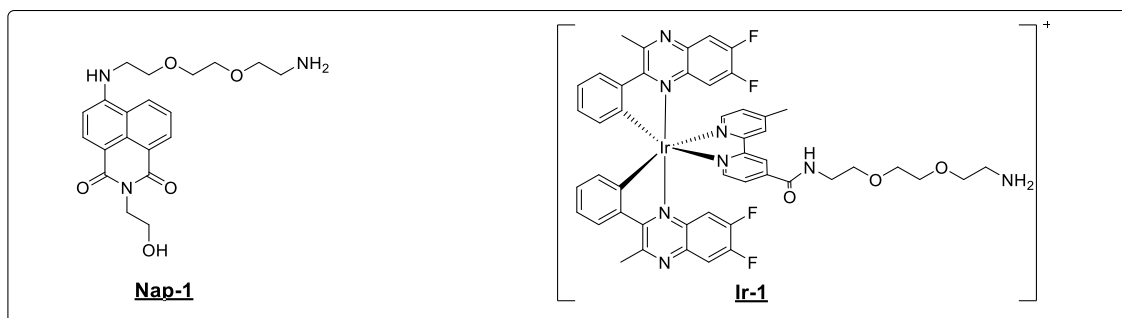


Figure 3.12: Structures of **Nap-1** and **Ir-1** luminophores

Synthesis of the organometallic **Ir-1** luminophore was achieved in 3 steps (Figure 3.13.). Firstly, the acid catalysed condensation of 1-phenylpropane-1,2-dione with 1,2-difluoro-4,5-diaminobenzene in ethanol yielded the quinoxaline ligand **QX-1** as in Phillips *et al.* (2018).¹⁵⁶ The chlorine-bridged iridium dimer species **Ir₂Cl₂(QX-1)₄** was synthesised by ligand substitution of the hydrated IrCl₃ precursor (presumably present in solution as [Ir(Cl₃)(H₂O)₃] in 2-ethoxyethanol at reflux. This dimer was used without further purification, splitting with the 5-methyl-2,2-bipyridyl-5'-**NBoc-EBDE** derivative to yield the final complex **Ir-1** as a red solid with a cumulative isolated yield of ~8%.

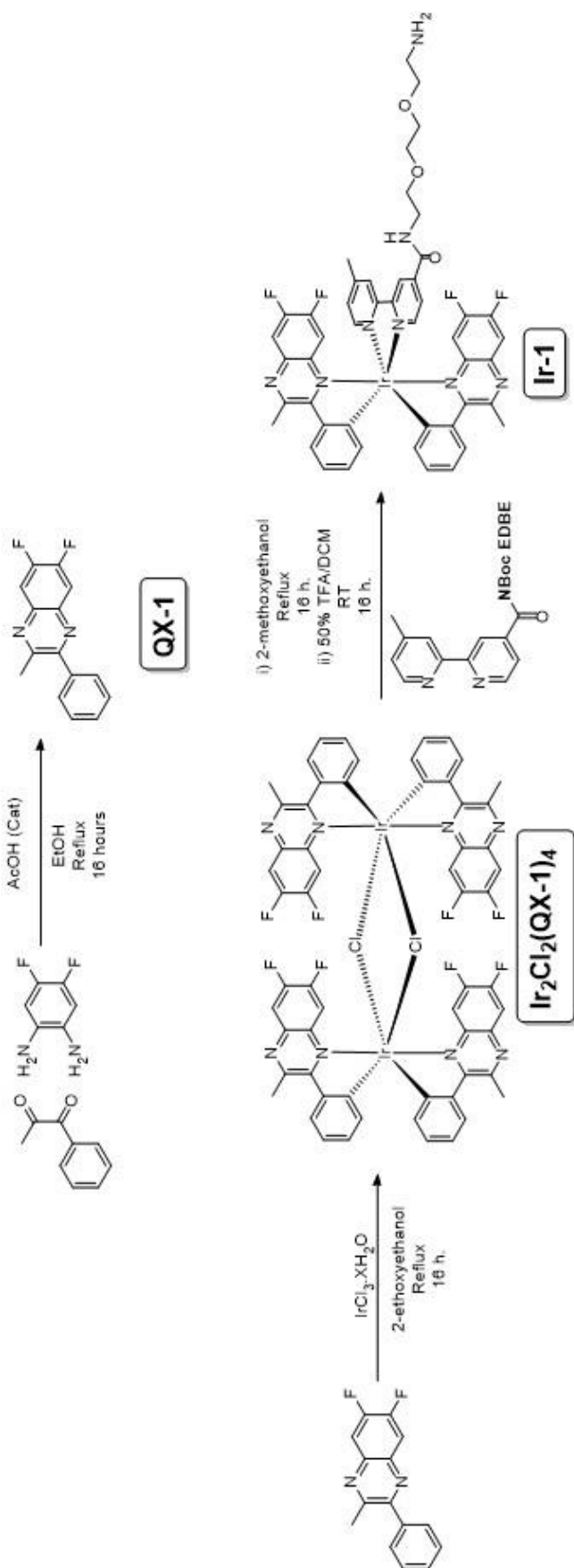


Figure 3.13: Synthetic route to the organometallic Ir(III) based complex, **Ir-1**.

Analysis by NMR spectroscopy (aromatic region of **Ir-1** shown in Figure 3.14), mass spectrometry (showing correct molecular ion peak in low and high resolution) are conclusive in the identification of the production of **Ir-1**. Where **QX-1** exhibited multiplet resonances around 7.41-7.56 ppm corresponding to the benzyl moiety attached to the quinoxaline. These appear to shift upfield, most extensively where the proton directly adjacent to the cyclometallating site shifts to ~6.53 ppm, and those in the meta- and para- positions to around 7.21 ppm (still observable by now occluded by the CDCl₃ residual peak). Significantly downfield resonances attributed to protons adjacent to the coordinating nitrogen atoms in the 2,2'-bipyridyl based ligand were also observed.

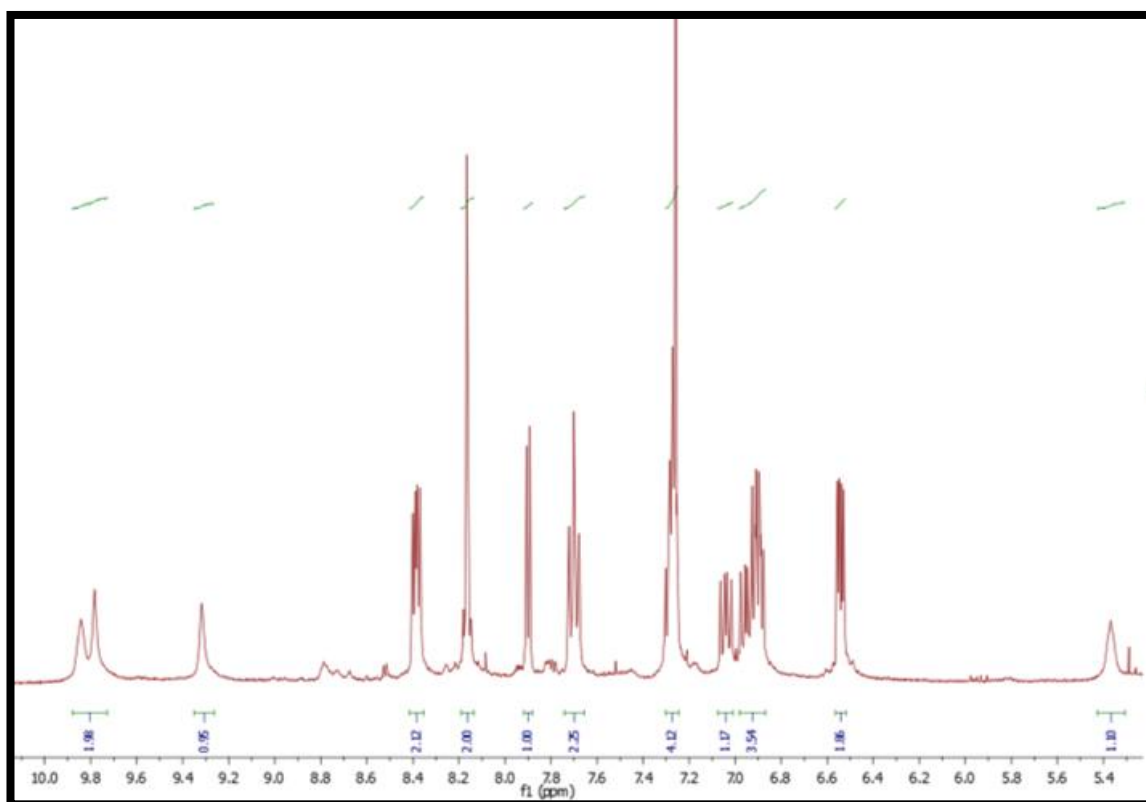


Figure 3.14.: Aromatic region of the ¹H NMR spectrum of **Ir-1**.

3.3.3.1. Optical properties of **Ir-1**

A summary of the optical properties of luminophores and **Ir-1** (along with that of **Nap-1**, previously described in Section 2.3.1) is detailed in Table 3.1. The UV-Visible and luminescence emission spectra is shown in Figure 3.15, and summarised in table 3.1.

Table 3.1: Summary of optical absorption and emission properties of luminophores **Nap-1** and **Ir-1** recorded in aerated water.

	$\lambda_{\max} / \text{nm}$ ($\epsilon / \text{dm}^3 \text{mol}^{-1} \text{cm}^{-1}$)	$\lambda_{\text{em}} / \text{nm}$	Stokes shift / cm^{-1}	$\tau_{\text{obs}} / \text{ns}$	$\phi / \%$
Nap-1	445 (8800)	542	4022	4.5	42%
Ir-1	258, 312 374 (15400) 477 (3100)	670	6039	210	0.5%

Ir-1 demonstrates a complex UV-Visible absorption spectrum, with multiple absorption bands below 600 nm. Phillips *et al.* described the absorption spectra (albeit in chloroform) of similar diquinoxaline 2,2',-bipyridil coordinated Ir(III) complexes, whereby high energy absorptions ($< 420 \text{ nm}$) are a composite of high probability overlapping ligand-centred transitions (various $\pi\text{-}\pi^*$ and $n\text{-}\pi^*$).¹⁵⁶ The strong absorption shoulder around 477 nm ($\epsilon = 3100 \text{ dm}^3 \text{mol}^{-1} \text{cm}^{-1}$) possess a degree of metal to ligand charge transfer character (MLCT). This extends with a slight shoulder around 580 nm. This observation has been attributed to the spin-forbidden $^3\text{MLCT}$ state, supported by time dependent DFT (TD-DFT) and transient absorption spectroscopy. The optical absorption properties of iridium (III) bisquinoxaline complexes such as **Ir-1** and those described by Phillips *et al.* are highly complex, and detailed characterisation and assignment is beyond the scope of this study. Luminescent emission centred around 670 nm, with a long emissive lifetime (210 ns) is supportive of phosphorescent emission from the spin forbidden $^3\text{MLCT}$ excited state to the singlet ground state. The low quantum yield of the iridium complex in the aerated aqueous solvent is unsurprising, representing a significant component of deactivation by molecular oxygen of the triplet excited state. Langdon Jones *et al.* previously found comparable ($\sim 2 \%$) quantum yields for similar complexes.

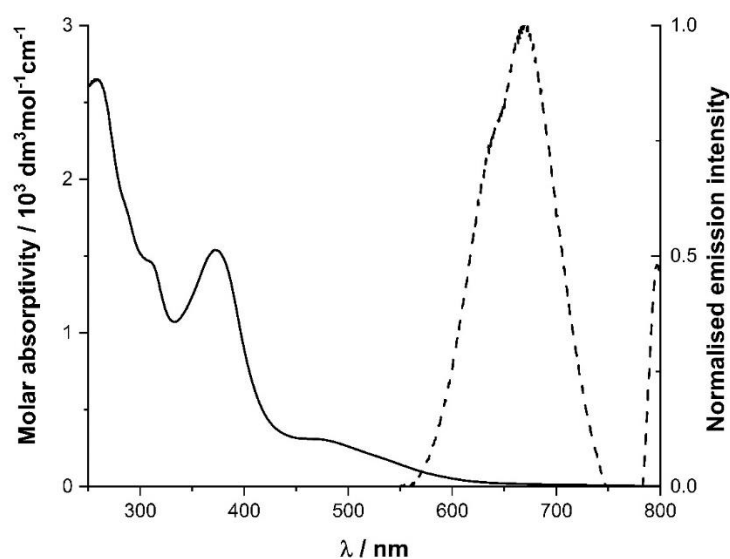


Figure 3.15: UV-Visible absorption spectrum (black solid line) and luminescence emission spectrum (black dashed line, $\lambda_{em} = 350$ nm, slits 8,8) of **Ir-1** in water.

3.3.4. Development of enzyme labile peptide luminophore co-functionalised ND suspensions suitable for surface modification by Sortase A **Nap-1/Srtpep1@ND** and **Ir-1/Srtpep1@ND**

In the development of bifunctional ND suspensions suitable for SrtA modification, a library of fluorescent covalently functionalised with the SrtA A peptide **SrtPep 1** and luminophores **Nap-1**, and **Ir-1**. These ND suspensions were prepared through the acetonitrile solvated method (method 3) described in Chapter 2, followed by deprotection of the 9-fluorenylmethoxycarbonyl (Fmoc) protecting group in 40% piperidine in acetonitrile (Figure 3.16).

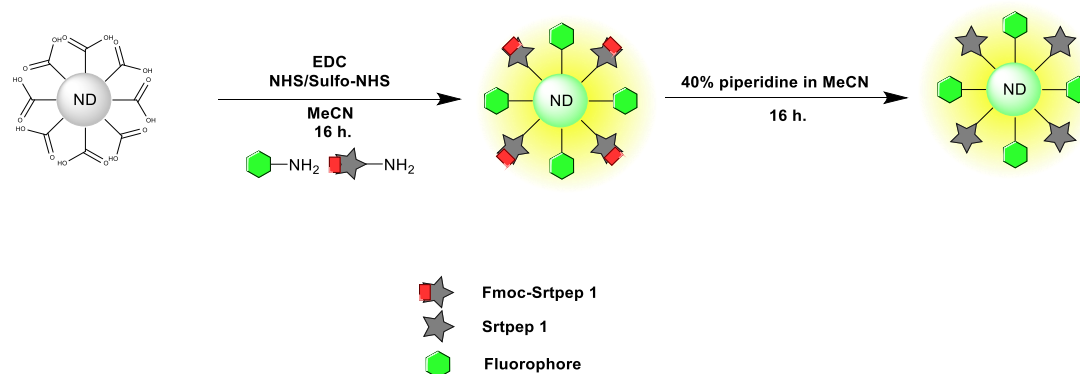


Figure 3.16: Schematic showing method of incorporation of SrtA recognition peptide and luminophore.

The protected SrtA recognition peptide, **Srt pep 1** (Figure 3.17) was attached *via* the lysine residue as it is critical to maintain the N-terminus of the polyglycine sequence (as detailed in section 3.2.1). Following deprotection with 40 % piperidine in MeCN, surface functionalised ND dispersions **Nap-1/Srtpep1@ND** and **Ir-1/Srtpep1@ND** were produced.

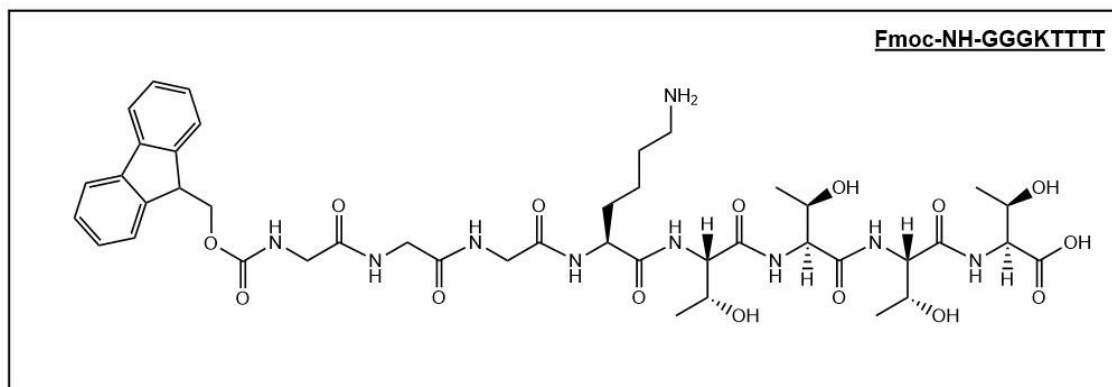


Figure 3.17: Structure of **Srt pep 1**.

3.3.4.1. Evaluating optical properties of protected and deprotected suspensions of **Nap-1/Srtpep1@ND** and **Ir-1/Srtpep1@ND**

Analysis of optical properties of **Nap-1/Srtpep1@ND** and **Ir-1/Srtpep1@ND** was performed to confirm preservation of optical properties of attached luminophores, as well as in confirmation of the attached Fmoc-protected sortase recognition peptide. A summary of optical properties of the deprotected surface functionalised ND dispersions is given in Table 3.2. Following functionalisation and deprotection, the aqueous dispersions of **Nap-1/Srtpep1@ND** and **Ir-1/Srtpep1@ND** exhibited faint yellow and red colours respectively, suggesting retention of the coloured **Nap-1** and **Ir-1** luminophores attached.

The UV-visible absorption spectrum of **Nap-1/Srtpep1@ND** (Figure 3.18) is dominated by a strong degree of scattering (evidenced by a strong background signal increasing in intensity in accordance with wavelength). Absorbance attributed to the ICT transition of **Nap-1** at c.a. 450 nm (as observed for **Nap-1@ND**, Section 2.3.2) can clearly be identified as a shoulder in the scattering pattern. Due to the scattering observed, no other features can be distinguished.

The UV-Visible absorption spectrum of **Ir-1/Srtpep1@ND** (Figure 3.18) is again dominated by scatter, appearing mostly featureless with a small shoulder observable around 280 nm, resembling the highest energy ligand centred absorption for the **Ir-1** luminophore (Section 3.3.3).

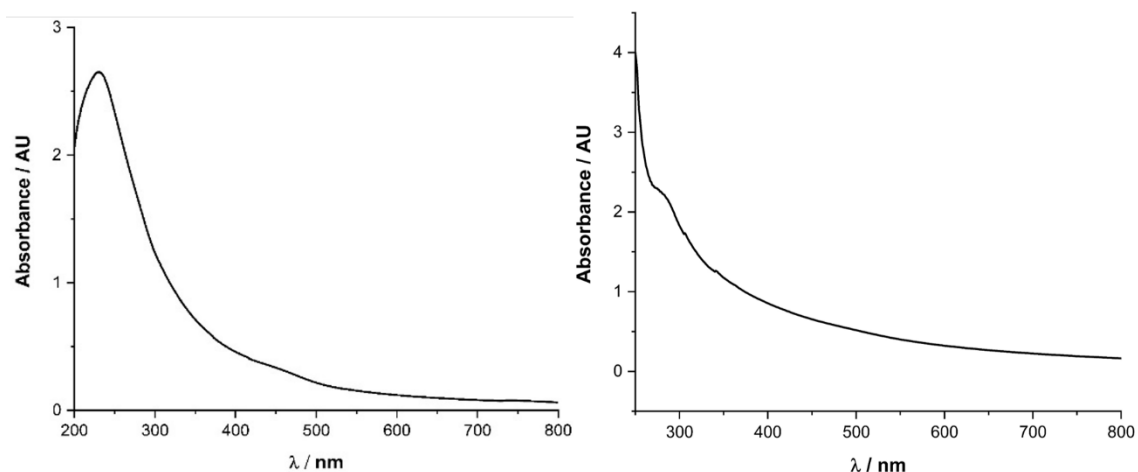


Figure 3.18: UV-visible absorption spectra of **Nap-1/Srtpep1@ND** (left) and **Ir-1/Srtpep1@ND** (right).

Luminescence emission spectra of **Nap-1/Srtpep1@ND** (Figure 3.19) prior to deprotection with 40% piperidine exhibit a dominant, featureless emission centred

around 320 nm ($\lambda_{\text{ex}} = 260$ nm), consistent with fluorescent emission from the 9-fluorenylmethyl environment,¹⁵⁸ in addition to a previously identified broad emission peak centred around 540 nm ($\lambda_{\text{ex}} = 450$ nm) attributed to fluorescence from **Nap-1**. Following deprotection, this peak is seen to almost completely disappear, indicating efficient and complete deprotection of the N-terminal amine.

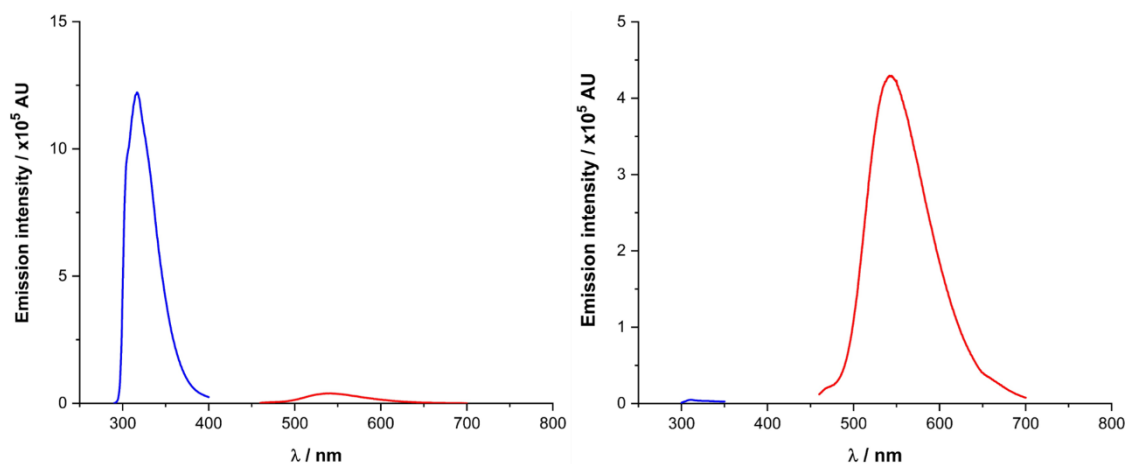


Figure 3.19: Luminescence emission spectra of **Nap-1/Srtpep1@ND** prior to (left) and following (right) deprotection with 40% piperidine in MeCN. $\lambda_{\text{ex}} = 260$ nm (blue solid lines), $\lambda_{\text{ex}} = 450$ nm (red solid lines). Slits at 4,4 nm. No correction or normalisation of was performed.

This is replicated in the emission spectra of protected and deprotected **Ir-1/Srtpep1@ND** (Figure 3.20), whereby almost complete loss of the luminescence emission signal around 320 nm following deprotection is observed. This emission signal was replaced by an band centred around 360 nm, attributed to ligand centred emission of the **QX-1** ligand. Broad emission from excitation at 450 nm around 670 nm was observed, attributed to the ³MLCT phosphorescent emission from the attached **Ir-1** complex. Phosphorescent emission (from a triplet excited state) was further supported through lifetime measurements, describing a long-lived excited state with a lifetime of 230 ns. This is of a similar order for lifetimes found for similar iridium quinoxaline complexes described by Phillips *et al.* 2018.¹⁵⁶

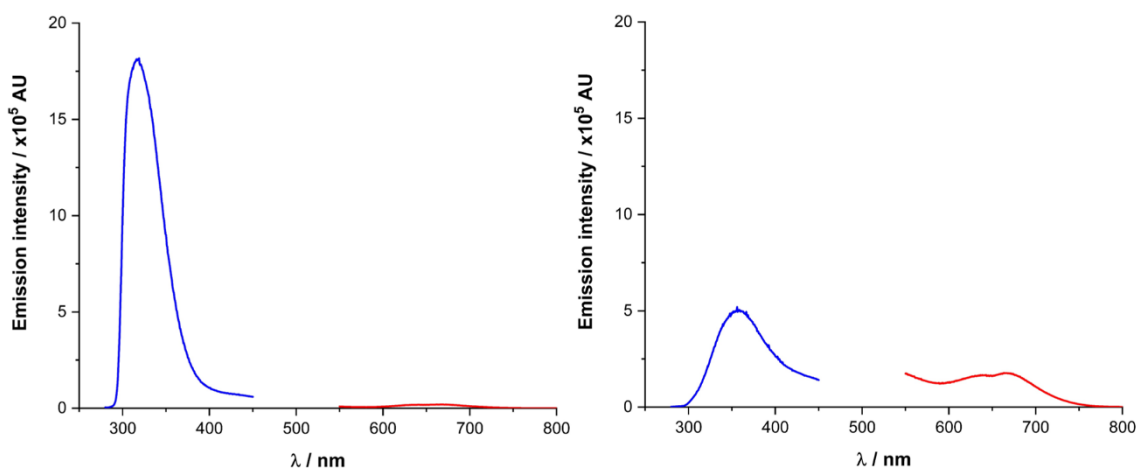


Figure 3.20: Luminescence emission spectra of **Ir-1/Srtpep1@ND** prior to (left) and following (right) deprotection with 40% piperidine in MeCN. $\lambda_{\text{ex}} = 260$ nm (blue solid lines), $\lambda_{\text{ex}} = 450$ nm (red solid lines). Slits at 8,8 nm. No correction or normalisation was performed.

Table 3.2: Summary of optical properties of **Nap-1/Srtpep1@ND** and **Ir-1/Srtpep1@ND**.

Compound	λ_{max} (UV-Vis) / nm	λ_{em} / nm	Lifetime / ns
Nap-1/Srtpep1@ND	258, 283, 445	543	3.9
Ir-1/Srtpep1@ND	380	640	230

Analysis of the optical properties of **Nap-1/Srtpep1@ND** and **Ir-1/Srtpep1@ND** confirmed the attachment of both the peptide and luminophores (as evidenced by dual emissive properties of the protected species), and the efficacy of the deprotection protocol (the abrogation of fluorescence emission pertaining to the 9-fluorenylmethyl group present).

3.3.4.2. Size distribution analysis of **Nap-1/Srtpep1@ND** and **Ir-1/Srtpep1@ND**

Size distributions and zeta potentials of aqueous dispersions of **Nap-1/Srtpep1@ND** and **Ir-1/Srtpep1@ND** are shown in Table 3.3 and Figure 3.21 with data for **ND-COOH** and **Nap-1@NDc** shown for comparison in Table 3.1.

Table 3.3: Size distribution analysis of aqueous suspensions of **ND-COOH** and surface functionalised ND samples **Nap-1/Srtpep1@ND**, **Ir-1/Srtpep1@ND** and **Nap-1@NDc**.

Sample	pH	Particle Diameter (HDD) / nm		PDI (DLS)	Zeta Potential / mV
		DLS	NTA		
ND-COOH	5.0	62	53±1	0.13	-43.0
Nap-1/Srtpep1@ND	5.8	189	142±2	0.25	-14.3
Ir-1/Srtpep1@ND	6.2	115	176±9	0.26	-30.0
Nap-1@NDc	5.2	182	165±3	0.12	-19.5

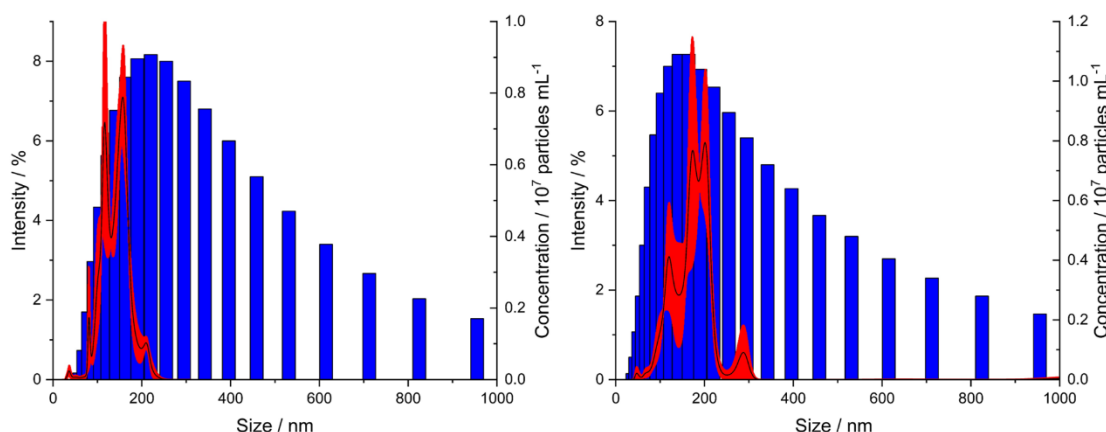


Figure 3.21: Particle sizes (hydrodynamic diameter) of dispersions of **Nap-1/Srtpep1@ND** and **Ir-1/Srtpep1@ND** in H₂O measured by DLS (blue bars) and NTA (black solid line with red error area).

Aqueous dispersions of **Nap-1/Srtpep1@ND** and **Ir-1/Srtpep1@ND** both exhibit aggregation to a similar degree to that of **Nap-1@NDc** (produced by method 3, Section 2.3.2). Particle diameters of **Nap-1/Srtpep1@ND** and **Nap-1@NDc** and by both NTA and DLS were found to be broadly similar (c.a. 142 nm by NTA and 185 by DLS). **Nap-1/Srtpep1@ND** is notably polydisperse (PDI = 0.26), in comparison with that of **Nap-1@NDc**. **Ir-1/Srtpep1@ND** exhibited similar particle diameters to the **Nap-1** functionalised ND species by NTA, however DLS measurements found smaller average

particle sizes in comparison (c.a. 175 nm by NTA and 115 nm by DLS), with dispersions also exhibiting a high degree of polydispersity (PDI = 0.26)

Zeta potential measurements of **Ir-1/Srtpep1@ND** found a larger (more negative) zeta potential of -30.0 mV, whereas **Nap-1** functionalised ND species generally exhibited zeta potentials of less than -20 mV. This is counterintuitive, given the attachment of the positively charged iridium complex in comparison with the neutral **Nap-1** luminophore. However, this could be a result of salt-charge screening (i.e. from the TFA counterion following deprotection of the Boc group in the final step).

Introduction of the co-functionalised sortase recognition peptide SrtPepA appeared to have a drastic increase on the polydispersity as evidenced by the increase PDI and broadness of size distributions by DLS and NTA measurements. As seen for **Nap-1@NDb** in Chapter 2, this brings into doubt whether the mean size determined for **Ir-1/Srtpep1@ND** particles by DLS is representative, as the DLS measurement is typically not too tolerant of polydisperse samples. Still, as for chapter 2, it is likely that size measurements by NTA are largely more representative of the polydisperse systems produced upon surface functionalisation with the co-substrates.

In summary, particle sizes of dispersions of ND particles surface co-functionalised with the sortase recognition peptide **GGKpep** and **Ir-1** and **Nap-1** respectively are broadly similar to those found for **Ru-1** and **Nap-1** functionalised species detailed in Chapter 2. The extra step in deprotection appears to have little effect on the particles colloidal properties, and surface functionalisation of ND appears tolerant of a wide variety of species.

3.3.4.3. XPS analysis of **Nap-1/Srtpep1@ND** and **Ir-1/Srtpep1@ND**

Normalised atomic percentages of carbon, nitrogen and present for **Nap1/Srtpep1@ND** and **Ir-1/Srtpep1@NDND-COOH**, **Nap-1@ND** calculated from XPS spectra are shown in Table 3.4. Initial survey spectra revealed elements present prior to a quantitative scan. Survey spectra of **Nap-1/Srtpep1@ND** and **Ir-1/Srtpep1@ND** are shown in the appendix of this thesis. XPS calculated atomic percentages for **ND-COOH** and **Nap-1@NDc** as detailed in Section 2.3.1.3 are included in **Table 3.4** for comparison.

Table 3.4: Normalised atomic percentages of carbon, nitrogen and oxygen in **Nap-1/Srtpep1** and **Ir-1/Srtpep1**.

Sample	Carbon %	Nitrogen %	Oxygen %
ND-COOH	87.84	0.36	11.80
Nap-1/Srtpep1 @ND	73.48	8.11	18.41
Ir-1/Srtpep1 @ND	70.47	12.17	17.36
Nap-1 @NDc	61.47	11.11	20.15

Surface co-functionalisation with **Nap-1/Srtpep1** and **Ir-1/Srtpep1** of ND yielded particles containing a similar atomic percentage of carbon, nitrogen and oxygen as for **Nap-1 @NDc**. **Nap-1/Srtpep1 @ND** was shown to contain around 8. % of nitrogen and whereas the **Ir-1/Srtpep1 @ND** species exhibited a greater (~12%) concentration. Considering the structures of the **Nap-1** and **Ir-1** (with 3 nitrogen atoms in **Nap-1**, compared to 6 in **Ir-1**), this is unsurprising and represents a different composition of the produced surface functionalised particles. Iridium was not able to be distinguished in the XPS spectrum of **Ir-1/Srtpep1 @ND**, possibly due to the overlap of the strongest signal in the XPS spectrum of ir (4f) (around 65 eV) with numerous low-energy environments and a relatively low detection limit.

Deconvolution of the C(1s) peak (Figure 3.22) of **Nap-1/Srtpep1 @ND** revealed four components: C(1s-1) (B.E. = 283.8 eV), C (1s-2) (B.E. = 284.5 eV), C (1s-3) (B.E. = 285.8) and C (1s-4) (287.8), respectively. Deconvolution of the C(1s) peak (Figure 3.21) of **Ir-1/Srtpep1 @ND** revealed four components: C(1s-1) (B.E. = 283.6 eV), C (1s-2) (B.E. = 284.0 eV), C (1s-3) (B.E. = 285.2) and C (1s-4) (287.4), respectively. These values are in good agreement with those found for surface functionalised ND species detailed in Section 2.3, representing the diamond (sp^3) **C-C**, surface associated carbon, oxidized **C-O** and highly oxidised **C=O** environments.

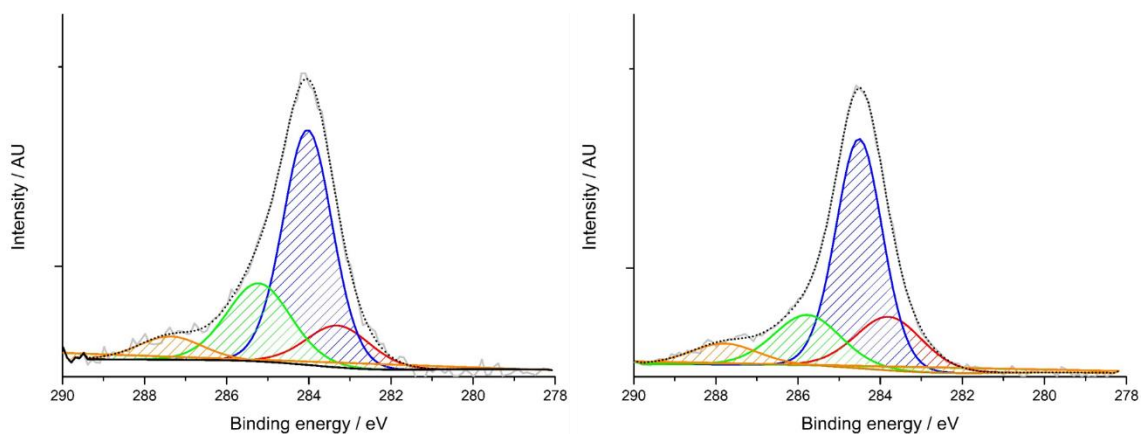


Figure 3.22: Deconvoluted XPS spectra of **Nap-1/Srtpep1@ND** (left) and **Ir-1/Srtpep1@ND** (right) showing components C1s-1 (red), C1s-2 (blue), C1s-3 (green) and C1s-4 (orange) fitted to the XPS spectral trace (light grey solid line) to give the fitted environment (black dashed line).

3.3.5. Evaluating the ability to modify luminophore/SrtPep-1 co-functionalised ND suspensions with SrtA using bespoke, synthesised peptide

The sortase recognition peptide **Srtpep1**, co-functionalised with luminophores **Nap-1** and **Ir-1** imparts the ability to further functionalise the produced particles through a sortase-mediated ligation step with SrtA (Figure 3.23). In order to evaluate the ability of SrtA to further modify the surface environment of these ND particles, the fluorescent conjugate peptide, **[Ru(bipy)₂L₁]-Srtpep2** was synthesised by solid phase peptide synthesis, which can then be used as the other component of the SrtA ligation. Identification of the luminescent spectral profile of the **[Ru(bipy)₂L₁]** complex following ligation and purification is in theory diagnostic of successful sortase modification.

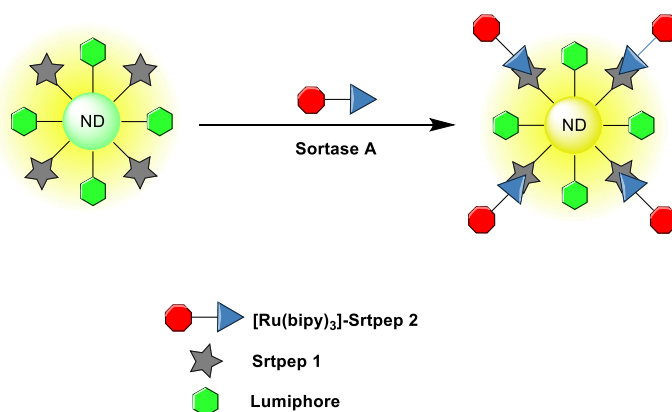


Figure 3.23: Depiction of functionalisation of **Nap-1/Srtpep1@ND** and **Ir-1/Srtpep1@ND** by Sortase A using the synthetic conjugate peptide **[Ru(bipy)₂L₁]-Srtpep2**.

3.3.5.1. Development of **[Ru(bipy)₂L₁]-LPYTGG**, a luminescent peptide conjugate suitable for Sortase A ligation with a polyglycine expressing peptide.

[Ru(bipy)₂L₁] (Figure 3.24) was synthesised from commercially available starting materials by Samuel. J. Adams (School of Chemistry, Cardiff University). Based on a the tris-bipyridyl coordination complex of Ru²⁺, **Ru(Bipy)₂L₁** exhibits a coordinated 5-methyl,5'-carboxy 2,2-bipyridine ligand (**L₁**), identical to that used in producing **Ru-1** described in Chapter 2.

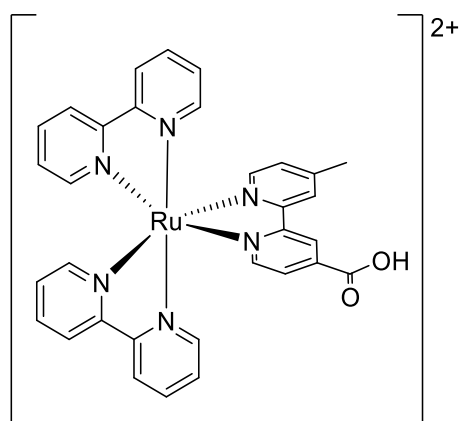


Figure 3.24: Structure of $[\text{Ru}(\text{Bipy})_2\text{L}_1]$.

The carboxylic acid bearing ruthenium complex, $[\text{Ru}(\text{Bipy})_2\text{L}_1]$, is suitable for employment in solid phase peptide synthesis. The hexameric peptide sequence LPYTGG was synthesised from the corresponding standard Fmoc-protected amino acids on 2-chlorotrityl resin through the manner described in SECTION 3.5.6.2., $[\text{Ru}(\text{bipy})_2\text{L}_1]$ was then conjugated through identical conditions as the prior amino acids, in a fivefold equivalent excess. Final deprotection, TFA cleavage and initial isolation through precipitation in ether was performed yielding conjugate $[\text{Ru}(\text{bipy})_2\text{L}_1]\text{-Srtpep2}$ (Figure 3.25) isolated as a red solid following lyophilisation.

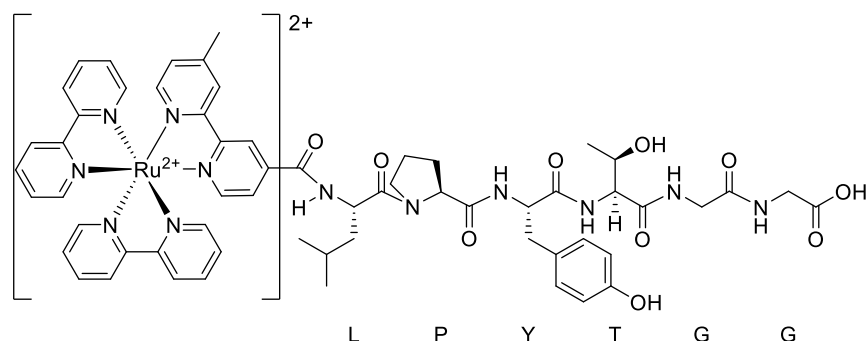


Figure 3.25: Structure of the Sortase Active $[\text{Ru}(\text{Bipy})\text{L}_1]\text{-Srtpep2}$.

The crude peptide isolate was evaluated by LCMS (Figure 3.27), which showed the far dominant species eluting at 15.0-15.5 minutes, whose mass spectrum (Figure 3.26) showed a single peak at $m/z = 608.3$. This corresponds to the theoretical mass of $[\text{Ru}(\text{bipy})_2\text{L}_1]\text{-Srtpep2}$ ($1216.31 \text{ g mol}^{-1}$), exhibiting a double positive charge, thus theoretically as $m/z = 608.155$. The $m/z = 0.15$ error margin is consistent with that of the single decimal place quadrupole detector employed.

Further confirmation of this species is seen in the close-up of the peak at 608.3, which displays an isotope pattern closely reminiscent of the theoretical isotope pattern of ruthenium.

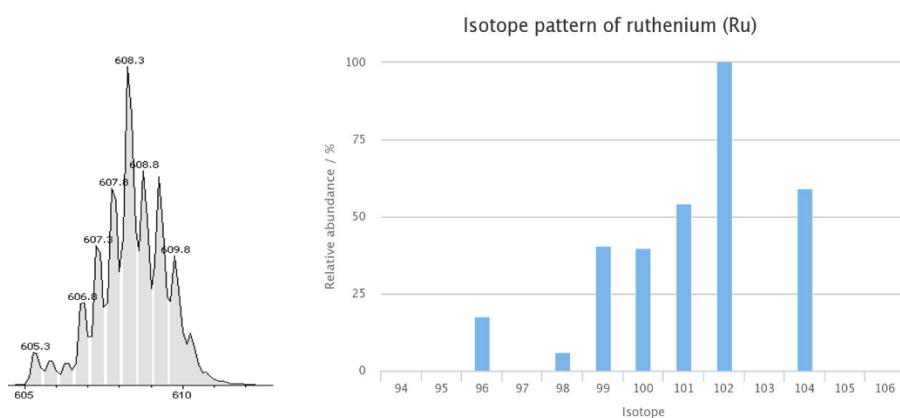


Figure 3.26: Comparison of the obtained isotope pattern of of **[Ru(bipy)₂L₁]-Srtpep2** with a theoretical pattern of ruthenium.

MS analysis of the peak at 9.8 minutes showed a molecular ion signal at $m/z = 607.4$ consistent with that of the proton adduct ($[M+H]^+$) **[Ru(bipy)₂L₁]** conjugated peptide (theoretical mass = 606.3). Later peaks corresponded to an unidentifiable mixture of compounds.

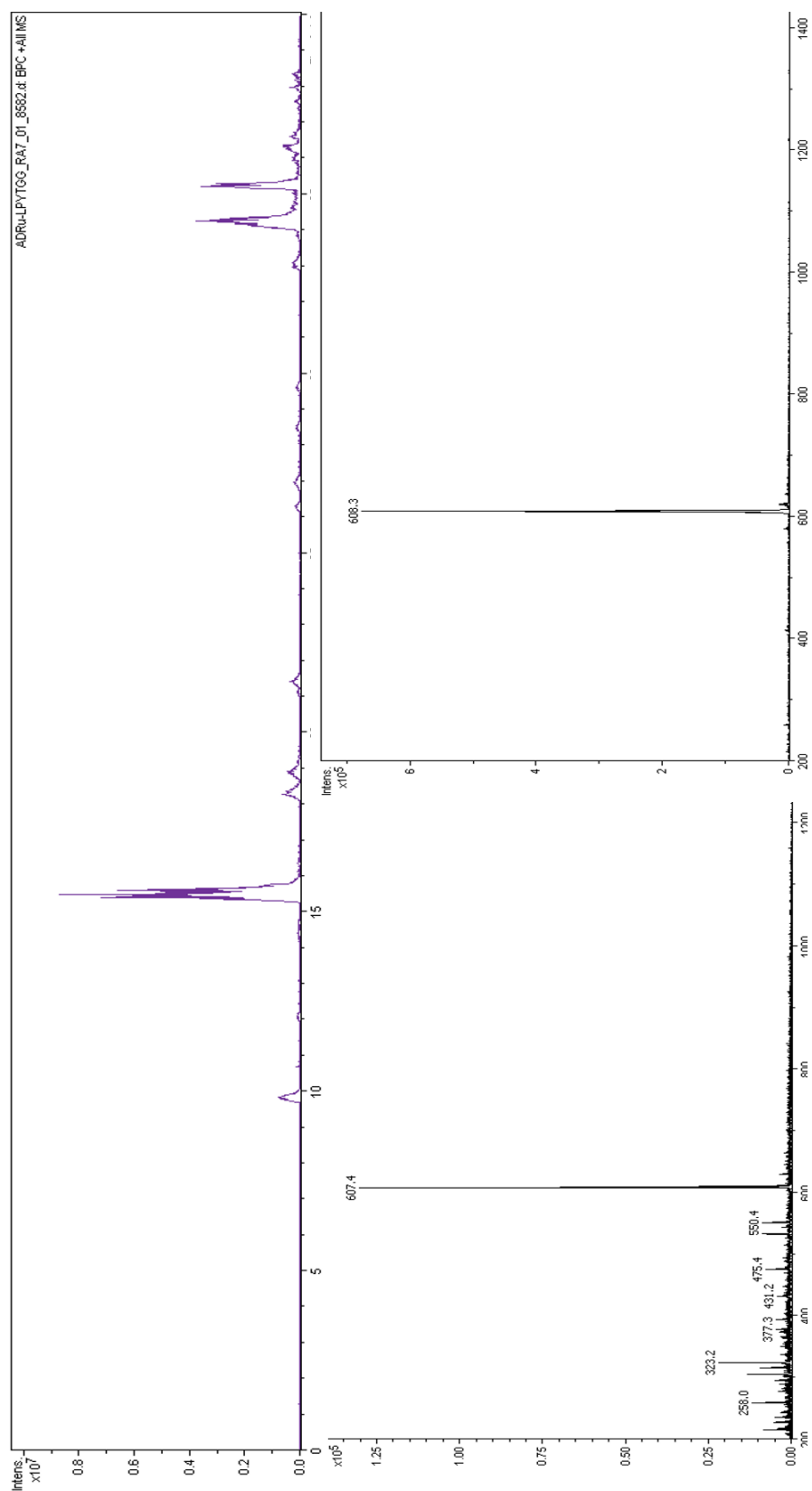


Figure 3.27: Top: LCMS chromatogram (TIC MS detection) of crude $[\text{Ru}(\text{bipy})_2\text{L}_1]\text{-Srtpep2}$. Bottom left: mass spectrum of peak at 9.8 minutes. Bottom right: mass spectrum of peak at 15.2 minutes.

LC-MS analysis of the crude peptide product showed the desired product, **[Ru(bipy)₂L₁]-Srtpep2** was produced in good purity. Little identifiable side products were found, and following preparatory LCMS using identical conditions, 4 mg of purified product was isolated upon lyophilisation.

Photophysical analysis of the purified **[Ru(bipy)₂L₁]-Srtpep2** conjugate elicited characteristic absorbance and emission properties of the **[Ru(bipy)₂L₁]** luminophore (Figure 3.28).¹⁵⁹ The UV-Visible absorption spectrum demonstrated a lowest energy absorption centred around 460 nm, arising from ¹MLCT transition. Absorbances below 400 nm are sharp and intense and arise from ligand centred transitions. The emission spectrum following excitation at 450 nm of **[Ru(bipy)₂L₁]-Srtpep2** describes an intense emission band centred around 660 nm, typical of ³MLCT emission from the **[Ru(bipy)₂L₁]** luminophore.

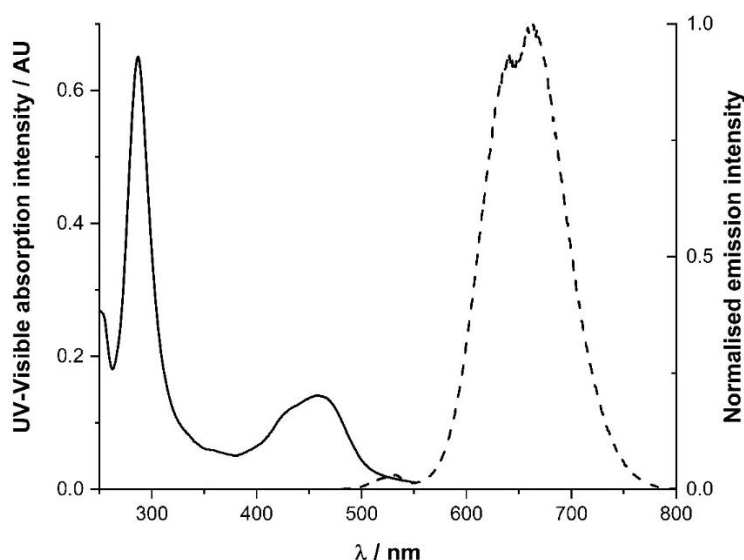


Figure 3.28: UV-Visible absorption and emission spectra of **[Ru(bipy)₂L₁]-Srtpep2**.

3.3.5.2. Sortase A mediated ligation of **[Ru(Bipy)₂L₁]-Srtpep2** to surface functionalised ND dispersions

Sortase A active ND suspensions **Nap-1/Srtpep1@ND** and **Ir-1/Srtpep1@ND** were incubated in with shaking at 350 rpm over 24 hours with a molar ratio of 10:1 of **[Ru(Bipy)₂L₁]-Srtpep2** (0.1 mmol) and *S.aureus* SrtA produced as detailed in Section 3.5.2 of this chapter. The reaction was buffered with 50 mM HEPES at 150 mM NaCl. Negative controls whereby no SrtA was added were included (keeping all other conditions identical), to ensure any identification of further functionalisation of ND suspensions with **[Ru(Bipy)₂L₁]-Srtpep2** was as a result of SrtA activity.

In both cases where SrtA was present upon incubation, a distinctive orange precipitate (presumably nanodiamond particles) was formed over 24 hours. Isolation of precipitate through centrifugation and several washes with water by sonication and redispersal was performed. The particles were found to exhibit very poor dispersibility in water, even following high power probe sonication. Particles were therefore suspended in 500 μL of methanol which yielded dispersions apparently stable (no notable sedimentation) over the course of 24 hours.

No precipitate was observed in either cases where Sortase A was absent. The Sortase A negative control suspensions were purified *via* dialysis (cellulose membrane MWCO = 3000), where it was observed that the remaining deep orange colour disappeared, indicating removal of unbound **[Ru(Bipy)₂L₁]-Srtpep2**.

Photophysical characterisation of resulting particle suspensions was performed in water. Aqueous suspensions of **Nap-1/Srtpep1 @ND** and **Ir-1/Srtpep1 @ND** treated with **[Ru(Bipy)₂L₁]-Srtpep2** in the absence of SrtA were evaluated directly following dialysis. 100 μL of the suspensions in methanol of **Nap-1/Srtpep1 @ND** and **Ir-1/Srtpep1 @ND** treated with **[Ru(Bipy)₂L₁]-LPYTGG** in the presence of Sortase A were diluted to 1 mL with water prior to analysis (final concentration of methanol at 10% v/v). Luminescence emission and excitation spectra of **Nap-1/Srtpep1 @ND** and **Ir-1/Srtpep1 @ND** treated with **[Ru(Bipy)₂L₁]-Srtpep2** in the presence and absence of Sortase A are shown in Figures 3.29 and 3.30 respectively.

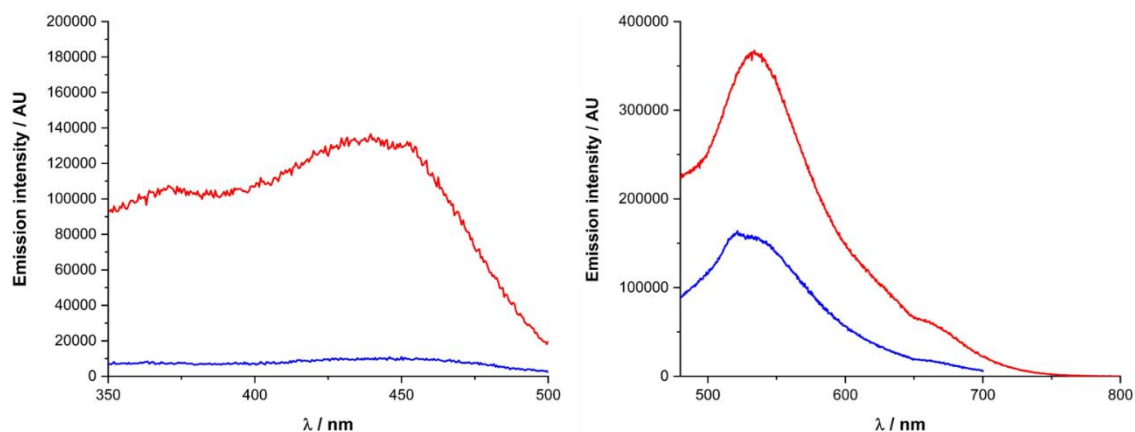


Figure 2.29: Left - Luminescence excitation ($\lambda_{\text{em}} = 700 \text{ nm}$), and emission ($\lambda_{\text{ex}} = 450 \text{ nm}$) spectra of **Nap-1/Srtpep1 @ND** following treatment with **[Ru(Bipy)₂L₁]-Srtpep2** either with 10 molar % of SrtA (Red) and without SrtA (Blue). Slits 4,4 nm.

Emission spectra of **Nap-1/Srtpep1 @ND** from excitation at 450 nm show a distinctive difference in the emission profiles depending on the utilisation of SrtA. Where both spectra exhibited intense emission centred around 540 nm, a distinct tail and shoulder

at higher wavelengths was identified in the emission trace of **Nap-1/Srtpep1@ND** where SrtA was present in the coupling reaction. This shoulder corresponding to emission centred around 650 nm is characteristic of $^3\text{MLCT}$ emission arising from the **[Ru(Bipy) $_2$ L $_1$]** luminophore attached to the corresponding sortase peptide recognition sequence (Section 3.3.4). Excitation spectra following emission at 700 nm described a characteristic absorption spectrum corresponding to the $^1\text{MLCT}$ absorption from the **[Ru(Bipy) $_2$ L $_1$]** luminophore. Neither feature was observable where SrtA was not present in the coupling reaction.

Emission and absorption profiles diagnostic of attachment of the **[Ru(Bipy) $_2$ L $_1$]** luminophore were not observed where Sortase A was absent, suggesting the critical role of Sortase A in the retention of the **[Ru(Bipy) $_2$ L $_1$]** luminophore. This suggests that Sortase A was able to further modify the surface of **Nap-1/Srtpep1@**

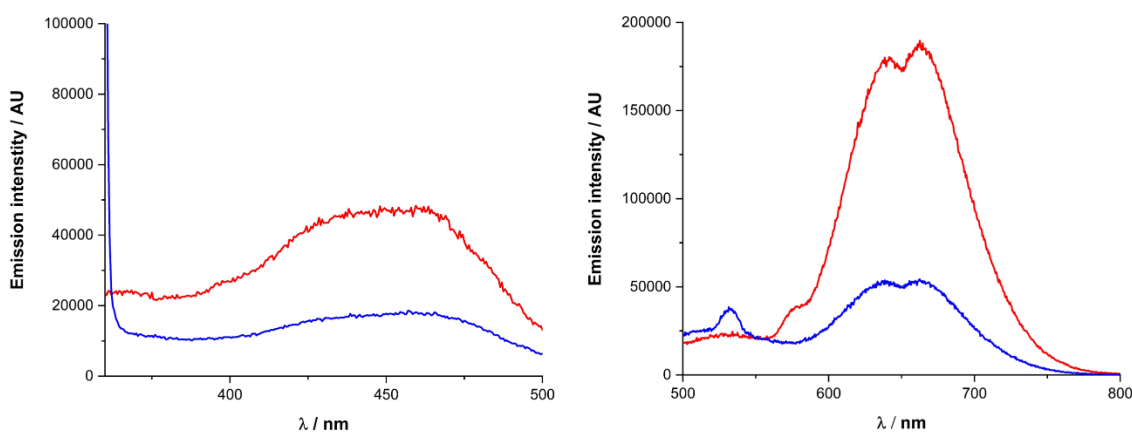


Figure 2.30: Luminescence excitation ($\lambda_{\text{em}} = 700$) and emission ($\lambda_{\text{ex}} = 450$ nm) spectra of **Ir-1/Srtpep1@ND** following treatment with **[Ru(Bipy) $_2$ L $_1$]-Srtpep2** either with 10 molar % of *S.aureus* SrtA (Red) or without SrtA (Blue). Slits 8,8 nm.

Changes in the photophysical properties of **Ir-1/Srtpep1@ND** (Figure 2.30) appear to be more subtle when comparing particle suspensions treated with and without Sortase A. Irrespective of the presence of SrtA in the coupling reaction, emission peaks centred around 670 nm were observed for **Ir-1/Srtpep1@ND** following coupling with **[Ru(Bipy) $_2$ L $_1$]-Srtpep2**. The emission profiles of the **Ir-1** and **[Ru(Bipy) $_2$ L $_1$]** luminophores broadly overlap (Sections 3.3.3 AND 3.3.4), making distinction extremely difficult. The excitation spectra of **IR-1/SRTPEP1@ND** following emission at 700 nm following coupling both showed an absorption profiles with centred around 450 nm. It remains impossible to accurately determine whether the **Ir-1/SRTPEP1@ND** species was able to be modified by SrtA through evaluation of their photophysical properties.

This is unsurprising given the broadly superimposable photophysical properties of the **Ir-1** and **[Ru(Bipy)₂L₁]** luminophores.

3.4. Chapter conclusions

The recombinant expression of SrtA was demonstrated in high yield and shown to be active yielding over 90% product formation in a ligation assay representative of the desired application in the further modification of ND. Synthesis of a novel iridium luminophore to provide an extended range of colour centres for a theorised end product of a biomaterial incorporating luminescent functionalised ND was achieved in good yield. The co-functionalisation of ND with **Ir-1** or **Nap-1** and the sortase recognition peptide **Srtpep1** was demonstrated via the proposed route, producing ND species **Ir-1/Srtpep1@ND** and **Nap-1/Srtpep1@ND**.

In the evaluation of the activity of **Ir-1/Srtpep1@ND** and **Nap-1/Srtpep1@ND** towards SrtA modification, the peptide-luminophore conjugate **[Ru(bipy)₂L₁]-Srtpep2** was synthesised by solid phase peptide synthesis, and attachment to the functionalised ND particle dispersions attempted. The photoluminescent features of **Nap-1/Srtpep1@ND** appear to clearly incorporate absorption and emission properties of the **[Ru(bipy)₂L₁]** luminophore where SrtA was present, appearing to confirm the activity of this suspension towards SrtA mediated ligation in the desired fashion. Results were less clear for SrtA modification in the same manner with **Ir-1/Srtpep1@ND**, due to the overlapping photophysical properties of the **Ir-1** and **[Ru(bipy)₂L₁]** luminophores.

In conclusion, the **Nap-1/Srtpep1@ND** dispersion appears to be active towards SrtA modification via the route designed. Further investigation of **Ir-1/SrtApep1@ND** is required, utilising either a new orthogonally luminescent Srtpep2 conjugate, or possibly through other characterisation to confirm attachment of the **[Ru(bipy)₂L₁]** luminophore via XPS or MP-AES.

3.5. Experimental

3.5.1. General reagents

Reagents and starting materials were obtained from commercial sources (i.e. Sigma Aldrich, Alfa Aesar, VWR and fluorochem) and used without further purification. Peptides GGGGKTTT (GGK_{pep}), GGGGTTTT and TTLPYTGG were obtained from Archichem Ltd and in >95% purity and used without further purification. Purified water from a Millipore Milli-Q purification system with an activity of not lower than 15 mΩcm⁻³.

3.5.2. Sequence of *S. aureus* SrtA (7M) employed

```
MQAKPQIPKDKSKVAGYIEIPDADIKEPVYPGPATREQLNRGVSFAKENQSLDDQNISI  
AGHTFIDRPNYQFTNLKAAKKGSMVYFKVGNETRKYKMTSIRNVKPTAVEVLDEQKG  
KDKQLTLITCDDYNEETGVWETRKIFVATEVKLEHHHHHH
```

3.5.3. Expression of *S. aureus* SrtA

A gene encoding a hexa-histidine tagged septamutant form of the *S. aureus* sortase A, harboured by a pET30b plasmid under the control of a T7 promoter, was obtained through Addgene in a holding strain of *E. coli* as an agar stab as a gift from Hidde Plough.^{134,160} An overnight culture (20 mL) was grown in LB media overnight at 37 °C from the agar stab. Plasmid DNA was isolated via miniprep and inspected by PAGE. Transformation with 1 μL of miniprep plasmid DNA into a BL21(DE3) expression strain of *E. coli* was achieved, yielding multiple (>10) colonies on an LB-agar plate. A 10 mL of LB was inoculated with one picked colony from the agar plate and grown at 37 °C overnight prior to the production of 3 glycerol stocks.

150 mL of LB media containing kanamycin (50 mg L⁻¹) was inoculated from the glycerol stock of BL21-DE3::srtA(7M) and grown overnight at 37 °C. This starter culture was then split equally between 4 large flasks containing 750 mL LB media, and grown at 37 °C. Bacterial growth was allowed to continue until OD₆₀₀ was between 0.6 and 0.8 across all flasks, upon which expression was induced through the addition of IPTG (1 mM), and the temperature reduced to 16 °C. Expression was allowed to continue overnight, upon which the cells were harvested by centrifugation (45 minutes, 4000 rpm). Cellular pellets were redispersed in chilled sortase extraction buffer, prior to disruption of the cell membranes by sonication (5 minutes total, cycling for 5 seconds on 10 seconds off). The lysate was then centrifuged for 35 minutes at 15000 rpm to remove cellular debris.

The SrtA containing crude lysate was then purified using Ni-NTA chromatography, eluting the purified protein with sortase elution buffer. SrtA was dialysed into sortase storage buffer (2 cycles, 1000-fold dilution). SrtA was then aliquoted into 1 mL portions, and flash frozen with liquid N₂ before being stored at -80 °C for later use. Aliquots were defrosted on ice prior to use and kept on ice. Once defrosted were utilized within 48 hours or discarded, not re-frozen.

3.5.3.1. Transformation protocol

Supercompetent *E. coli* BL21-DE3 cell stocks in 1.5 mL Eppendorf tubes were thawed on ice and 5 µL of plasmid DNA to be transformed was added and mixed by pipetting and left on ice for 30 minutes. The suspension was then immersed in a water bath at 42°C for 45 seconds, then placed back on ice. Sterile LB media (1 mL) was then added and mixed by pipetting. Cell cultures were then grown by shaking at 150 rpm at 37°C for 1 hour. The cultures were then spun down at 4000 rpm for 10 minutes, and most of the supernatant discarded, leaving 50-100 µL of liquid. The pellet was then resuspended in the remaining liquid and plated on LB agar containing the appropriate antibiotic and incubated at 37°C overnight.

3.5.4. Surface cofunctionalisation of ND-COOH with **Nap-1/Ir-1** and **SrtPep 1**

ND-COOH was dispersed in acetonitrile (0.25 mg mL⁻¹) and then stirred at room temperature with successive bath sonication steps centrifugation steps yielding a homogenous suspension. **Nap-1** or **Ir-1** as solutions in MeCN (to a final concentration of 1 mM) was added together with a solution of **Srtpep1** (final concentration of 1 mM) with EDC (1-ethyl-3-(3-dimethylaminopropyl)carbodiimide (final concentration of 20 mM), N-hydroxysuccinimide (final concentration of 20 mM) to a final volume of 10 mL (final concentration of ND-COOH 0.125 mg mL⁻¹) and stirred at 37 °C over 24 hours. The functionalised nanodiamond was pelleted by centrifugation (4400 rpm, 30 minutes), followed by subsequent washing steps in acetonitrile by bath sonication followed by centrifugation (4400 rpm, 30 minutes) until the supernatant was clear. A small amount of pelleted nanodiamond material was collected on the end of a glass pipette and dispersed in water *via* bath sonication of the snapped pipette tip in a centrifuge tube (pipette was then removed). The nanodiamond material was then redispersed by bath sonication in 40% piperidine in acetonitrile, and stirred overnight at RT. Following deprotection, the deprotection cocktail was added to 10 volumes of diethyl ether, and centrifuged at 4400 rpm for 30 minutes. The pellet containing nanodiamond particle matter was then washed multiple times with acetonitrile (*via* bath sonication and subsequent centrifugation at

4400 rpm for 30 minutes). The nanodiamond material was finally dispersed by probe sonication in water (5 mL, 30% amplitude, 30 minutes), followed by centrifugation (2000 rpm, 20 minutes) to remove residual titanium from the sonicator tip.

3.5.5. Sortase ligation assay with TTLPYTGG and GGGGTTTT

Peptides TTLPYTGG and GGGGTTTT at equimolar concentration of 0.1 mM were ligated by expressed SrtA(7M) (10 μ M) over 24 hours in sortase reaction buffer (pH 7.5, 50 mM HEPES, 150 mM NaCl), shaking (350 rpm) at 37 °C. 100 μ L aliquots were taken at 20, 40, 60, 120, 240 and 1440 minute time points from the reaction, quenched with 100 μ L of MeCN and stored overnight at 4 °C to ensure precipitation of SrtA. Aliquots were filtered and submitted to analysis by LCMS (Synapt G2-Si, ES+). Peaks were integrated from the TIC detection area, showing masses for 806.41(TTLPYTGG) and the ligated product (1327.64) at retention times of ~8.33 and ~8.60 minutes.

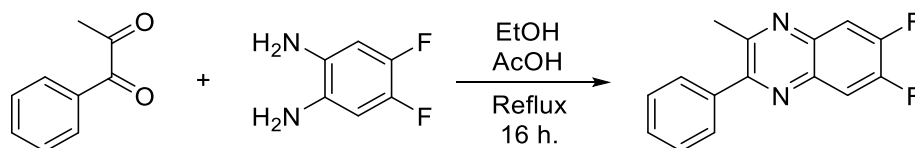
3.5.6. Sortase ligation with **Nap-1/Srtpep1@ND** and **Ir-1/Srtpep1@ND** and crude **[Ru(Bipy)₂L₁]-Srtpep2**

Suspensions (0.9 mL) of **Nap-1/Srtpep1@ND** and **Ir-1/Srtpep1@ND** were buffered at pH 7.5 in HEPES (50 mM) and NaCl (150 mM). **[Ru(Bipy)₂L₁]-Srtpep2** as a concentrated solution in water was added to a final concentration of 0.1 mM. Sortase A was added, following thawing on ice for 1h, to a final concentration of 10 μ M, to give a total final volume of 1 mL. For the control conditions, no sortase was added, with deionised water added to make up the volume. Suspensions were shaken at 350 rpm at 37 °C over 24 hours.

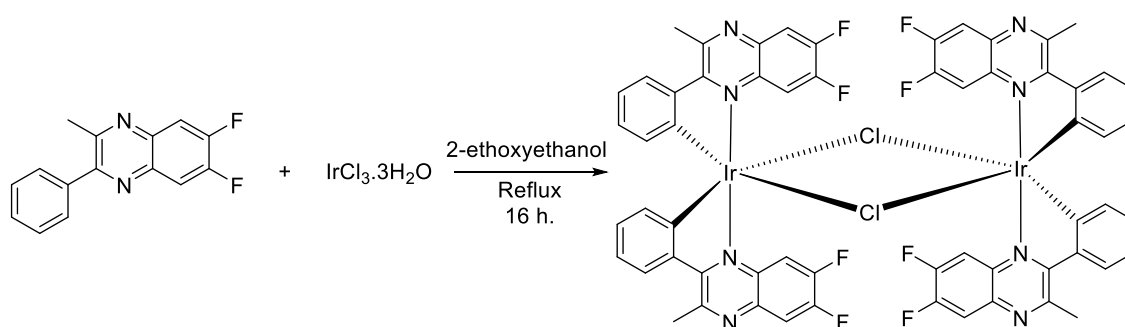
Following functionalisation *via* SrtA, conditions where sortase was present exhibited significant precipitation. The precipitate was collected *via* centrifugation (13000 rpm, 30 minutes), washed with water (1 mL), sonicated and re-centrifuged (13000 rpm, 30 minutes). The washing procedure was repeated 3 times. The precipitate, assumed to contain nanodiamond material was dispersed in methanol *via* probe sonication (0.5 mL, 30% amplitude, 5 minutes). For the sortase negative control reactions, dispersions did not precipitate, and therefore were dialysed 2x to water (1L) with sonication in between steps using a 3000 MWCO cellulose membrane.

3.5.7. Synthesis of compounds

3.5.7.1. Ir-1

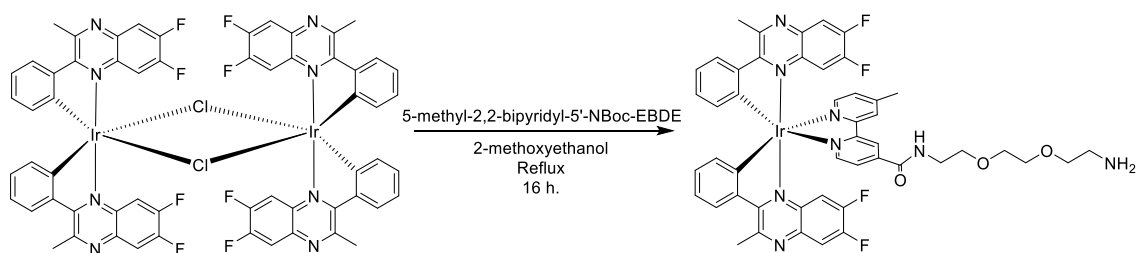
Synthesis of quinoxaline ligand QX-1

1-phenylpropane-1,2-dione (300 mg, 2.02 mmol) and 2,3-difluoro-4,5-diaminobenzene (320 mg, 2.23 mmol) were suspended in ethanol (15 mL). A drop of glacial acetic acid was added, and the mixture heated to reflux over 16 hours. Once allowed to cool, the product was precipitated through the addition of H₂O (50 mL). The precipitate was collected by filtration, washed with H₂O (3 x 15 mL) and diethyl ether (3 x 15 mL) to yield the product **QX-1** as a taupe solid (350 mg, 1.37 mmol, 68%). **¹H NMR** (500 MHz, CDCl₃) δ 7.80 – 7.75 (m, 1H), 7.74 – 7.69 (m, 1H), 7.56 (d, *J* = 7.4 Hz, 2H), 7.49 – 7.41 (m, 3H), 2.69 (s, 3H). **LRMS** found *m/z* = 257.08 for [M+H]⁺

Synthesis of $\text{Ir}_2\text{Cl}_2(\text{QX-1})_4$ 

QX-1 (300 mg, 1.17 mmol) and iridium trichloride hydrate (167 mg, 0.58 mmol) were suspended in 2-ethoxy ethanol (10 mL) and heated at reflux over 16 hours. Once allowed to cool, the product was precipitated through the addition of H_2O (50 mL) and filtered to collect the product $\text{Ir}_2\text{Cl}_2(\text{QX-1})_4$ (310 mg, 0.21 mmol, 36%) as a red-brown solid. Product was used without further purification in the next reaction step.

Synthesis of **Ir-1**



Ir₂Cl₂(QX-1)₄ (150 mg, 0.10 mmol) and 5-methyl-2,2-bipyridyl-5'-NBoc-EBDE (38 mg, 0.11 mmol) were dissolved in 2-methoxyethanol (7 mL) and stirred at reflux over 16 hours. Once allowed to cool, solvent was removed in-vacuo and the product mixture dissolved in a minimal amount of dichloromethane. The product was purified *via* silica gel column chromatography using initially dichloromethane as the eluent, then 95:5 dichloromethane/methanol collecting the product in a single 20 mL fraction. Solvent was then removed in vacuo to yield the Boc protected intermediate a red oil (43 mg, 41 μmol, 41%). The intermediate was deprotected by dissolving in 50% trifluoroacetic acid in dichloromethane overnight. Following deprotection, solvent was removed in-vacuo, methanol (20 mL) added and removed again in-vacuo, a process repeated three times. The product, **Ir-1** was finally isolated as a red oil (35 mg, 34 μmol, 85%).¹H NMR (400 MHz, CDCl₃) δ 9.82 – 9.69 (m, 2H), 9.29 – 9.19 (m, 1H), 8.35 – 8.30 (m, 2H), 8.13 – 8.06 (m, 2H), 7.84 (d, *J* = 5.7 Hz, 1H), 7.68 – 7.61 (m, 2H), 7.24 – 7.17 (m, occluded by solvent peak), 7.03 – 6.79 (m, 5H), 6.51 – 6.46 (m, 2H), 5.38 (s, 1H broad), 3.73 – 3.47 (m, occluded by solvent peak), 3.43 (t, *J* = 5.1 Hz, 2H), 3.28 (s, 3H), 3.26 (s, 3H), 2.52 (s, 3H). ¹³C NMR (101 MHz, CDCl₃) δ 162.11, 156.34, 155.04, 154.41, 152.83, 152.74, 146.54, 145.25, 144.94, 143.93, 143.82, 137.43, 137.41, 135.14, 135.09, 131.64, 131.56, 130.93, 130.73, 128.95, 128.29, 128.27, 127.41, 123.86, 123.69, 123.43, 115.75, 70.28, 70.22, 70.17, 69.94, 68.94, 63.78, 40.38, 40.37, 39.88, 28.43, 28.38, 27.62, 27.57, 21.40. ¹⁹F NMR (379 MHz, CDCl₃) δ -125.45 (1F, d, *J* = 22.2 Hz), δ -126.83 (1F, d, *J* = 22.2 Hz), δ -127.87 (1F, d, *J* = 22.4 Hz), δ -128.29 (1F, d, *J* = 22.6 Hz). LRMS found *m/z* = 1047.29 for M⁺. HRMS expected *m/z* = 1047.2940 for M⁺, found *m/z* = 1047.2944. FTIR v selected cm⁻¹; 2980, 2884, 2361, 1670, 1533, 1504, 1333, 1233, 1198, 1169, 1132, 876, 758.

3.5.7.2. **[Ru(Bipy)₂L₁]-Srtpep2**

[Ru(Bipy)₂L₁]-Srtpep2 was synthesised through solid phase peptide synthesis using Fmoc-Gly-2-chlorotrityl resin (Merck, 1.0 mmol g⁻¹ substitution) on a 0.5 mmol scale using standard Fmoc-AA-OH amino acids (obtained from Cambridge reagents, >95%) (using Fmoc-Tyr(OTBu)-OH) in a 5 eq. excess. Amino acids were weighed out into glass *vials* and stored dry below 0°C until immediate usage. Resin was swollen in ~15 mL of *n*-methylpyrrolidone (NMP) over 1 hour prior to deprotection of the already present glycine residue with 40% piperidine in NMP over 40 minutes. Following removal of the deprotection cocktail, the deprotected resin was washed with 3 x 20 mL of NMP. The consecutive amino acid was then dissolved in 10 mL of NMP containing 2% diisopropylethylamine (DIPEA), and 4.9 equivalents of (2-(1H-benzotriazol-1-yl)-1,1,3,3-tetramethyluronium hexafluorophosphate (HBTU) and hydroxybenzotriazole (HoBt) were added. The coupling mixture was gently agitated through bubbling N₂ gas over the course of 1 hour. Following coupling the coupling cocktail was drained and the resin again washed with 20 mL of NMP. This was repeated for all consequential amino acids.

[Ru(Bipy)₂L₁] was coupled in identical conditions, employing a 5 eq. excess but overnight. Following this final coupling the resin was washed with 10 x 20 mL of NMP (remaining brightly orange coloured) and the peptide conjugate product cleaved with 95% TFA, 2.5% TIPS 2.5% H₂O over 1 hour. The cleavage cocktail was filtered from the resin into a glass *vial* and the majority of TFA removed under a flow of N₂, prior to precipitation of the product with ice cold diethyl ether (40 mL). Centrifugation yielded the crude product as a bright orange oil, analysed by LC-MS (C18 column to contain >80% of the desired **[Ru(Bipy)₂L₁]-Srtpep2** product with some unconjugated LPYTGG peptide. Purification by semi-preparatory LC-MS utilising the same elution gradient and a C18 column, followed by lyophilisation yielded the final product as a red/orange solid (2.5 mg).

3.5.8. Analytical techniques employed

3.5.8.1. Particle size and colloidal stability

Analysis of the colloidal properties of **Nap-1/Srtpep1 @ND** and **Ir-1/Srtpep1 @ND** using DLS, Zeta potential measurements and NTA were performed in an identical fashion to that reported in Chapter 2.

3.5.8.2. X-Ray photoelectron spectroscopy

XPS analysis of **Nap-1/Srtpep1 @ND** and **IR-1/SRTPEP1 @ND** was performed in an identical fashion to that reported in Chapter 2.

3.5.8.3. Photophysical characterisation

UV-Visible measurements and both steady state and time resolved luminescence measurements were performed as per the method described in Chapter 2, using specific excitation and emission wavelengths and monochromator slit lengths given in respective results sections.

3.5.9. Buffers and reagents for biochemical protocols

LB media

Tryptone (10 g/L)

Yeast extract. (5 g/L)

Sodium chloride (5 g/L)

Sterilised in containers through autoclaving at 120 °C for 120 min

Sortase reaction buffer (10X)

HEPES (0.5M)

Sodium chloride (1.5M)

Solution was then adjusted to pH 7.5 and employed as appropriate diluted by a factor of 10.

Sortase lysis buffer

HEPES (50 mM)

Sodium chloride (150 mM)

Imidazole (20 mM)

Solution was then adjusted to pH 8.0

Sortase elution buffer

HEPES (50 mM)

Sodium chloride (150 mM)

Imidazole (500 mM)

Solution was then adjusted to pH 7.5

Sortase storage buffer

HEPES (50 mM)

Sodium chloride (150 mM)

Glycerol (10% v/v)

Solution was then adjusted to pH 7.5

SDS-PAGE Buffers

Resolving gel (14%)

Bis-acrylamide, 30% solution (4.5 mL)

Deionised H₂O (2.9 mL)

Resolving gel buffer (2.5 mL)

Ammonium persulfate (10%) (50 µL)

Tetramethylethylenediamine (10 µL)

Stacking gel (5%)

Bis-acrylamide, 30% solution (1.7 mL)

Deionised H₂O (5.7 mL)

Stacking gel buffer (2.5 mL)

Ammonium persulfate (10%) (50 µL)

Tetramethylethylenediamine (10 µL)

Resolving gel buffer

Tris base (1.5 M)

Sodium dodecyl sulfate solution (10% w/v)

Adjusted to pH 8.0

Stacking gel buffer

Tris base (0.5 M)

Sodium dodecyl sulfate DS solution (10% w/v)

Adjusted to pH 6.8

Running buffer

Tris base (250 mM)

Glycine (1.5 M)

Sodium dodecyl sulfate (35 mM)

Adjusted to pH 8.3

SDS sample buffer

Tris HCl (60 mM)
Sodium dodecyl sulfate (5% w/v)
Sucrose (10% w/v)
Glycerol (30% v/v)
 β -Mercaptoethanol (3% v/v)
Bromophenol blue (0.02 w/v)

Coomassie blue solution

Coomassie blue (0.25% w/v)
Methanol (45% v/v)
Acetic acid (9% v/v)

**Chapter 4. Development of controllable,
engineered curli mediated *E. coli* biofilms**

4.1. Introduction

4.1.1. Chapter aims

Curli are proteinaceous fibrils produced by *Escherichia coli* and, in conjunction with cellulose biosynthesis, are key components of biofilm development by this bacterium. The ultimate aim of this research was to develop biological materials which are capable of incorporating a functional ND component through incorporation of surface functionalised nanodiamond (ND) into the material matrix (Figure 4.1). These materials would have potential to exhibit controlled structural properties and exhibit poly-functional characteristics arising from incorporation of orthogonally functionalised ND.

This chapter assessed the effect that controlled curli production by *E. coli* had on biofilm formation, providing a template whereby incorporation of the SrtA recognition sequence LPYTGG at the C-terminus of the major structural protein in curli, CsgA, would, in theory yield a biofilm able to be adorned with appropriately labelled functional ND through SrtA transpeptidation. Following from this, the effect of the C-terminal LPYTGG tag on the biofilm forming capabilities of *E. coli* was established.

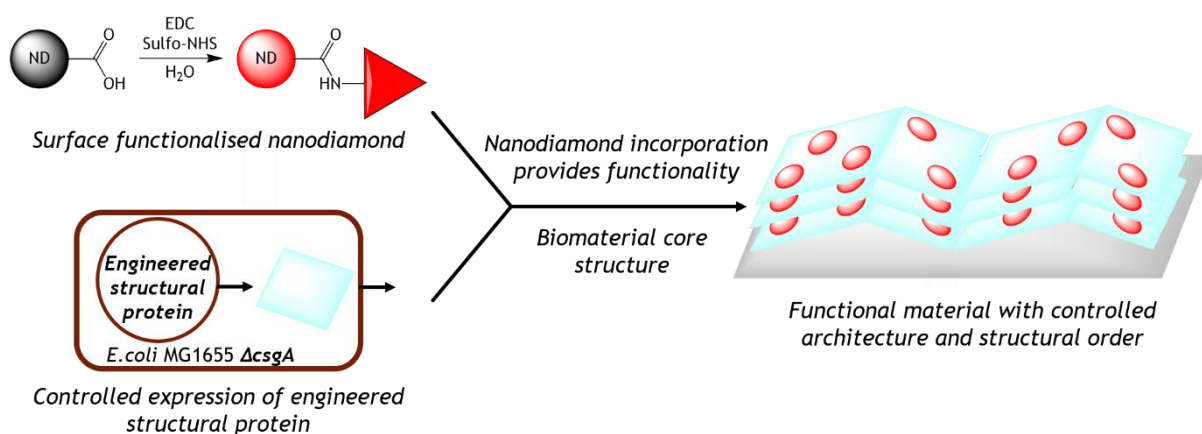


Figure 4.1: Schematic representation of project aims. Use of chemistry in the surface functionalisation of ND (top left) and synthetic biology in the production of the genetic circuit controllably producing structural protein (bottom left) together to (poly)functional bioengineered materials.

To produce a functional biofilm, it was necessary to develop a controllable way to impact *E. coli* biofilm formation through curli expression. In doing this the initial hypothesis is formed:

Current literature depicts curli formation as an essential step in the initial attachment phase of E. coli biofilm development. Through controlling curli expression, it would be possible to control the efficiency of E. coli biofilm formation.

Assuming this hypothesis holds true, producing a genetic construct system whereby curli production could be 'switched-on' through a stimulus (*i.e.* addition of a chemical) would facilitate the developed *E. coli* strain to produce large volumes of biofilm which could then be engineered to incorporate ND.

4.1.2. Role of curli amyloid in the biofilm environment of *Escherichia coli*

Aggregates of multicellular communities known as biofilms, formed by single celled microorganisms are one of the most widely distributed and successful modes of life ¹⁶¹. Bacterial cells in biofilms develop their surrounding environment, through production of extracellular polymeric substances (EPS), forming a habitat which confers tolerance and resistance to external stress factors (*e.g.* biocides, desiccation and extreme temperatures) ¹⁶².

Biofilms are comprised of intricate colonies of densely packed microorganisms (cell density ranging from 10^8 to 10^{11} cells/g wet weight ¹⁶³) and are typically polymicrobial ¹⁶². Cells in biofilms have also been shown to undergo differentiation within the biofilm community, leading to greater genetic diversity ¹⁶². Many species of microorganisms are capable of forming biofilms through the controlled production of EPS, forming the extracellular matrix and facilitating cell-cell adhesion and attachment to abiotic surfaces ¹⁶⁴. The formation of biofilms from microorganisms in planktonic state in a liquid culture is a complex and dynamic process typically described by four stages: initial surface contact, attachment, maturation and dispersion ¹⁶⁵.

The majority of the biofilm biomass comprises of hydrated EPS, as opposed to microbial cells ¹⁶⁶. The extracellular polymeric matrix of *E. coli* biofilms is extremely complex, consisting of a variety of proteins (predominantly curli ^{16,17}), polysaccharides, lipids and a comparatively minor (by mass) polynucleotide component ¹⁶⁷. Curli are extracellular amyloid fibrils, consisting mostly of a single component protein (CsgA). Curli is broadly classed as an 'adhesin', taking a leading role in the second stage of biofilm formation (attachment), promoting intercellular attachment and attachment to abiotic surfaces^{162,167,168}. The biogenesis of curli involves stringently controlled expression of several proteins that enable controlled release of this non-aggregate protein from the cell. ¹⁶

4.1.3. Amyloids as functional biofilm components

Amyloids are fibrillar, highly ordered structures of protein consisting predominantly of a cross β -sheet structure^{14,15} formed through aggregation of one or multiple component proteins.

Amyloid formation is often implicated in the pathogenesis of neurodegenerative diseases such as Alzheimer's disease (β -amyloid), Parkinson's disease (α -synuclein) and Creutzfeldt-Jakob type encephalopathy (prion protein).¹²⁻¹⁴ The aberrant misfolding and aggregation of the particular peptide or protein is attributed to the development of these diseases and a large volume of research has been conducted to investigate the role of amyloidogenesis in the development of disease.

Functional amyloid materials have been observed in multicellular eukaryotic organisms (e.g. the $M\alpha$ protein in humans, fungi and prokaryotes).¹⁶⁹ These amyloid materials are non-toxic to the producing organism and are typically beneficial.

Curli is an example of a functional amyloid and can promote biofilm formation through acting as a fimbrial adhesin (Figure 4.2). Fimbrial adhesins such as curli are most commonly implicated in the attachment phase of biofilm growth,^{16,165,170} and curli deficient strains show altered biofilm morphology or even no biofilm growth at elevated temperatures.¹⁷⁰

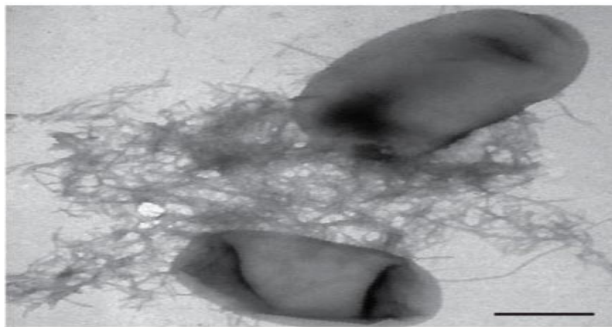


Figure 4.2: Electron micrograph of *E. coli* K12 BW25113 grown on a low-salt agar plate at 26°C, showing amyloid fibrils produced by cells, creating a cell-cell adhesive environment. Adapted from reference 15.

4.1.4. Curli biosynthesis in *Escherichia coli*

Curli production by *E. coli* involves the well-controlled expression of a number of genes (*csg*: curli specific genes). At least 7 proteins are encoded by the divergent *csgBAC* and *csgDEFG* operons and contribute to curli formation^{16,167,168}. The *csgBAC* operon contains the genes *csgA* and *csgB* and *csgC*, which upon expression produce the respective proteins CsgA, CsgB and CsgC.

CsgA is the major curli subunit and is a low molecular weight protein (~15 kDa) consisting of 151 amino acids (Figure 4.3). Soluble monomeric CsgA folds into a 5-strand β -helix with a period of ~23 residues (Figure 3.2) (predicted structure from computational experiments, validated from SS-NMR, EM and XDR data)¹⁷¹. The 5 chains arise from the 5 imperfect repeating units, maintaining contact in the β -helix through conserved hydrophobic and hydrophilic residues, which interact to stabilise the structure. The N-terminal 22 amino acid region of CsgA is not thought to be part of this β -helical structure, and is instead reported to be essential to the excretion of CsgA through the cell surface membrane *via* interaction with CsgE and CsgG¹⁷².

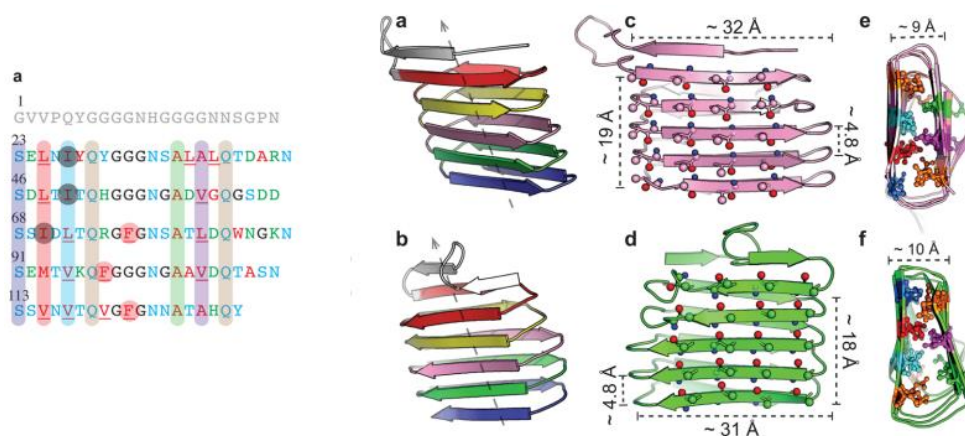


Figure 4.3: CsgA Sequence and contact predictions from multiple sequence alignment (Right). Left- β -Sheet predicted structures of CsgA in solution, as both left-handed (a, c and e) and right handed (b, d and f) helices. Adapted from reference 171.

In-vitro aggregation of CsgA occurs spontaneously over a broad (3.0 - 9.0) pH range, identified by Dueholm et al to imply that the ‘design’ of aggregation is very robust (*i.e.* the protein’s sole function is to participate in fibrillation).¹⁷³ The amyloid aggregation event of any protein consists of a lag-phase (very slow aggregation associated with a period of nucleation and seeding) followed by an exponential phase (rapid growth of amyloid fibrils) and is concentration dependant. At concentrations ranging between 5 and 30 μ m the lag phase typically lasts 2 h (at 37 °C)¹⁷⁴. *In-vivo*, however, CsgA

aggregation is very inefficient without the nucleator protein (CsgB) encoded on the same operon¹⁴. The nucleation event can also be observed *in-vitro* through a process termed 'seeding'. When adding preformed CsgA amyloid fibrils to soluble CsgA, the lag-phase is eliminated, proving that nucleation requires the change in protein conformation to the ideal-amyloid formation¹⁷⁵.

CsgB and CsgA share ~30% sequence identity, and are of identical predicted size, and both consist of similar repeat motifs¹⁴. It is hypothesised that CsgB interacts with the cell surface membrane *via* the 5th repeating unit, (however the mode of association is unknown), and nucleation of secreted CsgA by CsgB results in the amyloid fibrils attaching to cells.

Curli form an inter-cellular community through interbacterial complementation, where CsgA excreted by one cell can nucleate to and form fibrils at the surface of another cell, through interaction with CsgB expressed at the cell surface. This is best shown by colony formation by CsgA deficient (but CsgB proficient) and CsgB deficient (but CsgA proficient) strains of *E. coli* (Figure 4.4). Congo Red (CR) impregnated agar showed that amyloid fibril aggregation only occurred when both strains were present¹⁶.

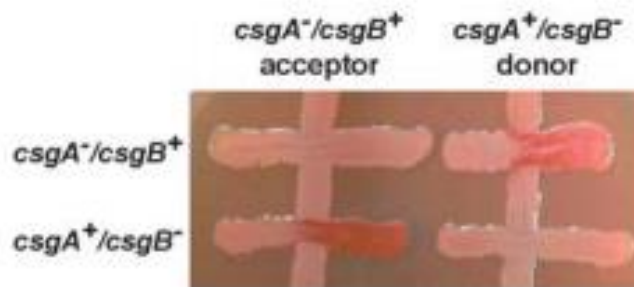


Figure 4.4: CR indicator agar demonstrating interbacterial complementation between *csgA*⁻ and *CsgB*⁻ strains of *E. coli*. Amyloid aggregation (evidenced by CR binding, darker red) only occurs when both strains were present. Adapted from reference 16.

The role of CsgC was not well understood until recently. Evans *et al.* reported its function as a periplasmic inhibitor of CsgA aggregation. CsgC is selective to CsgA in terms of its interaction and amyloid formation inhibition, related to its purported function as a chaperone, inhibiting potentially toxic intracellular amyloid formation. The route to which CsgC inhibits amyloid formation is likely through specific interaction with CsgA promoting the formation of off-target oligomeric species which do not exhibit the required conformation for amyloid templating.¹⁷⁶

Expression of the *csgBAC* operon is controlled by a dedicated transcription factor: *csgD*, encoded on the second curli related operon: *csgDEFG*. The *csgDEFG* operon encodes four proteins (CsgD, CsgE, CsgF and CsgG) essential for the excretion of CsgA through the outer membrane (OM), thus preventing the protein forming amyloid aggregates inside the cell.

CsgD is a transcriptional activator belonging to the FixJ/UhpA family. It contains a LuxR type DNA binding helix-turn-helix domain, with a high degree of sequence similarity to other DNA binding regions of proteins¹⁷⁷. CsgD not only controls expression of the *csg* operons, but also other genes associated with the adaptation of the cell to containment in a biofilm¹⁷⁸. CsgD expression is controlled directly and indirectly by several cell regulatory systems: OmpR/EnvZ, CpxA/R and Rcs, as well as RpoS (the stationary-phase sigma factor). Given that *csgD* controls expression of the *csgBA* operon, these regulatory systems have an important role in the control of biofilm generation.

The two component systems OmpR/EnvZ and CpxA/R consist of a sensor kinase (EnvZ and CpxA), which detect changes in osmolarity (EnvZ), envelope stress/misfolded periplasmic proteins (CpxA), and a response regulator (which controls expression of genes which effect the response, in this case OmpR and CpxR)¹⁶. The allele, *ompR234*, contains a mutation (L43R) of the *ompR* protein, and has been shown to promote biofilm formation in strains of *E. coli* that are otherwise biofilm deficient¹⁷⁹. Strains carrying the *ompR234* mutation can spontaneously colonise inert surfaces and generally produce fuller, thicker biofilms¹⁷⁹.

While both OmpR/EnvZ upregulate *csgD* expression, the CpxA/R Rcs pathways negatively regulate curli operon expression¹⁶, showing the complex level of control exerted on the expression of curli-related genes.

CsgE and F are chaperone proteins, which interact with CsgG, a protein which forms a nonameric homo-oligomeric pore at the outer-membrane (Figure 4.5). CsgE is located in the periplasm and is required for directing soluble CsgA to the CsgG pore. CsgF is located at the OM and required for the assembly of CsgB into a cell surface amyloid template¹⁷. Deletion of the CsgG gene results in no extracellular curli formation, nor internal accumulation or aggregation of *csgA* indicative of *csgA* proteolysis and down-regulation of curli associated genes¹⁸⁰. Application of periplasmic extracts containing only CsgE and CsgF in *in-vivo* aggregation experiments reveal inhibition of CsgA aggregation into mature amyloid fibrils, which is related to their chaperoning capacity *in-vivo*¹⁸⁰.

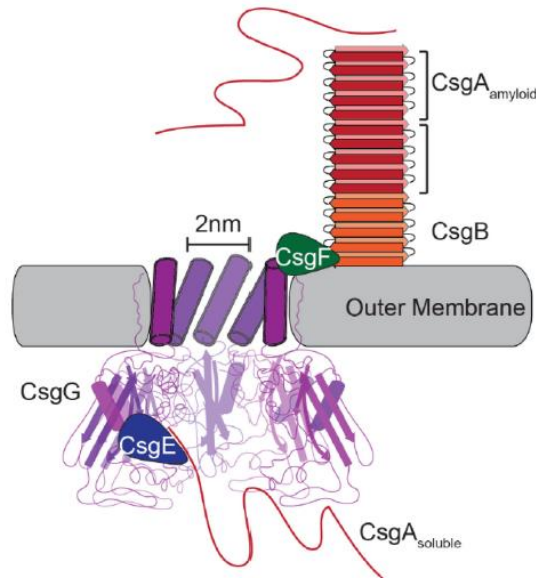


Figure 4.5: Mechanism of export of CsgA and CsgB via accessory proteins CsgE, CsgG and CsgF. Adapted from reference 180.

4.1.5. Design of *E. coli* strain demonstrating controllable curli production

Given the critical role of *csgA* in curli production, controlling *csgA* gene expression could facilitate an overarching control of biofilm formation. When *csgA* expression is absent, biofilm production in *E. coli* is severely impaired or arrested^{16,17,170}. Knockout of the *csgA* gene in *E. coli* is evident in the *E. coli* strain MG1655 ompR234 PRO Δ *csgA* (obtained from Chen et al¹⁸¹) and indeed, curli production is absent for this strain. Through incorporation of the *csgA* gene on a plasmid, under control of an inducible promoter (*i.e.* the P_L -TetO promoter), it is possible to impart chemical control on the expression of curli fibrils (Figure 4.6).

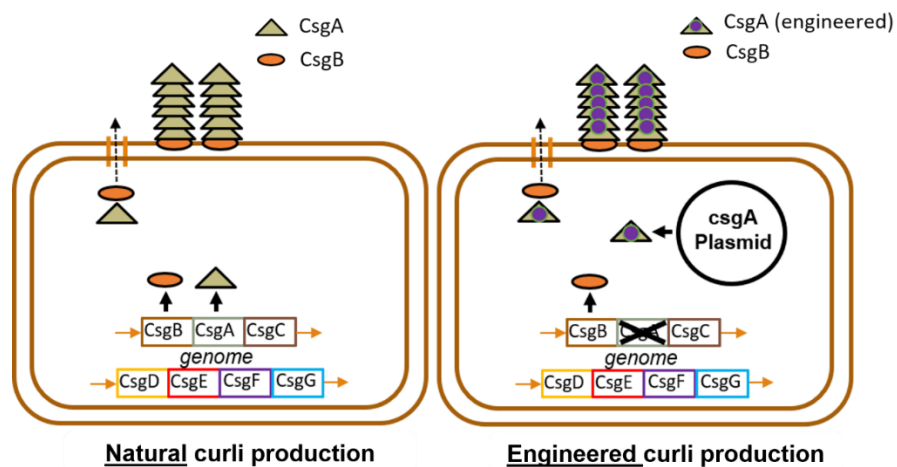


Figure 4.6: Route to engineered curli production under the control of an inducible promoter.

4.1.6. Overview of methods employed in biofilm analysis

Several methods in evaluating the biofilm environment have been described, differing in terms of culture scale and throughput.

Curli is not a product of planktonically cultured *E. coli* but is an integrated biofilm component. As such, there is a need to generate biofilms on an abiotic surface which is partly dependent on substrate-surface properties (e.g. charge/polarity^{167,182} and surface roughness¹⁸³), and extracellular adhesins^{16,17,164,179}.

Several critical reviews have been published on this subject, evaluating the contextual applicability, benefits and limitations of several biofilm generating methods^{162,166,184,185}. Here several methods of producing, and evaluating *E. coli* biofilms are detailed, identifying the selected approaches and highlighting why their use is most applicable in the context of this work.

4.1.6.1. Biofilm culture methods

In the case of the studied *E. coli* curli adhesin, the extracellular amyloid based proteinaceous fibrils act as an adhesive element of the ECM produced by *E. coli*, promoting attachment to abiotic surfaces and interbacterial complementation. Expression of curli specific genes essential to curli production is controlled by several global cell signalling pathways (through *csgD* expression), and thus in evaluating curli production, one must maintain conditions throughout experiment series' to assure representative results.

To achieve representative, reproducible biofilms, it is essential control culture medium content, inoculum size, temperature, mechanical environment (shaking/stirring) and medium flow (if applicable). Visualisation of the biofilm is achieved typically through binding of a dye such as Congo red (CR), or through direct observation by light microscopy and transmission electron microscopy (TEM). Advanced optical microscopy techniques (such as confocal fluorescence microscopy) allow for three-dimensional representations of biofilms to be generated in the form of z axis stacked image series.

Small volume biofilm cultures

Small volume cultures in microtiter plates, or devices derived from them (such as the Calgary biofilm device) allow for high-throughput evaluation of biofilm formation. Given the large number of conditions that can be screened in a single plate, this format is particularly suited to screening conditions of biofilm growth in response to medium content or ability different strains to form biofilms. Biofilm biomass is evaluated by

allowing a biofilm to form on the surface of the microtiter plate, before removal of planktonic cells through pipetting and washing steps¹⁸⁶. Evaluation of biofilm biomass can be performed through measuring light absorbance through the microtiter wells (from the cellular biomass), or through visualisation of biomass after its staining with an appropriate dye such as crystal violet (CV).

One potential limitation to the microtiter plate assay arises from cell-sedimentation during culture which means that the biomass evaluated may not arise solely from the biofilm. The Calgary device, incorporates a lid containing hanging 'pegs' which are inserted into the microtiter plate and it is on these pegs that the biofilm forms. This format eliminates the potential problem of sedimentation contributing to the measured biomass.

A low cellular volume typically occurs in small batch cultures where there is restricted nutrient supply, and in such cases formation of extensive biofilms is often difficult to achieve. Whilst the high-throughput nature of microtiter plates allows easy comparison of biofilm formation across conditions, formation of more extensive biofilms for materials science (as desired here, outlined in study aims section 3.1.3) is required. Other limitations to the microtiter plate format include the possibility to disrupt the biofilm formed through repeated washing and pipetting steps.

Larger volume biofilm devices

To produce biofilms representative of a studied environment (such as a water pipe, medical urinary catheter or marine environment) multiple biofilm growing devices on larger scales (over 100 mL culture sizes) have been developed. Some involve incorporation of culture-interfacing surfaces, described as 'coupons', which can be removed from the device following or during the experiment for further analysis. Examples of these devices are the Modified Robbins Device, rotary biofilm reactors, microfluidic devices, and the drip flow biofilm reactor (where a small volumes of culture media is flown over a standard microscopy slide).

The Modified Robbins Device is attached to a section of sterile tubing, and medium flows at a constant rate through the cylindrical shaped device, and collected at the other end. Designed for high flow rate and low nutrient contexts (such as biofilm formation in water pipes)¹⁸⁷, coupons are inserted into the device allowing the media to flow over the coupon surfaces for a length of time. Through altering hydrodynamic conditions (flow rate, for example) a range of conditions can be evaluated.

Several types of rotary biofilm reactors have been described in literature, with the CDC biofilm reactor (Biosurface technologies, Figure 4.7) detailed in ASTM standard

method for quantification of *Pseudomonas aeruginosa* biofilms. In these devices, media flow is controlled using a magnetic stirrer bar with baffle. Coupons (similar to that of the Robbins device) are placed in plastic rods and hung from the fitted lid so they are suspended in the stirred media. Advantages of this type of reactor include the ability to screen multiple surfaces and a high number of replicate conditions. Controlling stirrer speed and flow of medium can be undertaken to affect biofilm formation. However, throughput is limited as only one microbial strain can be tested for each run of the bioreactor, making screening of multiple strains time consuming.

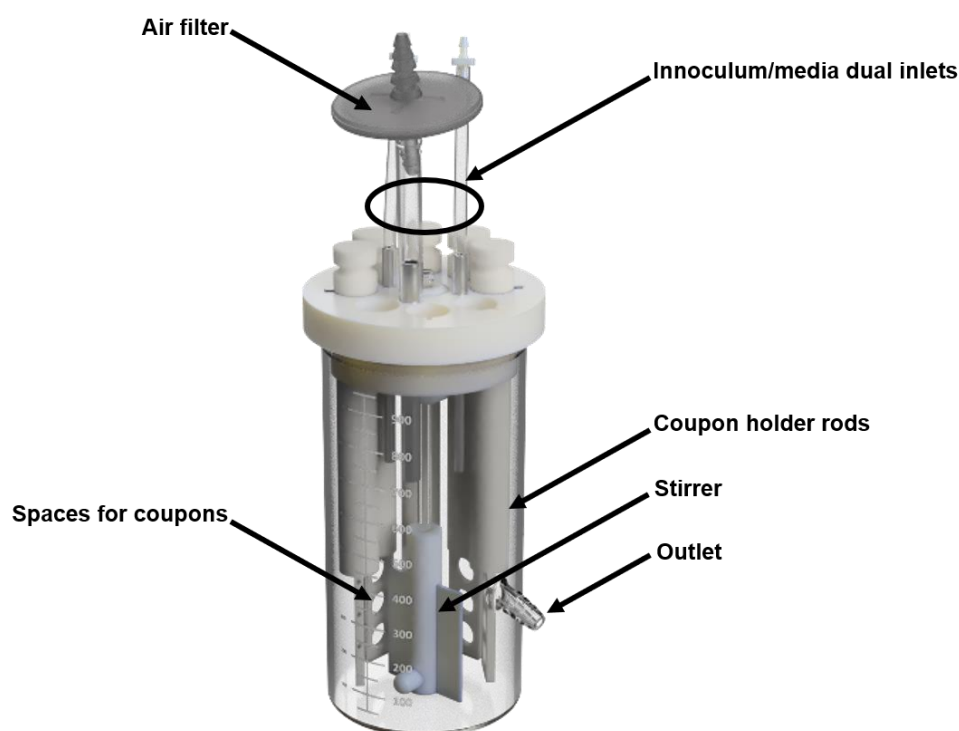


Figure 4.7: CDC bioreactor ® used in this study.

The CDC bioreactor ® was selected for use in this study, due to the potential to produce more extensive biofilms on a variety of surfaces, which could be further analysed with a large number of replicate samples. Given the materials aspect of this project, a larger quantity of biofilm was required, and the possibility to obtain multiple replicate samples from a single biofilm culture provided a suitable route to produce large volumes of biofilms suitable for ND attachment.

In deciding the route to reproducibly form *E. coli* biofilm, the next essential step is to identify reliable methods to evaluate the biofilm production. Several methods have

been developed to evaluate biofilm production, mostly independent of microorganism or identity of ECM, making direct analysis difficult.

4.1.6.2. Overview of methods employed in biofilm analysis

Given the highly complex biofilm environment, a wide variety of experimental techniques have been developed to evaluate biofilm formation. Techniques vary in throughput, but invariably rely on biofilm staining with a dye which either binds to the extracellular matrix or cellular component.

A summary of methods employed in biofilm analyses relevant to this study are shown in Table 4.1, with selected methods described in following sections. A large number of possible analytical techniques have been developed, often aimed at evaluating treatment regimens for disrupting pathogenic or deleterious biofilms. Only approaches suitable for materials science application are outlined here.

Table 4.1: Selected analytical techniques employed in biofilm analyses.

Method	Application	Advantages / Limitations	References
Colony Formation unit counting	Assesses culture formation from swabbed biofilms to give data on cellular content	Easy to perform with no specialised laboratory equipment / Technique difficult to reproduce; only evaluates microorganisms able to be swabbed from biofilm surface; no selectivity for biofilm bound cellular component.	188,189
Dye staining of biofilm with CR/CV	Indirect measurement of biofilm biomass through adsorption/retention of a dye such as crystal violet or Congo Red.	Versatile method with wide applicability towards high and low throughput assays / Lack of reproducibility; adsorption of dye common for a wide range of laboratory used plastics; no standardised method, poor detection limit; no selectivity towards any type of biomass or extracellular substance.	190,191
Confocal luminescence microscopy / COMSTAT quantification	Employs specific dyes such as propidium iodide (DNA staining of dead cells) or SYTO-0 (live cell staining). COMSTAT quantification from confocal Z-image series provides a wide array of parameters for a biofilm such as:	Detection and direct staining of biofilm matrix (often cellular component) provides detailed information on biofilm morphology on a cellular-scale. COMSTAT evaluation thereof provides huge amount of detail in quantifying parameters. Wide applicability through variable dyes available / Expensive and time	192,193

	Biomass, surface area and surface roughness.	consuming. Photobleaching of dyes often a problem over the course of Z-image series acquisition.	
--	--	--	--

4.1.6.2.1. Congo Red binding

Congo Red (CR, Figure 4.8) is a dye widely used in biochemistry and has been shown to bind both amyloid fibrils produced by curli and in the evaluation of curli production by *E. coli*^{14,194,195} (Figure 4.8). Binding of CR in indicator agar to curli (25 µg mL⁻¹) causes cultured streaks or colonies to appear red. CR can interact with cellulose and other polysaccharides^{14,195–197} present in the ECM of the *E. coli* biofilms, potentially leading to false-positive results depending on the strain of *E. coli* used. *E. coli* MC4100 derivatives such as LSR10 (MC4100 Δ*csgA*) are often used as it reportedly does not produce a great deal of cellulose, flagella or O-polysaccharides^{198–200}. *E. coli* MG1655 and its derivatives (including W3110) are reportedly unable to produce cellulose due to a premature stop codon in the *bcsQ* gene, essential for cellulose biosynthesis, however they have not been reported to downregulate flagella or O-polysaccharide formation.

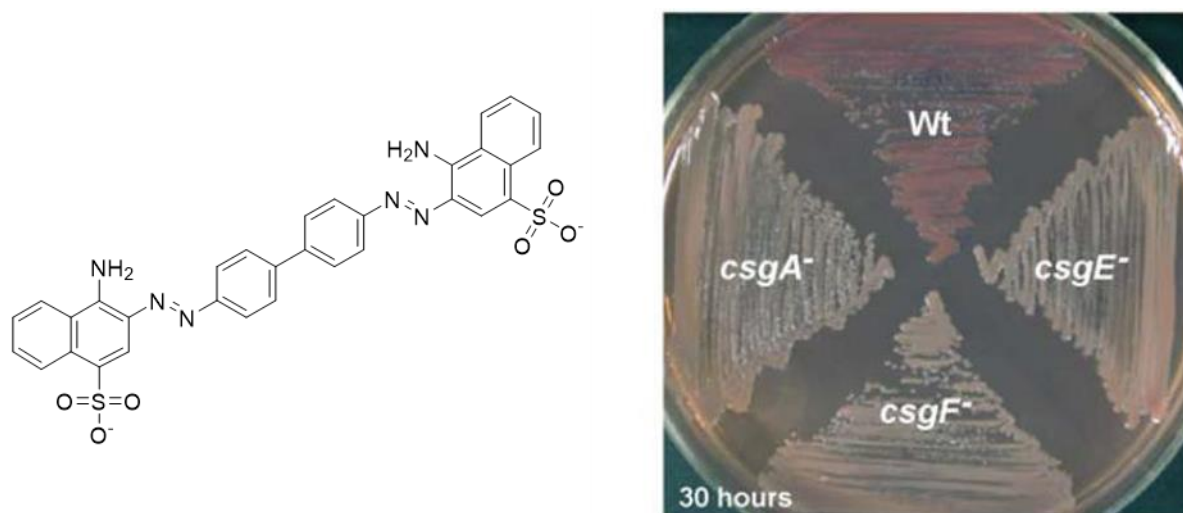


Figure 4.8: Left- structure of CR. Right- CR indicator plate showing the effect of deletion of curli specific genes A, F and E from the genome of *E. coli* MC4100.

4.1.6.2.2. Crystal violet assay

Another dye commonly employed in biofilm growth studies is crystal violet (CV; Figure 2) which stains both live and dead cells as well as some components of the ECM¹⁸⁴. The assay typically involves growth of biofilm in static liquid cultures in microtiter plates, followed by extensive washing to remove liquid culture and planktonic bacteria.

An aqueous CV solution at concentrations ranging from 0.1-1% (v/v) is then applied to the empty wells and left to bind biofilm present. Following another wash step, the bound CV is solubilised in ethanol, acetone or isopropyl alcohol, and the absorbance at 570 nm is measured. Issues arise with unspecific CV retention by certain plastics and the multiple wash steps leading to potential disruption of a formed biofilm, and lack of relevance when producing biofilm as a useful material.

4.1.6.2.3. Fluorescence microscopy and confocal fluorescence microscopy

Confocal fluorescence microscopy (CFM) is frequently used to image a stained biofilm. In this study, detection of cells and amyloid material in the biofilm extracellular matrix was *via* CFM and staining with propidium iodide (PI). PI cannot cross extracellular membranes of live cells ²⁰¹ and can therefore be used as a component of live-dead staining with a vital dye (SYTO9). Alternatively, in a biofilm treated overnight in 4% formal saline, it can be used to measure total (now all dead) cell content of the biofilm.

CFM generates images in a single focal plane (*i.e.* a 'slice' in the z-axis) of a fluorescence image. Through taking a series of slices a 3D image of the biofilm known as a Z-series of images can be constructed, yielding detailed information on the level of cellular retention in the biofilm. From 3-5 biological replicate samples (it is possible to build a representative and accurate description of the biofilm structure using COMSTAT2 analysis.

A Z-series of images obtained from CFM is composed of multiple slices of 2D images. The z-dimension of the images obtained arises from 'slicing' in the focal plane of a subject, through moving the subject stage in the Z-direction. Through moving at a constant step height, a 3D representation of a sample can be obtained with quantifiable parameters in the X, Y and Z directions, provided the image series dimensions are recorded.

4.1.7. Background to *Escherichia coli* strains employed in the present study

Escherichia coli W3110 was the positive control strain and was derived from *E. coli* MG1655, with an inversion mutation from the *rrnD* to *rrnE* genes. *Escherichia coli* W3110 is frequently used as the model strain for production of a curli dominant *E. coli* biofilm in the absence of cellulose production ^{197,202-204}. Cellulose biosynthesis is absent in K12 strains such as *E. coli* MG1655 and *E. coli* W3110 due to a premature stop codon in the essential *bcsQ* gene ¹⁹⁷.

Escherichia coli BL2-DE3 is a commercially available *E. coli* strain and reportedly does not produce significant amounts of curli at 37°C^{36,37}, and will only produce curli under certain conditions (mainly lower temperatures^{15,36}), making it an ideal negative control for curli production.

Escherichia coli MG1655 ompR234 PRO Δ csgA was gifted from T.K. Lu et al. The strain was produced to enable controlled production of engineered curli following deletion of the csgA gene encoding the main structural component of curli. The ompR234 mutation is a single point mutation in the ompR gene, reportedly affecting how csgD induces expression of curli specific genes involved in the excretion of csgA and B, resulting in a strain which effectively produces curli under a wide range of temperatures (including 37°C). The authors reported the abolishment of curli production following the deletion of the csgA gene, which was re-established following incorporation of a plasmid harbouring csgA under the control of an inducible promoter.¹⁸¹

4.2. Results and discussion

4.2.1. Plasmid and strain construction

All methods such as transformation, PCR, miniprep plasmid DNA isolation for example were undertaken according to Section 4.4 unless otherwise stated. Primers used for SDM are designed according to specifications outlined in Liu and Naismith²⁰⁵. All sequencing chromatographs are presented on the supplied multimedia disk, along with full gene sequences from analysis of CsgA and engineered versions thereof.

4.2.1.1. PFF753CcsgA

The final form of the plasmid employed in controlling biofilm production by *E. coli* MG1655 ompR234 PRO Δ csgA, PFF753CcsgA (Figure 4.9) was designed to incorporate *csgA* under the inducible pL-tetO promoter, to allow expression *via* the addition of supplementary anhydrotetracycline (aTC) to the culture medium. Also contained in the plasmid is *tetR* (expression of which yields the repressor protein involved in the pL-tetO promoter system), and a gene yielding a fusion protein of *S.aureus* SortaseA and green-fluorescent protein (GFP). The *ampR* gene confers resistance to ampicillin.

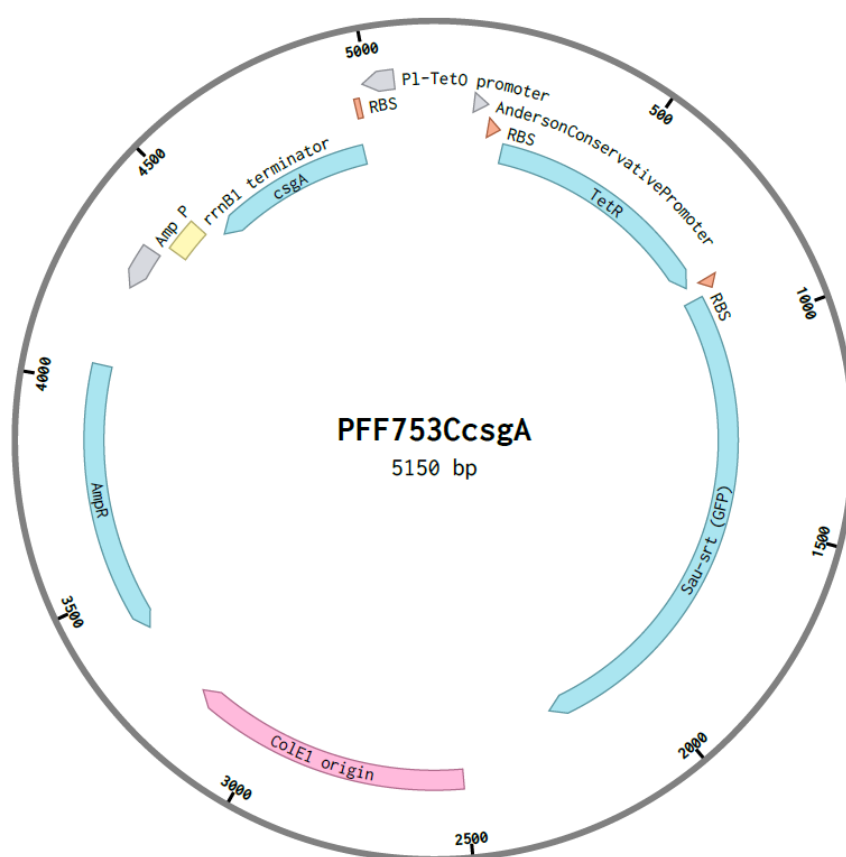


Figure 4.9: Plasmid map of PFF753CcsgA.

PFF753CcsG A was produced from the purchased version PFF753csg A following several steps to improve *csgA* expression and post-expression processing of the produced CsgA protein by *E. coli* (detailed in Section 4.4.1.4). Transformation of PFF753CcsG A into *E. coli* MG1655 ompR234 PRO Δ csgA yielded the strain able to controllably produce biofilm in response to aTC.

4.2.1.2. PFF753CcsG ASau

PFF753CcsG ASau was produced from PFF753CcsG A (proto) *via* site directed mutagenesis (detailed in Section 4.4.1.4). PFF753CcsG ASau contains the engineered *csgA* gene encoding for the C-terminal tagged- LPYTGG version of CsgA capable of sortase ligation (Figure 4.10), termed CsgASau.

4.2.1.3. PFF753CcsG ASauGGS

PFF753CcsG ASauGGS was produced from PFF753CcsG ASau *via* site directed mutagenesis (detailed in section 4.4.1.5). PFF753CcsG ASauGGS encodes the engineered CsgA protein containing a glycine-glycine-serine linker region between the C_terminus of CsgA and the LPYTGG sequence (Figure 4.10), Termed CsgASauGGS



Figure 4.10: Representation of relevant sections of plasmids PFF753CcsG A (top), PFF753CcsG ASau (middle) and PFF753CcsG ASauGGS (bottom) and their translated products showing the engineering of the C-terminal end of the produced CsgA protein.

4.2.2. Inspection of curli ECM production by *E. coli* MG1655 ompR234 PRO Δ csgA :: pFF753CcsG A

To provide initial confirmation of curli production following expression of curli specific genes in induced cultures of *E. coli* MG1655 ompR234 PRO Δ csgA :: PFF753CcsG A, liquid cultures of identical turbidity were filtered through a 0.22 μ m

polycarbonate membrane. The whole surface of the filter membrane was then examined, and images provided were representative of the surface as a whole.

Uninduced *E. coli* MG1655 ompR234 PRO Δ csgA :: PFF753CcsG cultures appeared to be evenly distributed across the filter membrane (Figure 4.11). Higher magnification revealed some small clusters, interspersed with single rod-like cells characteristic of *E. coli* distributed across the surface. At ultra-high resolution, single *E. coli* cells were clearly visible. The cluster observed showed no cell covering material adjoining neighbouring cells. It can be concluded from this that in an uninduced state no extracellular material was observed for liquid cultures.

An immediately obvious contrast was evident for induced liquid cultures of *E. coli* MG1655 ompR234 PRO Δ csgA::PFF753CcsG (Figure 4.12). An extensive network of rod-shape cells covering a large portion of the filter membrane surface was observed. Where no network was present, very few individual cells were evident, indicating the propensity of the induced cell populations to agglomerate. At higher magnification, large volumes of *E. coli* cells covered with an extracellular substance, appeared in a single mass of material. Imaging at ultra-high magnification confirmed the presence of this extracellular substance, with the highest magnification providing insight into its macrostructure. The presence of EPS covering induced *E. coli* populations was consistent with the production of a large volume of curli and other EPS components.

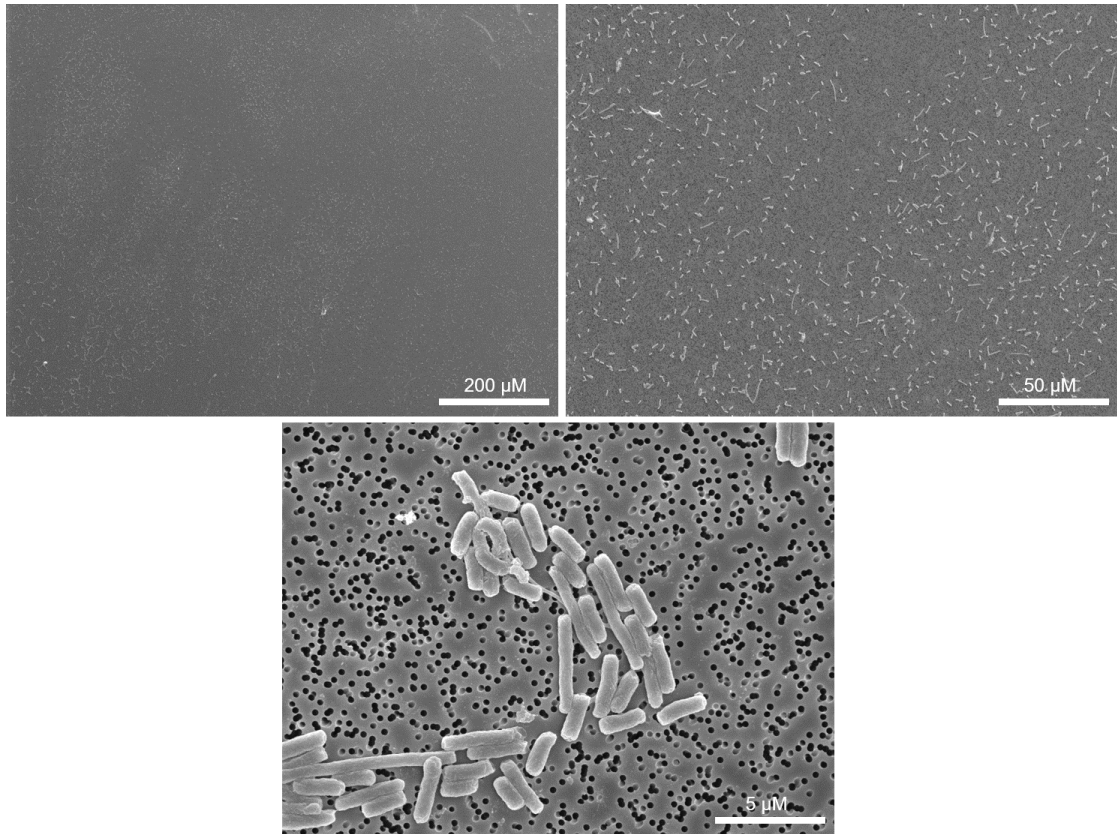


Figure 4.11: SEM micrographs of deposited *E. coli* MG1655 ompR234 PRO Δ csgA :: PFF753CcsG without aTC induction from a liquid culture.

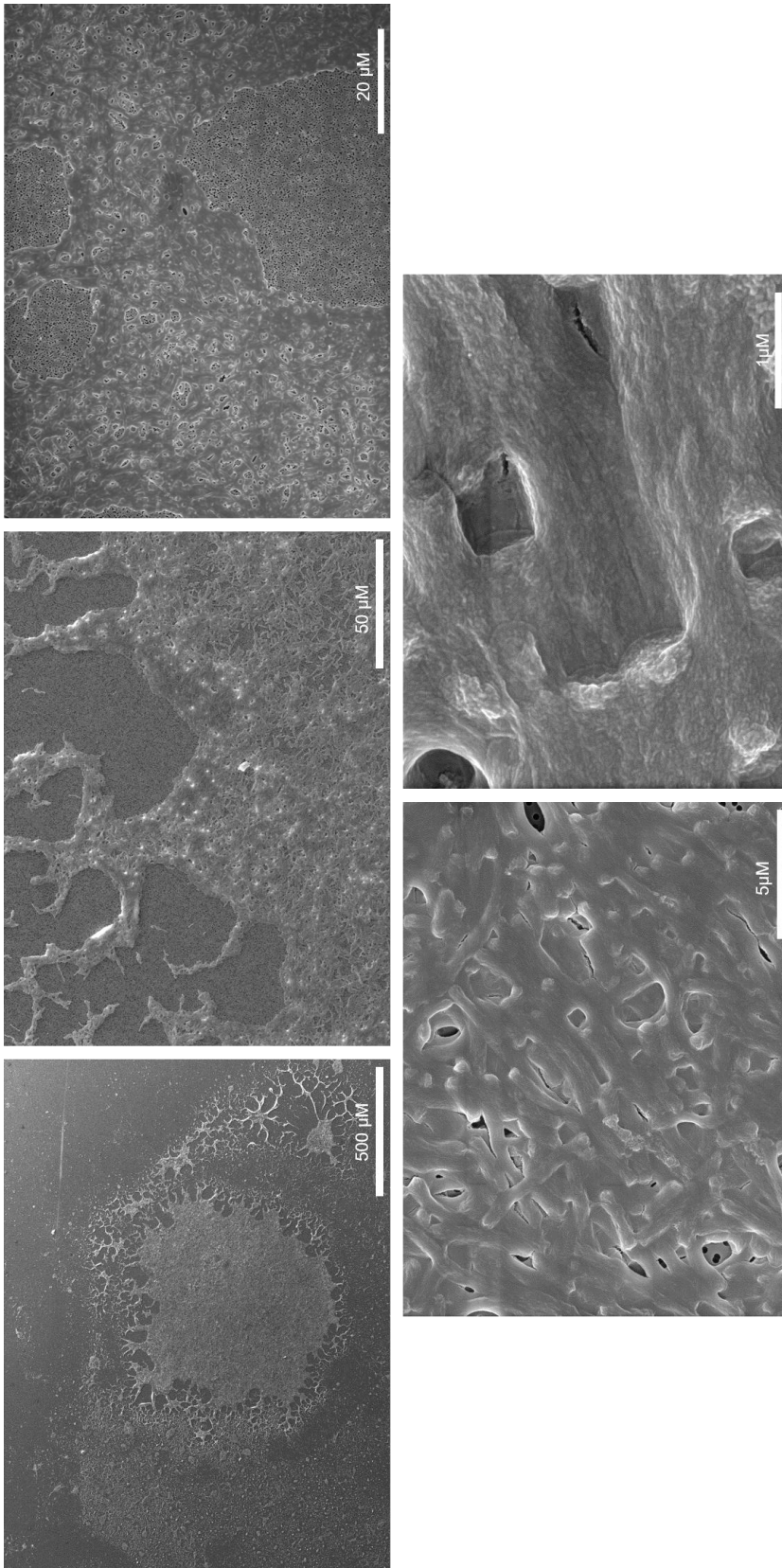


Figure 4.12: SEM micrographs of deposited networks of *E. coli* MG1655 ompR234 PRO Δ csgA :: PFF753CcsgA with aTC induction from a liquid culture.

4.2.3. Evaluation of curli production by reference strains and MG1655ompR234ΔcsgA::PFF753CCsgA in static culture over 72h

Biofilms formed on polycarbonate coupons from a static 72h culture in the CDC bioreactor were prepared as described in section 4.4.3.1. Coupons were washed twice carefully by immersion in sterile dH₂O before being fixed in 4% formal saline overnight prior to analysis.

4.2.3.1. Morphology and distribution of biofilm at the coupon surface

Maximum projection and 3D rendered images produced as described in 3.4.3.2 are shown for biofilms produced by *E. coli* strains BL21-DE3 (Figures 4.13 and 4.14, W3110 (Figures 4.15 and 4.16), MG1655 ompR234 ΔcsgA (Figures 4.17 and 4.18) and MG1655 ompR234 ΔcsgA :: PFF753CcsgA induced with 200 ng mL⁻¹ of anhydrotetracycline (aTC) (Figures 4.19 and 4.20) and without induction (Figures 4.21 and 4.22). CFM analysis and quantification was performed as outlined in section 4.4.3.2. Videos of 3D renderings are detailed in the appendix of this thesis.

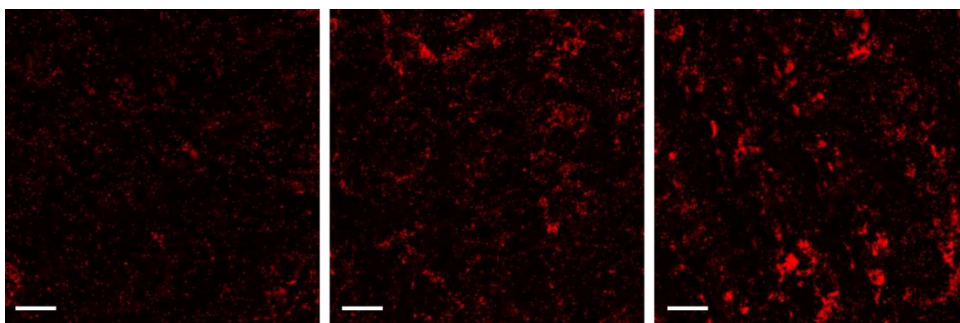


Figure 4.13: Maximum projection images of propidium iodide stained 72h static biofilms formed on a polycarbonate coupon surface by *E. coli* BL21-DE3 (scale bar represents 50 μm).

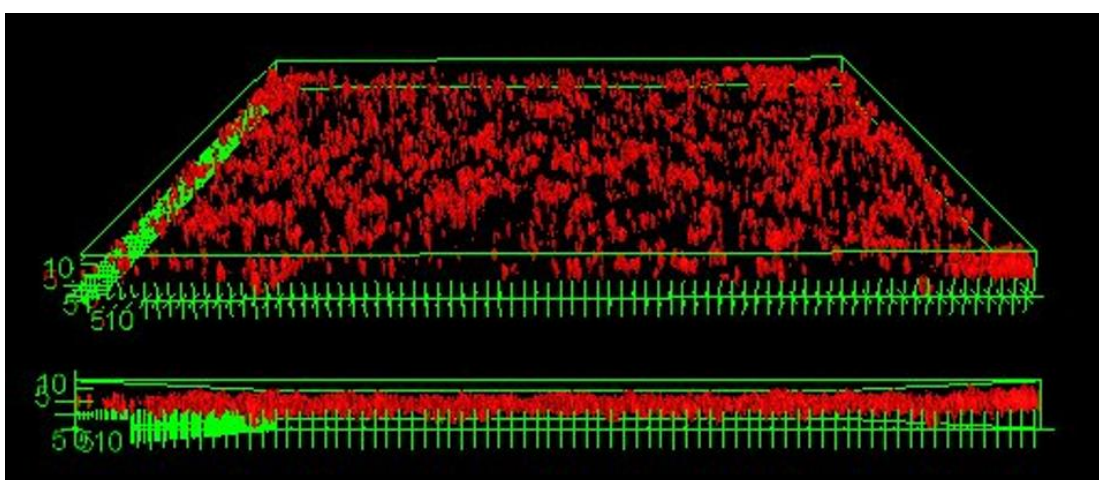


Figure 4.14: 3D projection image of propidium iodide stained 72h static biofilm formed on polycarbonate coupon surface by *E. coli* BL21-DE3 (tick marks represent 5 μm).

Propidium iodide (PI) staining of the biofilm following incubation in a bioreactor containing liquid *E. coli* BL21-DE3 culture for 72h revealed a very sparse, evenly distributed array of luminescence across the entire polycarbonate coupon (Figures 4.13 and 4.14). This fluorescence from PI was representative of the dead-cell component of the biofilm (i.e. total biofilm as previously treated with formal saline), indicating a relatively low surface coverage and thickness of biofilm.

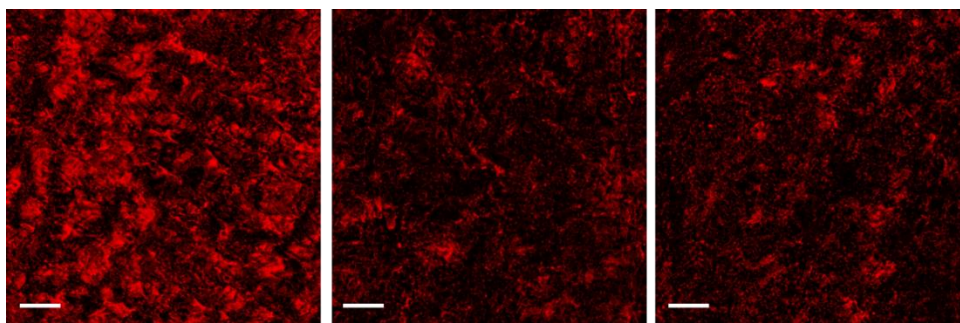


Figure 4.15: Maximum projection images of propidium iodide stained 72h static biofilms formed on polycarbonate coupon surface by *E. coli* W3110 (scale bar represents 50 μm).

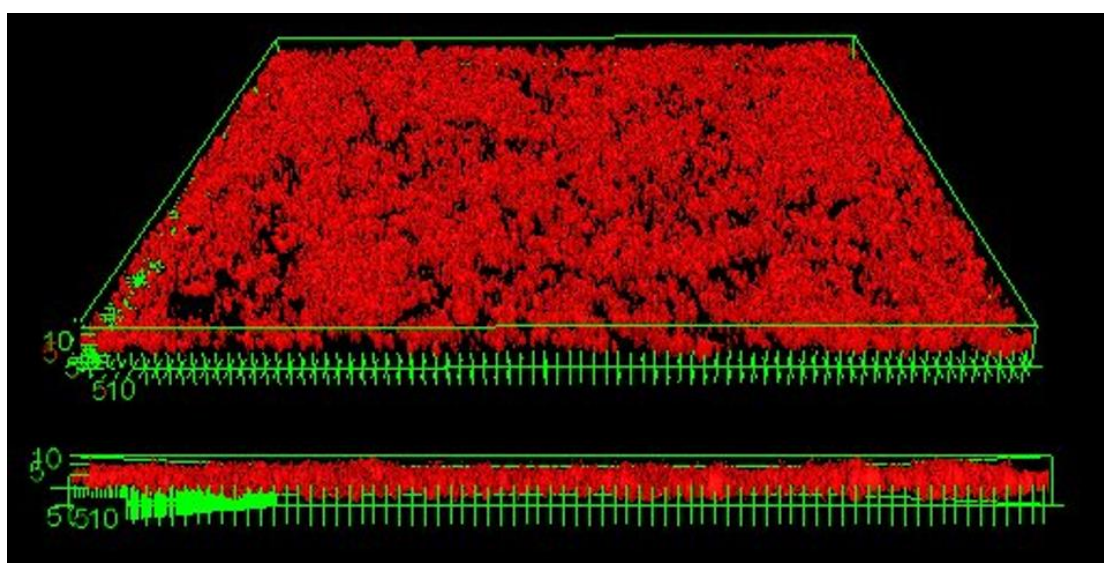


Figure 4.16: 3D projection image of PI stained 72h static biofilm formed on polycarbonate coupon surface by *E. coli* W3110 (tick marks represent 5 μm).

PI staining of the biofilm following incubation in a bioreactor containing liquid *E. coli* W3110 culture for 72h showed a distinct difference in the intensity and area of PI staining, as evidenced by the high degree of red-PI emission shown in Figures 4.15 and 4.16. Both the size of cellular aggregate clusters and number exceeded that seen for biofilms produced by the negative control strain, *E. coli* BL21-DE3, evidencing more extensive biofilm development.

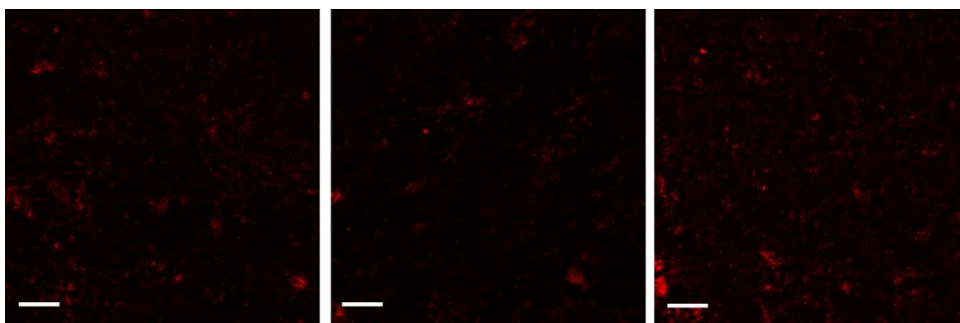


Figure 4.17: Maximum projection images of propidium iodide stained 72h static biofilms formed on polycarbonate coupon surface by *E. coli* MG1655 ompR234 PRO Δ csgA (scale bar represents 50 μ m).

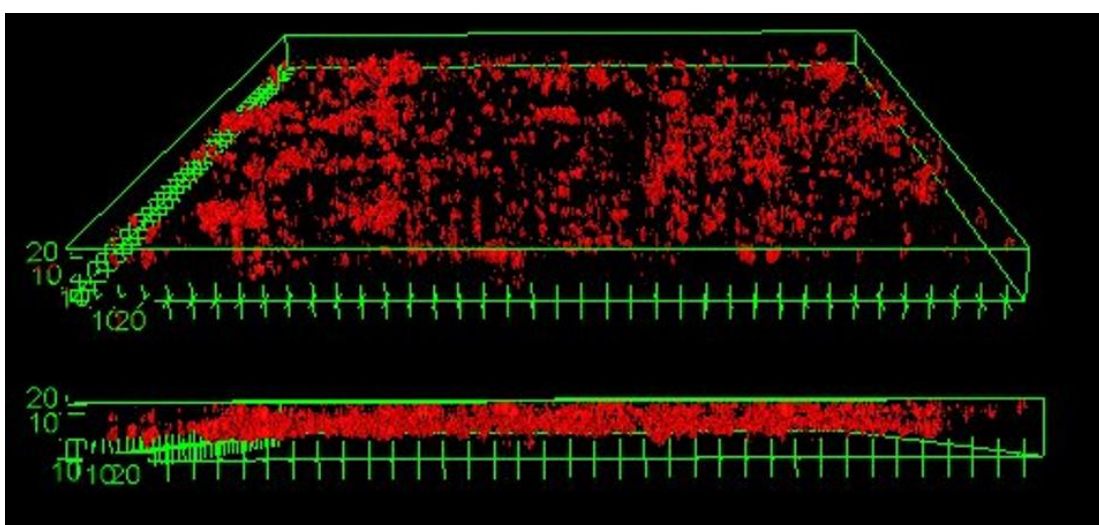


Figure 4.18: 3D projection image of PI stained 72h static biofilm formed on polycarbonate coupon surface by *E. coli* MG1655 ompR234 Δ csgA (tick marks represent 10 μ m).

PI staining of the biofilm following incubation in a bioreactor containing liquid *E. coli* MG1655 ompR234 Δ csgA culture for 72h revealed a very sparse, evenly distributed array of fluorescence around the entire coupon, as shown in Figures 4.17 and 4.18. This sparse cellular distribution was reminiscent of the biofilms depicted in Figures 4.13 and 4.14 from *E. coli* BL21-DE3, the negative control strain.

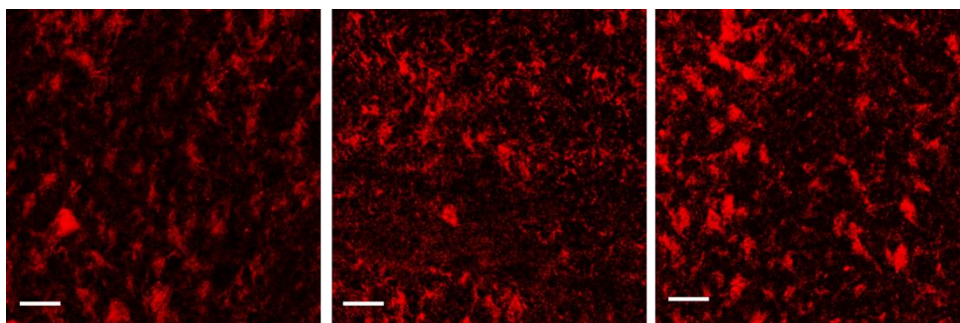


Figure 4.19: Maximum projection images of propidium iodide stained 72h static biofilms formed on polycarbonate coupon surface by *E. coli* MG1655 ompR234 PRO Δ csgA :: PFF753CcsgA without induction with aTC (scale bar represents 50 μ m).

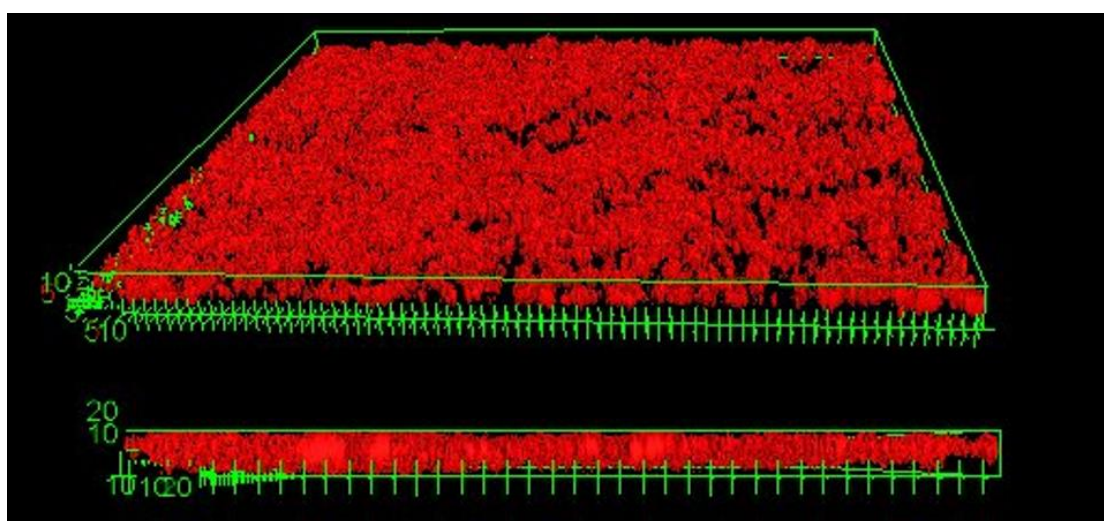


Figure 4.20: 3D projection image of PI stained 72h static biofilm formed on polycarbonate coupon surface by *E. coli* MG1655 ompR234 PRO Δ csgA :: PFF753CcsgA without induction with aTC (tick marks represent 10 μ m).

PI staining of the biofilm following incubation in a bioreactor containing liquid *E. coli* MG1655 ompR234 Δ csgA ::PFF753CcsgA culture for 72h with no aTC induction, revealed a high degree of surface associated biomass, as shown in figures 4.19 and 4.20, reminiscent of the cellular biomass at the coupon surface exhibited in the biofilm produced by *E. coli* W3110 (Figures 4.15 and 4.16).

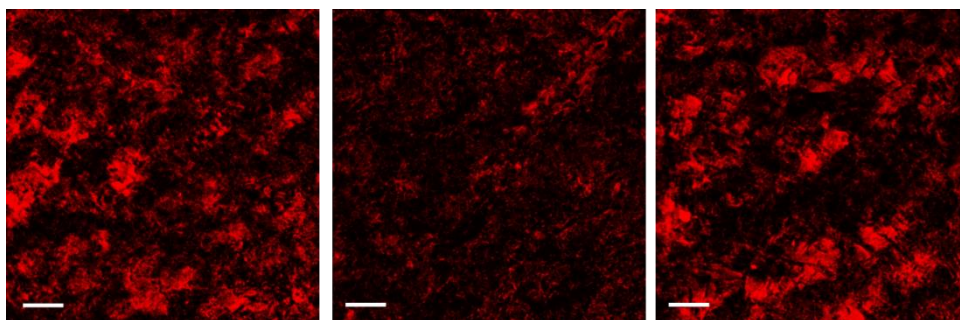


Figure 4.21: Maximum projection images of propidium iodide stained 72h static biofilms formed on polycarbonate coupon surface by *E. coli* MG1655 ompR234 PRO Δ csgA :: PFF753CcsG with induction with 200 ng mL⁻¹ aTC (scale bar represents 50 μ m).

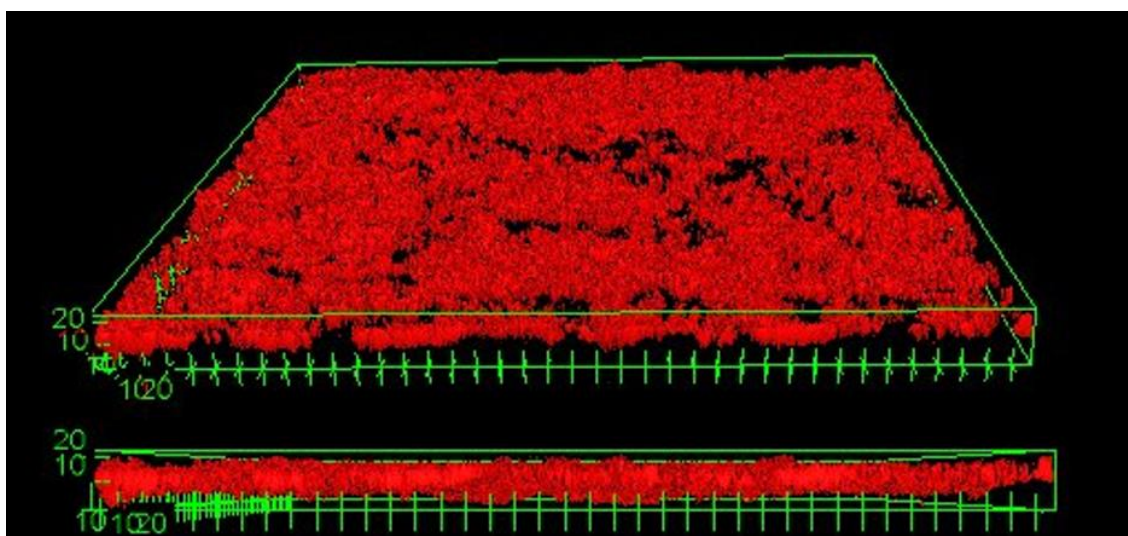


Figure 4.22: 3D projection image of propidium iodide stained 72h static biofilm formed on polycarbonate coupon surface by *E. coli* MG1655 ompR234 PRO Δ csgA :: PFF753CcsG with induction with 200 ng mL⁻¹ aTC (tick marks represent 10 μ m).

PI staining of the biofilm following incubation in a bioreactor containing liquid *E. coli* MG1655 ompR234 Δ csgA ::PFF753CcsG culture for 72h with aTC induction revealed a high degree of surface associated biomass, as shown in figures 4.21 and 4.22, reminiscent of the biomass exhibited in the biofilm produced by *E. coli* W3110.

The small quantity and sparse distribution of cellular biomass observed on the coupon surface for *E. coli* MG1655 ompR234 PRO Δ csgA was expected, as the Δ csgA mutation imparts an inability of the *E. coli* strain to efficiently produced curli, negatively affecting abiotic and intracellular attachment (critical to biofilm formation). This was further supported by the apparent similarity in cellular biomass to the negative control strain, *E. coli* BL21-DE3 which has previously been demonstrated not to produce curli

efficiently at 37 °C.^{170,206} This also supported the hypothesis that curli was essential to the irreversible attachment of *E. coli* to abiotic surfaces.

Conditions where *E. coli* MG1655 ompR234 PRO Δ csgA contained the csgA containing plasmid PFF753CcsgA appeared to show greatly extended cellular surface coverage of the polycarbonate coupon independent of activation of csgA expression through aTC induction. This infers a degree of basal expression of csgA independent of aTC induction.

4.2.3.2. COMSTAT 2 quantification of biofilm properties

COMSTAT analysis of all Z-series confocal datasets was performed for all conditions in triplicate, obtaining quantitative results describing biofilm biomass, thickness, surface area and surface roughness parameters (Table 4.2, Figure 4.23). All Z-series images were obtained with a Z-step height of 1 μ m and subjected to thresholding at a value of 20. Values were the arithmetic mean from each condition in triplicate.

Conditions in this section where biofilms were produced by *E. coli* MG1655 ompR234 PRO Δ csgA are described henceforth by their presence of the plasmid PFF753CcsgA (+ or -) and whether aTC was added to the culture (+ or -) respectively. For example, the -/- condition represented absence of the plasmid PFF753CcsgA and without aTC addition. Similarly, +/- represented the condition where PFF753CcsgA was present, but induction of aTC was not performed.

Table 4.2: Comstat evaluation of biofilms produced by *E. coli* strains over 72h in a static culture.

Condition	Biomass / $\mu\text{m}^3\mu\text{m}^{-2}$	Average Thickness of biomass / μm	Average Thickness in entire area / μm	Surface roughness (R*)	Surface area / cm^2	Surface area to biovolume ratio / $\mu\text{m}^2\mu\text{m}^{-3}$
BL21-DE3	0.82	11.20	2.80	1.50	0.71	5.99
W3110	3.54	12.06	7.87	0.71	2.12	4.25
-/-	0.40	12.92	2.17	1.67	0.46	7.65
+/-	2.99	12.62	7.92	0.77	2.05	4.59
+/+	3.30	15.22	9.57	0.77	1.98	4.20

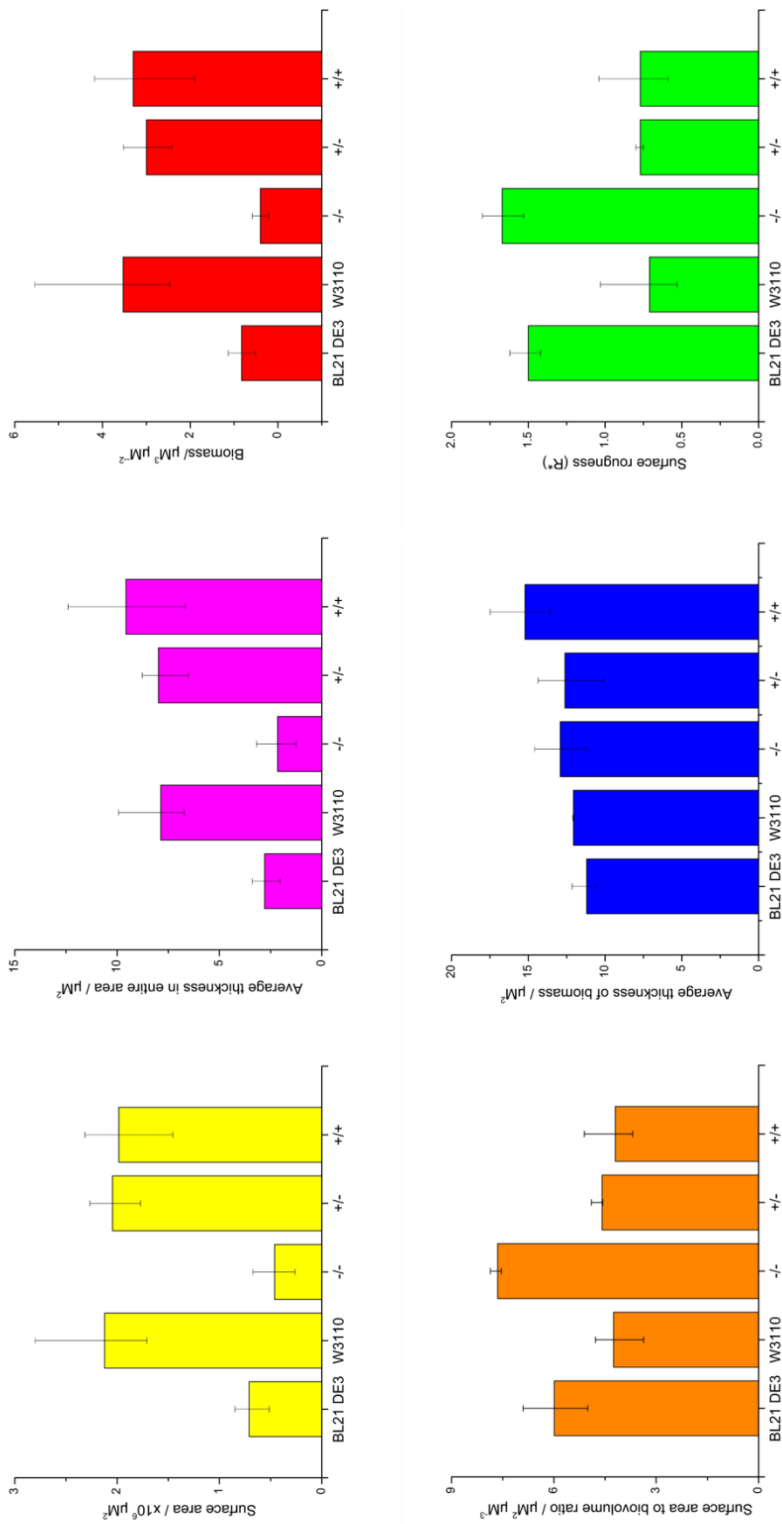


Figure 4.23: COMSTAT quantification results illustrating biofilm biomass (red bars), average thickness of biofilm (blue bars), average thickness in entire area (magenta bars), surface roughness (green bars), surface area (yellow bars) and surface area to biovolume ratio (orange bars).

Biofilms produced by the *csgA* negative control strain *E. coli* BL21-DE3 and *E. coli* MG1755 ompR234 PRO Δ *csgA* exhibited comparable biomass of $< 1 \mu\text{m}^3 \mu\text{m}^{-2}$, as well as a low average surface thickness of $< 3 \mu\text{m}$. Average surface area of biofilm was also very low compared with other conditions, $< 1 \text{cm}^2$. High surface area to biovolume ratios (in effect, reciprocal biomass) of $6 \mu\text{m}^2 \mu\text{m}^{-3}$ and greater were also observed, which was in agreement with the low biomass quantification. These results were consistent with the visual representations of the biofilms produced by *E. coli* BL21-DE3 and MG1655 ompR234 PRO Δ *csgA*, representing a very sparse distribution of small volumes of microcolonies covering a small portion of the imaged surface.

In contrast, biofilms produced from the +/- and +/- conditions exhibited biomasses, entire area thicknesses and surface areas (and surface area to biovolume ratios) that were in close agreement with those found for the positive control strain *E. coli* W3110. High biomass ($> 3.00 \mu\text{m}^3 \mu\text{m}^{-2}$), thickness (over $7.50 \mu\text{m}^2$) and surface area (over 2.00cm^2) contrasted with reduced surface roughness parameters (< 0.80) and surface area to biovolume ratio values (Below $5 \mu\text{m}^2 \mu\text{m}^{-3}$), which together demonstrate the ability of *E. coli* W3110, +/- and +/+ strains to produce a thicker, more uniform biofilm.

It appeared from these results, that the plasmid PFF753C*csgA* had a great impact on the ability of *E. coli* MG1655 ompR234 PRO Δ *csgA* to produce biofilm, likely due to expression of *csgA* from the plasmid itself. It does however suggest that due to the apparent similarity of biofilms produced in the presence and absence of aTC, that the P_L -TetO promoter controlling *csgA* expression was 'leaky' as the qualitative analysis of biofilm images suggest.

4.2.3.3. Statistical verification of COMSTAT 2 results

Statistical analysis (one-way ANOVA with post-hoc Tukey-Kramer) of the COMSTAT results elicited allowed evaluation of how the mean values of variables measured (such as biomass and surface area) differed between conditions. Depending on several factors including variance within groups and variance between groups and the degrees of freedom (arising from number of number of repeats and conditions), a critical value from the statistical test enabled comparison on which pairs of conditions were statistically independent.

Several assumptions are made in a one-way ANOVA experiment:

- Independent and identically distributed variables (*i.e.* random sampling: datasets are not linked and detection of one variable does not affect measurement of another)
- Homoscedasticity: the dependant variable has the same variance within each population
- Normality: dependant variable is normally distributed within each population

The first two conditions were met in these experiments. Samples were randomly collected and the measurement of the biomass from one image did not affect the measurement of another. Variance across experiments was identical as all sample sizes were identical (results collected in triplicate).

Data is normally distributed when the mean median and mode are equal, and therefore distributed about the mean as an asymptotic, symmetric bell curve. Given the very small sample size ($N = 3$ for each measurement) it is potentially difficult to accurately evaluate whether this data was normally distributed. Using the Shapiro-Wilk normality test the extent to which the data collected was normally distributed could be determined: as described in the appendix of this thesis. Box and whisker plots identify where data is possibly not normally distributed (*i.e.* the very 'bottom heavy' distribution of the *E. coli* W3110 biomass results, however to a large extent, the means seem to be well distributed between the data extremes. Results from Shapiro Wilk analysis indicated that data was sufficiently normally distributed (Sig. value was greater than 0.05) for all conditions and metrics aside from the SA/BV ratio measurements.

Results from one-way ANOVA analysis (Table 4.3) described how all datasets apart from 'average thickness in biomass' return significance values of below the critical value (Sig. 0.05), meaning that one or more conditions were statistically significant from each other. Average thickness in biomass appeared to be statistically identical across all conditions.

Table 4.3: Critical values from one-way ANOVA analysis of data described in Table 4.2 and Figure 4.23.

Metric	F	Sig.
Average thickness in entire area	11.621	0.001
Average thickness in biomass	2.649	0.096
Biomass	6.580	0.007
Roughness (R*)	20.070	0.000
Surface area	13.983	0.000
Surface area to biovolume ratio	14.763	0.000

Post-hoc Tukey-kramer analysis (Table 4.4) from the one-way ANOVA test describes grouping of results in a dataset by those statistically identical to one-another. As described by the one-way ANOVA test results, all conditions were seen to give statistically identical results when measuring average thickness in biomass. Surface area to biovolume ratio showed no difference between the +/+, +/-, *E. coli* BL21 and *E. coli* W3110 conditions, although both groupings had significance values very close to the critical value of 0.05.

Measuring the biomass of biofilm produced gave three distinct groupings. Group C had a very high significance value (0.959, +/+, +/-, W3110) suggesting very close agreement in mean values. Whilst the significance value of Group A and Group B were close to the critical value of 0.05 and an order of magnitude lower than that of group C. The groupings showed that the +/- and +/+ conditions do not necessarily show a degree of statistical difference in biofilm biomass to that of the negative control condition, BL21-DE3, casting doubt on whether the biomass of the supposedly curli positive conditions (+/+ and +/-) differed from that of the curli negative conditions (such as BL21-DE3).

The average thickness in entire area, roughness (R*) and surface area measurements were all in agreement, describing two distinct groupings: BL21-DE3 (negative control) and -/-, separate from W3110, +/- and +/+.

Table 4.4: Groupings from post-hoc Tukey-Kramer analysis.

	Group A (Sig.)	Group B (Sig.)	Group C (Sig.)
Average thickness in entire area	-/-, BL21-DE3 (0.990)	W3110, +/-, +/+ (0.738)	-
Average thickness in biomass	ALL GROUPS (0.069)	-	-
Biomass	-/-, BL21-DE3, +/- (0.060)	BL21-DE3, +/-, +/+ (0.074)	+/-, +/+, W3110 (0.959)
Roughness (R*)	BL21-DE3, -/- (0.759)	W3110, +/-, +/+ (0.995)	
Surface area	-/-, BL21-DE3 (0.921)	W3110, +/-, +/+ (0.990)	
Surface area to biovolume ratio	-/- (0.052)	+/+, +/-, W3110, BL21- DE3 (0.073)	

4.2.3.4. Significance of results obtained for 72h static biofilm experiments

It was clear from confocal fluorescence microscopy and COMSTAT 2 analysis that *E. coli* MG1655 ompR234 PRO Δ csgA did not form an extensive biofilm network on the polypropylene surface. The morphology and surface coverage evident in the maximum projection and 3D representations of the biofilm from the -/- condition appeared to be similar to that of *E. coli* BL21-DE3, the negative curli control. Both BL21-DE3 and -/- conditions showed very low surface thickness and coverage of the coupon surface compared to that of the +/+, +/- and W3110 conditions. This difference was confirmed by statistically verified COMSTAT 2 quantification of the biofilms: where average thickness on the entire area, surface roughness and surface area appeared to be reliable markers of surface coverage.

Average thickness entire area (ATEA) is a robust variable to determine the overall surface coverage of the biofilm, in contrast to the widely variable average thickness in

biomass (ATBM) measurement. This is due to the thickness represented by the different measurements:

- ATEA determines the average thickness from all thresholded signal across the measured area, derived from signal considering all voxels regardless of whether biomass was detected
- ATBM determines average thickness across area determined by COMSTAT 2 to be continuous biomass

The similarity between all conditions in the ABTM measurement describes how microcolonies of similar thicknesses were formed over 72h across all conditions. The difference revealed itself in the morphology and size of microcolonies, where the ATEA measurement describes the average thickness over the entire measured area *i.e.* where there was more biofilm coverage, the thickness measured was greater. The ATEA measurement does not give an accurate measurement of biofilm thickness, due to influence in the measurement from regions not containing biofilm at all, and therefore it can be concluded that over 72h, *E. coli* microcolony formation at the coupon surface occurred with uniform thickness across conditions of around 13 μm .

The high surface area exhibited by biofilms produced in the +/+, +/- and W3110 conditions correlate with the observed trend in biomass; where extensive networks of *E. coli* biofilms were observed. Biomass quantification also suggested this grouping, however statistical analysis suggested the differences could not be statistically verified.

Extensive biofilm formation over a 72h time period by *E. coli* MG1655 ompR234 ΔcsgA was reliant on the presence of plasmid PFF753CcsG. When present, the strain appeared to form extensive microcolonies covering a large majority of the observed surface. This appeared to be independent of the inducer aTC, responsible for activation of transcription *via* the P_L-TetO promoter.

4.2.4. Evaluation of curli production MG1655 ompR234 Δ CsgA :: PFF753CCsgA in flow culture over 24h

4.2.4.1 Morphology and distribution of biofilm at the coupon surface

Biofilms formed by *E. coli* MG1655 ompR234 Δ csgA :: PFF753CcsgA under flow conditions (experimental procedure detailed in sections 4.4.3.1) over 24h are shown as maximum projection images (Figures 4.24 and 4.26), and 3D renderings (Figures 4.25 and 4.27). The two conditions represented when expression was induced through supplementation of the media with 200 ng μ L⁻¹ of anhydrotetracycline (aTC) and were described as uninduced or induced. CFM analysis and quantification was performed as outlined in section 4.4.3.2. Videos of 3D renderings are detailed in the appendix of this thesis.

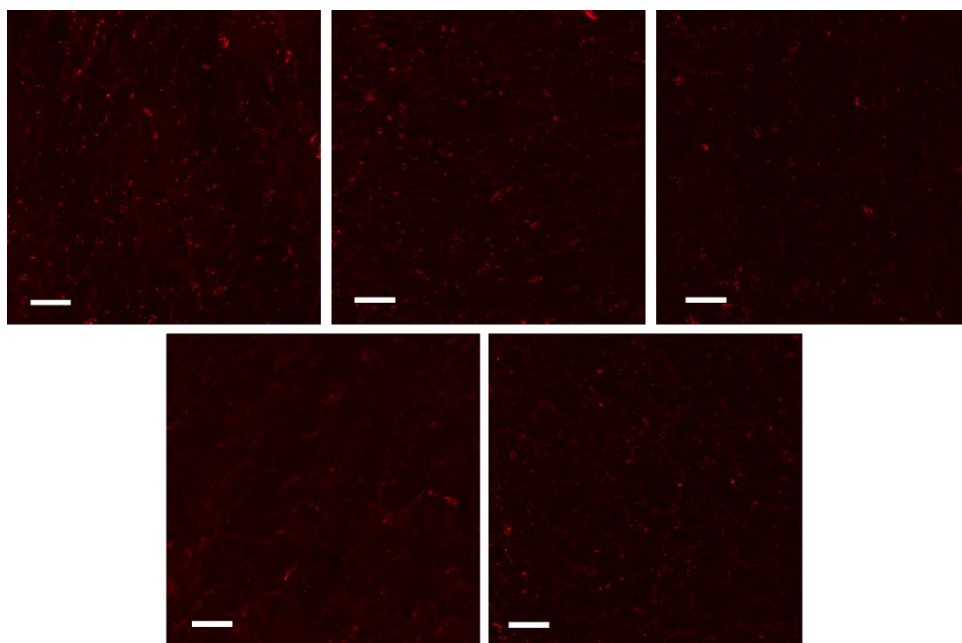


Figure 4.24: Maximum projection images of propidium iodide stained 24h flow system biofilms formed on polycarbonate coupon surface by *E. coli* MG1655 ompR234 PRO Δ csgA :: PFF753CcsgA without induction with 200 ng mL⁻¹ aTC (scale bar represents 50 μ m)

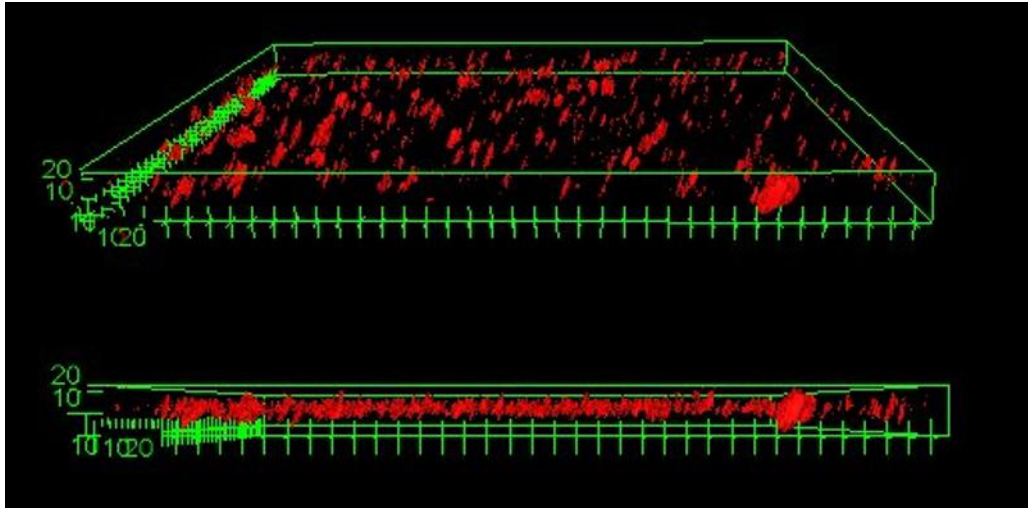


Figure 4.25: 3D projection image of PI stained 24h flow system biofilm formed on polycarbonate coupon surface by *E. coli* MG1655 ompR234 PRO Δ csgA :: PFF753CcsgA without induction with aTC (tick marks represent 10 μ m)

PI staining of the PC coupons from the bioreactor containing an *E. coli* MG1655 ompR234 PRO Δ csgA :: PFF753CcsgA culture without aTC induction showed a distinct lack of luminescence from PI indicating a low (dead) cellular volume at the PC coupon surface. This indicates a distinct lack of cellular surface coverage similar to that seen previously for 72h biofilms formed by *E. coli* BL21-DE3 and MG1655 ompR234 PRO Δ csgA (Section 3.2.3.1).

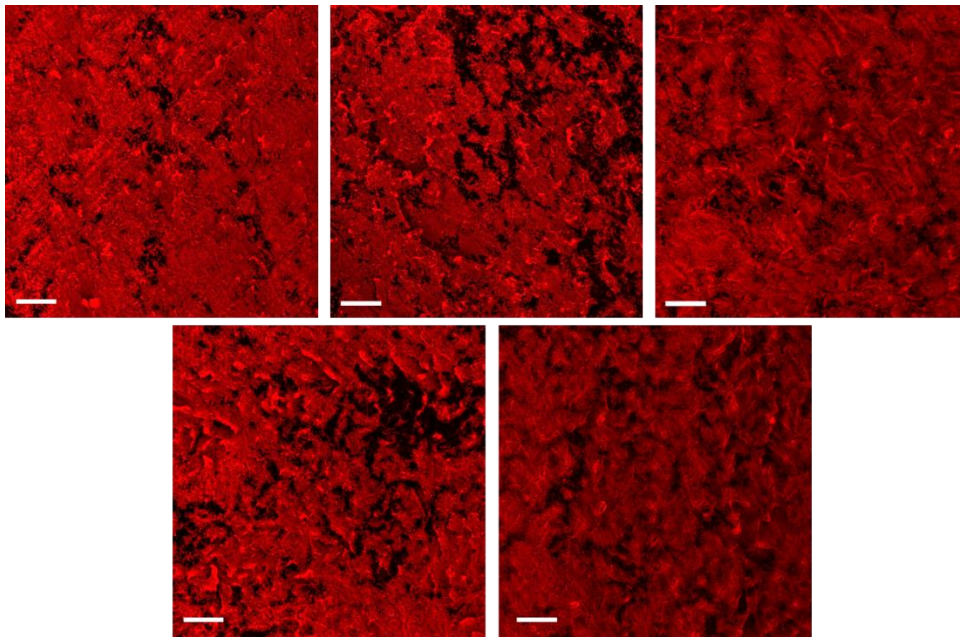


Figure 3.26: Maximum projection images of propidium iodide stained 24h flow system biofilms formed on polycarbonate coupon surface by *E. coli* MG1655 ompR234 PRO Δ csgA :: PFF753CcsG with induction with 200 ng mL⁻¹ aTC (scale bar represents 50 μ m)

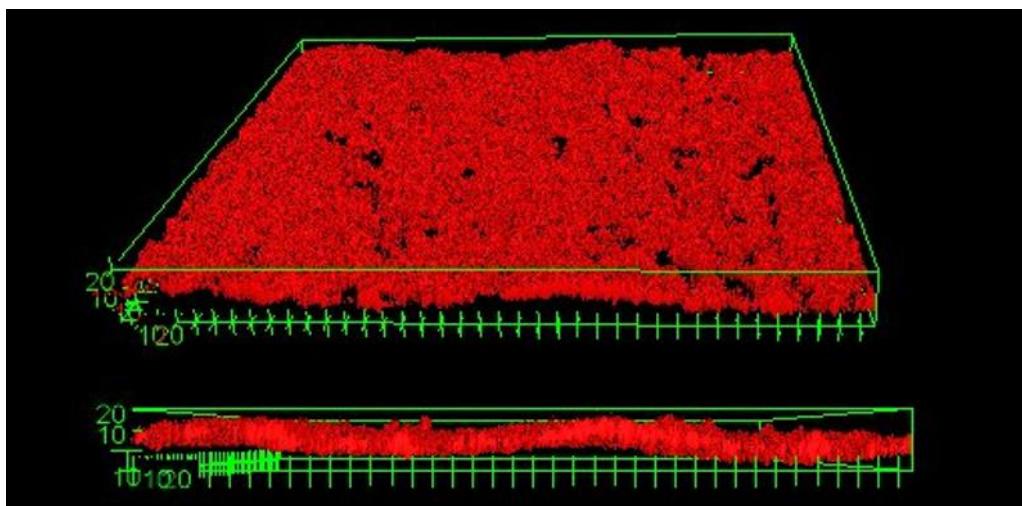


Figure 3.27: 3D projection image of PI stained 24h flow system biofilm formed on polycarbonate coupon surface by *E. coli* MG1655 ompR234 PRO Δ csgA :: PFF753CcsgA without induction with aTC (tick marks represent 10 μ m)

PI staining of the PC coupons from the bioreactor containing an *E. coli* MG1655 ompR234 PRO Δ csgA :: PFF753CcsgA culture with aTC (100 ng mL⁻¹) induction showed extensive luminescence from PI indicating a very high (dead) cellular volume at the PC coupon surface. This indicates extremely high cellular surface coverage, indicative of extensive biofilm formation from the induced *E. coli* MG1655 ompR234 PRO Δ csgA :: PFF753CcsgA culture population. In contrast with biofilms formed in the 72h static system (section 3.2.4), a very clear disparity can be observed between biofilms formed with induction of aTC.

Without induction, biofilm formation over 24h in a flow system was very sparse, closely resembling that for the curli negative BL21-DE3 biofilms shown in section 3.2.4. Well distributed individual aggregates of cells were observed spread over the imaged surfaces, very small in size and low in observable biomass.

Induction with 200 ng μ L⁻¹ of aTC over 24h under flow conditions appears to yield very thick biofilms, covering the entire imaged area. Channels in the biofilm matrix are observed, a characteristic property of a more mature biofilm.¹⁶⁷ In comparison with the 72h static biofilms, the induced 24h flow biofilm produced upon aTC induction appears thicker and denser, despite the shorter incubation time. This is likely attributed to the effect of replenishing media supply through flowing 5L of media through the bioreactor. It is likely that the increased flow shear forces and replenished supply of nutrients allows for the biofilm to develop further in a short space of time.

4.2.4.2. COMSTAT 2 quantification of biofilms

COMSTAT analysis of 24h flow biofilms formed by MG1655 ompR234 PRO Δ csgA :: PFF753CcsG with and without induction with 200 ng mL⁻¹ of aTC was performed as per the same parameters described in section 4.2.3. Mean values of biomass, average thickness, surface roughness, surface area and surface area to biovolume ratio are described in Table 4.5 and presented as bar charts in Figure 4.28 (with error bars representing minimum and maximum experimentally obtained values).

Table 4.5: Comstat evaluation of biofilms produced by *E. coli* strains over 24h in a flow culture with (+aTC) and without (-aTC) induction with 200 ng mL⁻¹ aTC.

Condition	Biomass / $\mu\text{m}^3\mu\text{m}^{-2}$	Average Thickness of biomass / μm	Average Thickness in entire area / μm	Surface roughness (R*)	Surface area / cM^2	Surface area to biovolume ratio / $\mu\text{m}^2\mu\text{m}^{-3}$
-aTC	0.17	15.12	1.23	1.84	0.56	5.21
+aTC	7.37	23.97	20.94	0.31	2.64	2.45

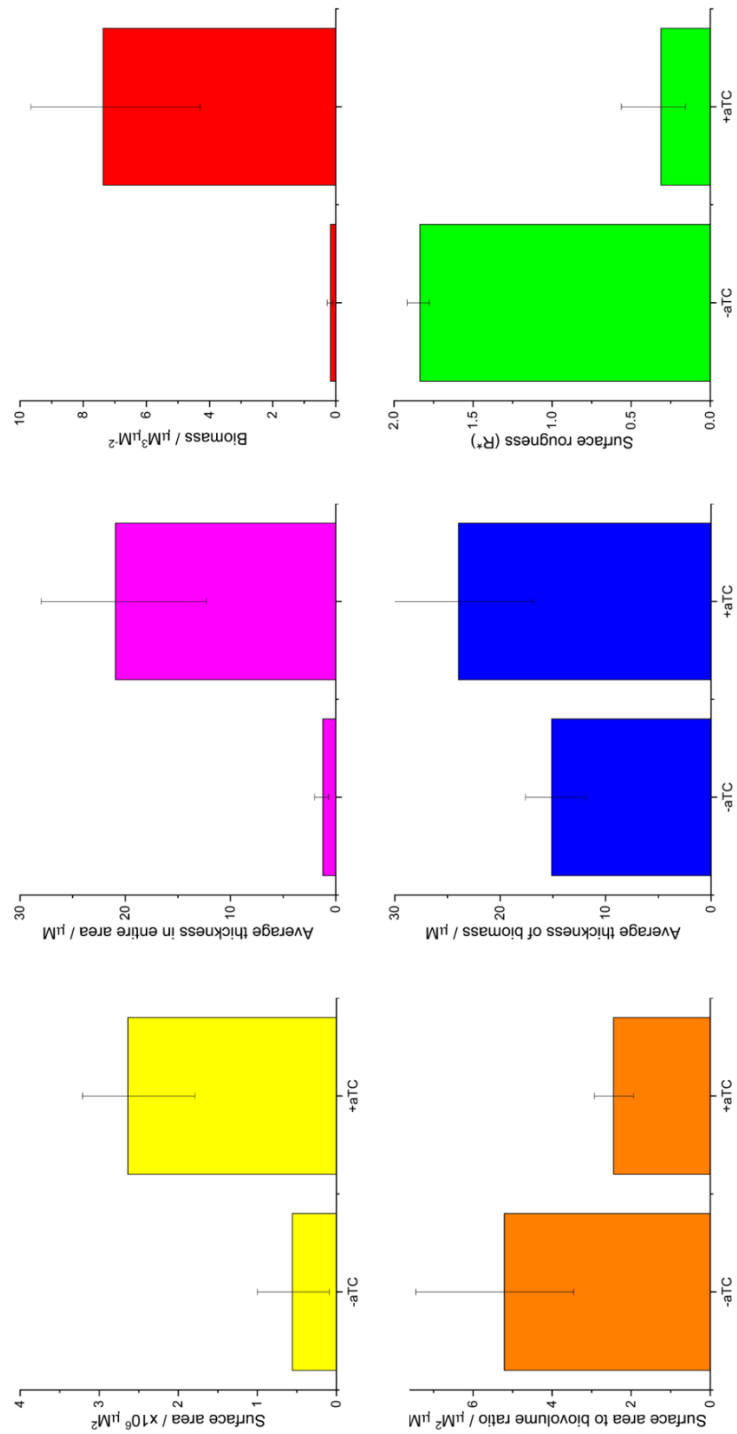


Figure 4.28: Comstat analysis results from 24h flow biofilms describing biofilm biomass (red bars), average thickness of biomass (blue bars), average thickness in entire area (magenta bars), surface roughness (green bars), surface area (yellow bars) and surface area to biovolume ratio (orange bars).

In agreement with qualitative observations described in section 3.2.5.1, a clear disparity in the properties of biofilms produced by *E. coli* MG1655 ompR234 PRO Δ csgA :: PFF753CcsG is seen depending on induction by aTC. Herein this section, the terms 'induced' and 'uninduced' biofilms represent biofilms formed by *E. coli* MG1655 ompR234 PRO Δ csgA :: PFF753CcsG with and without aTC induction respectively.

The mean biomass of the induced biofilm was found to be over forty times greater ($7.37 \mu\text{m}^3\mu\text{m}^{-2}$) in comparison with that of the uninduced biofilm ($0.17 \mu\text{m}^3\mu\text{m}^{-2}$), representing a disparity unmatched to those seen in the 72h static experiment. Additionally, in comparison with the biomass found for induced and uninduced biofilms in the 72h experiment ($\sim 3 \mu\text{m}^3\mu\text{m}^{-2}$) the induced biofilm formed over 24h under flow conditions appears to contain a much larger biovolume per unit of area (i.e. increased cellular matter content). This large degree of difference is maintained to a similar degree in surface roughness, average thickness of entire area and surface area measurements.

The mean thickness of formed biofilms when induced was also shown to increase for both entire area and of biomass measurements. Average thickness over entire area increased by nearly twenty times, from 1.23 when csgA expression was not induced to 20.94 μm . By comparison, the average thickness of biomass of biofilm increased by a smaller degree (15.12 μm to 24 μm) upon aTC induction. This represents both the formation of a biofilm which covers the entire coupon surface when csgA expression is induced, as well as suggesting that the actual thickness of the biofilm (where formed) increases to a degree.

In comparison of the 24 h flow biofilms with biofilms produced over 72h in a static culture (section 4.2.3), average thickness of induced biofilms over the entire area increased by a factor of 2 when comparing the 24h flow and 72h static conditions. Non-induced biofilm produced over 24 h in flow was of a similar thickness found for the negative control conditions detailed for the 72h static experiment (section 4.2.3).

The decrease in mean surface roughness by a factor of six following induction represents the more total surface coverage of the thicker, evenly distributed biofilm formed over when induced with aTC. One can see in the 3D representations shown in section 3.2.5.1 that where induction was not performed, small distributed aggregates are observed at the coupon surface, causing the 'roughened' surface. Where extensive biofilms are formed, this roughness decreases by a large degree as most of the surface is covered by biomass.

Again, the uninduced biofilm formed from the 24h flow experiment was found to exhibit a similar surface roughness to the negative curli control strains in the 72h static experiment. Biofilm morphology appears similar across these conditions (numerous sparsely distributed aggregate structures), giving rise to the rougher surface. The induced biofilm formed from the 24h flow experiment appears to be less rough than all conditions in the 72h static experiment, which supports the hypothesis that the increased extent of biofilm formation seen for the induced 24h flow experiments produces a flatter, thicker, evenly distributed biofilm containing a larger amount of biomass.

The increase in surface area by a factor of five where curli production is induced in the 24h flow experiment represents the increase in coverage by a large, structured, faceted biofilm such as the one seen in the 3D representation (section 4.2.4.2). The surface area to biovolume ratio decreases by a factor of two where comparing induced 24h flow biofilms with uninduced biofilms formed by the same technique, in agreement with the biomass and surface area measurements.

The surface area to biovolume ratio of biofilms produced from induced 24h flow cultures was lower than any seen in the 72h conditions, representing the smooth surface and increased biomass. The uninduced 24h flow biofilm showed similar surface area to biovolume ratios for all 72h static conditions.

4.2.4.3. Statistical verification of COMSTAT quantification

One-way ANOVA statistical analysis of data was performed to verify whether differences in mean metrics collected from COMSTAT 2 analysis are significant. Parameters required for the One-way anova test are as described in section 4.2.3.3, with the key requirement of all data to be normally distributed.

Normality was tested by shapiro-wilk analysis, which showed all data was sufficiently normally distributed (i.e. returned a significance value of over 0.05) for one-way anova analysis. Normality analysis and box and stem plots showing distribution of data are given in the appendix of this thesis.

One-way ANOVA verification shows that all metrics, other than average thickness in biomass, return statistically different mean values (significance value >0.05), and therefore the two conditions are significantly different from each other (Table 4.6). There is no need to perform a post-hoc Tukey-Kramer test, as there are only two conditions to measure.

From these results we conclude that aTC induction has a statistically significant impact on biofilm biomass, thickness (when measured over the entire area), surface roughness, surface area and surface area to biovolume ratio. As with the 72h biofilm experiment, the actual thickness of formed biofilms were unaffected by aTC induction.

Table 4.6: Critical values from one-way ANOVA analysis of data described in Table 4.5 and Figure 4.28.

Metric	F	Sig.
Average thickness in entire area	55.717	0.000
Average thickness in biomass	4.794	0.060
Biomass	62.757	0.000
Roughness (R*)	359.003	0.000
Surface area	43.262	0.000
Surface area to biovolume ratio	11.125	0.010

4.2.4.4. Significance of results for 24h flow biofilm experiments

Through altering the incubation time and introducing media flow-through, we elucidate a very well controlled mechanism whereby biofilm development by *E. coli* MG1655 ompR234 Δ csgA :: PFF753CcsG is mediated through aTC induced expression of csgA. Through confocal fluorescence microscopy of PI stained biofilms produced over 24h under flow conditions, a large disparity in the cellular coverage of biofilms produced was observable and confirmed through COMSTAT analysis.

These results suggest that where basal level of csgA expression allows for biofilm development over 72h in a static culture, extensive biofilm development over 24h in a media flow environment is reliant on extensive csgA expression, induced by aTC. Further to this, these results demonstrate the significantly increased biofilm production by *E. coli* MG1655 ompR234 Δ csgA :: PFF753CcsG under flow conditions in comparison to static conditions.

4.2.5. Evaluation of curli production MG1655 ompR234 Δ CsgA :: PFF753CCsgASau and PFF753CsgASauGGS in flow culture over 24h

4.2.5.1. Morphology and distribution of biofilm at the coupon surface

Biofilms formed by E. coli MG1655 ompR234 Δ csgA :: PFF753CsgASau and E. coli MG1655 ompR234 Δ csgA :: PFF753CsgASauGGS under flow conditions (experimental procedure detailed in Section 4.4.3.1) over 24h with induction with 200 ng mL⁻¹ are shown as maximum projection images (Figures 4.29 and 4.31), and 3D renderings (Figures 4.30 and 4.32) respectively. CFM analysis and quantification was performed as outlined in section 4.4.3.2. Videos of 3D renderings are detailed in the appendix of this thesis.

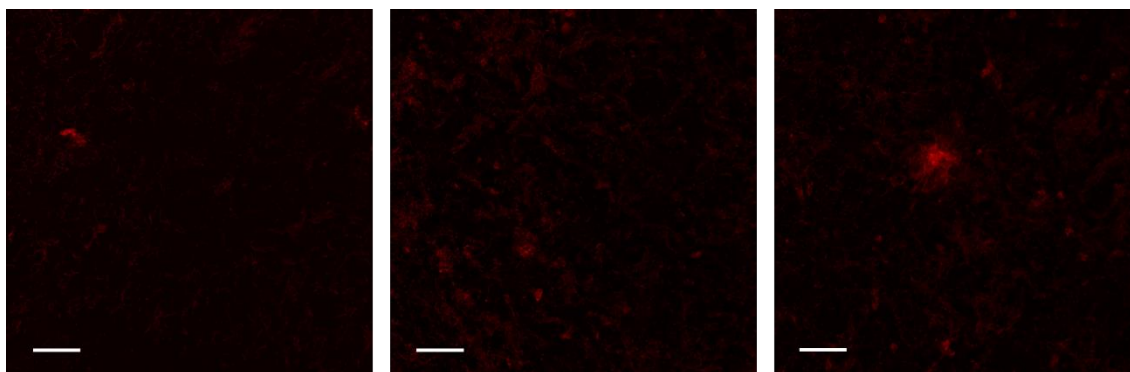


Figure 4.29: Maximum projection images of propidium iodide stained 24h flow system biofilms formed on polycarbonate coupon surface by *E. coli* MG1655 ompR234 PRO Δ csgA :: PFF753CcsgASau with induction with 200 ng mL⁻¹ aTC (scale bar represents 50 μ m).

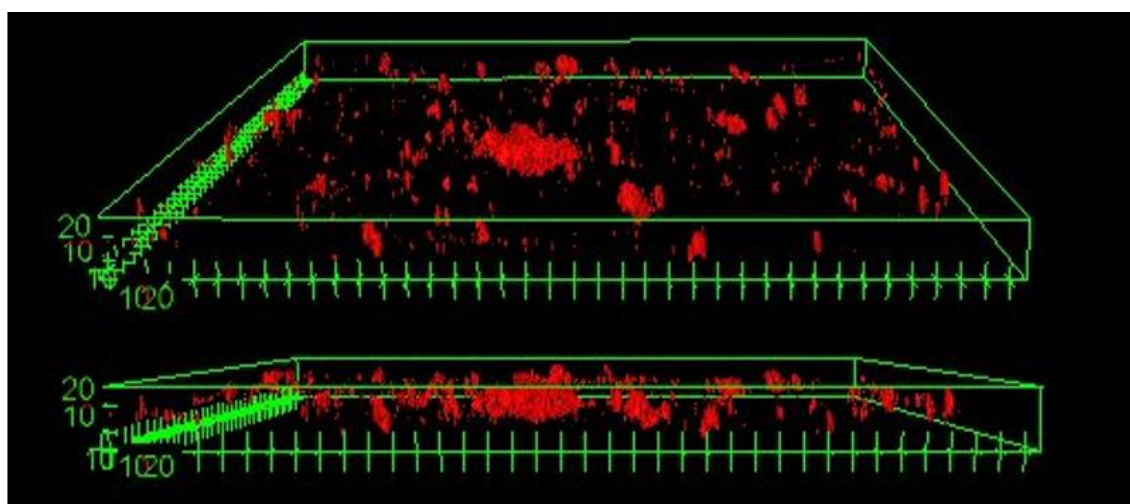


Figure 4.30: 3D projection image of PI stained 24h flow system biofilm formed on polycarbonate coupon surface by *E. coli* MG1655 ompR234 PRO Δ csgA :: PFF753CcsgASau with induction with aTC (tick marks represent 10 μ m).

PI staining of the PC coupons from the bioreactor containing an *E. coli* MG1655 ompR234 PRO Δ csgA :: PFF753CcsgASau (expressing the CsgA protein with a C-terminal SrtA tag) culture with aTC (200 ng mL⁻¹) induction showed a low level of luminescence from PI indicating a low (dead) cellular volume at the PC coupon surface. This indicates a reduced cellular surface coverage in comparison to the biofilm produced by induced *E. coli* MG1655 ompR234 PRO Δ csgA :: PFF753CcsgA (without the C-terminal SrtA tag) indicative of an aberrant effect upon the C-terminal inclusion of the -LPYTGG sequence on biofilm formation.

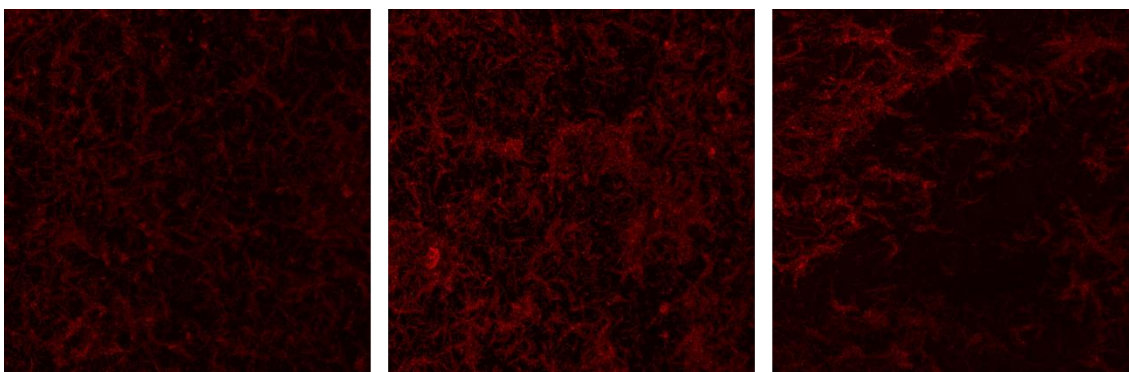


Figure 4.31: Maximum projection images of propidium iodide stained 24h flow system biofilms formed on polycarbonate coupon surface by *E. coli* MG1655 ompR234 PRO Δ csgA :: PFF753CcsgASauGGS with induction with 200 ng mL^{-1} aTC (scale bar represents $50 \mu\text{m}$).

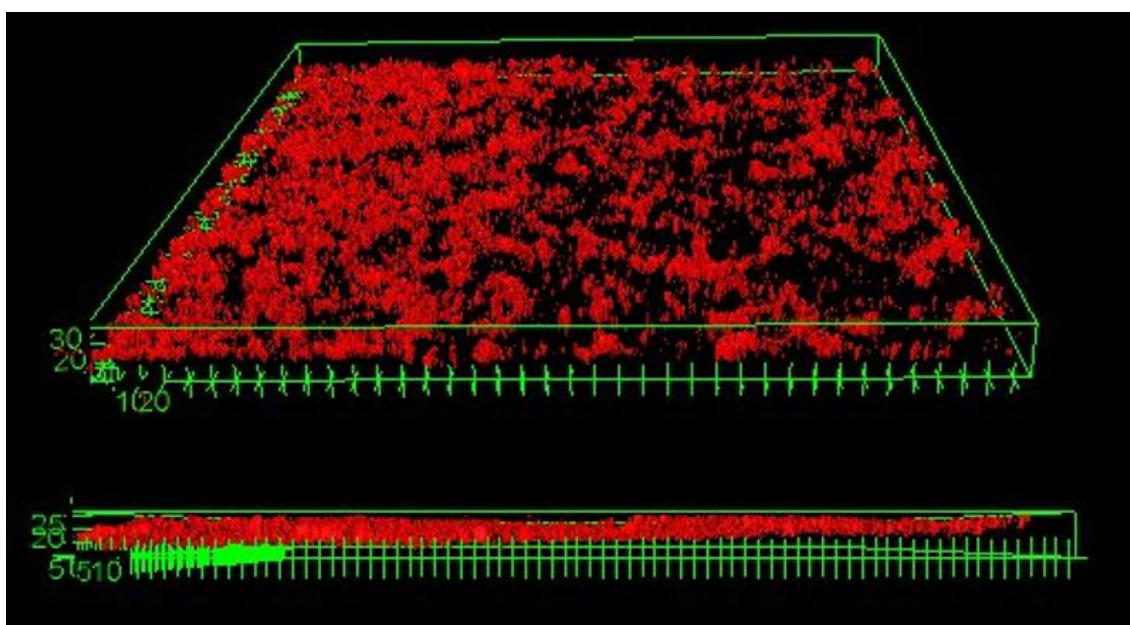


Figure 4.32: 3D projection image of PI stained 24h flow system biofilm formed on polycarbonate coupon surface by *E. coli* MG1655 ompR234 PRO Δ csgA :: PFF753CcsgASauGGS with induction with aTC (tick marks on top image represent $10 \mu\text{m}$, bottom image $5 \mu\text{m}$).

PI staining of the PC coupons from the bioreactor containing an *E. coli* MG1655 ompR234 PRO Δ csgA :: PFF753CcsgASauGGS (expressing the CsgA protein containing the C-terminal SrtA tag mediated by a flexible GGS linker region) culture with aTC (200 ng mL^{-1}) induction showed a moderate level of luminescence from PI indicating a moderate (dead) cellular volume at the PC coupon surface. A notable increase in biofilm surface coverage was observed in comparison to biofilms formed by *E. coli*

MG1655 ompR234 PRO Δ csgA :: PFF753CcsgASau (without the mediating flexible GGS linker). Biofilm formation was not however formed to a comparable extent observed for *E. coli* MG1655 ompR234 PRO Δ csgA :: PFF753CcsgA (without any C-terminal modification).

The confocal fluorescence micrographs appear to show inhibition of biofilm formation by the C-terminal -LPYTGG linker on the engineered CsgA protein expressed by PFF753CcsgASau. Some level of restoration in biofilm formation capability appears to occur where a flexible -GGS- linker region between the C-terminus of the wild-type CsgA protein and the -LPYTGG tag.

4.2.5.2. COMSTAT 2 quantification of biofilm properties

COMSTAT analysis of 24h flow biofilms formed by *E. coli* MG1655 ompR234 PRO Δ csgA :: PFF753CcsgASau (herein described as the SrtA tag condition), MG1655 ompR234 PRO Δ csgA :: PFF753CcsgASauGGS (herein described as the SrtA tag with linker condition) following induction 200 ng mL⁻¹ of aTC was performed as per the same parameters described in section 4.2.3. Data for COMSTAT analysis of biofilms formed by MG1655 ompR234 PRO Δ csgA :: PFF753CcsgA as discussed in section 4.2.4. is included here for comparative purposes (herein described as the no tag condition). Mean values of biomass, average thickness, surface roughness, surface area and surface area to biovolume ratio are described in Table 4.6 and presented as bar charts in Figure 4.33 (with error bars representing minimum and maximum experimentally obtained values).

Table 4.6: COMSTAT evaluation of biofilms produced by *E. coli* strains over 24h in a static culture.

Condition	Biomass / $\mu\text{m}^3\mu\text{m}^{-2}$	Average Thickness of biomass / μm	Average Thickness of entire area / μm	Surface roughness (R*)	Surface area / cm^2	Surface area to biovolume ratio / $\mu\text{m}^2\mu\text{m}^{-3}$
No tag	7.37	23.97	20.94	0.31	2.64	2.45
Srt A tag	0.79	19.05	3.34	1.65	0.51	4.53
Srt A tag with linker	3.67	29.61	19.40	0.71	1.89	3.46

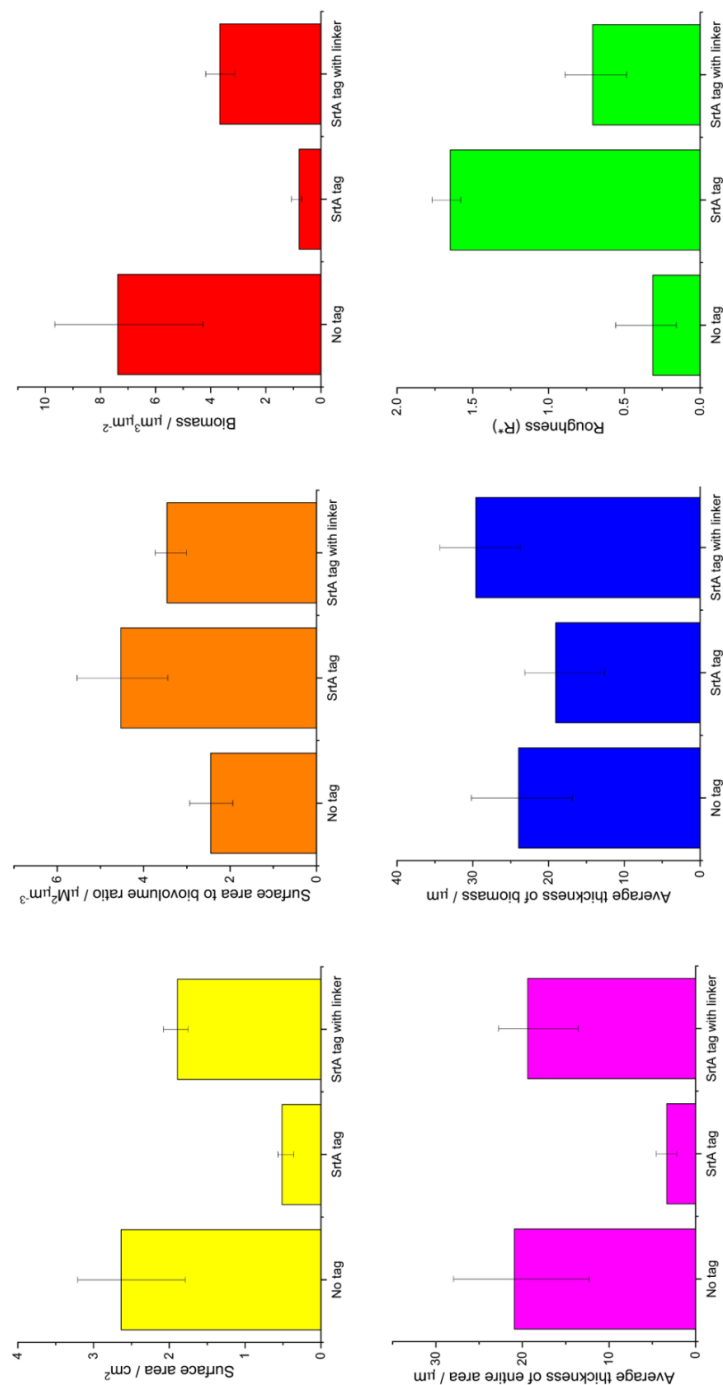


Figure 4.33: COMSTAT analysis results from 24h flow biofilms with no c-terminal tag, with a C-terminal SrtA tag and a C-terminal SrtA tag with a mediating flexible GGS linker region describing biofilm biomass (red bars), average thickness of biomass (blue bars), average thickness in entire area (magenta bars), surface roughness (green bars), surface area (yellow bars) and surface area to biovolume ratio (orange bars).

In confirmation with observations from the confocal fluorescence Z-image series (section 4.2.5.1), quantification of biofilm biomass, surface area, average thickness and surface roughness appear to represent the abrogation of biofilm formation following the inclusion of the C-terminal SrtA tag on expressed CsgA, which is partially mitigated by the inclusion of a mediating flexible GGS linker region between the CsgA protein and the SrtA tag.

Biofilm biomass, surface area, roughness and thickness of the SrtA tag condition appeared to be reminiscent of that of the non aTC induced biofilm formed by E. coli MG1655 ompR234 PRO Δ csgA :: PFF753C in the same conditions as described in section 4.2.4. Upon the introduction of the mediating GGS linker region, biofilm formation appears partially reestablished under the same conditions, with biofilm biomass, surface area and roughness appearing to be intermediary to the non-tagged and SrtA tagged CsgA mediated biofilms. Interestingly the average thickness of biofilm biomass appears to be increased when comparing the biofilm mediated by non-tagged CsgA and the tagged with linker CsgA, although significant overlap in the error bars of this measurement could indicate a lack of significance in this observation.

4.2.5.3. Statistical verification of COMSTAT quantification

One-way anova statistical analysis of data was performed to verify whether differences in mean metrics collected from COMSTAT analysis are statistically significant. Parameters required for the One-way anova test are as described in section 4.2.3.3 with the key requirement of all data to be normally distributed.

Normality was tested by Shapiro-Wilk analysis, which showed all data was sufficiently normally distributed (i.e. returned a significance value of over 0.05) for one-way anova analysis apart from where surface area to biovolume ratio was evaluated for the SrtA tag with linker condition. Normality analysis and box and stem plots showing distribution of data are given in the appendix of this thesis.

One-way anova verification (Table 4.7) shows that all metrics, other than average thickness in biomass, return statistically different mean values (significance value >0.05), and therefore all conditions are significantly different from each other.

Table 4.7: Critical values from one-way ANOVA analysis of data described in Table 4.6 and Figure 4.33.

Metric	F	Sig.
Average thickness in entire area	10.658	0.002
Average thickness in biomass	6.5515	0.012
Biomass	35.936	0.000
Roughness (R*)	2.347	0.000
Surface area	5.819	0.000
Surface area to biovolume ratio	27.765	0.010

Post-hoc Tukey-Kramer analysis (as outlined in section 4.2.3.3) of the one-way ANOVA test described a dataset whereby several groupings of datasets are statistically inseparable (Table 4.8). Biofilm biomass, surface roughness and surface area describe three sets of statistically distinct results where the no tag, SrtA tag and SrtA tag with linker conditions are distinct. The average thickness in biomass was identified by the one-way ANOVA to contain statistically inseparable means, grouping the n tag and SrtA tag conditions and the not tag and SrtA tag with linker conditions, again proof of the similar biomass thicknesses of biofilms produced across all *E. coli* described in this chapter. The no tag and SrtA tag with linker conditions appear to produce biofilms with indistinguishable average thicknesses over the entire area and surface area to biofilm ratios.

Table 4.8: Groupings from post-hoc Tukey-Kramer analysis of the no tag, SrtA tag and SrtA tag with linker conditions.

	Group A (Sig.)	Group B (Sig.)	Group C (Sig.)
Average thickness in entire area	SrtA tag (1.000)	No tag, SrtA tag with linker (0.624)	-
Average thickness in biomass	No tag, SrtA tag (0.248)	No tag, SrtA tag with linker (0.175)	-
Biomass	No tag (1.000)	SrtA tag (1.000)	SrtA tag with linker (1.000)
Roughness (R*)	No tag (1.000)	SrtA tag (1.000)	SrtA tag with linker (1.000)
Surface area	No tag (1.000)	SrtA tag (1.000)	SrtA tag with linker (1.000)
Surface area to biovolume ratio	SrtA tag (1.000)	No tag, SrtA tag with linker (0.173)	

4.2.5.4. Significance of results of 24h flow biofilms produced by *E. coli* producing engineered mutants of CsgA incorporating the SrtA tag

Confocal fluorescence microscopy appeared to show a very sparse biofilm cellular coverage of the polycarbonate coupon for biofilms produced by *E. coli* MG1655 ompR234 PRO Δ csgA :: PFF753CSau (expressing the engineered SrtA tagged CsgA). This was confirmed by statistically verified COMSTAT quantification, which demonstrated that for all measured parameters aside from average biomass thickness, a significant decrease in biofilm formation occurred over 24 hours in flow.

Biofilm formation was shown to be partially re-established, through the incorporation of a mediating flexible glycine-glycine-serine (GGS) linker region between the C-terminal SrtA tag and the CsgA protein (produced by PFF753CSauGGS). This was confirmed by confocal fluorescence microscopy and statistically verified COMSTAT

quantification, identifying a significant increase in biofilm formation supported by all measured parameters aside from average biomass thickness.

The impairment and partial reestablishment of biofilm formation upon the C-terminal modification of CsgA is indicative of reduced (and then ameliorated) amyloid aggregation ability of the engineered CsgA proteins CsgASau and CsgASauGGS, owing to their identified essential contribution to biofilm development (outlined in sections 4.2.3 and 4.2.4). Aligning the sequences to represent the semi-repeating unit structure of the β -barrel of CsgA computed by Tien et al.¹⁷¹ (outlined in Section 4.1.4) showing series repeating β -strands R1-R5 could suggest why the LPYTGG tag on the protein CsgASau affects amyloid aggregation, and why the GGS linker in CsgASauGGS partially re-established amyloid aggregation. The LPYTGG sequence aligns with the last 3-4 residues, part of the loop region joining the respective β -strands. This β -barrel structure likely resembles the amyloid folding in the aggregated protein. Through affecting the supramolecular interactions necessary in holding the amyloid folding together and significantly altering the conformation of monomeric CsgA, the LPYTGG sequence likely inhibits amyloidogenesis by the protein, which therefore affects biofilm formation. Through incorporating the flexible (and mostly benign in terms of supramolecular interactions) GGS linker region, the LPYTGG sequence is no longer aligned with the other repeating units. This would therefore promote CsgA amyloidogenesis to a greater extent, further supporting biofilm formation.

```

CsgA
GVVPQYGGGGNQGGGGNNSGPNSELNIYQYGGGNSALALQTDARN      R1
                  SDLTITQHGGGNGADVQGSDD                 R2
                  SSIDLTRGRFGNSATLDQWNGKN              R3
                  SEMTVKQFGGGNGAAVDQTASN                R4
                  SSVNVTQVGFGNATAHQY                    R5

CsgASau
GVVPQYGGGGNQGGGGNNSGPNSELNIYQYGGGNSALALQTDARN      R1
                  SDLTITQHGGGNGADVQGSDD                 R2
                  SSIDLTRGRFGNSATLDQWNGKN              R3
                  SEMTVKQFGGGNGAAVDQTASN                R4
                  SSVNVTQVGFGNATAHQYLPYTGG             R5

CsgASauGGS
GVVPQYGGGGNQGGGGNNSGPNSELNIYQYGGGNSALALQTDARN      R1
                  SDLTITQHGGGNGADVQGSDD                 R2
                  SSIDLTRGRFGNSATLDQWNGKN              R3
                  SEMTVKQFGGGNGAAVDQTASN                R4
                  SSVNVTQVGFGNATAHQYGGSLPYTGG         R5

```

Figure 4.34: Structural alignments of proteins CsgA, CsgASau and CsgASauGGS in line with the calculated β -barrel structure identified by Tian et al.¹⁷¹

4.3. Chapter conclusion

Results detailed in this chapter describe a system whereby biofilm formation is effectively controlled in *E. coli* MG1655 ompR234 Δ csgA :: PFF753CcsgA. Initial SEM results show the formation of large-scale networks of individual *E. coli* cells, connected by an extracellular substance ascribed to the formation of curli containing ECM.

72h static incubation from 400 mL of liquid *E. coli* MG1655 ompR234 Δ csgA :: PFF753CcsgA culture shows that the presence of plasmid PFF753CcsgA results in biofilms of similar morphology to the curli positive control *E. coli* W3110. Without plasmid PFF753CcsgA, *E. coli* MG1655 ompR234 Δ csgA does not produce significant quantities of biofilm, in agreement with the curli negative control strain *E. coli* BL21-DE3. These results are supported by extensive imaging analysis of biofilms whose (dead) cellular component is stained by propidium iodide, and quantification of images produced by COMSTAT 2 analysis. Statistical verification identified that measurement of biofilm biomass, surface area and average thickness (over entire area) result in two groupings of statistically identical values: curli negative (BL21-DE3 and *E. coli* MG1655 ompR234 Δ csgA) and curli positive (*E. coli* MG1655 ompR234 Δ csgA :: PFF753CcsgA +aTC, *E. coli* MG1655 ompR234 Δ csgA :: PFF753CcsgA -aTC and *E. coli* W3110). These results indicate that a potential basal level of CsgA production through a 'leaky' promoter controlling expression of the *csgA* gene, combined with the extended time allowed for biofilm production, result in biofilm formation independent of aTC induction of the *csgA* gene.

Through altering the incubation time and introducing media flow-through (24h flow experiments), we elucidate a very well controlled mechanism whereby biofilm development is mediated through induced expression of *csgA*. Biofilms produced by induced cell populations of *E. coli* MG1655 ompR234 Δ csgA :: PFF753CcsgA in a 5L flow experiment over 24h are thicker, denser and more mature than their uninduced counterparts. Again, results were supported by imaging analysis and quantification thereof. Results were statistically verified. This suggests that where basal level of *csgA* expression allows for biofilm development over 72h in a static culture, extensive biofilm development over 24h in a media flow environment is reliant on extensive *csgA* expression, induced by aTC.

It is likely that where over 72h in a static culture vessel, any small volume of curli or other potential extracellular adhesins allow for the initial phase of biofilm development. From this attachment, the longer incubation time would allow for biofilm development to 'catch-up' to that of the induced condition. This is not possible in the 24h flow condition,

where the sheer forces induced by media flow and the shorted incubation time do not allow for extensive biofilm development over the course of the experiment.

Following methodology development, the effect of incorporating a C-terminal SrtA tag on the CsgA protein (produced by PFF753CsgASau) and CsgA containing a C-terminal SrtA tag mediated by a flexible GGS linker sequence on biofilm formation was investigated. The incorporation of the SrtA tag appeared to abrogate biofilm formation, as evidenced by confocal fluorescence microscopy and COMSTAT quantification thereof. Biofilm formation was partially reinstated where the flexible GGS linker was incorporated. This is likely due to the effect of the LPYTGG sequence on the conformation of the monomeric CsgA protein, affecting the ability of CsgA to aggregate towards amyloid structures.

4.4. Experimental

Unless otherwise stated, antibiotic supplementation of media or agar was used with the concentrations described in Table 4.9

Table 4.9: Antibiotic concentrations used.

Antibiotic	Concentration / mg L ⁻¹
Kanamycin	50
Ampicillin	100

4.4.1. Plasmid constructs used in this study

4.4.1.1. Design of PFF753csgA(proto)

The starting plasmid, PFF753csgA(proto) was designed computationally using *snappene* (R) software. Promoter sequences, genes carrying antibiotic resistance, GFP and terminators were obtained from the *igem* database. Sequence of the *csgA* gene was obtained from Chen et al 2014¹⁸¹, Sortase A sequence obtained from plasmid pET30bSausrt(7M) (Chen et al 2011)²⁰⁷. Plasmid was sequenced through solid phase nucleotide synthesis by ThermoFisher Geneart (TM) and supplied as dehydrated nucleotide. To verify sequence, whole plasmid sequencing by ThermoFisher, as well as sequencing aiming to look at the *csgA* gene and the sortase gene was performed by us. Both confirmed the production of PFF753csgA(proto).

4.4.1.2. PFF753BcsgA(proto)

Due to an error in design, plasmid PFF753csgA(proto) was altered through site directed mutagenesis to correct the too large gap between the RBS and initial methionine codon of *csgA*, using primers PFF753RBSFIX (forward and reverse), using standard conditions described in section 3.4.4. 5 µL of the PCR product was transformed into *E. coli* XL1-Blue. Following selection and picking of colonies, plasmid DNA was isolated by miniprep prior to initial inspection by PAGE. Sequencing confirmed the deletion mutation yielding plasmid PFF753BcsgA(proto).

4.4.1.3. PFF753CCsgA(proto)

Plasmid PFF753B(proto) (supplementary info) was later found to contain an error in design, pertaining to the gap between ribosome binding site and gene start codon (ATG) (Figure 9), which includes an in-frame sequence prior to the 3' end of the *csgA* gene. This would produce a protein upon expression with a NSLWITSPF sequence

appended to the N-terminus of the protein. The N-terminal region of the CsgA protein is critical for the proper export of the protein from the cell, containing a Nsec and N22 regions responsible for the direction to the CSM and correct attachment to CsgE and G for transport through the membrane (respectively). Primers were designed to produce a circular PCR product containing a deletion of the MSLWITSPF region at the 3' end of the *csgA* gene using PFFNSecRepair (FWD and REV). Following PCR mutagenesis performed as described in section 3.4.4, the mixture was treated with 1 μ L of DpnI enzyme to destroy methylated template DNA for 1 h at 37 °C. Transformation with 2 μ L of the PCR mixture into prepared supercompetent *E. coli* XL1-blue cells. Plasmid isolation by miniprep from an overnight culture from a single colony, produced the isolated plasmid PFF753CcsG, which was inspected by poly agarose gel electrophoresis. Sequencing confirmed the deletion product PFF753CcsG was produced.

4.4.1.4. PFF753CcsG and PFF753CcsGASau

Plasmids PFF753CcsG and PFF753CcsGASau, were produced through SDM alteration of PFF753CcsG(proto), to yield genes encoding for respective C-terminal sortase tag fusion proteins of CsgA. PFF753CcsG was also produced, deleting the C-terminal LPYTG sequence. Primers were designed to either add an extra 5' glycine codon (plasmid PFF753CcsGASau, primers ADSDM1 and ADSDM2) or delete the LPYTG sequence entirely (plasmid PFF753CcsG, primers ADSDM5 and ADSDM6). Following PCR mutagenesis performed as described in section 4.4.4.2, the mixture was treated with 1 μ L of DpnI enzyme to destroy methylated template DNA for 1 h at 37 °C. Transformation (protocol outlined in section 4.4.4.3 with 2 μ L of the PCR mixture into prepared supercompetent *E. coli* XL1-blue cells, followed by plasmid isolation by miniprep, produced the isolated plasmids PFF753CcsG and PFF753CcsGASau, and which were inspected by poly agarose gel electrophoresis. Sequencing confirmed the desired products were produced.

4.4.1.5. PFF753CcsGASauGGS

Plasmid PFF753CcsGASauGGS was produced from PFF753CcsGASau through site directed mutagenesis by the protocol outlined in section 4.4.4.2 using primers ADSDM8 and ADSDM9. Following PCR Following PCR mutagenesis the mixture was treated with 1 μ L of DpnI enzyme to destroy methylated template DNA for 1 h at 37 °C. Transformation (protocol outlined in section 4.4.4.3 with 2 μ L of the PCR mixture into prepared supercompetent *E. coli* XL1-blue cells, followed by plasmid isolation by miniprep, produced the isolated plasmid PFF753CcsGASauGGS which was inspected

by poly agarose gel electrophoresis. Sequencing confirmed the desired products were produced.

4.4.2. *Escherichia coli* strains used in this study

The genotypes of *E. coli* strains used in this study are given in Table 4.10

Table 4.10: Overview of *E. coli* strains employed in study.

Strain	Genotype ^{42,43}
W3110	F- LAM- IN(rrnD-rrnE)1 rph-1
BL21-DE3	fhuA2 [lon] ompT gal (λ DE3) [dcm] Δ hsdS λ DE3 = λ sBamHIo Δ EcoRI-B int::(lacI::PlacUV5::T7 gene1) i21 Δ nin5
MG1655 ompR234 PRO Δ csgA	F- LAM- rph-1 ompR234 PRO Δ CsgA
MG1655 ompR234 PRO Δ csgA ::PFF753CCsgA	F- LAM- rph-1 ompR234 PRO Δ CsgA carrying plasmid PFF753CCsgA

4.4.2.1. MG1655 ompR234 PRO Δ csgA

Escherichia coli MG1655 ompR234 PRO Δ csgA was obtained as a gift from the laboratory of Timothy K. Lu as an agar stab. This was streaked onto a LB-agar plate supplemented with kanamycin and grown overnight at 37 °C. A single colony from this plate was picked, and grown overnight in LB media (10 mL) supplemented with kanamycin shaking at 250 rpm at 37 °C. The culture was split into 5 aliquots of 0.5 mL in sterile microcentrifuge tubes, and flash-frozen with liquid N₂ following the addition of 0.5 mL sterile 50% glycerol (v/v). As these glycerol stocks are from the same colony on the streaked plate, they were considered to be genetically identical and all suitable for use in preparation of chemically competent cell stocks for plasmid incorporation.

4.4.2.2. W3110

Escherichia coli W3110 was obtained from Yale University Coli Genetic Stock Centre (CSGC) as lyophilised bacteria deposited on a piece of filter paper. Full detail of how this sample was prepared can be found on the CSGC website:

<https://cgsc2.biology.yale.edu/FAQonProcs.php> (Feb 2019). The paper was placed in LB media (10 mL) and the culture grown overnight shaking at 250 rpm at 37 °C. The liquid culture was streaked out onto a LB-agar plate and grown overnight at 37 °C. A single colony was picked and grown in LB media (10 mL) overnight, shaking at 250 rpm at 37 °C. The culture was split into 5 aliquots of 0.5 mL in sterile microcentrifuge tubes, and flash-frozen with liquid N₂ following the addition of 0.5 mL sterile 50% glycerol (v/v). As these glycerol stocks are from the same colony on the streaked plate, they are genetically identical

4.4.2.3. BL21-DE3 RP codonplus

BL21-DE3 RP codonplus (Agilent technologies) was obtained from Dr Robert Mart (School of Chemistry, Cardiff University) as a gift, plated on LB agar and a single colony picked and grown with shaking 37 °C overnight. Glycerol stocks were then produced, and cultures produced from these when required.

4.4.2.4. XL-1 Blue

The cloning strain XL1-Blue (Agilent technologies™) was obtained as a glycerol stock from Dr Robert Mart (School of Chemistry, Cardiff university). Used only for DNA cloning, chemically competent stocks were produced through the method described in section X in order for plasmid transformation.

4.4.3. Control of curli biofilm formation by *Escherichia coli* with plasmid PFF753CcsgA

4.4.3.1. Growth of curli biofilm on polypropylene coupons in CDC bioreactor®

The bioreactor used in this study is the CDC bioreactor® (Figure 3.26) from biosurface technologies. In each use the full complement of 24 polypropylene coupons purchased from biosurface technologies were used.

Static biofilm culture method

The bioreactor containing the full complement of 24 polypropylene coupons was filled with 400 mL of low-salt LB media and sterilised by autoclave. A culture from a glycerol stock of the target strain was prepared in LB media and shaken overnight at 250 rpm at 37 °C. The cooled bioreactor was inoculated with the overnight culture, adding 4 mL of 0.1 OD culture to the media, ensuring to re-cover the inlet tube to avoid infection. Where the media was supplemented with the appropriate antibiotic, this was added as a filter sterilised solution prior to inoculation.

Biofilm growth was allowed to occur for the appropriate time before the apparatus was drained of liquid culture medium. The liquid culture was drained from the apparatus and coupons were removed from their rods in a category 2 safety cabinet to prevent contamination. Coupons were washed carefully in two successive petri dishes of sterile water, before being carefully dabbed dry and placed in a 24-well microtitre plate. 3 coupons were selected at random and swabbed tenfold with a dampened wooden swap, and each swab was streaked on LB-AGAR plates for gram-staining to determine the presence of contaminating microorganisms, which were grown at 37 °C overnight.

Following removal from the apparatus, coupons were fixed with a 4% formal saline (1 mL per well in microtitre plate) solution overnight at room temperature. Formal saline was then removed by pipetting and the coupons were washed with three 1 mL portions of sterile water, taking care to pipette gently so to not disturb the biofilm layer. Coupons were then dried under a laminar flow hood before being stored at 4 °C for analysis. Coupons were not stored longer than two weeks before analysis.

Flow biofilm culture method

The bioreactor containing the full complement of 24 coupons was sterilised by autoclaving, along with 5L of low-salt LB media in a vessel and tubing. Once cooled, the apparatus was set up according to Figure 4.35, where tubing connecting the bubble trap with the media container was passed through a peristaltic pump, and the bubble trap connected to the bioreactor. Media was flowed into the reactor at the maximum rate, until approximately 350 mL had filled the bioreactor. A culture from a glycerol stock of the target strain was prepared in LB media and shaken overnight at 250 rpm at 37 °C. The cooled bioreactor was inoculated with the overnight culture, adding 4 mL of 0.1 OD culture to the media, ensuring to re-cover the inlet tube to avoid infection. Where the media was supplemented with the appropriate antibiotic, this was added as a filter sterilised solution prior to inoculation.

Biofilm growth was allowed to occur for the appropriate time before the apparatus was drained of liquid culture medium. The liquid culture was drained from the apparatus and coupons were removed from their rods in a category 2 safety cabinet to prevent contamination. Coupons were washed carefully in two successive petri dishes of sterile water, before being carefully dabbed dry and placed in a 24-well microtitre plate. 3 coupons were selected at random and swabbed tenfold with a dampened wooden swap, and each swab was streaked on LB-AGAR plates for gram-staining to determine the presence of contaminating microorganisms, which were grown at 37 °C overnight.

Following removal from the apparatus, coupons were fixed with a 4% formal saline (1 mL per well in microtitre plate) solution overnight at room temperature. Formal saline was then removed by pipetting and the coupons were washed with three 1 mL portions of sterile water, taking care to pipette gently so to not disturb the biofilm layer. Coupons were then dried under a laminar flow hood before being stored at 4 °C for analysis. Coupons were not stored longer than two weeks before analysis.

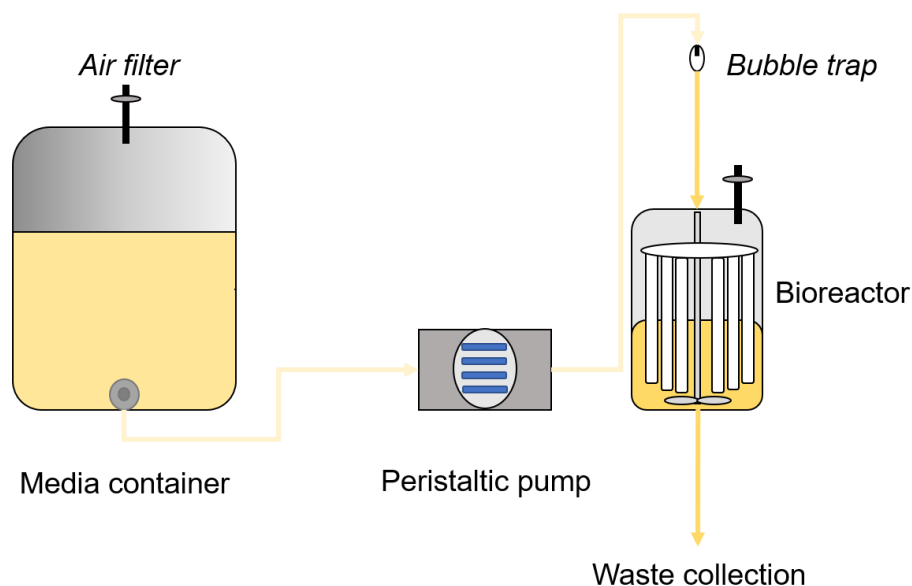


Figure 4.35: Diagram showing flow biofilm culture apparatus set up. Light yellow represents sterile media whilst darker yellow represents inoculum.

4.4.3.2. Confocal fluorescence microscopy

Confocal fluorescence microscopy was performed with a Leica SP5 confocal microscope, with all laser lines at 20% total power. Staining with 20 μ m propidium iodide was done immediately prior to loading the coupon for measurement. Sequential scanning was performed with the following settings:

- Emission of PI collected following excitation with 543 nm laser line at 60%, detecting emission between 600 and 700 nm, with a gain of 720 mV
- Reflection of the PC coupon surface collected following illumination with the 488 nm laser line at 20% detecting from 468-488 nm with a gain of 420 mV.

Data was processed without colour correction or other alteration, and Z-series images were cut off at the point where the reflection signal saturated the detector in the series, as to avoid any fluorescence from the plastic coupon being analysed as biofilm.

Z-stacks were then represented as both 3D representations and maximum projection images, as well as being evaluated by COMSTAT 2 analysis.

4.4.3.3. COMSTAT 2 analyses Z-series of the stained biofilm

In each 2D slice of a confocal Z-series, as with other digital images, the image is composed of many pixels (Picture Elements) which is the smallest square area which makes up the image. The size of the pixels depends on the resolution of the image, which in the case for this study is 1024x1024 pixels (1048576 total pixels), and remains constant provided the resolution is unchanged. This translates to each pixel representing a finite area in the XY plane of the confocal image acquired. For example, where a 2D slice represents a total of 150156.25 μm^2 , each pixel represents an area of 0.143 μm^2 . To convert this 2D information into imaging the whole 3D volume of a confocal z-series image, each slice is stacked on top of each other, and each pixel in a slice will have a pixel on top and below it (excluding the first and last slice in each series). From this we obtain voxels, a 3D pixel, where the X and Y lengths were the dimensions of the pixel from the 2D images and the Z length is the step height (distance between each slice). It is therefore critical throughout comparing data series to maintain a constant step-height, as to maintain the same voxel dimensions throughout the experiment.

Therefore, images obtained from the Leica SP5 confocal microscopy (with the 40x objective lens, where the 2D resolution of 1024x2014 pixels represented 150156.25 μm^2), where each z-series is obtained with a Z step height of 1 μm , would be comprised of voxels each with a volume of 0.143 μm^3 .

Thresholding

In order to process data, COMSTAT 2 requires voxels to contain binary information, i.e. each voxel is either 'on' (biofilm present in voxel) or 'off' (no biofilm present in voxel). Pixels in images obtained from CLSM (and by extension, voxels derived from them) are of variable intensity, depending on the intensity of luminescent emission at that point in space, and are therefore not binary.

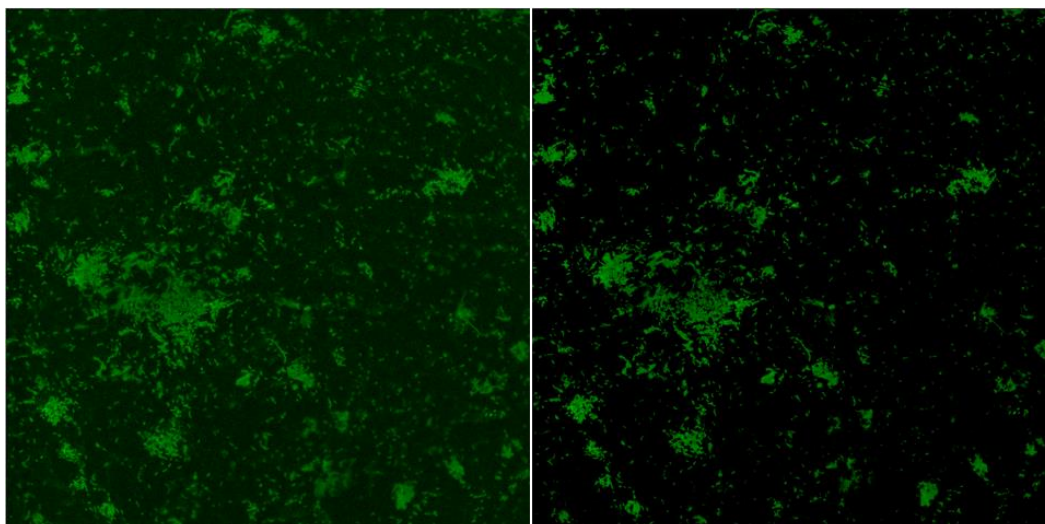


Figure 4.36: Example of thresholding in COMSTAT 2 of a single slice in a z-series image of a biofilm produced by *E. coli* (from this work). The uncorrected image (left) was subjected to thresholding with a value of 20 to produce the binary image (right).

To obtain binary pixel data, slices in a z-series image subjected to binary threshold filtering, where pixels above a threshold intensity are 'on' and those below the intensity are 'off' (Figure 4.36). In effect, this forces an intensity limit on each pixel in the dataset to either contain or not contain biofilm (represented by luminescent emission of the staining component). Applying thresholding to each slice in a z-series image yields a binary image suitable for COMSTAT 2 analysis.

To accurately compare results from COMSTAT 2 analysis of Z-series images across a dataset, both the z-step height when collecting the images and the thresholding value needs to be constant, otherwise individual Z-series images of biofilms will be quantified differently and incomparable.

Data produced from COMSTAT 2 analysis includes measurement of biofilm biomass, thickness, surface area (and surface area to volume ratio), dimensionless roughness coefficient (R^*).

Biomass is a measure of density of the biofilm. When biofilms are stained with propidium iodide (a dead cell stain), this value represents the (dead) cellular component of biomass of the biofilm. It is calculated by the number of voxels containing biofilm divided by the total area containing biofilm.

Average thickness measurements are conducted in two modalities:

- i) Average thickness over entire area. The average height of biofilm determined from voxel stacking in the Z-direction over the entire measured area.

- ii) Average thickness of biomass. The average height of biofilm determined from voxel stacking in the Z-direction over only areas in the XY plane displaying biofilm containing voxels

Surface area (and surface area to volume ratio) is calculated by counting all voxels in a series containing surface facing biofilm (i.e. is not completely surrounded by biofilm containing voxels on all sides).

Dimensionless roughness coefficient determines the variability in biofilm height through the following expression:

$$R^* = \frac{1}{N} \sum_{i=1}^N \frac{|L_{fi} - \overline{L_f}|}{\overline{L_f}}$$

where L_{fi} is the i 'th individual height measurement, $\overline{L_f}$ is the average thickness and N is the number of thickness measurements.

4.4.3.4. Scanning electron microscopy

Two *E. coli* MG1655 *ompR234 ΔcsgA* :: PFF753CcsG liquid cultures (10 mL) were prepared in LB media supplemented with ampicillin and kanamycin from an overnight culture grown from a glycerol stock, and shaken at 150 rpm at 37 °C until the OD₆₀₀ value reached 1.0 (approximately 6.5 h). Following this, aTC was added to a final concentration of 100 ng mL⁻¹, and cultures grown in the same conditions for a further 4 h.

Cells were diluted to an OD₆₀₀ value of 0.1 in 0.1 M sodium cacodylate buffer (pH 7.4) containing glutaraldehyde (XX % v/v) and incubated at room temperature without shaking over 2 h. Cell suspensions were then filtered through a 0.22 μm filter membrane under a moderate vacuum, taking care not to over-dry the filter membranes. To remove glutaraldehyde, membranes were then incubated in 0.1 M sodium cacodylate buffer (pH 7.4) for 5 minutes prior to a second round of filtration. Membranes were then dried through sequential solutions of ethanol in increasing concentration (starting at 50% up to 100% v/v in water) and incubated for 10 minutes in hexamethyldisilazane before being dried overnight in a vacuum desiccator. Samples were then sputter-coated with a gold/palladium mixture prior to being loaded into the TESCAN VEGA FEG SEM. Images were obtained at 15 keV.

4.4.4. General biochemical protocols

4.4.4.1. PCR with PrimeSTAR® HS DNA polymerase

Polymerase chain reactions (PCR's) performed in this report were undertaken using PrimeSTAR® HS DNA polymerase (Takara), supplied as a premix containing PrimeSTAR® HS DNA polymerase (1.25 units per 25 µL), PrimeSTAR buffer including Mg²⁺ (2 mM) and dNTP's (0.4 mM) with the components listed in Table 4.11.

Table 4.11: Composition of PCR mixture employed in this project.

Component	Amount / µL
PrimeSTAR® premix	25
Template DNA (25 – 100 ng µL ⁻¹)	1
Forward primer (10 µm)	1
Reverse primer (10 µm)	1
Water	22

Thermocycling conditions (Table 4.12) of the PCR reaction invariably involved a three-step heating protocol for 30 cycles (from Takara primeSTAR information manual), with alterations on extension time to compensate for the length of the copied section of DNA and occasionally altering annealing temperatures depending on primer properties.

Table 4.12: Thermocycling conditions used for PCR reactions in this study

Step	Temperature	Time	Number of cycles
Initial denaturation	95°C	60	1
Denaturation Annealing Extension	95°C 62°C 72°C	30 5 60 per kb	30
Final extension	72°C	5 minutes	1
Final Hold	4°C	indefinite	

4.4.4.2. Site directed mutagenesis

Site directed was performed using identical PCR conditions described in section 3.4.4.1, using partially overlapping primer pairs (Table 4.13) designed to either incorporate an insertion, deletion or mutation (Figure 4.36), first described by Liu and Naismith et al. Semi-overlapping primers allow the produced PCR product to be

circularised, removing the need for ligation following the procedure. To avoid primer heterodimer formation, the melting temperature (T_m) of the non-overlapping region was designed to be between 10-15 °C higher than that of the overlapping region.

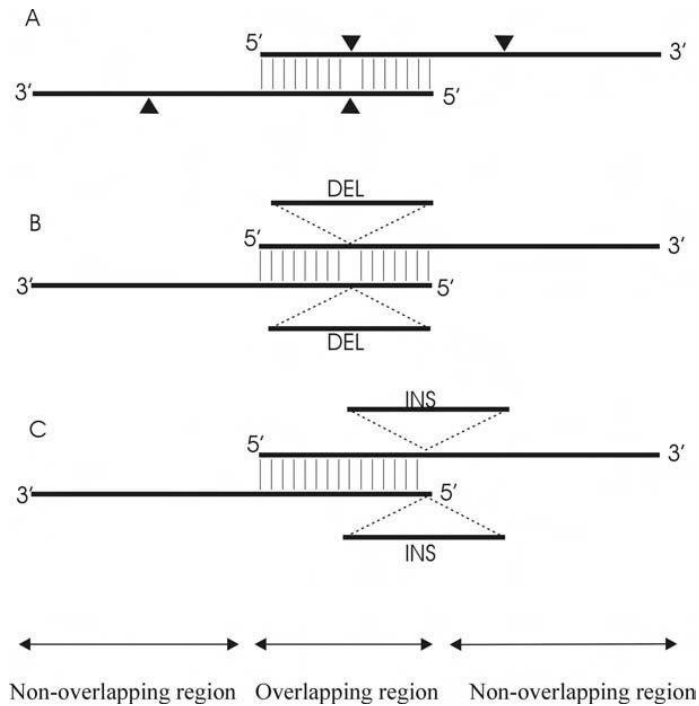


Figure 4.37: Design of semi-overlapping primers (solid black line) for point (A), mutations represented by black wedges), deletion (B) and insertion (C) mutations of a template plasmid. Figure adapted from Naismith et al. ²⁰⁵

Table 4.13: Primers employed in this study.

Name	Sequence	Use
PFF753RBSFIXfwd	CATGCGGTACCTTGTCCCCT CTTTCTCTAGAATGCAGGTCA GTG	Deletion mutation to remove extraneous sequence between RBS and csgA gene
PFF753RBSFIXRev	GGACAAGGTACCGCATGAAG CTGCTGAAAGTTGCAGCAATT G	Deletion mutation to remove extraneous sequence between RBS and csgA gene
PFFNsecrepairfwd	CAAAGTAGATGAAGCTGCTG AAAGTTGCAGCAATTGCAGC C	Remove MSLWITSPF in frame sequence at N-terminus of csgA gene
PFFNsecrepairrev	GCAGCTTCATCTAGTTTGTCC CCTCTTTCTCTAGAATGCAG	Remove MSLWITSPF in frame sequence at N-terminus of csgA gene
ADSDM1	GTCTCGATCCTTATCCACCG GTATACGGCAGATAC	FWD direction insertion of G at LPYTG terminus of csgA gene in PFF753C(proto)
ADSDM2	GGATAAGGATCGAGACGCGT TGGTACGCGTG	REV direction insertion of G at LPYTG terminus of csgA gene in PFF753C(proto)
ADSDM5	ATCCTTAATACTGATGTGCGG TTGCATTATTGCCAAAGC	REV direction deletion of entire LPYTG motif at Cterm of csgA gene in PFF753C(proto)
ADSDM6	GCACATCAGTATTAAGGATG GATCGAGACGCGTTGG	FWD direction deletion of entire LPYTG motif at Cterm of csgA gene in PFF753C(proto)
ADSDM7	GGTGGATCTCTGCCGTATAC CGGTGGATAAGGATCGAGAC GCGTTG	FWD direction insertion of GGS sequence between csgA gene and LPYTG sequence of PFF753CcsgASau
ADSDM8	CGGCAGAGATCCACCATACT GATGTGCGGTTGCATTATTGC CAAAGCCAACCTGG	FWD direction insertion of GGS sequence between csgA gene and LPYTG sequence of PFF753CcsgASau

4.4.4.3. Transformation of supercompetent *E. coli* cell stocks with plasmid DNA

The appropriate supercompetent *E. coli* cell stocks were thawed on ice. 1 μ l of isolated plasmid DNA to be transformed was added and mixed by pipetting and left to stand on ice for 30 minutes. Mixtures were then immersed in a water bath at 42 °C for 45 seconds exactly. Sterile LB (1 μ l) was then added and mixed by pipetting. Cell cultures were then grown by shaking at 150rpm at 37°C for 1 h. The cultures were then centrifuged at 4000rpm for 10 minutes, whereupon the majority of the supernatant was discarded. The pellet was then resuspended in the remaining medium and plated on LB-agar containing appropriate antibiotic and incubated at 37°C overnight.

4.4.4.4. Miniprep plasmid isolation

Overnight cultures in LB media supplemented with appropriate antibiotic (5-20 mL) of *E. coli* strains containing the desired plasmid DNA were grown at 37 °C, shaken at 150 rpm. The cultures were centrifuged at 4000 rpm for 15 minutes and supernatants discarded. The pellet was then resuspended in buffer P1 (250 μ L) by pipetting. The mixture was then transferred to a sterile microcentrifuge tube before buffer P2 (250 μ L) was added and the suspension mixed slowly with a pipette. Buffer N3 (350 μ L) was then added after no more than 5 minutes and mixed with a pipette until a homogenous suspension was obtained. This was then spun down at 13000 rpm for 10 minutes. The supernatant was then decanted into a QIAprep spin column and centrifuged at 13000rpm for 1 minute and the flow-through discarded. The spin column washed by adding 750 μ L of buffer PE which was then centrifuged at 13000 rpm for 1 minute, discarding flow-through. To remove traces of PE, the dry column was centrifuged for a further minute at 13000 rpm. The spin column was then transferred to a clean tube and 30 μ L of sterile deionised water was added and left to stand for 1-2 minutes. DNA was eluted from the column by centrifugation at 13000 rpm for 1 minute.

4.4.4.5. Preparation of glycerol stocks of *E. coli* strains

Overnight cultures (5 mL) of the desired *E. coli* strains (i.e. strains containing a desired plasmid) were grown in LB media overnight without antibiotic at 37 °C with shaking at 150 rpm. Cultures were divided into 0.5 mL aliquots in sterile microcentrifuge tubes followed by the addition of an equivolume of sterile 50% glycerol in water (v/v). The closed tubes were then flash frozen with liquid N₂, prior to storing indefinitely at -80 °C.

4.4.4.6. Poly agarose gel electrophoresis

The desired mass of agarose was suspended in TAE buffer to give the desired concentration of agarose (usually 1-2% v/v) which was then heated carefully in a domestic microwave until the agarose fully dissolved, whereupon safe-red DNA stain was added (5 μ L for a 100 mL gel). The solution was poured into a casting mould with the desired. DNA samples (5 μ L) were mixed with 10x fast digest green buffer (2 μ L) and loaded into the sample wells alongside a DNA marker. Electrophoresis was undertaken at a constant voltage (100 V) for 40 minutes. Images of the gel were obtained using ultraviolet illumination in a Syngene Bio Imaging Geneflash light box with a camera and printer attached.

4.4.5. Buffers and reagents

All buffers and solutions were in deionised H₂O unless specified

Qiagen Miniprep buffers

Buffer P1

Tris HCl (50 mM)
Ethylenediaminetetraacetate (10 mM)
RNase A (100 μ g / MI)
Adjusted to pH 8.0, stored at 2-5°C

Buffer P2

Sodium hydroxide (0.2 M)
Sodium dodecyl sulfate (1% w/v)

Buffer N3

Guanidinium hydrochloride (4 M)
Potassium acetate (0.5 M)
Adjusted to pH 4.2

Buffer PE

Sodium chloride (20 mM)
Tris HCl (2 mM)
Ethanol (80% w/v)
Adjusted to 7.5

SDS-PAGE Buffers

Resolving gel (14%)

Bis-acrylamide, 30% solution (4.5 mL)
Deionised H₂O (2.9 mL)
Resolving gel buffer (2.5 mL)
Ammonium persulfate (10%) (50 µL)
Tetramethylethylenediamine (10 µL)

Stacking gel (5%)

Bis-acrylamide, 30% solution (1.7 mL)
Deionised H₂O (5.7 mL)
Stacking gel buffer (2.5 mL)
Ammonium persulfate (10%) (50 µL)
Tetramethylethylenediamine (10 µL)

Resolving gel buffer

Tris base (1.5 M)
Sodium dodecyl sulfate solution (10% w/v)
Adjusted to pH 8.0

Stacking gel buffer

Tris base (0.5 M)
Sodium dodecyl sulfate DS solution (10% w/v)
Adjusted to pH 6.8

Running buffer

Tris base (250 mM)
Glycine (1.5 M)
Sodium dodecyl sulfate (35 mM)
Adjusted to pH 8.3

SDS sample buffer

Tris HCl (60 mM)
Sodium dodecyl sulfate (5% w/v)

Sucrose (10% w/v)
Glycerol (30% v/v)
 β -Mercaptoethanol (3% v/v)
Bromophenol blue (0.02 w/v)

Coomassie blue solution

Coomassie blue (0.25% w/v)
Methanol (45% v/v)
Acetic acid (9% v/v)

Agarose Gel buffers

TAE buffer

Tris base (40 mM)
Acetic acid (20 mM)
Ethylenediaminetetraacetate (2 mM)
Adjusted to pH 8.2

LB media

Tryptone (10 g/L)
Yeast extract. (5 g/L)
Sodium chloride (5 g/L)
Sterilised in containers through autoclaving at 120 °C for 120 min

Chapter 5. Development of luminescent naphthalimide conjugated Re(I) and Tc(I) complexes

5.1. Chapter aims

Building from the synthesis 4-amino-1,8-naphthalimide lumiphores bearing the terminal primary amine (**Nap-1**) for conjugation to ND, dipicolylamine based ligands (**L^x**, Figure 5.1) were developed for chelation of *fac*-tricarbonyl Re(I) and ^{99m}Tc(I) metals in the development of mitochondrial targeting bioimaging probes. These ligands once coordinated to the metal species with a *facial* grouped geometry with carbon monoxide co-ligands provide a linked fluorescent functionality through the 4-amino-1,8-naphthalimide to the metal complex. Coordination complexes of Re(I) and ^{99m}Tc(I) are well employed in bioimaging, with complexes of this type exhibiting advantageous characteristics (e.g. charge, lipophilicity and stability) towards both *in-vitro* and *in-vivo* application. In the development of several ligands with different linker moieties, the solubilities of the ligands in aqueous media can be tuned.

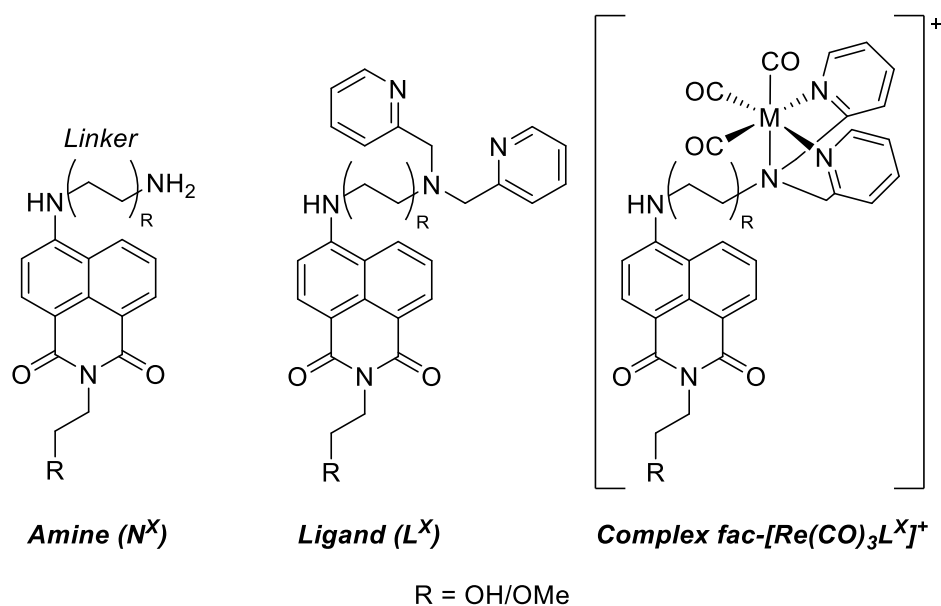
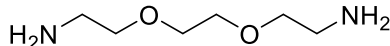
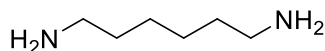
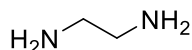
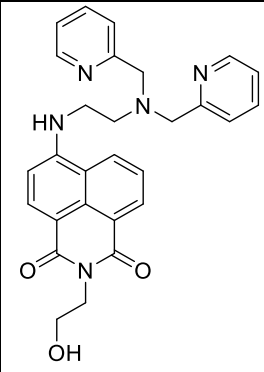
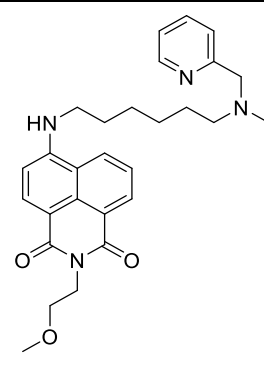
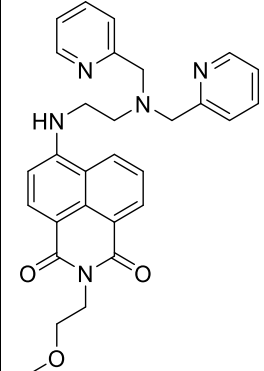
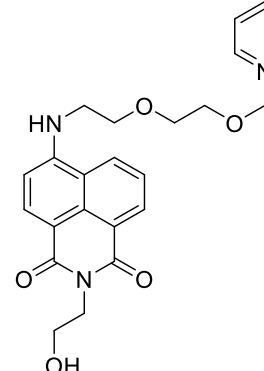
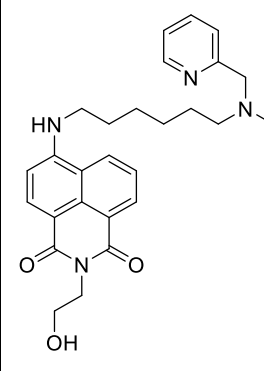
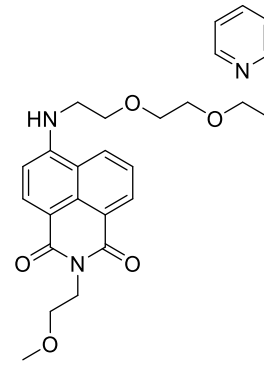
**Linkers:**

Figure 5.1: Structure development of ligands **L^x** for coordination to M = Re(I) and ^{99m}Tc(I) from amine terminated 4-amino-1,8-naphthalimides **N^x**.

Six novel ligands (**L¹-L⁶**, Table 5.1) were synthesised and coordinated to Re(I) (***fac*-[Re(CO)₃(L^x)⁺**) to probe their photophysical properties and solubility in a variety of

media. Ligand **L⁵** was consequently chosen for further study, owing to its optimal water solubility relevant to the ^{99m}Tc radiolabelling process (Discussed in section 5.2.4). Mitochondrial targeting and biodistribution characteristics of **L⁵** and **fac-[Re(CO)₃(L⁵)]BF₄** were evaluated through a variety of imaging methods. The analogous ^{99m}Tc complex, **fac-[^{99m}Tc(CO)₃(L⁵)]⁺** was synthesised in aqueous media by Juozas Domarkas et al (S.J. Archibald group, Positron Emission Tomography Research Centre and Department of Chemistry and Biochemistry, University of Hull). Mitochondrial targeting of **fac-[^{99m}Tc(CO)₃(L⁵)]⁺** was further established in *in-vitro* assessment, and stability in biological media as well as *In-vivo* distribution was assessed through radio-HPLC and SPECT-CT experiments respectively.

Table 5.1: Structures of ligands **L**₁-**L**₆.

Compound	Compound
 L ¹	 L ⁴
 L ²	 L ⁵
 L ³	 L ⁶

5.2. Introduction

5.2.1. General characteristics of an ideal bioimaging probe

The biological environment is extraordinarily diverse and complex, meaning a huge variety of factors to consider when designing biological probes. The effective function of a biological sensor or drug depends on a seemingly endless list of factors, including toxicity, solubility/lipophilicity, cell/membrane permeability and metabolic stability.²⁰⁸

5.2.1.1. Toxicity

In limiting the toxicity of a biological probe, one can reduce the impact of the respective probe on the imaged system, leading to an increasingly representative description of the probed environment. Of course, where *in-vivo* multicellular imaging is targeted, it is important to reduce potential harm to the patient/animal in the imaging process.

In-vitro cytotoxic effects can be attributed to a large number of causes including (but not limited to); DNA binding/intercalation (affecting replication/mutation, e.g. ethidium bromide)²⁰⁹, generation of reactive oxygen species (ROS, such as phototoxic rhenium-porphyrin species)²¹⁰, inhibition of enzymes critical to metabolic function (i.e. drug-drug interaction effects on cytochrome P450 and associated enzymes)²¹¹ and inhibition of protein synthesis apparatus (diphtheria toxin)²¹². Whilst toxicity/structure relationships are often complex and difficult to identify, several methods including the tetrazolium/formazan dye based MTT/MTS assays can evaluate general cytotoxic effects *in-vitro*, allowing for initial screening and evaluation of toxic effects on a cellular scale.

Routes to which an exogenous compound can exhibit toxicity *in-vivo* (i.e. on a multicellular level) are innumerable, depending on subject species, state of health and localisation of a compound within a living subject. In general screening of *in-vivo* toxic effects requires years of detailed, multispecies study, often a limiting factor in drug development.

5.2.1.2. Metabolic stability

Development of a metabolically stable biological probe is essential, as a rapidly degraded probe results in a shorted utilisable lifetime for data collection, as well as possible toxic effects arising from the degradation products. Screening of compound degradation in a variety of buffers (varying pH environments in different biological contexts) and sera by LC-MS analysis allows for comprehensive evaluation of compound

stabilities *in-vitro* and *in-vivo*. Photostability of luminescent species can be evaluated through continuous photocycling between the ground and excited states. In the context of inorganic chemistry, achieving both thermodynamically and kinetically inert metal coordination environments is ideal in the development of a metabolically stable metal-conjugate probe.

5.2.1.3. Permeability and solubility

A degree of water solubility is essential in administration of a biological probe in the predominantly aqueous intra- and extracellular environment. Solubility and permeability are interdependent, generally highly permeable compounds are increasingly insoluble and vice-versa, thus generally it is critical to strike a good balance between both factors to develop an optimal biological probe.²¹³ Several active (e.g. endocytosis) and passive (pore diffusion) uptake mechanisms can apply in terms of probe uptake into a cellular environment, depending on numerous chemical factors. Permeability relies on the probe in question being able to cross the phospholipid bilayer environment of biological membranes, with a (negatively) charged hydrophilic outer and hydrophobic (lipophilic) inner. Therefore, species charge and lipophilicity are critical factors.²¹³ Cationic species are commonly associated with increased permeability owing to opposing charge interactions with phospholipids at the exterior of the membrane bilayer.²¹⁴ Species with moderate lipophilicity often exhibit a good balance between cellular penetration/activity and solubility in aqueous media essential to administration. Lipophilicity (LogP/D) has been identified as a crucial parameter in the biodistribution and metabolism of organometallic compounds.²¹⁵ LogP/D values between 0 – 3 often provide a good balance between solubility and lipophilicity.²¹³

5.2.2. Re(I) and Tc(I) coordination complexes in bioimaging

Re(I) and Tc(I) coordination compounds have been applied in a variety of therapeutic and diagnostic functions. ^{99m}Tc exhibits particularly suitable radiological properties ($t_{1/2} = 6.01\text{ h}$, $\gamma = 142.7\text{ keV}$) for *in-vivo* bioimaging, achieving an optimal balance in effective imaging time and minimal radiotoxicity. No stable isotopes of Tc (I) exist, thus Re (I) is often employed as an analogue when designing ligand coordinate systems for Tc (I), owing to their similar coordination chemistry (d^6 valence shell electron configuration). Radionuclide isotopes of Re (I) are also relevant in this context (¹⁶⁸Re $t_{1/2} = 3.68\text{ d}$, $\beta = 1.07\text{ MeV}$, $\gamma = 137\text{ keV}$, ¹⁸⁸Re $t_{1/2} = 16.98\text{ h}$, $\beta = 2.12\text{ MeV}$, $\gamma = 155\text{ keV}$), and thus both Re(I) and ^{99m}Tc(I) analogues warrant investigation as biological probes.

5.2.2.1. Cationic $fac\text{-}\{M(\text{CO})_3\}$ based Re(I) and Tc(I) complexes utilised in bioimaging

Re (I)/ ^{99m}Tc (I) complexes utilised in this context are generally cationic ²¹⁶, and can be intrinsically luminescent (such as for the $fac\text{-}[M(\text{CO})_3(\text{N}^{\wedge}\text{N})\text{L}]^+$ complexes, $\text{N}^{\wedge}\text{N}$ = aromatic diimine, L = ancillary lewis base type ligand such as pyridyl derivative) or optically benign (such as for the $fac\text{-}[M(\text{CO})_3(\text{dipicolylamine})]^+$ complexes) (Figure 5.2). The cationic nature of these complexes imparts particular suitability towards mitochondrial imaging. ^{112,216,217}

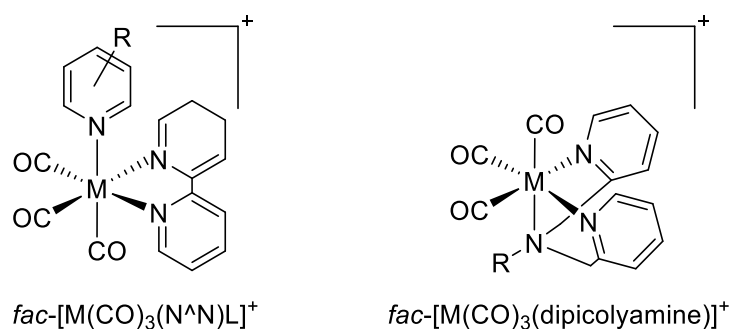


Figure 5.2: Examples of cationic $M = \text{Re(I)}/^{99m}\text{Tc(I)}$ complexes exhibiting $fac\text{-}\{M(\text{CO})_3\}$ geometry employed in bioimaging.

Luminescence of the $fac\text{-}[M(\text{CO})_3(\text{N}^{\wedge}\text{N})\text{L}]^+$ arises from absorption ($^1\text{MLCT}$) around 350-400 nm, ²¹⁸ intersystem crossing to and phosphorescent emission from the $^3\text{MLCT}$ excited state. Several examples of these luminescent Re(I)/ ^{99m}Tc (I) complexes utilising 2,2'-bipyridil and 1,10-phenanthroline ligands with a variety of ancillary ligands have been reported, whereby photophysical properties and biodistribution can be varied through varying $\text{N}^{\wedge}\text{N}$ and ancillary ligand identities, with strong evidence of mitochondrial localisation. ²¹⁶⁻²²⁰

The second mode of coordination of Re(I)/ ^{99m}Tc (I) (in $fac\text{-}[M(\text{CO})_3(\text{dipicolylamine})]^+$ complexes) which does not comport any significant intrinsic luminescence emission or MLCT absorption can be particularly useful in development of bimodal imaging agents, as a separate luminescent moiety (such as a 4-amino-1,8-naphthalimide derivative) can be attached *via* the tertiary amine site in the dipicolylamine chelate. Therefore, optical properties and radiological emission can be separated entirely, with the metal centre providing the whole-body SPECT-CT information (as well as imparting cellular penetration and biodistribution properties) independent of luminescence emission.

Preceding work by Langdon Jones et al where similar dipicolyl-4-amino-1,8-naphthalimide linked $fac\text{-}[\text{Re}(\text{CO})_3(\text{L}^*)]^+$ complexes (Figure 5.3) demonstrated the

promising *in-vitro* distribution towards mitochondria in human osteoarthritic, HepG2 (human liver cancer) and HeLa (human breast cancer) cells, particularly that of the complex detailed in figure 5.3, **ELJ-fac[Re(CO)₃(L²)]BF₄**. **ELJ-fac[Re(CO)₃(L²)]BF₄** exhibited excellent cellular uptake, and a level of concentration dependant organelle staining. At higher agent concentrations significant rapid mitochondrial membrane staining was observed (for human osteoarthritic cells, Figure 5.3). Imaging of the fish parasite *S. vortens*, including colocalization studies with tetramethylrhodamine ethyl ester (TMRE) provided further evidence of mitochondrial localisation.

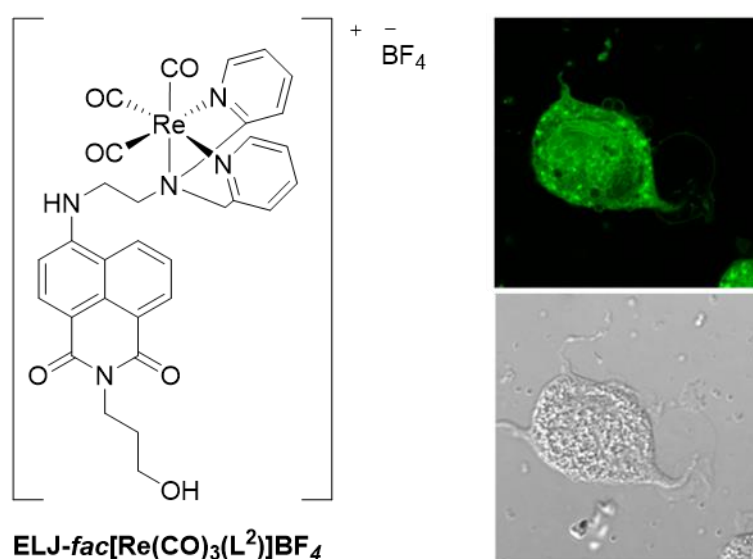


Figure 5.3: Left: structure of **ELJ-fac[Re(CO)₃(L²)]BF₄**, previously employed in *in-vitro* studies. Right: imaging of osteoarthritic cells undergoing apoptosis showing staining of mitochondrial membranes by **ELJ-fac[Re(CO)₃(L²)]BF₄** using fluorescence (top) from **ELJ-fac[Re(CO)₃(L²)]BF₄** ($\lambda_{\text{ex}} = 504 \text{ nm}$; $\lambda_{\text{em}} = 515 \text{ nm}$) and transmitted light (bottom).

Despite promising *in-vitro* imaging with **ELJ-fac[Re(CO)₃(L²)]BF₄**, the solubility of the respective ligand was highly limiting towards producing the analogous ^{99m}Tc complex through the method described by Alberto et al in PBS.²²¹ Through the utilisation of a more water-soluble analogue of these complexes, this study builds on this work and allows for radiolabelling in this manner to be achieved.

5.2.2.2. Other Re(I) and Tc(I) coordination modes utilised in bioimaging

Other coordination modes of Re(I)/Tc(I) utilised in bioimaging include the neutral dirhenium pyridazine and *fac*-[Re(CO)₃(N^N)Cl] complexes (Figure 5.4).^{222,223}

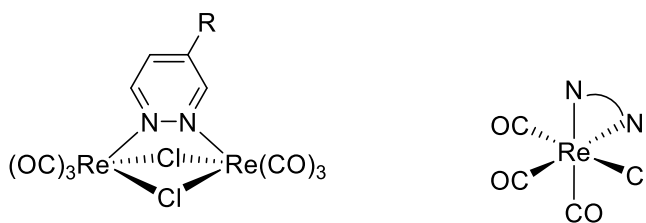


Figure 5.4: Neutral dirhenium pyridazine (left) and *fac*-[Re(CO)₃(N^N)Cl] luminescent complexes utilised in bioimaging.

Ferri *et al* described a series of dirhenium pyridazine di-chlorine bridged phosphorescent complexes. Absorption around 370-409 nm (1:1 MeCN:H₂O) arising from $d\pi(\text{Re})-\pi^*(\text{diazine})$ charge transfer (R = COOH/C₃H₆-COOH).²²² Interestingly, the presence of an alkyl spacer between the carboxylic acid 'R' group has an enormous impact on the emissive capabilities of the complexes, whereby a total lack of emission is seen where no linker is present. Triplet emission ($\tau_{\text{obs}} = 1600$ ns in deaerated solutions) occurs for the alkyl spaced complex around 610 nm in 1:1 MeCN:H₂O. Absorption characteristics are modulated upon the conjugation to peptide nucleic acids (PNA), inducing hypsochromic shifts in the CT absorption, however emission characteristics were not demonstrated. Mitochondrial localisation was not observed, instead general cytoplasmic and nuclear staining properties were observed upon staining of HEK-293 cells with 3 μM of the complex-PNA conjugates.²²²

Clède *et al.* demonstrated utilisation of *fac*-[Re(CO)₃(N^N)Cl] in the perinuclear staining of MDA-MB-231 cells.²²³ The described complexes utilising the pyta N^N ligand demonstrated absorption around 335 nm (in MeCN) arising from ¹MLCT absorption, with long-lived triplet emission around 500-530 nm. By modulating lipophilicity through incorporation of an alkyl chain off the pyta ligand, Clède *et al.* demonstrated the effect of increasing lipophilicity on cellular penetration. Again no evidence for mitochondrial localisation was observed.

5.2.3. Mitochondrial targeting in bioimaging

Mitochondrial targeting is a key aspect of evaluating biological function in bioimaging. One can create a parallel between mitochondria function and cell health due to the crucial role of mitochondria in producing ATP for energetic processes in cell metabolism. Additionally, rapid growth associated with malignant tumor development in cancers results in a reduced number and overall functionality of mitochondria in tumor cells, associated with a hypoxic and reducing environment.

As a result of this, mitochondrial targeting/accumulating probes in bioimaging are highly informative of cellular health and in distinguishing between normal and tumor-differentiated cells.

Several examples already detailed in this introduction of Re(I)/Tc(I) coordination compounds demonstrate mitochondrial localisation, and often cationic, ^{112,218,222} with the notable exception of the neutral *fac*-[Re(CO)₃(phen)L] (L=carboxylic acid derivative ancillary ligands) complexes described by Skiba *et al.* ²¹⁶

5.2.3.1. Mitochondrial membrane potential dependant uptake

Mitochondrial membrane potential (MMP) is the electronic potential across the impermeable inner mitochondrial membrane, around negative potential of around -150 mV to -170 mV in healthy cells. ²²⁴ Mitochondrial dysfunction results in disruption of the MMP ²²⁵, occurring upon apoptotic and necrotic cell death whereby depolarisation occurs ²²⁶ (therefore abrogating uptake of pyruvate and other compounds associated with oxidative respiration).

In developing luminescent (or otherwise detectable) probes whose localisation in mitochondria depend on MMP, one can evaluate cellular function through monitoring mitochondrial accumulation of said probe. In general cationic species are essential for MMP dependant mitochondrial uptake ^{224,227,228}. Phosphonium-based radiologically tagged lipophilic cations such as the ⁶⁴Cu labelled species (Zhou and Liu, 2011) ²²⁹ and dually ⁶⁴Cu/Rhodamine (luminescent) functionalised (Yan *et al.*) ²³⁰ have shown MMP dependant uptake, as well as increased tumor cell uptake owing to their mitochondrial accumulation.

A phosphonium BODIPY based, bright luminescent cationic species developed by Nigam *et al.* (2016) ²²⁷ demonstrated MMP dependant uptake into mitochondria as evidenced by colocalization studies. Depolarisation of the mitochondrial membrane achieved through treatment with CCCP caused decreases in uptake of a factor around 85%, further proving MMP dependence.

To date, MMP dependence on mitochondrial uptake of Re(I) and Tc(I) coordination compounds has not been demonstrated. The neutral *fac*-[Re(CO)₃(phen)L] produced by Skiba *et al.* showed no association between MMP and mitochondrial localisation. ²¹⁶

5.3. Results and discussion

5.3.1. Synthesis of ligands **L**¹-**L**⁶

The 4-amino-1,8-naphthalimide based ligands bearing dipicolylamine chelating units **L**¹-**L**⁶ were produced from 4-chloro-1,8-naphthalic anhydride in a 3 or 4 step synthesis (Figure 5.15).

The first synthetic step to produce **L**¹-**L**⁶ was identical, involving the nucleophilic (S_N2) substitution of the anhydride moiety of the starting material with either ethanolamine or the methyl protected version, 2-methoxyethylamine to give compounds **C**¹ and **C**². This was achieved in both cases in high (~80%) yield.

From **C**¹ and **C**², syntheses of the ligands diverged according to the linker length and identity employed. Ligand precursors **N**¹-**N**⁶ were produced through S_NAr substitution of the chloride on **C**¹ and **C**² with the mono-Boc protected diamine linker in DMSO and subsequent deprotection thereof (Method **A**). **N**¹ and **N**² exhibit an ethyl chain linker (using mono-Boc ethylene diamine) with the corresponding -OH (**N**¹) or -OMe (**N**²) termination at the other end of the naphthalimide species. **N**³ and **N**⁴ exhibit a hexyl chain linker (using 1,6-diaminohexane), again with the corresponding -OH (**N**³) and -OMe (**N**⁴) termination. Finally, **N**⁵ and **N**⁶ exhibit the diether-diethyl linker group (from mono-Boc 2,2'-(ethylenedioxy)bis(ethylamine)), also with the corresponding -OH (**N**⁵) and (-OMe) (**N**⁶) terminations. Ligand precursor (**N**⁵) is identical to the water-soluble naphthalimide employed in chapters 2 and 4, termed **Nap-1**. For clarity in the context of this chapter, this chemical species will be referred in this chapter only as **N**⁵.

The hexyl-chain linker naphthalimide ligand precursors **N**³ and **N**⁴ were synthesised in one step, affording the desired products with a 42-44% yield. The ethyl (**N**¹ and **N**²) and diether diethyl (**N**⁵ and **N**⁶) linker bearing precursors were synthesised in two steps, utilising the mono-BOC protected diamines to aid aqueous-workup. **N**⁵ and **N**⁶ required purification through silica gel column chromatography, due to the presence of an unidentified 4-amino-1,8-naphthalimide (identified from the bright fluorescent yellow colour of the spot on a TLC plate) impurity, possibly from substitution from the secondary Boc protected amine. Following deprotection in 50% TFA/DCM; **N**¹, **N**², **N**⁵ and **N**⁶ were isolated in moderate cumulative yields (27 – 36%), in all cases limited by the initial S_NAr step. The moderate yields obtained for ligand precursors **N**¹-**N**⁶ are likely due to the difficulty of extraction of the product from the high boiling point DMSO solvent, which was observed to result in a partial emulsion forming upon separation and extraction from the aqueous/DMSO phase to chloroform/DCM, in addition to incomplete formation of the product in the S_NAr reaction.

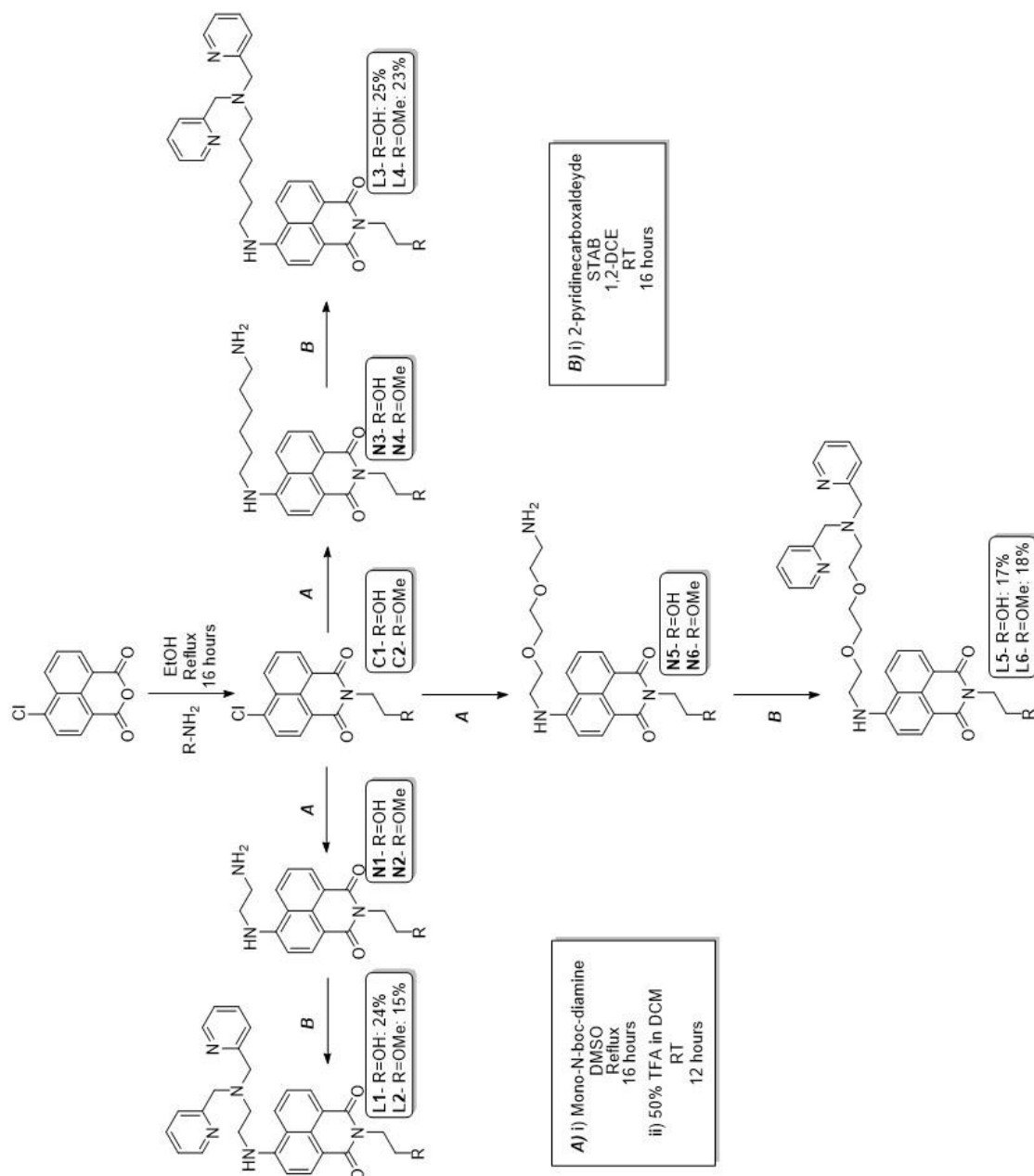


Figure 5.5: Synthetic routes to ligands **L¹-L⁶** from commercially available 4-chloro-1,8-naphthalic anhydride.

Ligands **L¹-L⁶** were synthesised from the deprotected amine ligand precursors **N¹-N⁶** (termed accordingly) *via* reductive amination with 2-pyridinecarboxaldehyde (2 equivalents respective of the amine precursor) using sodium tris-acetoxyborohydride (STAB, 2.5 equivalents respective of the amine precursor) in 1,2-DCE with ~4% triethylamine (ensuring deprotonation of any $\text{-NH}_3^+\text{TFA}^-$ salts from TFA deprotection). Reductive amination of **N¹-N⁶** proceeded with varied yields from 51% (**L₂**) to 95% (**L₃**).

Cumulative yields of ligands **L¹-L⁶** were between 15-25% with respect to the commercially available starting material (4-chloronaphthalic anhydride), which was

reasonable over the course of a 3-4 step synthesis. Sources of reduced yield likely lie primarily in the loss of product during purification following the S_NAr step, due to emulsification upon separation of the aqueous/DMSO mixture and chloroform/DCM.

5.3.2. Synthesis of rhenium complexes $fac-[Re(CO)_3(L^x)]BF_4$

Complexes $fac-[Re(CO)_3(L^x)]BF_4$ (respective of ligand identity) were produced from ligands L^1-L^6 through substitution of the facial orientated tricarbonyl triacetonitrile precursor, $[Re(CO)_3MeCN_3]^+$ (Figure 5.12). Substitution of the weakly coordinating acetonitrile ligands is promoted through thermodynamic stabilisation through chelation, and kinetic stabilisation of the *fac*-tricarbonyl coordination geometry.

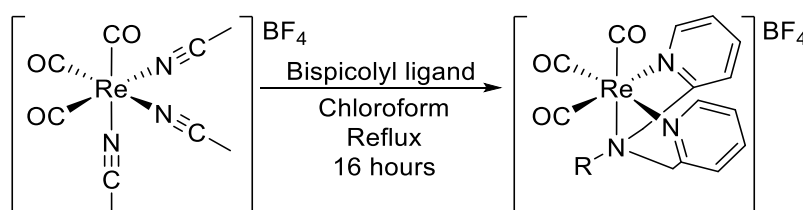


Figure 5.6: Chelation of rhenium by the dipicolylamine chelating units present in L^1-L^6 (R group represents linker and naphthalimide) through substitution of the labile acetonitrile ligands in the precursor.

Reaction conditions employed to produce the detailed complexes were identical: heating overnight at reflux in chloroform in the absence of light with silver tetrafluoroborate. In all cases, precipitation from a minimum solvent volume through the addition of hexane or ether yielded the isolated cationic *fac* tricarbonyl tridentate complexes as yellow or orange solids in moderate yields (around 20-30%). Precipitation of the coloured solids from the increasingly non-polar solvent system supports the production of the BF_4 salt, luminescent naphthalimide linked dipicolylamine complexes as the majority of the ligand precursors were isolated as oils.

The respective 1H NMR spectra (Example shown in Figure 5.7, detailed in section 5.4.10) provided unequivocal confirmation that the desired complexes were produced. 1H NMR spectra of complexes $fac-[Re(CO)_3(L^x)]BF_4$ exhibited extensive shifts in the aromatic region (respective of the ligand spectra) corresponding to the change in electronic environment following donation of electron density by the bispicolylamine nitrogen and tertiary amine lone pairs to the metal centre.

In addition to mild shifts of aliphatic resonances corresponding to the ethyl environments on the linker groups, a distinctive feature arising from coordination of the dipicolyl unit is observed in for all $fac-[Re(CO)_3(L^x)]BF_4$ complexes. The respective

ligand **L**¹-**L** displayed a singlet around ~3.9 ppm (4H) corresponding to the methyl environment between the tertiary amine and 2-pyridyl groups on the dipicolylamine chelating unit. In this case two protons in each methyl group are homotopic, and thus, magnetically equivalent. Following complexation, this environment is no longer present. Coordination of both pyridyl groups *via* the nitrogen atom to rhenium results in each methyl group no longer able to freely rotate and are now diastereotopic and magnetically inequivalent, leading to ²J_{HH} geminal coupling (²J_{HH} = 16 Hz) (Figure 5.7).

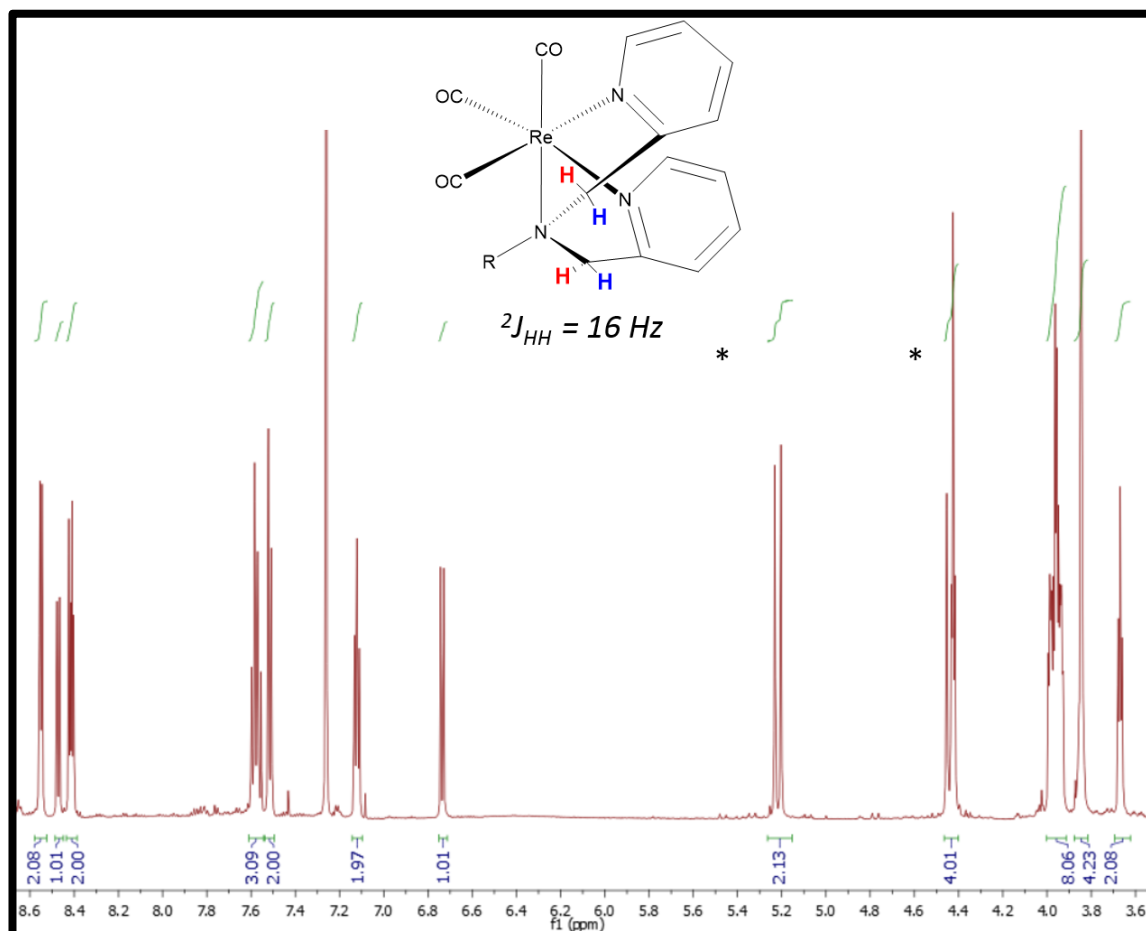


Figure 5.7: ¹H NMR spectrum of *fac*-[Re(CO)₃(L⁵)]BF₄ (structure top left) with diastereotopic methyl resonances starred at around 5.2 ppm and 4.4 ppm.

This feature was observed in the aliphatic region of the ^1H NMR spectra of all **fac-[Re(CO)₃(L^x)]BF₄** complexes. Whilst the geminal $^2J_{\text{HH}}$ coupling constant remained the same across all complexes, interestingly, the separation of the two diastereotopic resonances was shown to differ drastically depending on the naphthalimide/linker environment. The smallest separation (appearing similar to a quartet) of 0.3 ppm was observed for **fac-[Re(CO)₃(L²)]BF₄**, increasing to 1.3 ppm for **fac-[Re(CO)₃(L⁴)]BF₄**. This differed according not only to linker identity but also the termination of the alkyl chain at the bottom of the 1,8-naphthalimide moiety. This is consistent to previous observations made by Langdon-Jones *et al.* who observed similar disparities in separation of the equivalent resonances 4-amino-1,8-naphthalimide linked dipicolylamine *fac*-tricarbonyl complexes.¹¹²

^{13}C NMR spectra of complexes **fac-[Re(CO)₃(L^x)]BF₄** (example given in Figure 5.8, detailed in section 5.4.10), example shown in Figure 5.8 for **fac-[Re(CO)₃(L⁵)]BF₄**) exhibited distinctive resonances characteristic of both the metal carbonyl environment (single peak *cf.* 195 ppm) and the naphthalimide carbonyl environment (2 peaks around 165 ppm).

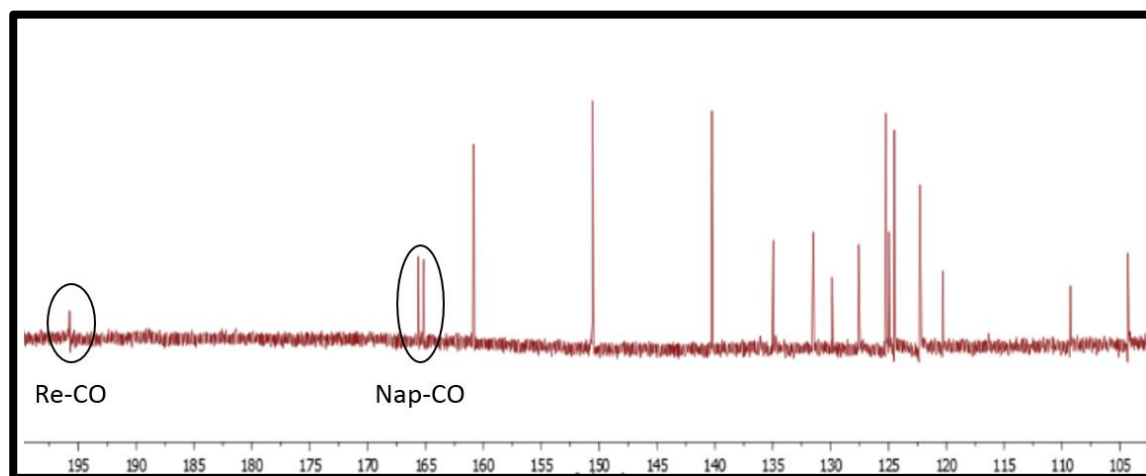


Figure 5.8: Selected region of ^{13}C NMR spectrum of for **fac-[Re(CO)₃(L⁵)]BF₄** showing metal carbonyl resonance *c.f.* 195 ppm and naphthalimide resonances *c.f.* 165 ppm.

Formation of the corresponding rhenium tricarbonyl complexes exhibiting facial geometry is further supported by infra-red spectroscopy. The IR spectrum of all **fac-[Re(CO)₃(L^x)]BF₄** complexes exhibits a sharp resonance around 1054 cm^{-1} , from the symmetric stretch of the B-F bond in the tetrafluoroborate counterion. Further to this, all complexes exhibited two or three metal carbonyl resonances around $2040\text{--}1900\text{ cm}^{-1}$ (Table 5.2) indicative of a pseudo C_3 symmetry for **fac-[Re(CO)₃(L₁₋₂)]BF₄**, and a C_s

symmetry for other complexes, in addition to the two naphthalimide carbonyl resonances around 1640-1680 cm^{-1}

Table 5.2: Metal carbonyl CO stretches observed for rhenium complexes *fac*- $[\text{Re}(\text{CO})_3(\text{L}^x)]\text{BF}_4$.

Complex	$\nu_{\text{CO}} / \text{cm}^{-1}$
<i>fac</i> - $[\text{Re}(\text{CO})_3(\text{L}^1)]\text{BF}_4$	1904, 2027
<i>fac</i> - $[\text{Re}(\text{CO})_3(\text{L}^2)]\text{BF}_4$	1910, 2029
<i>fac</i> - $[\text{Re}(\text{CO})_3(\text{L}^3)]\text{BF}_4$	1944, 2031, 2050
<i>fac</i> - $[\text{Re}(\text{CO})_3(\text{L}^4)]\text{BF}_4$	1907, 2029, 2056
<i>fac</i> - $[\text{Re}(\text{CO})_3(\text{L}^5)]\text{BF}_4$	1928, 2031, 2048
<i>fac</i> - $[\text{Re}(\text{CO})_3(\text{L}^6)]\text{BF}_4$	1908, 2029, 2048

5.3.3. Optical properties of ligands L^1 - L^6 and corresponding *fac*- $[\text{Re}(\text{CO})_3(\text{L}^6)]\text{BF}_4$ complexes

Before radiolabelling and imaging studies were undertaken, the optical properties of ligands L^1 - L^6 and the corresponding *fac*-tricarbonyl rhenium complexes were evaluated. It was hypothesised that due to the (unconjugated) linker length between the metal centre and luminescent centre (naphthalimide group), complexation would have little effect on the luminescent properties, identified for similar naphthalimide-rhenium tricarbonyl complexes reported by Langdon Jones *et al.* .¹¹²

UV-Visible absorption properties and both steady state and time resolved properties of emission characteristics were recorded in two solvents for all ligands and complexes (Table 5.3) Optical characteristics in acetonitrile were recorded across all species, ligands L^1 - L^4 (and their corresponding rhenium complexes) were also recorded in chloroform. Ligands L^5 and L^6 were also optically characterised in water, owing to their excellent solubility therein.

5.3.3.1. UV-Visible absorption spectra

UV-Visible absorption data (Table 5.3) was recorded for ligands **L¹-L⁶** and their corresponding rhenium complexes. Selected spectral traces for ligand **L⁴** and **[Re(CO)₃(L⁴)]BF₄**, **L⁵** and **[Re(CO)₃(L⁵)]BF₄** are shown in Figure 5.9. Ligands **L¹-L⁴** and their corresponding *fac*-**[Re(CO)₃(L^x)]BF₄** complexes exhibited very poor water solubility, to the end where optical characterisation therein was not possible. In contrast, **L⁵** and **L⁶** exhibited excellent water solubility, as per their design (through choice of the more polar 2,2'-(ethylenedioxy)bis(ethylamine linker), and thus were characterised as both acetonitrile and water solutions. Acetonitrile proved to be an ideal common solvent for all ligands and complexes in this study, as all compounds were shown to exhibit significant solubility therein.

Table 5.3: Lowest energy UV-visible absorption maxima recorded for ligands **L1-L6** and for the corresponding **[Re(CO)₃(L¹)]BF₄** complexes in acetonitrile, chloroform and water.

Compound	λ_{abs} ($\epsilon / \text{M}^{-1} \text{cm}^{-1}$)/ nm (MeCN)	λ_{abs} ($\epsilon / \text{M}^{-1} \text{cm}^{-1}$)/ nm (CHCl ₃)	λ_{abs} ($\epsilon / \text{M}^{-1} \text{cm}^{-1}$)/ nm(H ₂ O)
L¹	434 (9310)	428 (7800)	-
L²	436 (10420)	427 (8160)	-
L³	435 (8240)	433 (7300)	-
L⁴	430 (8600)	429 (8000)	-
L⁵	429 (8910)	-	448 (10220)
L⁶	429 (7920)	-	448 (2620)
[Re(CO)₃(L¹)]BF₄	432 (7510)	430 (8560)	-
[Re(CO)₃(L²)]BF₄	433 (19200)	430 (14300)	-
[Re(CO)₃(L³)]BF₄	434 (10100)	430 (16300)	-
[Re(CO)₃(L⁴)]BF₄	431 (13020)	425 (13660)	-
[Re(CO)₃(L⁵)]BF₄	429 (8100)	-	446 (7190)
[Re(CO)₃(L⁶)]BF₄	430 (12240)	-	445 (10700)

All ligands **L¹-L⁶** and their corresponding complexes showed higher energy absorptions around 260-290 nm corresponding to π - π^* and n - π^* transitions characteristic of the naphthalimide species, which do not exhibit a significant degree of solvatochromism. The

lowest energy absorptions of ligands, L^1-L^6 and their corresponding $[Re(CO)_3(L^x)]BF_4$ complexes appeared to remain unchanged respective of linker identity; exhibiting a featureless, broad emission profile centred around 430 nm in acetone. This absorption was shown to exhibit significant solvatochromism, displaying a hypsochromic shift to around 420 nm for L^1-L^4 in chloroform, and bathochromic shift to around 445 nm in water. No trend in intensities of respective transitions was observed.

The solvatochromic nature of this lowest energy transition is in agreement with the assignment as arising from intramolecular charge transfer (ICT), through donation from the secondary amine in the 4 position on the 1,8-naphthalimide towards the imide moiety on the same group. Given the charged excited state the solvatochromic nature of this ICT transition is expected. A move towards a higher energy transition in the less polar chloroform ($\epsilon = 5.69$ with respect to acetonitrile, $\epsilon = 36.64$) suggests destabilisation of the charged excited state, increasing its energy and thus the energy gap between ground and excited state (Figure X). The inverse was also observed when moving to a more polar solvent such as water ($\epsilon = 78.54$), where a bathochromic shift represents stabilisation of the charged excited state.

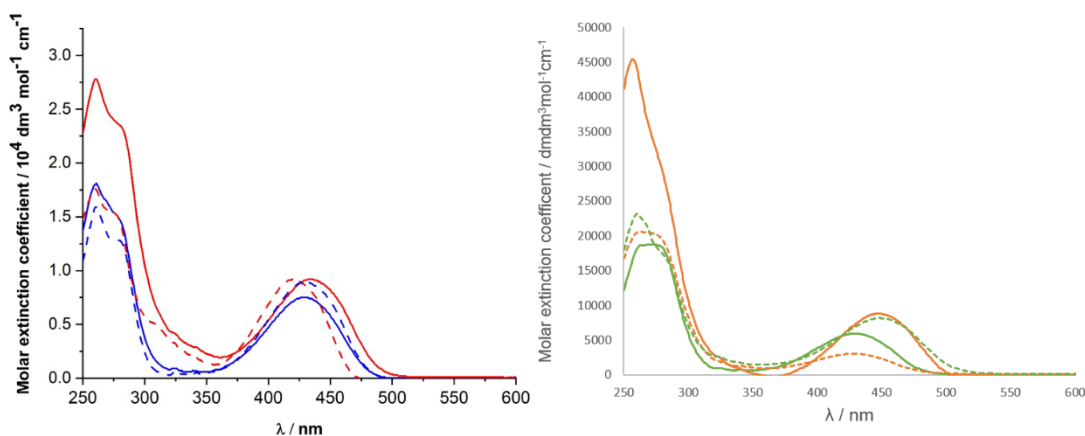


Figure 5.9: UV-Visible absorption spectra of selected ligands and complexes in this study. Left: Ligand L^4 (blue) and $[Re(CO)_3(L^4)]BF_4$ (red) in acetonitrile (solid lines) and chloroform (dashed lines). Right: Ligand L^5 (green) and $[Re(CO)_3(L^5)]BF_4$ (orange) in acetonitrile (solid lines) and water (dashed lines).

5.3.3.2. Luminescence emission properties of ligands L^1-L^6 and their corresponding $[Re(CO)_3(L^x)]BF_4$ complexes

Luminescence emission properties of ligands L^1-L^6 and their corresponding $[Re(CO)_3(L^x)]BF_4$ complexes from excitation at 405 nm, or 295 nm (for lifetime

measurements) is summarised in Table 5.4, and selected spectral traces are shown in Figure 5.10.

Bright emission in the yellow-green region of the visible spectrum at ambient temperature was observed for all ligands L^1 - L^6 and their corresponding $[\text{Re}(\text{CO})_3(L^x)]\text{BF}_4$ complexes. Emission maxima appeared consistent across all ligands and complexes in acetonitrile (~ 520 nm) from excitation at 405 nm, and again a significant solvatochromic shift in emission to around 505-512 nm in chloroform and to 540-550 nm in water. This corresponds to Stokes shifts in the order of at least 3500 cm^{-1} . Emission spectral profiles appeared broad and featureless (Figure 5.17), and relatively consistent across all ligands and complexes. One outlier, emission at 483 nm by $[\text{Re}(\text{CO})_3(L^4)]\text{BF}_4$ is intriguing, as this was not reflected in the emission spectrum of L^4 ($\lambda_{\text{em}} = 505$ nm) and corresponds to a much lower Stokes shift of 2825 cm^{-1} .

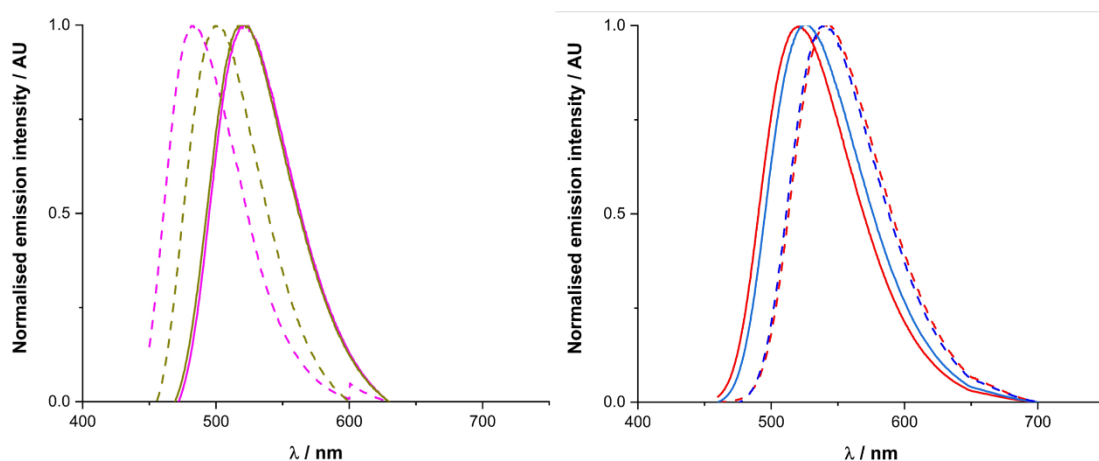


Figure 5.10: Normalised emission spectra of ligands L^4 and L^5 and their corresponding $[\text{Re}(\text{CO})_3(L^x)]\text{BF}_4$ complexes. Right: L^4 (taupe) and $[\text{Re}(\text{CO})_3(L^4)]\text{BF}_4$ (magenta) in acetonitrile (solid lines) and chloroform (dashed lines). Left: L^5 (red) and $[\text{Re}(\text{CO})_3(L^5)]\text{BF}_4$ in acetonitrile (solid lines) and chloroform (dashed lines)

Table 5.4: Summary of luminescence emission properties of **L¹-L⁶** and corresponding **[Re(CO)₃(L^x)]BF₄** complexes from excitation o^a measurements obtained in aerated solutions. ^a $\lambda_{ex} = 405$ nm; ^b $\lambda_{ex} = 295$ nm; ^c using aerated MeCN solution of [Ru(bipy)₃](PF₆)₂ as a reference; ^d in acetonitrile; ^e in chloroform; ^f in water; ^g calculated from lowest energy (ICT) UV-Visible absorption and maximal emission intensity from excitation at 405 nm.

Compound	$\lambda_{em} /$ nm ^a	Stokes shift / cm ⁻¹ ^g	$\tau_{obs} /$ ns ^b	$\phi / \%$ ^c
L ¹	518 ^d	3736 ^d	11.1 ^d	15 ^d
	508 ^e	3679 ^e	9.8 ^e	19 ^e
L ²	521 ^d	3742 ^d	10.5 ^d	22 ^d
	510 ^e	3811 ^e	8.5 ^e	17 ^e
L ³	518 ^d	3790 ^d	9.7 ^d	28 ^d
	508 ^e	3303 ^e	1.4, 8.8 (94%) ^e	28 ^e
L ⁴	517 ^d	3968 ^d	9.5 ^d	31 ^d
	505 ^e	3454 ^e	8.1 ^e	35 ^e
L ⁵	542 ^f	3871 ^f	3.4, 6.0 (64%) ^f	39 ^f
	521 ^e	4116 ^d	9.4 ^d	12 ^e
L ⁶	549 ^f	4106 ^f	5.4 ^f	8 ^f
	520 ^e	4079 ^d	9.7 ^e	30 ^e
[Re(CO) ₃ (L ¹)]BF ₄	515 ^d	3838 ^d	10.9 ^d	67 ^d
	503 ^e	3267 ^e	9.1 ^e	23 ^e
[Re(CO) ₃ (L ²)]BF ₄	519 ^d	3827 ^d	9.8 ^d	30 ^d
	504 ^e	3415 ^e	9.2 ^e	37 ^e
[Re(CO) ₃ (L ³)]BF ₄	520 ^d	4025 ^d	9.8 ^d	26 ^d
	512 ^e	3510 ^e	7.7 ^e	29 ^e
[Re(CO) ₃ (L ⁴)]BF ₄	517 ^d	3859 ^d	10.2 ^d	40 ^d
	483 ^e	2825 ^e	8.0 ^e	38 ^e
[Re(CO) ₃ (L ⁵)]BF ₄	540 ^f	3903 ^f	6.0 ^f	49 ^f
	526 ^e	4299 ^d	10.0 ^d	15 ^e
[Re(CO) ₃ (L ⁶)]BF ₄	539 ^f	3919 ^f	5.9 ^f	57 ^f
	516 ^e	3876 ^d	11.1 ^d	17 ^e

Luminescent lifetime (τ_{obs}) of ligands **L¹-L⁶** (obtained in aerated solutions) and corresponding **[Re(CO)₃(L^x)]BF₄** complexes also showed moderation with respect to solvent. Lifetimes of around the order of 10 ns in acetonitrile, 8-9 ns in chloroform and 3.9 -6 ns in water were generally found to fit to a single exponent. Notable exceptions to this, where for **L³** and **L⁵** a biexponential decay pattern was found, could be attributed to error associated with fitting a decay curve to experimental data.

Finally, quantum yield values obtained in aerated solutions were shown to be generally moderate to high (20-50%), with some exceptions. It is unlikely that that outliers represent significant changes in luminescent characteristics. Very high quantum yields of **[Re(CO)₃(L⁵)]BF₄** and **[Re(CO)₃(L⁶)]BF₄** are encouraging, as they indicate very efficient and bright luminescence from ICT excitation, suggesting good suitability towards both *in-vitro* and *in-vivo* imaging.

From evaluation of luminescent characteristics of ligands **L¹-L⁶** and the corresponding **[Re(CO)₃(L^x)]BF₄**, it can be concluded that emission occurs from the singlet (as evidenced by the low nanosecond order lifetimes) excited state, characteristic of luminescent 4-amino-1,8-naphthalic anhydride species. This is further supported by the solvatochromic nature of the emitting state, as well as the high quantum yields obtained, comparable to other similar naphthalimide species in the literature.¹¹⁴ It appears from data obtained that both the absorption and emission properties of the naphthalimide lumiphore are insensitive to the metal-coordinate environment for complexes **[Re(CO)₃(L^x)]BF₄**, unsurprising in considering the unconjugated linker separating the luminescent naphthalimide moiety and bispicolyl metal chelate.

5.3.3.3. Optical properties summary

The optical properties of all **fac-[Re(CO)₃(L^x)]BF₄** are broadly consistent with their respective ligands, **L¹-L⁶**. Absorption spectra confirm the presence of a solvatochromic, broad, intense ICT absorption in all cases around $\lambda_{\text{max}} = 400 - 450$ nm. Emission characteristics confirm the singlet emitting state following ICT excitation, with a emissive lifetime of between 4 – 11 ns.

Ligands **L¹-L⁴** and their corresponding **fac-[Re(CO)₃(L^x)]BF₄** complexes exhibited poor water solubility, however displayed positive optical characteristics such as intense ICT absorption and bright emission with a large (generally > 3500 cm⁻¹) Stokes shift. These positive optical characteristics were comported through for ligands **L⁵** and **L⁶**, which also maintained acceptable water solubility upon complexation with Re(CO)₃.

Ligands **L**⁵ and **L**⁶ prove therefore to be the most suitable for further imaging study, and application in water based radiolabelling with the analogous *fac*-^{99m}Tc(CO)₃ for further study, as the comparable *fac*-[Re(CO)₃(**L**⁵)]BF₄ and *fac*-[Re(CO)₃(**L**⁶)]BF₄ complexes again exhibited acceptable water solubility and act as a reliable mimic for the radioactive ^{99m}Tc complexes produced.

5.3.4. Radiolabelling of **L**⁵ with technetium-99m

Following establishment of the Re(I) coordination chemistry and optical properties of these complexes radiolabelling (performed by Juozas Domarkas *et al.*) of the selected **L**⁵ ligand was undertaken.

The method employed (Alberto *et al.* ^{221,231}, Figure 5.11) requires a good ligand solubility in the (aqueous) phosphate buffered saline solvent. Given the very limited water solubility of ligands **L**¹-**L**⁴, these were discounted for use in radiolabelling studies, as they would certainly hinder significant radiolabelling in such a manner. **L**⁵ was chosen due to the alcohol termination from the naphthalimide moiety, presumably achieving increased water solubility, yielding the radioactive ^{99m}Tc complex [^{99m}Tc(CO)₃(**L**⁵)]⁺, exhibiting analogous coordination geometry to the studied *fac*-[Re(CO)₃(**L**⁵)]BF₄ complex.

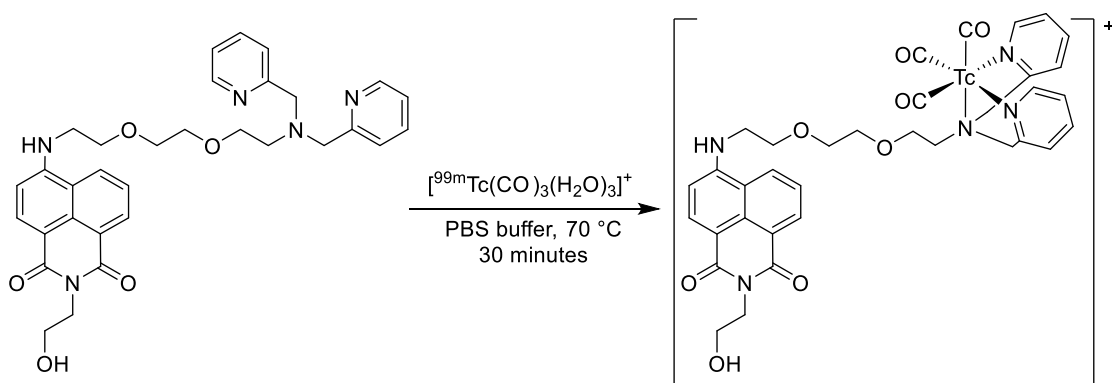


Figure 5.11: Radiolabelling of **L**⁵ with *fac*-[^{99m}Tc(CO)₃(H₂O)₃]⁺ to give complex *fac*-[^{99m}Tc(CO)₃(**L**⁵)]⁺.

Preliminary radiolabelling studies (Table 5.5) with freshly reduced *fac*-[^{99m}Tc(CO)₃(H₂O)₃]⁺ (10-40 MBq, 1.3-2.6 mM final precursor concentration, pH 7-8 buffered with 5 mM PBS) at 70 °C indicated good radiolabelling yields with **L**⁵ concentrations ranging from 0.2 mM to 2.0 mM (Table 5.5) of around 50 %, obtained through integration of radio-HPLC traces. Yields varied from 41% at the highest concentration of **L**⁵ (2.0 mM) after 60 minutes, to 52-57 % for other **L**⁵ concentrations. Where **L**⁵ was present in concentrations greater than 0.2 mM, radiolabelling yield plateaued after 30 minutes, with no significant increase in yield observed from increasing

reaction time. Experiments varying $fac-[^{99m}Tc(CO)_3(H_2O)_3]^+$ concentration showed no observable effect on radiochemical yield at 0.53-1.32 mM L^5 concentration, and thus L^5 radiolabelling conditions are optimised at 0.53-1.32 mM L^5 concentration, at pH 7-8 (PBS), 70 °C over 30 minutes with 10-40 MBq $fac-[^{99m}Tc(CO)_3(H_2O)_3]^+$. Purification by semi-preparatory radio-HPLC yielded $fac-[^{99m}Tc(CO)_3(L^5)]^+$ with extremely high purity as measured by radio-HPLC detailed in the appendix of this thesis.

Table 5.5: Radiochemical yields for the formation of $fac-[^{99m}Tc(CO)_3(L^5)]^+$ at 70 °C in PBS buffer with respect to L^5 concentration.

[L^5] / mM	Radiochemical yield / %		
	30 mins	60 mins /	90 mins
0.2	43	47	53
0.4	51	53	55
1.0	56	57	57
2.0	42	41	43

5.3.5. *In-vitro* assessment of properties relevant to biodistribution and stability

In order to more accurately rationalise any localisation or other behaviours of **fac-[^{99m}Tc(CO)₃(L⁵)]⁺** in following *in-vitro* and *in-vivo* studies, Juozas Domarkas *et al.* discerned several key parameters relevant to the compounds applicability in biological systems. Lipophilicity (log D_{7.4}), serum and urine stability were determined.

Lipophilicity is commonly measured as LogP, the logarithm of the partition coefficient over water and octan-1-ol (Equation 5.1). In the case where biological systems are concerned, this is usually represented instead as LogD, identically determined to LogP but with respect to the distribution coefficient (partition coefficient measured at a specific pH of the aqueous phase using buffered solution in place of water, Equation 5.2). LogD, measured with PBS at pH 7.4 partitioned over octanol) was determined at 0.67 ± 0.06, which suggests that although **fac-[^{99m}Tc(CO)₃(L⁵)]⁺** exhibits ideal water solubility, its lipophilicity is of significant order to be able to cross the membrane barrier upon cellular penetration.

$$P = \frac{[\text{Species}]_{\text{octanol}}}{[\text{Species}]_{\text{water}}}$$

Equation 5.1: Determination of the partition coefficient, P, for a particular chemical species.

$$D_{7.4} = \frac{[\text{Species}]_{\text{octanol}}}{[\text{Species}]_{\text{Buffered aqueous solution at pH 7.4}}}$$

Equation 5.2: Determination of the distribution coefficient, D, at pH 7.4 for a particular chemical species.

Serum and urine stability are also critical factors in determining whether a tracer species is suitable for *in-vivo* imaging. Clearly, a chemical species such as a metal complex which dissociates or otherwise degrades rapidly in serum or urine risks exhibiting increased toxicity, lower clearance rates and otherwise aberrant effects in its utilisation as a tracer. The kinetically inert *fac*-tricarbonyl rhenium chelate species, **fac-[^{99m}Tc(CO)₃(L⁵)]⁺** unsurprisingly exhibited very high stability upon incubation at 37 °C in human serum and urine, as measured by radio-HPLC (detailed in the appendix of this thesis), with no degradation in either serum or urine measured over 3 hours.

5.3.6. Bioimaging studies with **fac-[M(CO)₃(L₅)]BF₄** (M = Re, ^{99m}Tc)

In investigating the behaviour of **fac-[^{99m}Tc(CO)₃(L₅)]⁺** (and the analogous rhenium complex) in biological systems, and evaluating its potential as a specific mitochondrial marker, several bioimaging studies were undertaken. Information at a cellular level was evaluated through detailed *in-vitro* studies with human MCF-7 (breast cancer) and U-87 (brain cancer) cells and rat cardiomyocytes (H9c2 cell line), evaluating toxicity (cell viability assays) and mitochondrial localisation (colocalization studies). Evaluating characteristics as a whole-body, *in-vivo* imaging agent utilising the radio-tracing capabilities of **fac-[^{99m}Tc(CO)₃(L₅)]BF₄** was undertaken through live mouse studies, with particular focus on clearance routes. In evaluating the behaviour of **fac-[^{99m}Tc(CO)₃(L₅)]BF₄** at a cellular level and whole-body level, the applicability of the bimodal luminescent radiotracer was established.

5.3.6.1. Cell viability

Cellular toxicity of **fac-[Re(CO)₃(L₅)]BF₄** was evaluated through MTS assay by (human U-87 glioblastoma cell line) by Juozas Domarkas *et al.* (Figure 5.12).

Briefly, the MTS assay employs the MTS tetrazolium dye (Figure 5.12) which is reduced by NAD(P)H reliant dehydrogenase enzymes in a cellular environment. Reduction of the colourless MTS tetrazolium species results in the formation of the highly coloured MTS formazan species, thus providing the measurable colorimetric output. The ability of a cell to reduce the tetrazolium species relies on the metabolic activity (and thus 'healthy' function) due to NAD(P)H flux, cells with reduced metabolism (due to, for example, the presence of a toxic species) reduce less of the tetrazolium species, and thus upon MTS assay result in reduced colorimetric output.²³²

Toxicity of a compound is represented by a CC₅₀ value, the concentration of the compound that will kill half the cellular population in a previously healthy culture. Through the MTS cytotoxicity assay, the CC₅₀ value of **fac-[Re(CO)₃(L₅)]BF₄** was determined at 72.7 μM (Figure 5.12), representing very low cytotoxicity *in-vitro* for the compound. Given the analogous chemistry exhibited by ^{99m}Tc (I) and Re (I) complexes, the value obtained for **fac-[^{99m}Tc(CO)₃(L₅)]⁺** is representative of the theoretical toxicity of the analogous ^{99m}Tc (I) complex, however this does not take into account toxicity arising from emission of ionising radiations from the radioactive **fac-[^{99m}Tc(CO)₃(L₅)]⁺** compound.

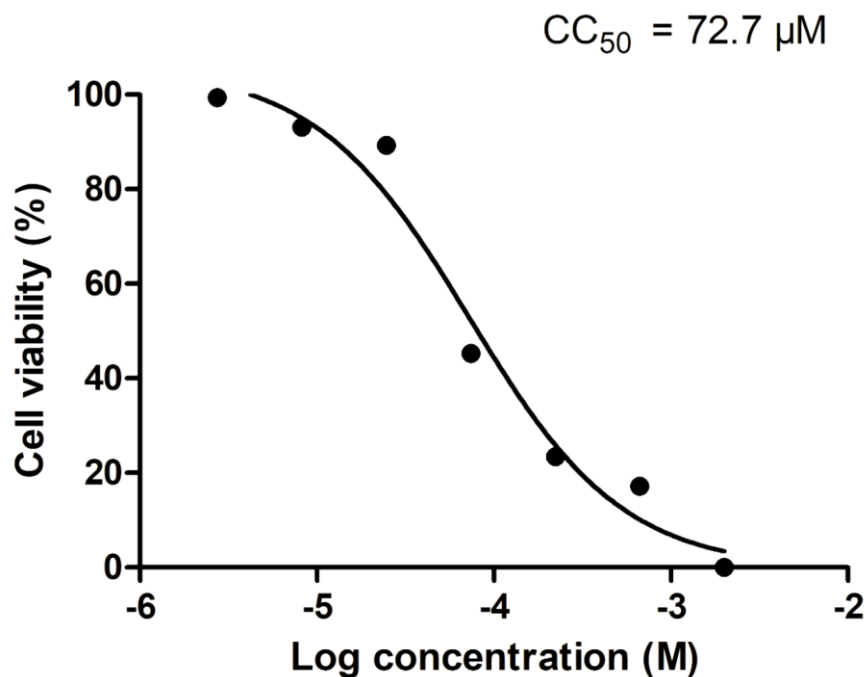
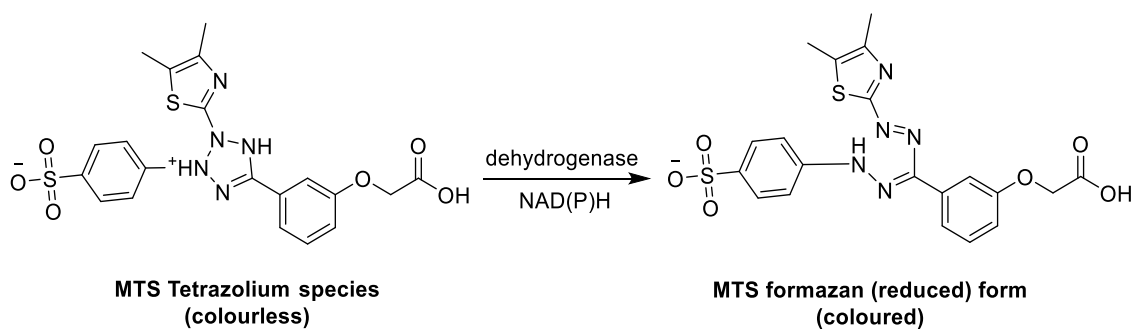


Figure 5.12: Cell viability (MTS) assay for U-87 cells incubated with differing concentrations of $\text{fac-}[\text{Re}(\text{CO})_3(\text{L}_5)]\text{BF}_4$.

5.3.6.2. *In-vitro* mitochondrial uptake studies of $\text{fac-}[\text{}^{99\text{m}}\text{Tc}(\text{CO})_3(\text{L}_5)]\text{BF}_4$

To evaluate the behaviour of $\text{fac-}[\text{}^{99\text{m}}\text{Tc}(\text{CO})_3(\text{L}_5)]^+$ towards mitochondria, uptake studies towards freshly isolated mitochondria were undertaken by Juozas Domarkas *et al.* (Figure 5.13). $\text{fac-}[\text{}^{99\text{m}}\text{Tc}(\text{CO})_3(\text{L}_5)]^+$ exhibited rapid and extensive acculation in mitochondria ($58.68 \pm 6.5\%$) in comparison with complexes exhibiting the cationic triphenylphosphonium moiety (up to $8.30 \pm 0.63\%$ ²¹⁴), commonly employed in mitochondrial targeting. This represents significant improvements and a positive outlook for *in-vitro* mitochondrial targeting.

Additionally, this uptake was shown to be dependent on the mitochondrial membrane potential (MMP), demonstrated by the almost complete destruction of mitochondrial uptake when the MMP was depolarised through the use of carbonyl cyanide

m-chlorophenylhydrazine (CCCP) (1.35 ± 0.14 %). This is significant in that it identifies a potential for $\text{fac-}^{99\text{m}}\text{Tc}(\text{CO})_3(\text{L}_5)^+$ to be employed in evaluation of mitochondrial function *in-vitro*, which by extension evaluates apoptotic state and cellular viability.

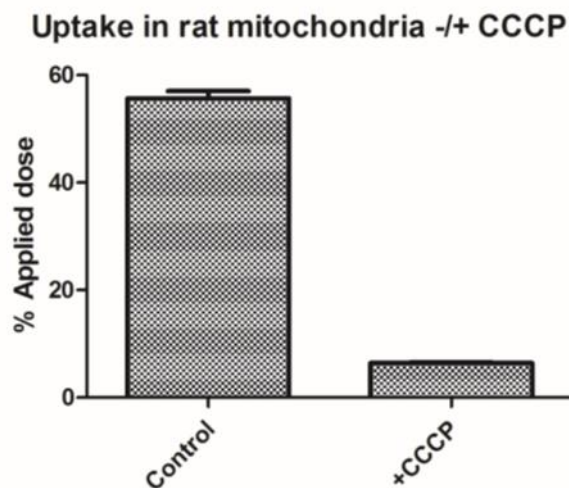


Figure 5.13: Mitochondrial uptake of $\text{fac-}^{99\text{m}}\text{Tc}(\text{CO})_3(\text{L}_5)^+$ both with and without CCCP membrane depolarisation.

5.3.6.3. *In-vitro* imaging of human breast cancer cells (MCF-7) and rat cardiomyocytes (H9c2), mitochondrial localisation studies

Whole cell *in-vitro* mitochondrial uptake was evaluated through the use of confocal fluorescence microscopy in human breast cancer cells (MCF-7 cell line). Co-localisation studies by Juozas Domarkas *et al.* (Figure 5.13) with $\text{fac-}[\text{Re}(\text{CO})_3(\text{L}_5)]\text{BF}_4$ and the benzyl chloride based commercial mitochondrial stain (MitoTacker deep red, MDR) showed a good degree of overlap (overlap coefficient 0.66), suggesting a high degree of co-localisation. This represents, therefore, the ability of $\text{fac-}[\text{Re}(\text{CO})_3(\text{L}_5)]\text{BF}_4$, and by extension, the analogous $^{99\text{m}}\text{Tc}$ (I) complex to localise towards the mitochondria, providing a significant feature in the employment of the complex in a bioimaging context.

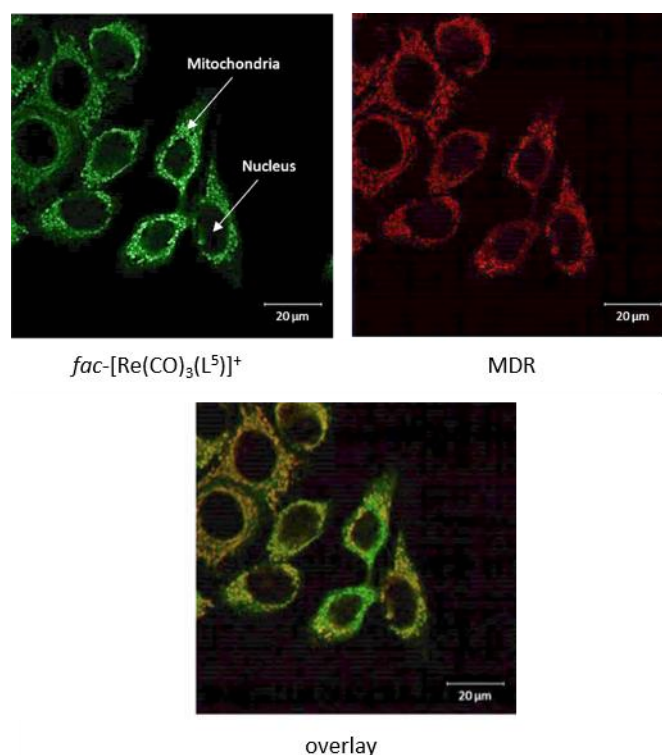


Figure 5.13: Maximum projection representations of confocal fluorescence microscopy studies of MCF-7 cells incubated with $fac-[Re(CO)_3(L_5)]BF_4$ (top left) and MDR (top right) and the overlay of both images (bottom, overlap coefficient = 0.66).

5.3.6.4. *In-vivo* imaging

Following establishment of the *in-vitro* characteristics of $fac-[Re(CO)_3(L_5)]BF_4$ in the context of bioimaging, SPECT/CT *in-vivo* imaging utilising radioemission by $fac-[^{99m}Tc(CO)_3(L_5)]^+$ (Figure 5.14). Administration *via* of $fac-[^{99m}Tc(CO)_3(L_5)]^+$ to a healthy 'naïve' mouse did not result in obvious signs of toxicity during the study. SPECT/CT imaging of the mouse demonstrated rapid clearance following administration *via* the biliary and renal system. Urine analysis demonstrated that the tracer remained stable following excretion ($85.4\% \pm 1.4\%$), suggesting its suitability for further *in-vivo* analysis in the future.

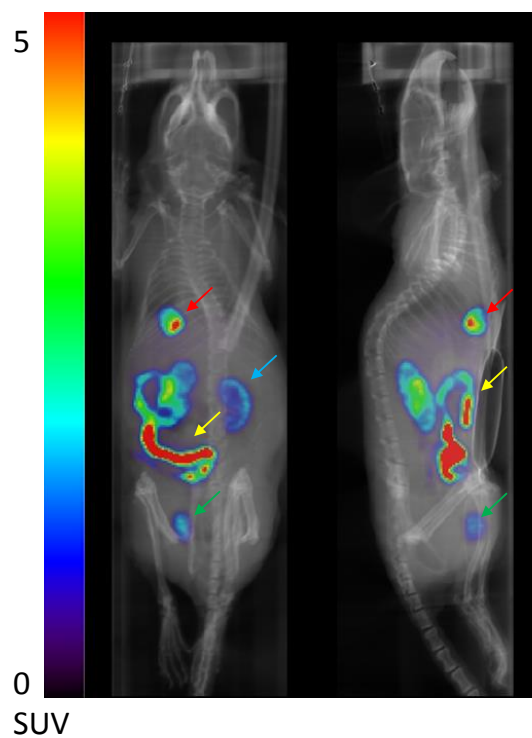


Figure 5.14: SPECT and CT overlaid images with SPECT images acquired using the radiotracer $fac-[^{99m}\text{Tc}(\text{CO})_3(\text{L}_5)]^+$. Sagittal and coronal views show the localisation of the tracer after 22-60 minutes.

5.2.4. Chapter conclusion

This study demonstrates the synthesis, detailed characterisation of six novel ligands, **L¹-L⁶** and corresponding **fac-[Re(CO)₃(L₅)]BF₄** complexes. These ligands and complexes demonstrate bright fluorescence arising from excitation of the ICT band and subsequent fluorescent emission from the singlet excited state. In characterising ligands and complexes, unequivocal evidence of their syntheses was provided, and their spectroscopic properties identified in detail.

L⁵, selected due to its high degree of water solubility, was further utilised in radiolabelling with [^{99m}Tc(CO)₃(H₂O)₃]⁺ to give the luminescent radiotracer **fac-[^{99m}Tc(CO)₃(L₅)]⁺**. Owing to their highly similar coordination chemistry, **fac-[^{99m}Tc(CO)₃(L₅)]⁺** and the corresponding Re(I) complex, **fac-[Re(CO)₃(L₅)]BF₄** are considered to be interchangeable in evaluating biological activity and relevance. Combinatory studies, evaluating important characteristics such as lipophilicity (LogD_{7.4} = 0.67 ± 0.06) and serum/urine stability (no degradation over 3 hours) of **fac-[^{99m}Tc(CO)₃(L₅)]⁺**, demonstrated the applicability towards biomodal imaging in an *in-vivo* and *in-vitro* context, displaying a good balance between solubility and cell penetration

The applicability of **fac-[^{99m}Tc(CO)₃(L₅)]⁺**/**fac-[Re(CO)₃(L₅)]BF₄** in a bioimaging context was further supported by its low cytotoxicity (CC₅₀ = 72.7 μM), extensive MMP dependant mitochondrial uptake (55.68 ± 6.5 %, reducing to 1.35 ± 0.14 % upon MMP depolarisation).

In-vitro imaging in human MCF-7 cells provided further evidence for mitochondrial localisation at a cellular level, through co-localisation studies with MDR. *In-vivo* SPECT/CT imaging confirmed the ability of **fac-[^{99m}Tc(CO)₃(L₅)]⁺** to act as a radiotracer in whole-body studies, and confirmed good stability in *in-vitro* measurements (urine stability ~ 85%), and a high degree of renal and biliary system clearance.

These results show a great deal of improvement on previous bioimaging studies with *fac*-tricarbonyl Re(I) and Tc(I) naphthalimide conjugates, owing primarily to the high degree of solubility of the ligand **L⁵** due to the polar bisethylenedioxy based linker. **fac-[^{99m}Tc(CO)₃(L₅)]⁺** studies *in-vitro* and *in-vivo* are continuing, and due to the MMP dependant mitochondrial uptake could provide an essential basis of cellular health identification and tumor localisation *in-vivo*. The potential medical impact of these ligands and complexes is significant, owing to their relatively low toxicity.

Future work could be focused on evaluating modified lipophilicity and charge distribution to further evaluate a structure/function relationship. Several modifications on

the basic design looking at modifying the orthogonal naphthalimide terminations could provide a basis for such studies.

5.4. Experimental

5.4.1. General considerations

Reagents were obtained commercially (Sigma, TCI, Merck) and used without further purification. UV-Visible absorption spectroscopy and luminescence emission spectroscopy was performed as outlined in chapter 2, with monochromator slit widths set at 4,4 nm unless stated otherwise. NMR spectroscopy was performed using BRUKER 300 MHz, 400 MHz and 600 MHz NMR spectrometers.

5.4.2. Radiolabelling of ligand L1-L6 with ^{99m}Tc

The respective ligand (L1-L6) in a glass vial was dissolved in 50 μL of methanol prior to dilution with 100 μL of phosphate buffered saline. The solution was degassed by sonication and purged with argon over 10 minutes. Freshly reduced $[\text{}^{99m}\text{Tc}(\text{CO})_3(\text{H}_2\text{O})_3]^+$ in reduction medium ($\sim 500 \mu\text{L}$) (up to 400 MBq). The final concentration of ligand was between 0.5-1.3 mM. The reaction mixture was incubated at 70 $^\circ\text{C}$, shaking at 600 rpm for 30 minutes, whereupon it was cooled to room temperature and injected onto semi-preparatory HPLC (ACE5 C18 5 \AA 100 x 250). Product containing fraction (RCY = $47 \pm 18\%$, $n = 3$, corrected for decay to beginning of reaction) eluting at 12-14 minutes was collected, diluted with deionised water and loaded onto a homemade SPE cartridge containing 80-100 mg of Oasis C18 sorbent. The cartridge was washed with 2-3 mL of deionised water and dried by a current of inert gas. The product was eluted with 500 μL of ethanol, prior to evaporation under gentle heating with inert gas current and the product redissolved into phosphate buffered saline. For in vivo evaluation, the formulation was filter sterilised with a 0.22 μm filter prior to administration. The decay correction preparatory yield was $21 \pm 11\%$ ($n = 3$). Preparation time was less than 2 hours from commencement of synthesis.

5.4.3. Lipophilicity measurements

Lipophilicity (partition coefficient, LogP) values were obtained using the shake-flask method. An aliquot of the respective $[\text{}^{99m}\text{Tc}(\text{CO})_3(\text{LX})]^+$ complex in ethanol ($\sim 1 \text{ MBq}$) was dried in a 1.5 mL Eppendorf tube and dissolved in 1 mL of a 1:1 mixture of octanol and PBS (pH?). The solution was vigorously mixed in a vortex shaker for 5 minutes at room temperature. Phase separation was achieved through centrifugation at 14500 rpm for 2 minutes. 50 μL of each phase was then diluted to 1 mL and measured using AGC.

5.4.4. Serum stability

An aliquot of the respective $[^{99m}\text{Tc}(\text{CO})_3(\text{LX})]^+$ complex in ethanol (~3 MBq) was dried and dissolved in 0.5 mL of human blood serum in a HPLC vial. This was incubated at 37 °C with shaking at 600 rpm for 3 hours. Aliquots were taken at time 0, 30 min, 60 min, 1 h, 2h and 3. Protein serum component was precipitated through addition of double volume of ice-cold methanol and removed by centrifugation. The supernatant was analysed by radio-HPLC.

5.4.5. *In-vivo* SPECT imaging and stability

All animal procedures were approved by the University of Hull Animal Welfare Ethical Review Body (AWERB) and carried out in accordance with the Animals in Scientific Procedures Act 1986 and the UKCCCR Guideline 2010 by approved protocols following institutional guidelines (Home Office Project License number 60/4549 held by Dr. Cawthorne). After imaging experiments, mice urine was collected, proteins were precipitate by addition of double volume of ice cold methanol and removed by centrifugation at 14.5 krpm for 5 min and supernatant was analysed by radio-HPLC indicating $85.4 \pm 1.4\%$ stability (n=1, triplicate analyses).

5.4.6. *In vitro* analysis

5.4.6.1. Cell culture

MCF-7 cells were purchased from the European Collection of Cell Cultures and grown in PRMI-1640 media. H9c2 (2-1 clone) cells were purchased from LGC-PromoChem (Teddington, UK) and grown in IMDM media. Media was supplemented with 10% fetal calf serum (FCS). Human glioblastoma cell line from (U87) from ATCC and it was cultured using DMDM media with 10% (v/v) heat inactivated fetal bovine serum (FBS). Media and FCS were purchased from Gibco/Life Technologies, UK. Cells were maintained in Nunc 75 cm² tissue culture flasks (Fischer Scientific, UK) inside a humidified 5% CO₂ incubator at 37 °C. Both cell lines were divided bi-weekly for maintenance of stock at a divided ratio of 1:8-1:10 for MCF-7 cells and 1:3-1:5 for H9c2 cells. For confocal and flow cytometry experiments cells were counted and seeding densities (below) were used.

5.4.6.2. Toxicity

Cells were seeded in 96 well plate with 1000 cells/well in 200 μ L growth medium. The plates were incubated overnight at 37 °C allow cells to adhere. After 18 h media was removed from the wells and 100 μ l of treated media with various concentrations of

compounds was added. The plates were returned to the incubator. After 72 h, MTS reagent (Promega, UK) 20 μ L was added to the wells. Plates were incubated for 3 h at 37 °C. Absorbance reading were taken at 490 nm using Synergy HT microplate reader (Biotek, USA). The absorbance value of each triplicate were averaged and the media only absorbance was subtracted. Compounds reading were normalised to the control reading. Empty plate and compound added background analysis was carried out to ensure low levels of non-specific fluorescence.

5.4.6.3. Flow cytometry

1 x 10⁵ cells/well were seeded in six-well plates and cultured for 2-3 days until 70-80% confluent. Cell media was removed and 1 mL 0.1% FCS-containing media was added. Carbonyl cyanide m-chlorophenylhydrazone (CCCP, Sigma Aldrich, UK) in DMSO (50 mM, 1 μ L) was added into three wells (1 mL total volume) and 0.1% DMSO was added to the remaining three control wells (as a control). Plates were placed inside a CO₂ incubator for 30 mins, followed by the addition of compound (500 nM, 50 μ L media) to both groups. Plates were incubated inside the CO₂ incubator at 37 °C for 1 hour, subsequently, media was removed and the cells were washed twice with ice cold PBS buffer. Cells were harvested into PBS with cell scraper and isolated by centrifugation at 200 \times g for 5 min at 4 °C. The pellet was re-suspended in 300 μ L of PBS and the cell suspension transferred into polypropylene FACS tubes (Falcon 2054) and analysed by a FACScan flow cytometer (BD Biosciences Europe, Erembodegem, Belgium). Dot plot was used to gate cells and the FL-1 channel was used to measure variation in fluorescence intensities. Mean fluorescence intensities were used to quantify for comparison.

5.4.6.4. Confocal microscopy

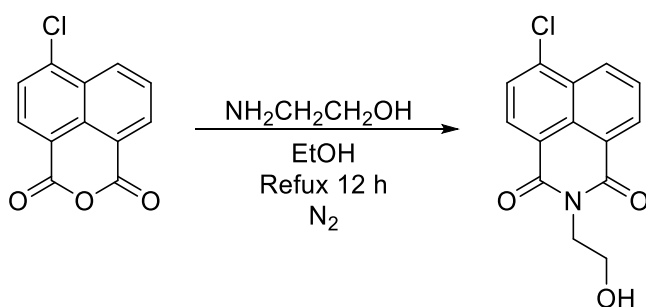
MCF-7 cells (2.5 \times 10³) and H9c2 cells (4 \times 10³) were seeded in Mattak confocal dishes (P35G-1.2-20-C, 35 mm²) and cultured for 2-3 days until 70-80% confluent. After reaching desired cell density, the growth media was replaced with 1 mL 0.1% FCS-containing media and cells were treated with compound 1 or 2 (500 nM, 50 μ L) for 1 hour inside a CO₂ incubator under 5% CO₂. Mitotracker deep red (MDR, 250 nM, 20 μ L) was added 1 hour prior to compound to obtain double labelled cells for mitochondrial co-localisation study. After 30 min, the cells were washed twice with 1 mL PBS and media containing 15 mM HEPES was added. Unstained control samples of cells were used to check for auto fluorescence. 14 Live cell images were obtained using ZEN software on

a Zeiss LSM 710 inverted confocal microscope, equipped with an incubator chamber at 37 °C. Images were obtained using a Zeiss 63× water objective.

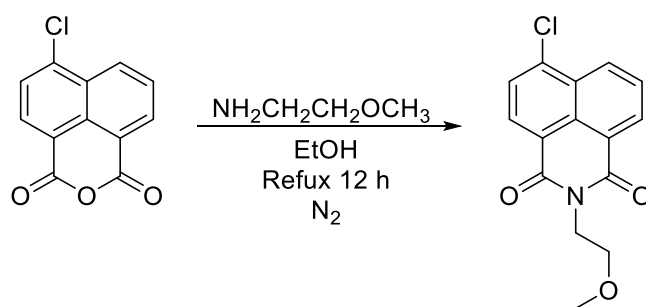
To measure the degree of overlap between subcellular localisation of 1 or 2 and MDR, a colocalisation coefficient was calculated following standard methods. 1 Single-label control samples were prepared to eliminate fluorescence overlap between two fluorescence channels; in addition to 1, 2 or MDR, untreated cells were assessed in order to eliminate background fluorescence. Single-label control samples were imaged under the same exposure settings as double-labelled samples. Exact coordinates were determined using crosshairs at X and Y coordinates from single-labelled controls and were identical for double-labelled samples. Once the exact coordinates were determined, the ZEN software gave tables containing values of co-localisation coefficient and overlap coefficient.

5.4.7. Synthesis of compounds

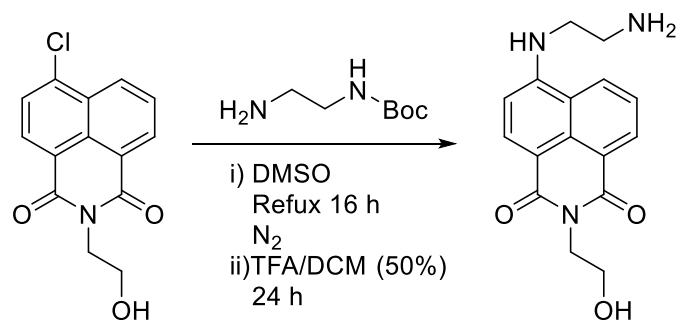
5.4.7.1. Ligands and precursors



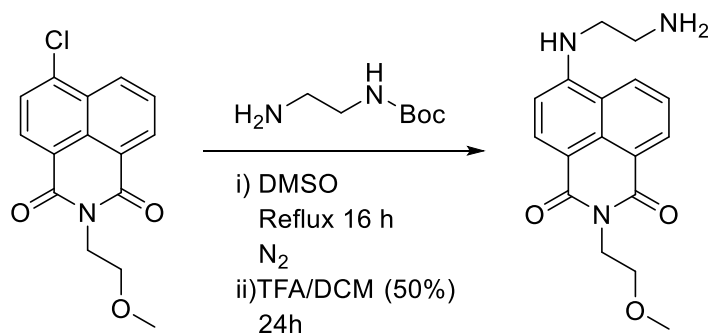
Synthesis of compound **C1:** 4-chloro-1,8-naphthalic anhydride (2.0 g, 8.6 mmol) was dissolved in ethanol (60 mL) and ethanolamine (0.8 mL, 12.9 mmol) was added. The solution was then heated at reflux for 12 hrs under a nitrogen atmosphere. Upon cooling to 0 °C precipitation occurred, and filtration yielded **C1** as a yellow solid (2.0 g, 85 %). ^1H NMR (400 MHz, CDCl_3): δ_{H} 8.70 (d, $J = 6.8$ Hz, 1H), 8.64 (d, $J = 8.4$ Hz, 1H), 8.54 (d, $J = 7.6$ Hz, 1H), 7.88 (m, 2H), 4.48 (t, $J = 4.8$ Hz, 2H), 4.01 (t, $J = 4.8$ Hz, 2H) ppm. LRMS ES^+ found $m/z = 275.03$ [M^+].



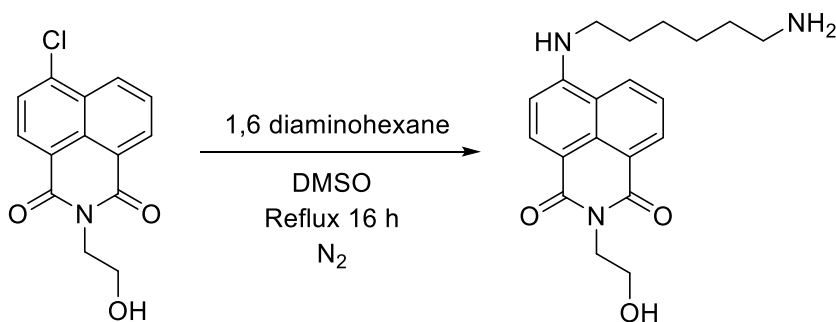
Synthesis of compound **C²:** Prepared as for **C**¹ except using 2-methoxy ethylamine (0.9 g, 12.9 mmol), yielding **C**² as a yellow solid (2.0 g, 79 %). ¹H NMR (400 MHz, CDCl_3): δ_{H} 8.68 (d, $J = 7.0$ Hz, 1H), 8.61 (d, $J = 8.1$ Hz, 1H), 8.52 (d, $J = 8.2$ Hz, 1H), 7.91 – 7.80 (m, 2H), 4.44 (t, $J = 5.7$ Hz, 2H), 3.73 (t, $J = 5.7$ Hz, 2H), 3.38 (s, 3H) ppm. LRMS ES⁺ found $m/z = 289.05$ [M^+].



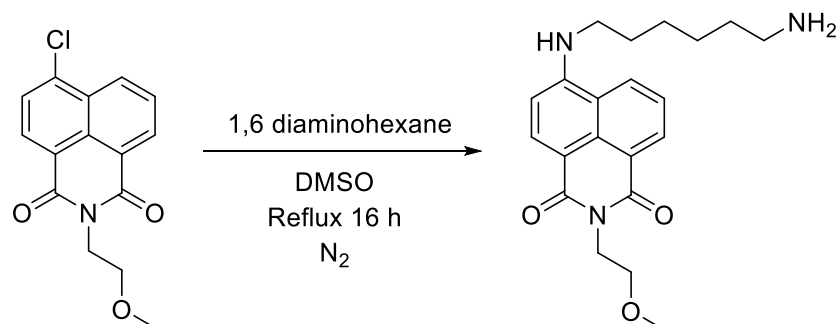
Synthesis of N¹: C¹ (0.3 g, 1.01 mmol) was dissolved in DMSO (4 mL) and *N-tert*-Boc-ethylenediamine was added (0.47 g, 2.93 mmol) and the solution heated at reflux for 16 hours under a nitrogen atmosphere. The solution was flooded with 30 mL of water and neutralised with 0.1 M HCl. The product was then extracted with dichloromethane (3 x 15 mL) and washed with water (3 x 10 mL) and brine (3 x 10 mL). The solvent was then reduced to a minimum and precipitation induced by the dropwise addition of petroleum ether. Filtration of the precipitate followed by washing with diethyl ether (5 mL) yielded the Boc-protected intermediate product as a bright orange solid (0.27 g, 65 %). ¹H NMR (300 MHz, CDCl₃): δ_H 8.55 (d, *J* = 7.3 Hz, 1H), 8.42 (d, *J* = 8.5 Hz, 1H), 8.27 (d, *J* = 8.3 Hz, 1H), 7.59 (t, *J* = 7.7 Hz, 1H), 7.19 (s, 1H), 6.55 (d, *J* = 8.3 Hz, 1H), 4.45 (t, *J* = 4.3 Hz, 2H), 3.97 (s, 2H), 3.65 (dd, *J* = 10.2, 5.3 Hz, 2H), 3.49 – 3.38 (m, 2H), 1.42 (s, 9H) ppm. ¹³C{¹H} NMR (101 MHz, CDCl₃): δ_C 163.89, 163.10, 150.08, 134.03, 130.78, 129.32, 128.73, 124.48, 121.99, 120.37, 108.76, 103.95, 57.96, 41.47, 40.36, 37.31 ppm. LRMS ES⁺ found *m/z* = 400.19 [M+H]⁺. Deprotection of the intermediate product was achieved by stirring the solution of the intermediate in 50% TFA in DCM for 24 hours under a nitrogen atmosphere. The solvents were then removed under vacuum, and the residue dissolved in methanol and the solvent removed again. This was repeated in triplicate to yield the final product as an oily yellow solid (0.178 g, 60 %). ¹H NMR (300 MHz, d₆-DMSO): δ_H 8.63 (d, *J* = 8.3 Hz, 2H), 8.42 (d, *J* = 7.2 Hz, 2H), 8.26 (d, *J* = 8.4 Hz, 2H), 7.78 (s, 2H), 7.69 (t, *J* = 7.8 Hz, 2H), 6.84 (d, *J* = 8.5 Hz, 2H), 4.84 (s, *J* = 46.7 Hz, 2H), 4.11 (t, *J* = 6.3 Hz, 4H), 3.73 – 3.51 (m, 8H), 3.39 (s, 2H), 3.17 (s, 4H) ppm. ¹³C{¹H} NMR (101 MHz, d₆-DMSO): δ_C 163.89, 163.10, 150.08, 134.03, 130.78, 129.32, 128.73, 124.48, 121.99, 120.37, 108.76, 103.95, 57.96, 41.47, 40.36, 37.31 ppm. LRMS ES⁺ found *m/z* = 332.12 [M+Na]⁺. HRMS expected *m/z* = 322.1162 for [M+Na]⁺ found *m/z* = 322.1163



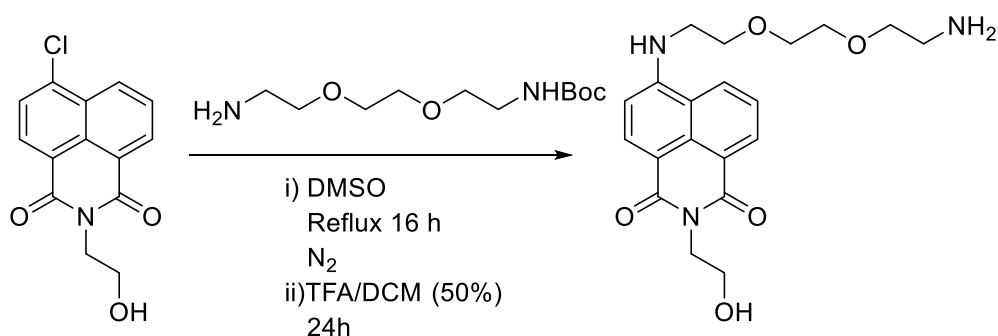
Synthesis of \mathbf{N}^2 : Prepared as for \mathbf{N}^1 but using \mathbf{C}^2 (0.3 g, 1.0 mmol), yielding the intermediate product as a bright orange solid (0.157 g, 38 %). ^1H NMR (400 MHz, CDCl_3): δ_{H} 8.51 (d, $J = 7.3$ Hz, 1H), 8.38 (d, $J = 8.4$ Hz, 1H), 8.20 (d, $J = 8.4$ Hz, 1H), 7.54 (t, $J = 7.5$ Hz, 1H), 7.02 (s, 1H), 6.50 (d, $J = 8.3$ Hz, 1H), 5.03 (s, 1H), 4.36 (t, $J = 5.6$ Hz, 2H), 3.65 (t, $J = 5.7$ Hz, 2H), 3.58 (s, 2H), 3.39 (s, 2H), 3.32 (s, 3H), 1.41 (s, 8H) ppm. $^{13}\text{C}\{^1\text{H}\}$ NMR (101 MHz, CDCl_3): δ_{C} 164.33, 158.65, 150.24, 134.77, 131.32, 129.94, 127.14, 124.71, 122.77, 120.39, 103.30, 80.85, 77.24, 69.84, 58.80, 46.87, 39.50, 38.96, 28.37 ppm. LRMS found $m/z = 414.20$ $[\text{M}+\text{H}]^+$. Deprotection yielded the final product as an orange oil (0.103 g, 87 %). MR (400 MHz, CD_3OD): δ_{H} 8.41 (d, $J = 7.6$ Hz, 2H), 8.28 (d, $J = 8.8$ Hz, 1H), 7.65 – 7.49 (m, 2H), 6.78 (d, $J = 8.7$ Hz, 1H), 4.24 (t, $J = 6.0$ Hz, 2H), 3.69 (t, $J = 6.1$ Hz, 2H), 3.59 (t, $J = 6.0$ Hz, 2H), 3.27 (m, 2H), 3.25 (s, 3H) ppm. LRMS found $m/z = 336.13$ $[\text{M}+\text{Na}]^+$. HRMS expected $m/z = 336.1319$ for $[\text{M}+\text{Na}]^+$, found $m/z = 336.1320$



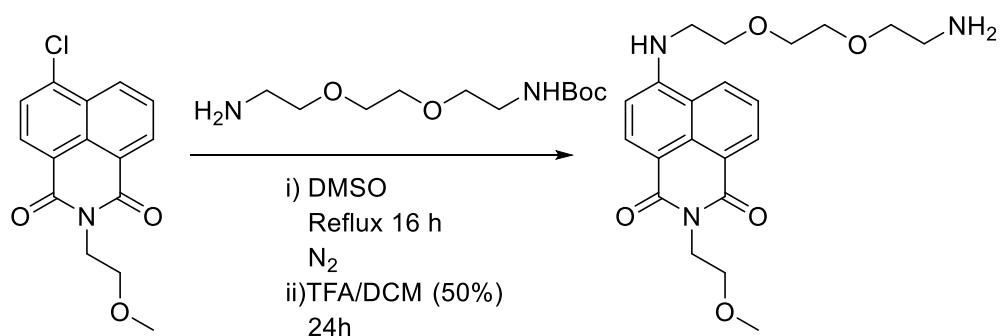
Synthesis of N³: **C¹** (0.75 g, 2.73 mmol) was dissolved in DMSO (4 mL) and 1,6 diaminohexane (0.4 mL, 4.1 mmol) was added and the solution heated at reflux for 16 hours. The solution was flooded with 30 mL of water and neutralised with 0.1 M HCl. The product was then extracted with dichloromethane (3 x 15 mL) and washed with water (3 x 10 mL) and brine (3 x 10 mL). The solvent was then reduced to a minimum and precipitation induced by the dropwise addition of petroleum ether. Filtration of the precipitate followed by washing with diethyl ether (5 mL) yielded the product as an orange solid (0.422 g, 44 %). ¹H NMR (300 MHz, CDCl₃): δ_H 8.58 (d, *J* = 7.4 Hz, 1H), 8.46 (d, *J* = 7.6 Hz, 1H), 8.10 (d, *J* = 8.1 Hz, 1H), 7.69 – 7.57 (m, 1H), 6.75 – 6.66 (m, 1H), 5.36 (s, 1H), 4.51 – 4.40 (m, 2H), 4.03 – 3.92 (m, 2H), 3.50 – 3.34 (m, 2H), 2.78 – 2.67 (m, 2H), 1.95 – 1.75 (m, 2H), 1.65 – 1.41 (m, 6H) ppm. ¹³C NMR (126 MHz, CDCl₃) δ 165.58, 165.01, 150.88, 135.09, 131.38, 130.03, 127.61, 124.36, 122.09, 120.31, 108.23, 104.03, 60.41, 43.27, 42.02, 41.22, 32.52, 28.28, 26.80, 26.41. LRMS found *m/z* = 356.20 [M+H]⁺, HRMS expected *m/z* = 356.1896 found *m/z* = 356.1965



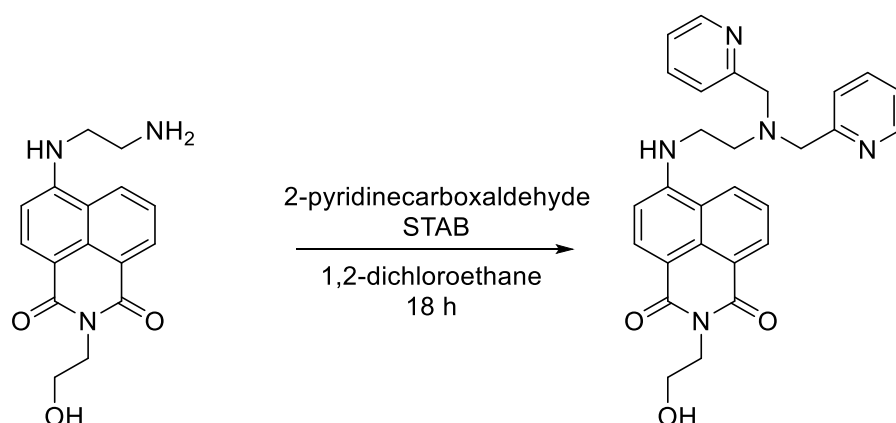
Synthesis of **N⁴:** Prepared as for **N**³ but using **C**² (0.75 g, 1.38 mmol) yielding the product as an orange solid (0.420 g, 42 %). ¹H NMR (400 MHz, CDCl₃): δ_H 8.59 (d, *J* = 7.4 Hz, 1H), 8.47 (d, *J* = 8.3 Hz, 1H), 8.09 (d, *J* = 8.4 Hz, 1H), 7.63 (d, *J* = 7.7 Hz, 1H), 6.72 (d, *J* = 8.2 Hz, 1H), 5.32 (s, 1H), 4.45 (t, *J* = 5.8 Hz, 2H), 3.75 (t, *J* = 5.8 Hz, 2H), 3.57 – 3.30 (m, 5H), 2.74 (t, *J* = 6.6 Hz, 2H), 1.91 – 1.75 (m, 2H), 1.61 – 1.39 (m, 6H) ppm. ¹³C NMR (126 MHz, CDCl₃) δ 165.04, 164.97, 164.41, 150.14, 149.91, 134.82, 134.74, 131.30, 129.94, 129.87, 126.81, 126.50, 124.56, 124.49, 122.62, 122.55, 120.21, 120.16, 109.40, 109.14, 104.15, 104.09, 69.71, 58.66, 43.33, 41.19, 38.87, 28.62, 28.47, 26.90, 26.81, 26.40. LRMS found *m/z* = 370.21 [M+H]⁺. HRMS expected *m/z* = 370.2127 for [M+H]⁺, found *m/z* = 370.2125.



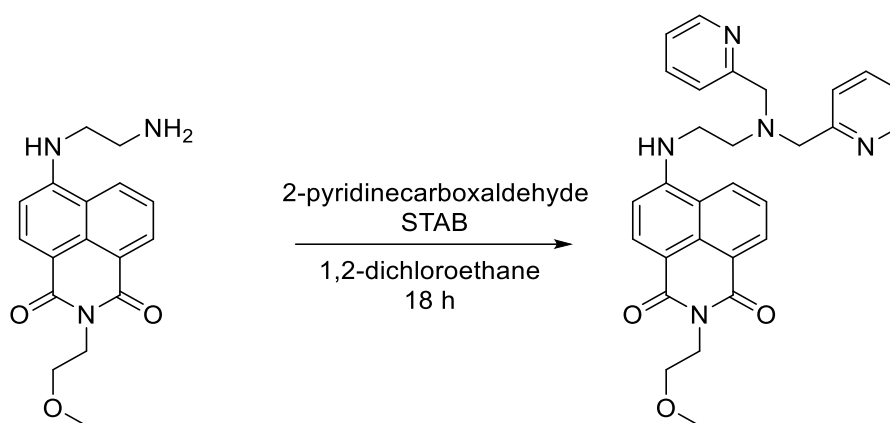
Synthesis of N^5 : C^1 (0.75 g, 2.72 mmol) was dissolved in DMSO (5 mL) and *N*-tert-butyl (2-(2-(2-aminoethoxy)ethoxy)ethyl)carbamate (1.4 g, 5.64 mmol) was added and the solution heated at reflux for 16 hours under a nitrogen atmosphere. Upon being allowed to cool the solution was flooded with 30 mL of water and neutralised with 0.1 M HCl. The product was then extracted with dichloromethane (3 x 15 mL) and washed with water (3 x 10 mL) and brine (3 x 10 mL). The crude intermediate product was then purified further through the use of silica gel column chromatography using 3:2 acetone hexane with 4% triethylamine as the eluent. The solvents were then removed under vacuum yielding the intermediate product as a red oil (0.40 g, 30%). ^1H NMR (300 MHz, CDCl_3): δ_{H} 8.37 (d, $J = 6.8$ Hz, 1H), 8.28 (d, $J = 8.4$ Hz, 1H), 8.08 (d, $J = 8.1$ Hz, 1H), 7.46 (t, $J = 7.5$ Hz, 1H), 6.53 (d, $J = 8.4$ Hz, 1H), 6.03 (s, 1H), 5.00 (s, 1H), 4.36 (t, $J = 4.8$ Hz, 2H), 3.92 (t, $J = 4.5$ Hz, 2H), 3.82 (t, $J = 5.1$ Hz, 2H), 3.64 (m, 4H), 3.57 – 3.45 (m, 4H), 3.28 (d, $J = 4.8$ Hz, 2H), 1.34 (s, 9H) ppm. LRMS found $m/z = 389.18$ $[\text{M}+\text{H}]^+$. Deprotection of the intermediate product was achieved by stirring in 50% TFA in DCM (10 mL) for 24 hours under a nitrogen atmosphere. The solvents were then removed under vacuum, and the residue dissolved in methanol and the solvent removed again. This was repeated in triplicate to yield N^5 as a red oil (0.29 g, 91%). ^1H NMR (300 MHz, CD_3OD): δ_{H} 8.31 – 8.19 (m, 2H), 8.09 (m, 1H), 7.43 (m, 1H), 6.61 (m, 1H), 4.23 (m, 2H), 3.80 (t, $J = 5.1$ Hz, 2H), 3.72 – 3.64 (m, 6H), 3.59 – 3.51 (m, 2H), 3.30 – 3.25 (m, 2H), 3.11 – 3.01 (m, 2H) ppm. $^{13}\text{C}\{^1\text{H}\}$ NMR (75 MHz, CD_3OD): δ_{C} 164.78, 150.78, 149.04, 134.14, 133.04, 130.55, 128.31, 128.01, 127.62, 123.86, 108.00, 103.65, 70.03, 68.62, 66.54, 59.03, 42.69, 39.22 ppm. LRMS found $m/z = 388.18$ $[\text{M}+\text{H}]^+$. HRMS expected $m/z = 388.1794$ for $[\text{M}+\text{H}]^+$, found $m/z = 388.1857$.



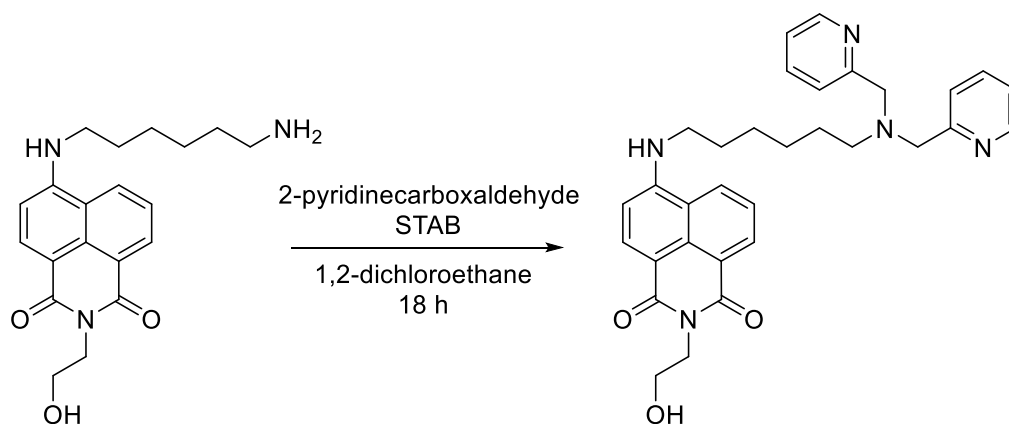
Synthesis of N⁶: Prepared as for **N**⁵ but using **C**² (0.75 g, 2.59 mmol), first yielding the intermediate product as a red oil (0.46 g, 35%). ¹H NMR (400 MHz, MeOD) δ 8.35 (d, *J* = 7.8 Hz, 1H), 8.19 (d, *J* = 8.6 Hz, 1H), 7.50 (t, *J* = 7.9 Hz, 1H), 6.70 (d, *J* = 8.6 Hz, 1H), 4.23 (t, *J* = 6.1 Hz, 1H), 3.75 (t, *J* = 5.5 Hz, 1H), 3.67 – 3.62 (m, 1H), 3.62 – 3.55 (m, 8H), 3.27 (s, 1H), 2.96 (t, *J* = 5.1 Hz, 1H), 1.36 (s, 9H) ppm. Deprotection yielded the **N**⁵ as a red oil (0.32 g, 88 %). ¹H NMR (400 MHz, CD₃OD): δ_H 8.35 (d, *J* = 7.8 Hz, 2H), 8.19 (d, *J* = 8.6 Hz, 1H), 7.50 (t, *J* = 7.9 Hz, 1H), 6.70 (d, *J* = 8.6 Hz, 1H), 4.23 (t, *J* = 6.1 Hz, 2H), 3.75 (t, *J* = 5.5 Hz, 2H), 3.67 – 3.62 (m, 2H), 3.62 – 3.55 (m, 8H), 3.27 (s, 3H), 2.96 (m, *J* = 5.1 Hz, 2H) ppm. ¹³C{¹H} NMR (400 MHz, CD₃OD): δ_C 116.2, 165.6, 152.4, 135.7, 132.2, 131.0, 139.2, 125.5, 123.2, 121.7, 109.5, 105.2, 71.6, 71.4, 70.7, 70.1, 67.9, 58.9, 44.2, 40.5, 39.7 ppm. LRMS found *m/z* = 402.20 [M+H]⁺. HRMS expected *m/z* = 402.1951 for [M+H]⁺, found *m/z* = 402.2028.



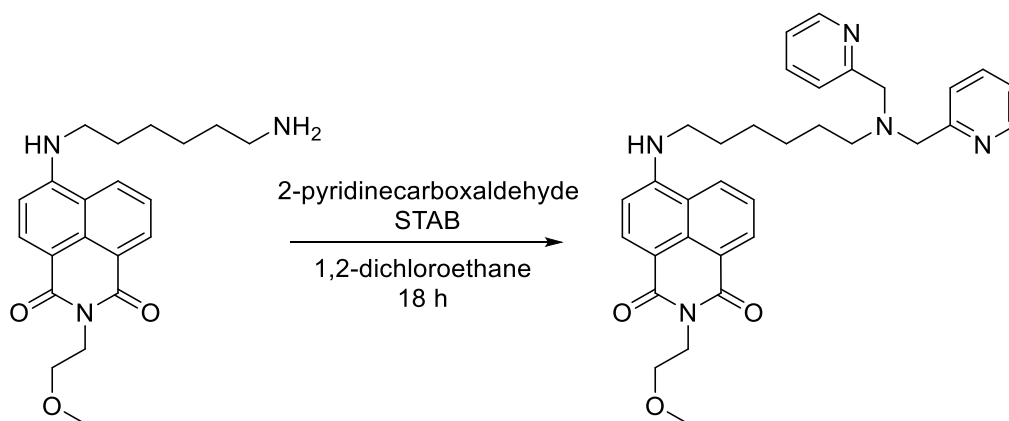
Synthesis of **L¹:** **N**¹ (0.11 g, 0.37 mmol) was dissolved in 1,2-dichloroethane and 2-pyridinecarboxaldehyde (0.07 mL, 0.74 mmol) was added and the solution stirred for 2 hours under a nitrogen atmosphere. Sodium trisacetoxyborohydride (0.24g, 1.11 mmol) was then added and the solution stirred at room temperature for 18 hours. The solution was then neutralised with saturated NaHCO₃ and the product extracted into chloroform, washed with water (3 x 20 mL) and brine (3 x 20 mL). The organic layer was collected then dried over MgSO₄ and filtered, and the solvent removed to yield the product as an orange oil (0.13 g, 73 %). ¹H NMR (400 MHz, CDCl₃): δ_H 8.80 (d, *J* = 8.9 Hz, 1H), 8.57 (d, *J* = 7.3 Hz, 1H), 8.52 – 8.49 (m, 2H), 8.35 (d, *J* = 8.6 Hz, 1H), 7.98 (s, 1H), 7.68 – 7.60 (m, 1H), 7.55 – 7.47 (m, 2H), 7.31 (d, *J* = 7.6 Hz, 2H), 7.12 – 7.07 (m, 2H), 6.48 (d, *J* = 8.1 Hz, 1H), 4.70 (s, 1H), 4.43 – 4.38 (m, 2H), 3.95 (s, 4H), 3.93 – 3.89 (m, 2H), 3.36 – 3.31 (m, 2H), 3.01 – 2.96 (m, 2H) ppm. ¹³C NMR (151 MHz, CDCl₃) δ 195.73, 164.76, 164.11, 160.85, 150.53, 140.25, 134.54, 131.29, 129.82, 127.09, 125.21, 125.00, 124.53, 122.60, 122.29, 120.43, 104.65, 70.46, 70.15, 69.79, 68.32, 67.72, 67.40, 58.72, 38.90, 3.67 LRMS found *m/z* = 482.22 [M+H]⁺. HRMS expected *m/z* = 482.2192 for [M+H]⁺, found *m/z* = 482.2202. UV-vis. (MeCN) λ_{max} (ε / dm³mol⁻¹cm⁻¹): 434 (9300), 280 (19600), 262 (20400) nm.



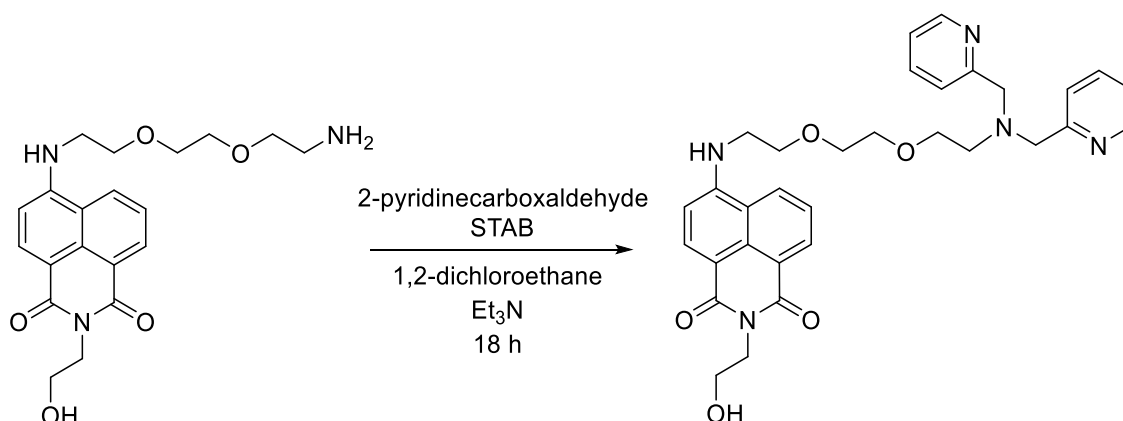
Synthesis of L²: Prepared as for L¹, but using N² (0.10 g, 0.32 mmol), 2-pyridine carboxaldehyde (0.06 mL, 0.64 mmol), and sodium trisacetoxyborohydride (0.203 g, 0.13 mmol). Recrystallization from chloroform yielded the product as a yellow crystalline solid (0.08g, 51 %). ¹H NMR (400 MHz, CDCl₃): δ_H 8.83 (d, *J* = 8.2 Hz, 1H), 8.64 (d, *J* = 7.7 Hz, 1H), 8.59 – 8.56 (m, 2H), 8.42 (d, *J* = 8.6 Hz, 1H), 7.91 (s, 1H), 7.73 – 7.67 (m, 2H), 7.60 – 7.52 (m, 2H), 7.40 – 7.36 (m, 2H), 7.18 – 7.13 (m, 2H), 6.55 (d, *J* = 8.7 Hz, 1H), 4.44 (t, *J* = 6.0 Hz, 2H), 4.22 (t, *J* = 5.9 Hz, 2H), 4.01 (s, 4H), 3.73 (t, *J* = 6.3 Hz, 2H), 3.40 (s, 3H), 3.05 (t, *J* = 5.2 Hz, 2H) ppm. ¹³C{¹H} NMR (101 MHz, CD₃OD): δ_C 153.26, 150.32, 147.84, 134.27, 131.02, 129.74, 128.47, 127.97, 124.60, 122.14, 120.86, 118.93, 109.67, 103.90, 69.27, 57.54, 48.94, 40.24, 39.01, 38.77, 38.45, 37.74, 36.45, 22.65, 13.02, 10.02 ppm. LRMS found *m/z* = 512.23 for [M+O+H]⁺. HRMS expected *m/z* = 512.2281 for [M+O+H]⁺, found *m/z* = 512.2292. UV-vis. (MeCN) λ_{max} (ε / dm³mol⁻¹cm⁻¹): 436 (10420), 280 (12900), 262 (18200) nm.



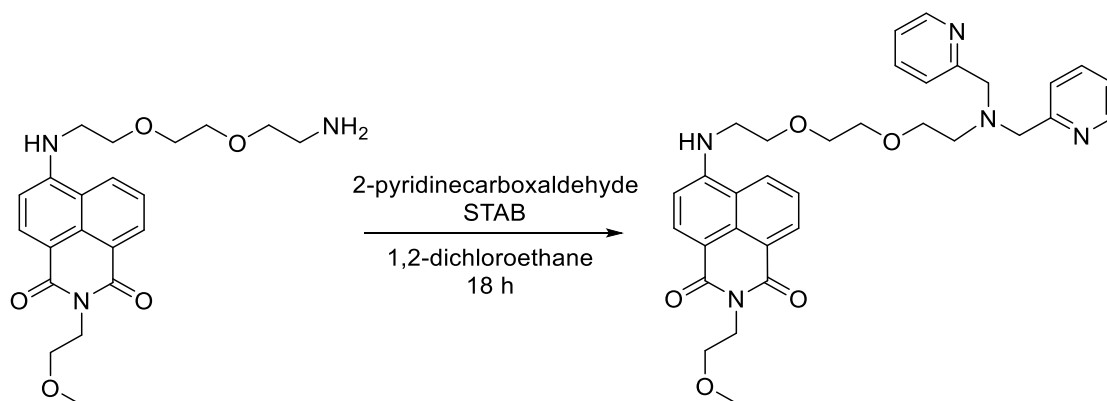
Synthesis of L³: Prepared as for **L¹** but using **N³** (0.21 g, 0.565 mmol), 2-pyridine carboxaldehyde (0.13 mL, 1.12 mmol) and sodium trisacetoxyborohydride (0.36 g, 1.68 mmol). Product was isolated as an orange oil (0.386 g, 95 %). ¹H NMR (400 MHz, CDCl₃): δ_H 8.48 (d, *J* = 4.7 Hz, 1H), 8.28 (d, *J* = 7.2 Hz, 1H), 8.18 (d, *J* = 8.4 Hz, 1H), 8.02 (d, *J* = 8.4 Hz, 1H), 7.59 (t, *J* = 7.6 Hz, 1H), 7.47 (d, *J* = 7.8 Hz, 1H), 7.35 (t, *J* = 7.8 Hz, 1H), 7.11 – 7.06 (m, 1H), 6.42 (d, *J* = 8.5 Hz, 1H), 5.91 (s, 1H), 4.36 (t, *J* = 4.1 Hz, 1H), 3.96 (t, *J* = 4.6 Hz, 1H), 3.76 (s, 2H), 3.23 (t, *J* = 5.6 Hz, 1H), 2.48 (t, *J* = 7.1 Hz, 1H), 1.70 – 1.64 (m, 1H), 1.53 – 1.48 (m, 1H), 1.37 – 1.25 (m, 2H) ppm. ¹³C{¹H} NMR (101 MHz, CDCl₃): δ_C 164.25, 163.88, 158.88, 149.05, 147.87, 147.50, 135.65, 135.43, 133.59, 130.08, 128.52, 125.53, 123.30, 121.96, 121.26, 121.22, 120.95, 119.47, 118.98, 107.92, 103.03, 63.29, 60.72, 59.38, 53.17, 42.49, 41.50, 27.55, 25.90, 25.87, 25.66 ppm. LRMS found *m/z* = 554.28 for [M+O+H]⁺. HRMS expected *m/z* = 554.2753 for [M+O+H]⁺, found *m/z* = 554.2762. UV-vis. (MeCN) λ_{max} (ε / dm³mol⁻¹cm⁻¹): 433 (7300), 279 (18200, sh), 263 (20400) nm.



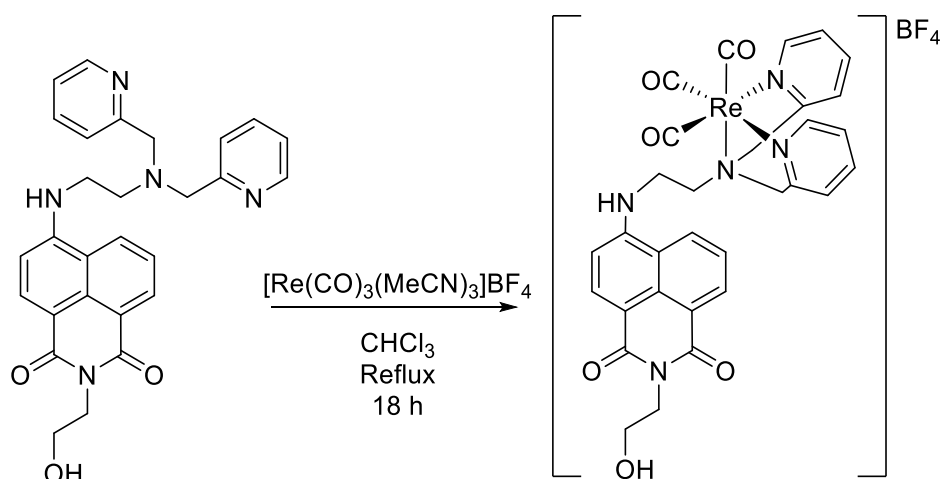
Synthesis of L⁴: Prepared as for L¹ but using N⁴ (0.20 g, 0.51 mmol), 2-pyridine carboxaldehyde (0.1 mL, 1.08 mmol) and sodium trisacetoxyborohydride (0.34 g, 1.62 mmol). Product isolated as an orange oil (0.194 g, 69 %). ¹H NMR (400 MHz, CDCl₃) δ 8.56 – 8.49 (m, 3H), 8.43 (d, *J* = 7.7 Hz, 1H), 8.07 (d, *J* = 8.6 Hz, 1H), 7.63 (t, *J* = 7.7 Hz, 2H), 7.59 – 7.49 (m, 3H), 7.16 – 7.09 (t, *J* = 6.4 Hz, 2H), 6.66 (d, *J* = 8.3 Hz, 1H), 5.37 (s, 1H), 4.42 (t, *J* = 5.8 Hz, 2H), 3.81 (s, 4H), 3.42 – 3.32 (m, 5H), 2.56 (t, *J* = 7.1 Hz, 2H), 1.96 – 1.67 (m, 4H), 1.66 – 1.52 (m, 2H), 1.52 – 1.29 (m, 2H). ¹³C{¹H} NMR (75 MHz, CDCl₃): δ_c 187.12, 182.37, 164.83, 164.20, 159.79, 149.76, 148.91, 136.50, 134.58, 131.16, 129.76, 126.28, 124.46, 122.98, 122.71, 122.02, 120.11, 109.54, 104.13, 77.53, 77.10, 76.68, 69.85, 60.40, 58.76, 54.21, 43.54, 38.91, 28.68, 26.92, 26.76, 1.05 ppm. LRMS found *m/z* = 552.29 for [M+H]⁺. HRMS expected *m/z* = 552.2955 for [M+H]⁺, found *m/z* = 552.2969. UV-vis. (MeCN) λ_{max} (ε / dm³mol⁻¹cm⁻¹): 429 (7000), 282 (14200, sh), 263 (17500) nm.



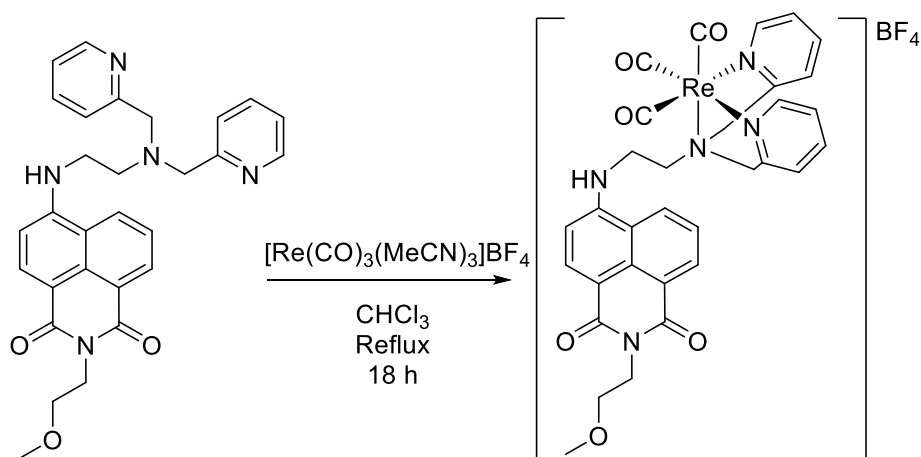
Synthesis of L⁵: N⁵ (0.075 g, 0.19 mmol) was dissolved in 5 % triethylamine in 1,2-dichloroethane and (20 mL) and 2-pyridinecarboxaldehyde (0.07 mL, 0.74 mmol) was added and the solution stirred for 2 hours under a nitrogen atmosphere. Sodium trisacetoxyborohydride (0.24g, 1.11 mmol) was then added and the solution stirred at room temperature for 18 hours. The solution was then neutralised with saturated NaHCO₃ and the product extracted into chloroform, washed with water (3 x 20 mL) and brine (3 x 20 mL). The organic layer was then dried over MgSO₄ and filtered, and the solvent removed yielding L⁵ as an orange oil (0.13 g, 73 %). ¹H NMR (400 MHz, CDCl₃): δ_H 8.80 (d, *J* = 8.9 Hz, 1H), 8.57 (d, *J* = 7.3 Hz, 1H), 8.52 – 8.49 (m, 2H), 8.35 (d, *J* = 8.6 Hz, 1H), 7.98 (s, 1H), 7.68 – 7.60 (m, 1H), 7.55 – 7.47 (m, 2H), 7.31 (d, *J* = 7.6 Hz, 2H), 7.12 – 7.07 (m, 2H), 6.48 (d, *J* = 8.1 Hz, 1H), 4.70 (s, 1H), 4.43 – 4.38 (m, 2H), 3.95 (s, 4H), 3.93 – 3.89 (m, 2H), 3.36 – 3.31 (m, 2H), 3.01 – 2.96 (m, 2H) ppm. ¹³C NMR (75 MHz, CDCl₃) δ 165.52, 165.05, 159.26, 150.55, 148.88, 136.61, 134.76, 131.23, 129.77, 127.74, 124.27, 123.24, 122.13, 120.49, 109.09, 103.98, 77.52, 77.09, 76.67, 70.29, 69.25, 68.64, 61.91, 60.60, 53.83, 43.35, 42.60. LRMS found *m/z* = 570.27 for [M+H]⁺. HRMS expected *m/z* = 570.2711 for [M+H]⁺, found *m/z* = 570.2708. UV-vis. (MeCN) λ_{max} (ε / dm³mol⁻¹cm⁻¹): 429 (8190), 279 (19200, sh), 260 (21000) nm.



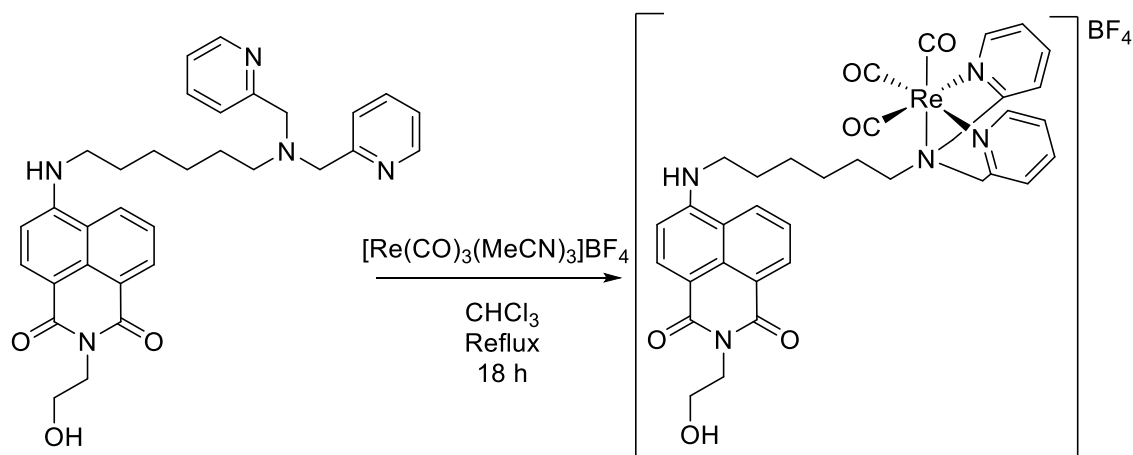
Synthesis of L⁶: Prepared as for **L**⁵ but using **N**⁶ (0.06 g, 0.15 mmol), 2-pyridine carboxaldehyde (0.03 g, 0.3 mmol) and sodium trisacetoxyborohydride (0.1 g, 0.45 mmol) and triethylamine (2 mL). **L**² was isolated as a red oil (0.063 g, 72 %). ¹H NMR (500 MHz, CDCl₃): δ_H 8.47 (d, *J* = 7.3 Hz, 1H), 8.42 (d, *J* = 4.3 Hz, 2H), 8.38 (d, *J* = 8.4 Hz, 1H), 8.17 (d, *J* = 7.9 Hz, 1H), 7.53 (t, *J* = 7.1 Hz, 2H), 7.45 – 7.38 (m, 3H), 7.06 – 7.02 (m, 2H), 6.60 (d, *J* = 8.5 Hz, 1H), 6.24 (s, 1H), 4.35 (t, *J* = 6.0 Hz, 2H), 3.87 (s, 4H), 3.79 (t, *J* = 4.7 Hz, 2H), 3.66 (t, *J* = 6.0 Hz, 2H), 3.61 (d, *J* = 4.8 Hz, 4H), 3.55 – 3.52 (m, 2H), 3.48 (d, *J* = 4.8 Hz, 2H) ppm. ¹³C NMR (126 MHz, CDCl₃) δ 165.02, 164.38, 159.72, 150.04, 149.12, 136.60, 134.74, 131.39, 130.10, 127.08, 124.66, 123.08, 122.95, 122.47, 122.15, 120.74, 110.21, 104.34, 70.48, 70.35, 69.95, 69.67, 68.71, 60.87, 58.92, 53.66, 43.28, 39.08. LRMS found *m/z* = 584.28 [M+H]⁺. HRMS expected *m/z* = 584.2867 for [M+H]⁺, found *m/z* = 584.2873. UV-vis. (MeCN) λ_{max} (ε / dm³mol⁻¹cm⁻¹): 429 (7920), 281 (19600), 263 (20600) nm.

5.4.7.2. *fac*-[Re(CO)₃L^x]BF₄ complexes

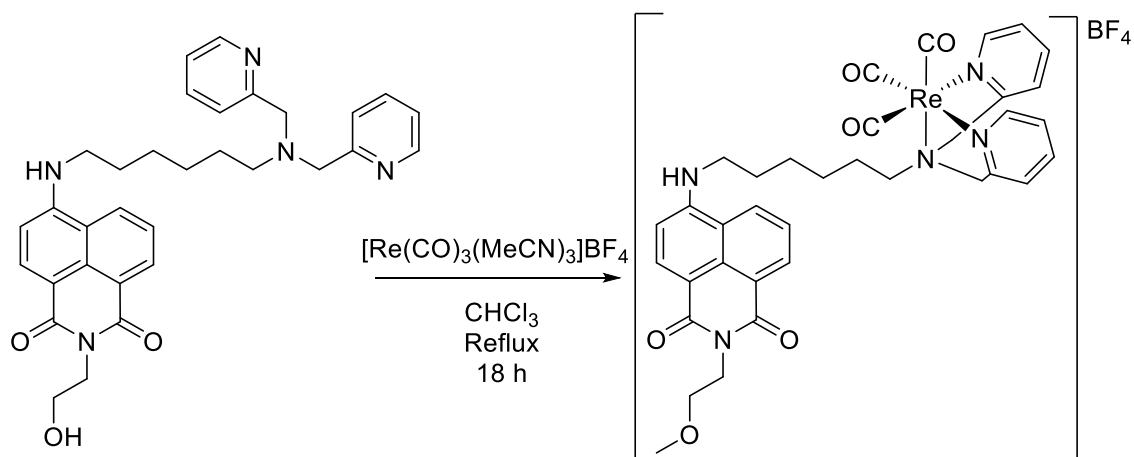
Synthesis of *fac*-[Re(CO)₃(L¹)]BF₄: Compound L¹ (50 mg, 0.10 mmol) was dissolved in chloroform and *fac*-[Re(CO)₃(MeCN)₃]BF₄ (54 mg, 0.11 mmol) was added and the solution stirred at reflux under a nitrogen atmosphere for 18 hrs. Upon being allowed to cool, the solvent was reduced to a minimum and the product precipitated upon the dropwise addition of hexane. The product was then filtered to yield *fac*-[Re(CO)₃(L¹)]BF₄ as an orange solid (21.5 mg, 35%). ¹H NMR (300 MHz, CD₃CN): δ_H 8.78 (d, *J* = 5.3 Hz, 2H), 8.54 (d, *J* = 7.5 Hz, 1H), 8.44 (dd, *J* = 8.3, 5.4 Hz, 2H), 7.89 (t, *J* = 7.7 Hz, 2H), 7.77 – 7.69 (m, 1H), 7.49 – 7.41 (m, 2H), 7.35 – 7.27 (m, 2H), 6.95 (d, *J* = 8.5 Hz, 1H), 6.40 (s, 1H), 5.01 – 4.81 (m, 4H), 4.22 (apparent dd, *J* = 12.3, 6.4 Hz, 2H), 4.03 – 3.92 (m, 2H), 3.74 (t, *J* = 6.2 Hz, 2H) ppm. ¹³C{¹H} NMR (151 MHz, d₆-DMSO): δ_C 196.90, 195.60, 164.33, 163.59, 160.98, 152.34, 152.29, 150.52, 141.21, 141.20, 141.15, 134.51, 131.30, 129.79, 129.02, 126.29, 125.18, 123.85, 122.64, 120.89, 109.47, 104.79, 67.77, 67.68, 67.42, 58.45, 58.41, 41.93. LRMS found *m/z* = 752.15 for [M]⁺. LRMS found *m/z* = 752.15 for [M]⁺. HRMS expected *m/z* = 752.1506 for [M]⁺, found *m/z* = 752.1515. FTIR (solid, cm⁻¹) ν = 351, 357, 365, 376, 384, 397, 403, 438, 457, 538, 772, 1057, 1369, 1578, 1638, 1684, 1904, 2027 2890 (broad). UV-vis. (MeCN) λ_{max} (ε / dm³mol⁻¹cm⁻¹): 430 (8560), 281 (18900, sh), (21000) nm.



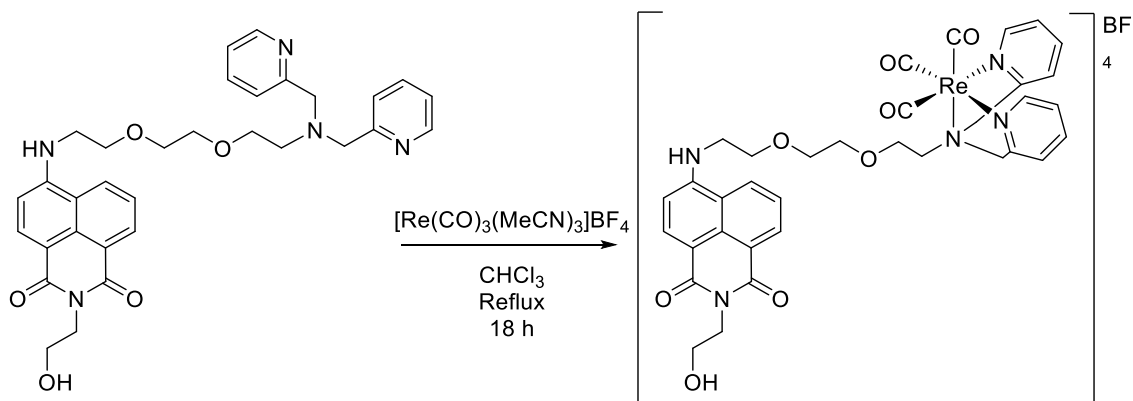
Synthesis of $fac\text{-[Re(CO)}_3\text{(L}^2\text{)]BF}_4$: Prepared as for $fac\text{-[Re(CO)}_3\text{(L}^1\text{)]BF}_4$ but using compound L^2 (58 mg, 0.1 mmol) to give the product, $fac\text{-[Re(CO)}_3\text{(L}^2\text{)]BF}_4$ as a yellow solid (22 mg, 0.028mmol, 28%) . $^1\text{H NMR}$ (400 MHz, CDCl_3): δ_{H} 8.68 (d, $J = 8.0$ Hz, 1H), 8.64 (d, $J = 5.3$ Hz, 2H), 8.59 (d, $J = 7.3$ Hz, 1H), 8.48 (d, $J = 8.2$ Hz, 1H), 7.81 – 7.66 (m, 5H), 7.22 – 7.17 (m, 2H), 6.73 (d, $J = 8.5$ Hz, 1H), 5.80 (d, $J = 16.0$ Hz, 2H), 4.52 (d, $J = 16.0$ Hz, 2H), 4.41 (t, $J = 5.8$ Hz, 2H), 4.28 – 4.15 (m, 4H), 3.71 (t, $J = 6.7$ Hz, 2H), 3.37 (s, 3H) ppm. $^{13}\text{C NMR}$ (151 MHz, CDCl_3) δ 195.74, 195.73, 164.76, 164.11, 160.85, 150.59, 150.53, 140.25, 134.54, 131.29, 129.82, 127.09, 125.21, 125.00, 124.53, 122.60, 122.29, 120.43, 70.46, 70.46, 70.15, 69.79, 68.32, 67.72, 67.40, 58.72, 43.70, 38.90, 15.28, 3.67. LRMS found $m/z = 766.17$ for $[\text{M}]^+$. HRMS expected $m/z = 766.1657$ for $[\text{M}]^+$, found $m/z 766.1671$. FTIR (solid, cm^{-1}) $\nu = 203, 222, 230, 237, 270, 291, 314, 326, 345, 357, 374, 392, 397, 419, 590, 1034, 1055, 1578, 1638, 1684, 1910, 2029, 2342, 2359$. UV-vis. (MeCN) λ_{max} ($\epsilon / \text{dm}^3\text{mol}^{-1}\text{cm}^{-1}$): 433 (9800), 280 (18400, sh), 261 (22500) nm.



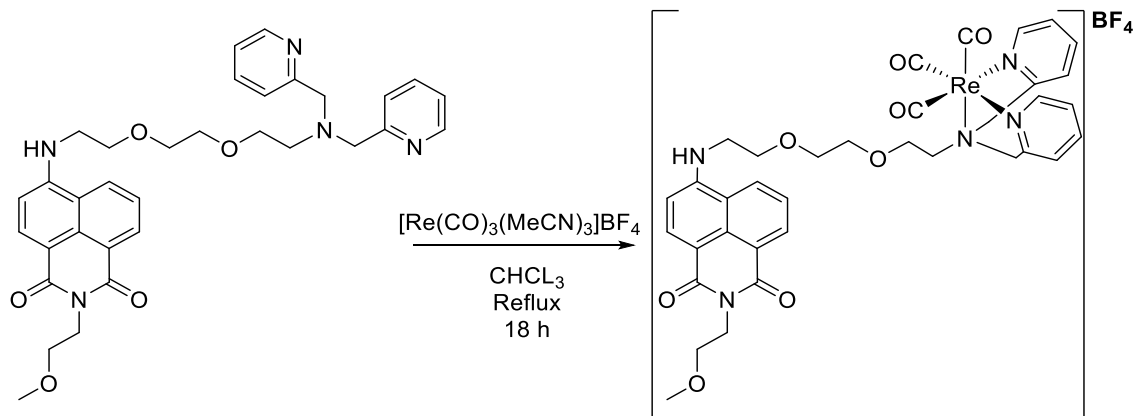
Synthesis of $fac\text{-[Re(CO)}_3\text{(L}^3\text{)]BF}_4$: Prepared as for $fac\text{-[Re(CO)}_3\text{(L}^1\text{)]BF}_4$ but using compound L^3 (58 mg, 0.1 mmol) to give the product $fac\text{-[Re(CO)}_3\text{(L}^3\text{)]BF}_4$ as an orange solid (31 mg, 0.039 mmol, 39%). $^1\text{H NMR}$ (400 MHz, CDCl_3) δ 8.68 (d, $J = 8.0$ Hz, 1H), 8.64 (d, $J = 5.3$ Hz, 2H), 8.59 (d, $J = 7.3$ Hz, 1H), 8.48 (d, $J = 8.2$ Hz, 1H), 7.81 – 7.66 (m, 5H), 7.22 – 7.17 (m, 2H), 6.73 (d, $J = 8.5$ Hz, 1H), 5.80 (d, $J = 16.0$ Hz, 2H), 4.52 (d, $J = 16.0$ Hz, 2H), 4.41 (t, $J = 5.8$ Hz, 2H), 4.28 – 4.15 (m, 4H), 3.71 (t, $J = 6.7$ Hz, 2H), 3.37 (s, 3H). $^{13}\text{C}\{^1\text{H}\}$ NMR (151 MHz, CD_3OD): δ_{C} 197.13, 196.19, 166.18, 165.72, 161.91, 161.34, 153.23, 151.64, 141.75, 135.67, 132.45, 131.10, 129.28, 127.20, 127.02, 126.08, 124.81, 124.73, 110.94, 105.56, 70.70, 68.94, 68.91, 58.94, 49.85, 40.47, 39.88 ppm. LRMS found $m/z = 808.21$ for $[\text{M}]^+$. HRMS expected $m/z = 808.2145$ for $[\text{M}]^+$, found $m/z = 808.2132$. FTIR (solid, cm^{-1}) $\nu = 349, 368, 372, 378, 393, 397, 413, 704, 733, 1072, 1125, 1263, 1379, 1460, 1582, 1638, 1721, 1944, 2031, 2050, 2930$ (broad). UV-vis. (MeCN) λ_{max} ($\epsilon / \text{dm}^3\text{mol}^{-1}\text{cm}^{-1}$): 434 (10100), 279 (18200), 256 (22400) nm.



Synthesis of $fac\text{-[Re(CO)}_3\text{(L}^4\text{)]BF}_4$: Prepared as for $fac\text{-[Re(CO)}_3\text{(L}^1\text{)]BF}_4$ but using compound L^4 (62 mg, 1.0 mmol) to give the product $fac\text{[Re(CO)}_3\text{(L}^4\text{)]BF}_4$ as an orange solid (19 mg, 0.023 mmol, 23%). $^1\text{H NMR}$ (400 MHz, CDCl_3) δ 8.66 – 8.54 (m, 3H), 8.52 (d, $J = 7.2$ Hz, 1H), 8.41 (d, $J = 8.3$ Hz, 1H), 7.71 (t, $J = 7.9$ Hz, 2H), 7.63 (t, $J = 10.7$ Hz, 3H), 7.15 – 7.10 (m, 3H), 5.73 (d, $J = 16.0$ Hz, 2H), 4.45 (d, $J = 16.0$ Hz, 2H), 4.34 (t, $J = 6.3$ Hz, 2H), 4.21 – 4.08 (m, 4H), 3.64 (t, $J = 6.4$ Hz, 2H), 3.31 (s, 3H), 1.14 (t, $J = 7.1$ Hz, 4H). $^{13}\text{C NMR}$ (151 MHz, MeOD) δ 195.52, 164.77, 164.25, 160.51, 159.92, 151.82, 150.21, 140.52, 140.34, 134.40, 130.92, 128.80, 127.73, 125.62, 125.43, 124.61, 123.40, 123.32, 109.53, 104.15, 69.29, 67.53, 67.50, 57.54, 48.47, 48.20, 48.10, 47.17, 46.56, 39.06, 38.48, 7.80. LRMS found $m/z = 822.23$ for $[\text{M}]^+$. HRMS expected $m/z = 822.2301$ for $[\text{M}]^+$, found $m/z = 822.2290$ for $[\text{M}]^+$. FTIR (solid, cm^{-1}) $\nu = 349, 361, 372, 380, 388, 403, 409, 418, 430, 437, 451, 457, 478, 520, 538, 626, 644, 769, 1022, 1055, 1352, 1379, 1578, 1611, 1639, 1681, 1907, 2029, 2056$. UV-vis. (MeCN) λ_{max} ($\epsilon / \text{dm}^3\text{mol}^{-1}\text{cm}^{-1}$): 431 (13020), 276 (24400, sh), 260 (26100) nm.



Synthesis of *fac*-[Re(CO)₃(L⁵)]BF₄: Prepared as for *fac*-[Re(CO)₃(L¹)]BF₄ but using compound L⁵ (62 mg, 0.10 mmol) to give the product *fac*[Re(CO)₃(L⁵)]BF₄ as an orange solid (26 mg, 0.031 mmol, 31%). ¹H NMR (300 MHz, CDCl₃): δ_H 8.54 (d, *J* = 5.0 Hz, 2H), 8.47 (d, *J* = 7.4 Hz, 1H), 8.41 (d, *J* = 8.4 Hz, 2H), 7.62 – 7.46 (m, 5H), 7.12 (t, *J* = 6.4 Hz, 2H), 6.73 (d, *J* = 7.6 Hz, 1H), 5.22 (d, *J* = 17.0 Hz, 2H), 4.48 – 4.37 (m, 4H), 4.01 – 3.90 (m, 8H), 3.84 (s, 4H), 3.66 (t, *J* = 5.1 Hz, 2H) ppm. ¹³C NMR (151 MHz, CDCl₃) δ 195.80, 165.59, 165.12, 160.83, 150.51, 140.00, 134.96, 131.50, 129.88, 127.58, 125.25, 124.96, 124.50, 122.30, 120.33, 109.29, 104.33, 77.23, 77.02, 76.81, 70.45, 70.13, 68.39, 67.71, 67.41, 62.49, 43.29, 42.71, 3.65. LRMS found *m/z* = 840.20 [M+H]⁺, HRMS expected *m/z* = 840.2043 for [M+H]⁺, found *m/z* = 840.2029. FTIR (solid, cm⁻¹) *v* = 217, 22, 237, 252, 287, 302, 316, 329, 354, 376, 385, 395, 397, 750, 1058, 1274, 1581, 1635, 1683, 1928, 2031, 2048, 2331, 2358, 2908 (Broad). UV-vis. (MeCN) λ_{max} (ε / dm³mol⁻¹cm⁻¹): 429 (8100), 279 (13300), 262 (18000) nm.



Synthesis of $fac\text{-[Re(CO)}_3\text{(L}^6\text{)]BF}_4$: Prepared as for $fac\text{-[Re(CO)}_3\text{(L}^5\text{)]BF}_4$ but using compound L^6 (62 mg, 1.0 mmol) to give the product $fac\text{[Re(CO)}_3\text{(L}^6\text{)]BF}_4$ as an orange solid (26 mg, 0.023 mmol, 23%). $^1\text{H NMR}$ (300 MHz, CDCl_3): δ_{H} 8.54 (d, $J = 4.9$ Hz, 2H), 8.50 – 8.34 (m, 3H), 7.62 – 7.46 (m, 5H), 7.11 (t, $J = 5.7$ Hz, 2H), 6.73 (d, $J = 8.4$ Hz, 1H), 5.23 (d, $J = 16.6$ Hz, 2H), 4.46 (s, 1H), 4.40 (t, $J = 6.3$ Hz, 3H), 4.03 – 3.91 (m, 5H), 3.85 (s, 4H), 3.72 (t, $J = 6.1$ Hz, 3H), 3.69 – 3.63 (m, 2H), 3.39 (s, 3H) ppm. $^{13}\text{C NMR}$ (151 MHz, MeOD) δ 195.81, 164.73, 164.19, 160.54, 151.54, 151.12, 139.90, 134.49, 130.83, 129.85, 127.58, 125.12, 124.34, 122.95, 122.07, 120.19, 108.16, 103.83, 70.22, 70.10, 69.35, 69.27, 68.63, 68.04, 67.77, 57.48, 42.96, 38.36. LRMS found $m/z = 854.21$ $[\text{M}]^+$, HRMS expected $m/z = 854.2196$ for $[\text{M}]^+$, found $m/z = 854.2190$. FTIR (solid, cm^{-1}) $\nu = 361, 368, 380, 388, 395, 401, 419, 440, 467, 484, 521, 538, 772, 1057, 1395, 1580, 1645, 1684, 1908, 2029, 2048, 2980$. UV-vis. (MeCN) λ_{max} ($\epsilon / \text{dm}^3\text{mol}^{-1}\text{cm}^{-1}$): 430 (12240), 281 (21000), 261 (23100) nm.

Thesis summary

From the successful development of functional ND particles and engineered *E. coli* biofilms in this work, the potential for the development of hybrid functional materials consisting of a biological material and nanoparticle functional aspect appears clear. This study therefore presents a viable route in the production of ND functionalised hybrid biofilm-based materials.

The potential for the surface functionalisation of ND with one or multiple species has been demonstrated with a focus on luminescent species as functional agents. **Nap-1** and **Ru-1** functionalised ND species were extensively characterised (Chapter 2), probing the colloidal properties, surface chemical environment and particle morphologies. SrtA enzyme active ND species exhibiting the luminophores **Nap-1** and **Ir-1** and the SrtA tag **srtApep1** were also produced and characterised (Chapter 3). SrtA modification with **[Ru(bipy)₂L₁]-Srtpep2** was well demonstrated for the **Nap-1/SrtApep1@ND** species, although further work remains in identifying whether the analogous **Ir-1** species is similarly active.

ND technologies presented here present a template for the development of further functionalised, more sophisticated particle dispersions which could incorporate multiple functional elements; either through the surface association of multiple functional elements or the use of ND lattice core-defect functionalities in conjunction with surface associated functionalities. Whilst the functional agents incorporated could differ, the fundamental surface modification chemistry developed in this thesis would be applicable regardless, provided similarly carboxyl terminated ND species were used.

Where this work outlines a genetic system whereby this is possible, it also identifies a potential problem in that the amyloid aggregation of the adhesin CsgA is highly sensitive to C-terminal modification. Whilst this was mitigated in part through incorporation of a linker region between the C-terminal ligation tag and the protein, care is clearly required in such alteration. Next steps include the demonstration of SrtA activity of the engineered biofilms, through incorporation of ND or other species, and characterisation by CFM and EM techniques developed in this thesis.

Through the further modification and development of the ligand **L⁵** from the water soluble **Nap-1** fluorophore, a bimodal imaging agent exhibiting optical/SPECT activity based on the *fac*-tricarbonyl technetium complex of **L⁵** was demonstrated to have a good applicability towards both *in-vivo* and *in-vitro* imaging, with specific potential as an MMP dependant microchondial localisation agent exhibiting good clearance routes *in-vivo*. Development of such materials is widely applicable in producing novel, bright, specific imaging agents increasing the breadth of such tools useful in medical imaging.

Bibliography

1. Cheng, A. A. & Lu, T. K. Synthetic Biology: An Emerging Engineering Discipline. *Annu. Rev. Biomed. Eng.* **14**, 155–178 (2012).
2. Le Feuvre, R. A. & Scrutton, N. S. A living foundry for Synthetic Biological Materials: A synthetic biology roadmap to new advanced materials. *Synth. Syst. Biotechnol.* **3**, 105–112 (2018).
3. Keating, K. W. & Young, E. M. Synthetic biology for bio-derived structural materials. *Curr. Opin. Chem. Eng.* **24**, 107–114 (2019).
4. Chen, J. *et al.* Composite of silver nanoparticles and photosensitizer leads to mutual enhancement of antimicrobial efficacy and promotes wound healing. *Chem. Eng. J.* **374**, 1373–1381 (2019).
5. Park, J.-S. & Kang, Y. C. Uniquely structured Sb nanoparticle-embedded carbon/reduced graphene oxide composite shell with empty voids for high performance sodium-ion storage. *Chem. Eng. J.* **373**, 227–237 (2019).
6. Merkel, T. C. *et al.* Ultrapermeable, Reverse-Selective Nanocomposite Membranes. *Science* **296**, 519–522 (2002).
7. Malmqvist, M. Surface plasmon resonance for detection and measurement of antibody-antigen affinity and kinetics. *Curr. Opin. Immunol.* **5**, 282–286 (1993).
8. Aydin, S. A short history, principles, and types of ELISA, and our laboratory experience with peptide/protein analyses using ELISA. *Peptides* **72**, 4–15 (2015).
9. Vieth, W. R., Venkatasubramanian, K., Constantinides, A. & Davidson, B. Design and Analysis of Immobilized-Enzyme Flow Reactors. in *Applied Biochemistry and Bioengineering* (eds. Wingard, L. B., Katchalski-Katzir, E. & Goldstein, L.) **1**, 221–327 (Elsevier, 1976).
10. Hutchings, G. & Edwards, J. Application of Gold Nanoparticles in Catalysis. in *Frontiers of Nanoscience* **3**, 249–293 (2012).
11. Mahmoudi, M., Sant, S., Wang, B., Laurent, S. & Sen, T. Superparamagnetic iron oxide nanoparticles (SPIONs): Development, surface modification and applications in chemotherapy. *Adv. Drug Deliv. Rev.* **63**, 24–46 (2011).
12. Tian, F., Bonnier, F., Casey, A., Shanahan, A. E. & Byrne, H. J. Surface enhanced Raman scattering with gold nanoparticles: effect of particle shape. *Anal. Methods* **6**, 9116–9123 (2014).
13. Bera, D., Qian, L., Tseng, T.-K. & Holloway, P. H. Quantum Dots and Their Multimodal Applications: A Review. *Materials* **3**, 2260–2345 (2010).
14. Hammar, M., Bian, Z. & Normark, S. Nucleator-dependent intercellular assembly of adhesive curli organelles in *Escherichia coli*. *Proc. Natl. Acad. Sci. U. S. A.* **93**, 6562–6566 (1996).
15. Hammar, M., Arnqvist, A., Bian, Z., Olsén, A. & Normark, S. Expression of two csg operons is required for production of fibronectin- and congo red-binding curli polymers in *Escherichia coli* K-12. *Mol. Microbiol.* **18**, 661–670 (1995).
16. Barnhart, M. M. & Chapman, M. R. Curli biogenesis and function. *Annu. Rev. Microbiol.* **60**, 131–147 (2006).
17. Evans, M. L. & Chapman, M. R. Curli biogenesis: Order out of disorder. *Biochim. Biophys. Acta BBA - Mol. Cell Res.* **1843**, 1551–1558 (2014).
18. Li, D. *et al.* Structure-Based Design of Functional Amyloid Materials. *J. Am. Chem. Soc.* **136**, 18044–18051 (2014).
19. Flemming, H.-C. *et al.* Biofilms: an emergent form of bacterial life. *Nat. Rev. Microbiol.* **14**, 563–575 (2016).
20. Mochalin, V. N., Shenderova, O., Ho, D. & Gogotsi, Y. The properties and applications of nanodiamonds. *Nat. Nanotechnol.* **7**, 11–23 (2012).
21. Krueger, A. & Lang, D. Functionality is Key: Recent Progress in the Surface Modification of Nanodiamond. *Adv. Funct. Mater.* **22**, 890–906 (2012).

22. Alkahtani, M. H. *et al.* Fluorescent nanodiamonds: past, present, and future. *Nanophotonics* **7**, 1423–1453 (2018).
23. Lakowicz, J. R. *Principles of Fluorescence Spectroscopy*. (Springer US, 2006).
24. Marian, C. M. Spin–orbit coupling and intersystem crossing in molecules. *Wiley Interdiscip. Rev. Comput. Mol. Sci.* **2**, 187–203 (2012).
25. Biehler, E., Mayer, F., Hoffmann, L., Krause, E. & Bohn, T. Comparison of 3 spectrophotometric methods for carotenoid determination in frequently consumed fruits and vegetables. *J. Food Sci.* **75**, C55-61 (2010).
26. Berlman, I. B. 4 - COMPOUNDS. in *Handbook of Fluorescence Spectra of Aromatic Molecules (Second Edition)* (ed. Berlman, I. B.) 67–95 (Academic Press, 1971). doi:10.1016/B978-0-12-092656-5.50009-5
27. Berlman, I. B. 7 - APPENDIX. in *Handbook of Fluorescence Spectra of Aromatic Molecules (Second Edition)* (ed. Berlman, I. B.) 417–459 (Academic Press, 1971). doi:10.1016/B978-0-12-092656-5.50012-5
28. Han, J. & Burgess, K. Fluorescent Indicators for Intracellular pH. *Chem. Rev.* **110**, 2709–2728 (2010).
29. Roy, R., Hohng, S. & Ha, T. A practical guide to single-molecule FRET. *Nat. Methods* **5**, 507–516 (2008).
30. Löber, G. The fluorescence of dye-nucleic acid complexes. *J. Lumin.* **22**, 221–265 (1981).
31. Ban, T., Hamada, D., Hasegawa, K., Naiki, H. & Goto, Y. Direct Observation of Amyloid Fibril Growth Monitored by Thioflavin T Fluorescence. *J. Biol. Chem.* **278**, 16462–16465 (2003).
32. Lou, Z., Li, P. & Han, K. Redox-Responsive Fluorescent Probes with Different Design Strategies. *Acc. Chem. Res.* **48**, 1358–1368 (2015).
33. Huang, K. C., Mukhopadhyay, R., Wen, B., Gitai, Z. & Wingreen, N. S. Cell shape and cell-wall organization in Gram-negative bacteria. *Proc. Natl. Acad. Sci.* **105**, 19282–19287 (2008).
34. Chaudhuri, R. R. & Henderson, I. R. The evolution of the Escherichia coli phylogeny. *Infect. Genet. Evol.* **12**, 214–226 (2012).
35. Gordon, D. M. Chapter 1 - The ecology of Escherichia coli. in *Escherichia coli (Second Edition)* (ed. Donnenberg, M. S.) 3–20 (Academic Press, 2013). doi:10.1016/B978-0-12-397048-0.00001-2
36. Stromberg, Z. R. *et al.* Pathogenic and non-pathogenic Escherichia coli colonization and host inflammatory response in a defined microbiota mouse model. *Dis. Model. Mech.* **11**, dmm035063 (2018).
37. Bachmann, B. J. Pedigrees of some mutant strains of Escherichia coli K-12. *Bacteriol. Rev.* **36**, 525–557 (1972).
38. Delbrück, M. Interference Between Bacterial Viruses. *J. Bacteriol.* **50**, 151–170 (1945).
39. Blattner, F. R. *et al.* The Complete Genome Sequence of Escherichia coli K-12. *Science* **277**, 1453–1462 (1997).
40. Sano, Y. & Kageyama, M. The sequence and function of the recA gene and its protein in Pseudomonas aeruginosa PAO. *Mol. Gen. Genet. MGG* **208**, 412–419 (1987).
41. Taylor, R. G., Walker, D. C. & McInnes, R. R. E. coli host strains significantly affect the quality of small scale plasmid DNA preparations used for sequencing. *Nucleic Acids Res.* **21**, 1677–1678 (1993).
42. Hayashi, K. *et al.* Highly accurate genome sequences of Escherichia coli K-12 strains MG1655 and W3110. *Mol. Syst. Biol.* **2**, 2006.0007 (2006).
43. BL21(DE3) Competent E. coli | NEB. Available at: <https://www.neb.com/products/c2527-bl21de3-competent-e-coli#Product%20Information>. (Accessed: 27th July 2018)

44. XL-1 Blue - EcoliWiki. Available at: https://ecoliwiki.org/colipedia/index.php/XL-1_Blue. (Accessed: 13th August 2019)
45. Voet, D. & Voet, J. G. *Biochemistry*. (Wiley, 2004).
46. Addgene: Protocol - Bacterial Transformation. Available at: <https://www.addgene.org/protocols/bacterial-transformation/>. (Accessed: 15th August 2019)
47. Plasmid Miniprep Kit: QIAprep Spin Miniprep Kit - QIAGEN Online Shop. Available at: <https://www.qiagen.com/gb/products/discovery-and-translational-research/dna-rna-purification/dna-purification/plasmid-dna/qiaprep-spin-miniprep-kit/#productdetails>. (Accessed: 15th August 2019)
48. Addgene: Promoters. Available at: <https://www.addgene.org/mol-bio-reference/promoters/>. (Accessed: 15th August 2019)
49. Promoters/Catalog/Anderson - parts.igem.org. Available at: <http://parts.igem.org/Promoters/Catalog/Anderson>. (Accessed: 15th August 2019)
50. Addgene: Plasmid Cloning by Restriction Enzyme Digest (with Protocols). Available at: <https://www.addgene.org/protocols/subcloning/>. (Accessed: 15th August 2019)
51. Engler, C., Kandzia, R. & Marillonnet, S. A One Pot, One Step, Precision Cloning Method with High Throughput Capability. *PLOS ONE* **3**, e3647 (2008).
52. Gibson, D. G. *et al.* Enzymatic assembly of DNA molecules up to several hundred kilobases. *Nat. Methods* **6**, 343–345 (2009).
53. Salomon, M., Christie, J. M., Knieb, E., Lempert, U. & Briggs, W. R. Photochemical and Mutational Analysis of the FMN-Binding Domains of the Plant Blue Light Receptor, Phototropin \dagger , \ddagger . *Biochemistry* **39**, 9401–9410 (2000).
54. Reginald H. Garrett, C. M. G. ; W. M. G. I. B. M. S. *Biochemistry, International Edition*. (Brooks Cole - M.U.A).
55. Lutz, R. & Bujard, H. Independent and tight regulation of transcriptional units in *Escherichia coli* via the LacR/O, the TetR/O and AraC/I1-I2 regulatory elements. *Nucleic Acids Res.* **25**, 1203–1210 (1997).
56. Tabor, S. Expression Using the T7 RNA Polymerase/Promoter System. *Curr. Protoc. Mol. Biol.* **11**, 16.2.1-16.2.11 (1990).
57. Chien, A., Edgar, D. B. & Trela, J. M. Deoxyribonucleic acid polymerase from the extreme thermophile *Thermus aquaticus*. *J. Bacteriol.* **127**, 1550–1557 (1976).
58. Taq and Other Thermostable DNA Polymerases. in *Principles and Technical Aspects of PCR Amplification* (eds. van Pelt-Verkuil, E., van Belkum, A. & Hays, J. P.) 103–118 (Springer Netherlands, 2008). doi:10.1007/978-1-4020-6241-4_7
59. PrimeSTAR HS DNA Polymerase. Available at: <https://www.takarabio.com/products/pcr/high-fidelity-pcr/primestar-hs-dna-polymerase>. (Accessed: 15th August 2019)
60. Schrand, A. M., Hens, S. A. C. & Shenderova, O. A. Nanodiamond Particles: Properties and Perspectives for Bioapplications. *Crit. Rev. Solid State Mater. Sci.* **34**, 18–74 (2009).
61. Mochalin, V. N., Shenderova, O., Ho, D. & Gogotsi, Y. The properties and applications of nanodiamonds. *Nat. Nanotechnol.* **7**, 11–23 (2012).
62. Barnard, A. S., Russo, S. P. & Snook, I. K. Ab initio modeling of B and N in C29 and C29H24 nanodiamond. *J. Chem. Phys.* **118**, 10725–10728 (2003).
63. Barnard, A. S. & Sternberg, M. Crystallinity and surface electrostatics of diamond nanocrystals. *J. Mater. Chem.* **17**, 4811–4819 (2007).
64. Osswald, S., Yushin, G., Mochalin, V., Kucheyev, S. O. & Gogotsi, Y. Control of sp²/sp³ carbon ratio and surface chemistry of nanodiamond powders by selective oxidation in air. *J. Am. Chem. Soc.* **128**, 11635–11642 (2006).
65. Danilenko, V. V. On the history of the discovery of nanodiamond synthesis. *Phys. Solid State* **46**, 595–599 (2004).

66. Schrand, A. M., Hens, S. A. C. & Shenderova, O. A. Nanodiamond Particles: Properties and Perspectives for Bioapplications. *Crit. Rev. Solid State Mater. Sci.* **34**, 18–74 (2009).
67. Greiner, N. R., Phillips, D. S., Johnson, J. D. & Volk, F. Diamonds in detonation soot. *Nature* **333**, 440–442 (1988).
68. Chang, Y.-R. *et al.* Mass production and dynamic imaging of fluorescent nanodiamonds. *Nat Nano* **3**, 284–288 (2008).
69. Butler, J. E. & Sumant, A. V. The CVD of Nanodiamond Materials. *Chem. Vap. Depos.* **14**, 145–160 (2008).
70. Vul', A. Y., Dideikin, A. T., Aleksenskii, A. E. & Baidakova, M. V. CHAPTER 2: Detonation Nanodiamonds: Synthesis, Properties and Applications. in *Nanodiamond* 27–48 (2014). doi:10.1039/9781849737616-00027
71. Dolmatov, V. Y. Detonation synthesis ultradispersed diamonds: properties and applications. *Russ. Chem. Rev.* **70**, 607–626 (2001).
72. Rondin, L. *et al.* Surface-induced charge state conversion of nitrogen-vacancy defects in nanodiamonds. *Phys. Rev. B* **82**, 115449 (2010).
73. Butenko, Yu. V. *et al.* The Thermal Stability of Nanodiamond Surface Groups and Onset of Nanodiamond Graphitization. *Fuller. Nanotub. Carbon Nanostructures* **14**, 557–564 (2006).
74. Pavlov, E. V. & Skrjabin, J. A. Method for removal of impurities of non-diamond carbon and device for its realization. (1994).
75. Osswald, S., Yushin, G., Mochalin, V., Kucheyev, S. O. & Gogotsi, Y. Control of sp²/sp³ Carbon Ratio and Surface Chemistry of Nanodiamond Powders by Selective Oxidation in Air. *J. Am. Chem. Soc.* **128**, 11635–11642 (2006).
76. Zou, Q., Wang, M. Z. & Li, Y. G. Analysis of the nanodiamond particle fabricated by detonation. *J. Exp. Nanosci.* **5**, 319–328 (2010).
77. Krueger, A. & Lang, D. Functionality is Key: Recent Progress in the Surface Modification of Nanodiamond. *Adv. Funct. Mater.* **22**, 890–906 (2012).
78. Mochalin, V., Osswald, S. & Gogotsi, Y. Contribution of Functional Groups to the Raman Spectrum of Nanodiamond Powders. *Chem. Mater.* **21**, 273–279 (2009).
79. Shenderova, O. *et al.* Surface Chemistry and Properties of Ozone-Purified Detonation Nanodiamonds. *J. Phys. Chem. C* **115**, 9827–9837 (2011).
80. Portet, C., Yushin, G. & Gogotsi, Y. Electrochemical performance of carbon onions, nanodiamonds, carbon black and multiwalled nanotubes in electrical double layer capacitors. *Carbon* **45**, 2511–2518 (2007).
81. Ginés, L. *et al.* Positive zeta potential of nanodiamonds. *Nanoscale* (2017). doi:10.1039/C7NR03200E
82. Arnault, J. C. & Girard, H. A. Hydrogenated nanodiamonds: Synthesis and surface properties. *Curr. Opin. Solid State Mater. Sci.* **21**, 10–16 (2017).
83. Ackermann, J. & Krueger, A. Efficient surface functionalization of detonation nanodiamond using ozone under ambient conditions. *Nanoscale* **11**, 8012–8019 (2019).
84. Liu, Y., Gu, Z., Margrave, J. L. & Khabashesku, V. N. Functionalization of Nanoscale Diamond Powder: Fluoro-, Alkyl-, Amino-, and Amino Acid-Nanodiamond Derivatives. *Chem. Mater.* **16**, 3924–3930 (2004).
85. Havlik, J. *et al.* Benchtop Fluorination of Fluorescent Nanodiamonds on a Preparative Scale: Toward Unusually Hydrophilic Bright Particles. *Adv. Funct. Mater.* **26**, 4134–4142 (2016).
86. Sushkov, A. O. *et al.* All-Optical Sensing of a Single-Molecule Electron Spin. *Nano Lett.* **14**, 6443–6448 (2014).
87. Neitzel, I., Mochalin, V., Knoke, I., Palmese, G. R. & Gogotsi, Y. Mechanical properties of epoxy composites with high contents of nanodiamond. *Compos. Sci. Technol.* **71**, 710–716 (2011).

88. Behler, K. D. *et al.* Nanodiamond-Polymer Composite Fibers and Coatings. *ACS Nano* **3**, 363–369 (2009).
89. Dolmatov, V. Yu. Polymer-diamond composites based on detonation nanodiamonds. Part 1. *J. Superhard Mater.* **29**, 1–11 (2007).
90. Maitra, U., Prasad, K. E., Ramamurty, U. & Rao, C. N. R. Mechanical properties of nanodiamond-reinforced polymer-matrix composites. *Solid State Commun.* **149**, 1693–1697 (2009).
91. Huang, H., Pierstorff, E., Osawa, E. & Ho, D. Active nanodiamond hydrogels for chemotherapeutic delivery. *Nano Lett.* **7**, 3305–3314 (2007).
92. Chen, M. *et al.* Nanodiamond-Mediated Delivery of Water-Insoluble Therapeutics. *ACS Nano* **3**, 2016–2022 (2009).
93. Boudou, J.-P., David, M.-O., Joshi, V., Eidi, H. & Curmi, P. A. Hyperbranched polyglycerol modified fluorescent nanodiamond for biomedical research. *Diam. Relat. Mater.* **38**, 131–138 (2013).
94. Fu, C.-C. *et al.* Characterization and application of single fluorescent nanodiamonds as cellular biomarkers. *Proc. Natl. Acad. Sci. U. S. A.* **104**, 727–732 (2007).
95. Yu, S.-J., Kang, M.-W., Chang, H.-C., Chen, K.-M. & Yu, Y.-C. Bright Fluorescent Nanodiamonds: No Photobleaching and Low Cytotoxicity. *J. Am. Chem. Soc.* **127**, 17604–17605 (2005).
96. Chang, I. P., Hwang, K. C. & Chiang, C.-S. Preparation of Fluorescent Magnetic Nanodiamonds and Cellular Imaging. *J. Am. Chem. Soc.* **130**, 15476–15481 (2008).
97. Turcheniuk, K. & Mochalin, V. N. Biomedical applications of nanodiamond (Review). *Nanotechnology* **28**, 252001 (2017).
98. Wu, Y. & Weil, T. Nanodiamonds for Biological Applications. *Phys. Sci. Rev.* **2**, (2017).
99. Zhang, Q., Naito, K., Tanaka, Y. & Kagawa, Y. Grafting Polyimides from Nanodiamonds. *Macromolecules* **41**, 536–538 (2008).
100. Zhang, Q. *et al.* Fluorescent PLLA-nanodiamond composites for bone tissue engineering. *Biomaterials* **32**, 87–94 (2011).
101. Krueger, A., Liang, Y., Jarre, G. & Stegk, J. Surface functionalisation of detonation diamond suitable for biological applications. *J. Mater. Chem.* **16**, 2322–2328 (2006).
102. Schrand, A. M. *et al.* Are Diamond Nanoparticles Cytotoxic? *J. Phys. Chem. B* **111**, 2–7 (2007).
103. Say, J. M. *et al.* Luminescent nanodiamonds for biomedical applications. *Biophys. Rev.* **3**, 171–184 (2011).
104. Fu, C.-C. *et al.* Characterization and application of single fluorescent nanodiamonds as cellular biomarkers. *Proc. Natl. Acad. Sci. U. S. A.* **104**, 727–732 (2007).
105. Schirhagl, R., Chang, K., Loretz, M. & Degen, C. L. Nitrogen-Vacancy Centers in Diamond: Nanoscale Sensors for Physics and Biology. *Annu. Rev. Phys. Chem.* **65**, 83–105 (2014).
106. Mohan, N., Chen, C.-S., Hsieh, H.-H., Wu, Y.-C. & Chang, H.-C. In Vivo Imaging and Toxicity Assessments of Fluorescent Nanodiamonds in *Caenorhabditis elegans*. *Nano Lett.* **10**, 3692–3699 (2010).
107. Chapman, R. & Plakhotnik, T. Quantitative luminescence microscopy on Nitrogen-Vacancy Centres in diamond: Saturation effects under pulsed excitation. *Chem. Phys. Lett.* **507**, 190–194 (2011).
108. Malvern Instruments. Zetasizer nano series user manual. (2009).
109. Konno, H. Chapter 8 - X-ray Photoelectron Spectroscopy. in *Materials Science and Engineering of Carbon* (eds. Inagaki, M. & Kang, F.) 153–171 (Butterworth-Heinemann, 2016). doi:10.1016/B978-0-12-805256-3.00008-8

110. Moulder, J. F., Stickle, W. F., Sobol, P. E. & Bombon, K. D. *Handbook of X-ray Photoelectron spectroscopy*. (Physical Electronics Inc., 1995).
111. Chang, M. S., Kim, T., Kang, J. H., Park, J. & Park, C. R. The effect of surface characteristics of reduced graphene oxide on the performance of a pseudocapacitor. *2D Mater.* **2**, 014007 (2015).
112. Langdon-Jones, E. E. *et al.* Fluorescent Rhenium-Naphthalimide Conjugates as Cellular Imaging Agents. (2014). doi:10.1021/ic500142z
113. Martinez, R. D., Mancini, P. M. E., Vottero, L. R. & Nudelman, N. S. Solvent effects on aromatic nucleophilic substitutions. Part 4. Kinetics of the reaction of 1-chloro-2,4-dinitrobenzene with piperidine in protic solvents. *J. Chem. Soc. Perkin Trans. 2* **0**, 1427–1431 (1986).
114. Banerjee, S. *et al.* Recent advances in the development of 1,8-naphthalimide based DNA targeting binders, anticancer and fluorescent cellular imaging agents. *Chem. Soc. Rev.* **42**, 1601–1618 (2013).
115. Bardajee, G. R., Li, A. Y., Haley, J. C. & Winnik, M. A. The synthesis and spectroscopic properties of novel, functional fluorescent naphthalimide dyes. *Dyes Pigments* **79**, 24–32 (2008).
116. Turnbull, W. L. *et al.* A dual modality ^{99m}Tc/Re(I)-labelled T140 analogue for imaging of CXCR4 expression. *Org. Biomol. Chem.* **17**, 598–608 (2019).
117. Lim, D. G. *et al.* Comprehensive evaluation of carboxylated nanodiamond as a topical drug delivery system. *Int. J. Nanomedicine* **11**, 2381–2395 (2016).
118. Rück-Braun, K. *et al.* Formation of Carboxy- and Amide-Terminated Alkyl Monolayers on Silicon(111) Investigated by ATR-FTIR, XPS, and X-ray Scattering: Construction of Photoswitchable Surfaces. *Langmuir* **29**, 11758–11769 (2013).
119. Frank, M. *et al.* Dinuclear Rull and/or OsII complexes of bis-bipyridine bridging ligands containing adamantane spacers: synthesis, luminescence properties, intercomponent energy and electron transfer processes. *Inorganica Chim. Acta* **242**, 281–291 (1996).
120. Paterson, G. K. & Mitchell, T. J. The biology of Gram-positive sortase enzymes. *Trends Microbiol.* **12**, 89–95 (2004).
121. Perry, A. M., Ton-That, H., Mazmanian, S. K. & Schneewind, O. Anchoring of Surface Proteins to the Cell Wall of *Staphylococcus aureus* III. LIPID II IS AN IN VIVO PEPTIDOGLYCAN SUBSTRATE FOR SORTASE-CATALYZED SURFACE PROTEIN ANCHORING. *J. Biol. Chem.* **277**, 16241–16248 (2002).
122. Kline, K. A., Dodson, K. W., Caparon, M. G. & Hultgren, S. J. A tale of two pili: assembly and function of pili in bacteria. *Trends Microbiol.* **18**, 224–232 (2010).
123. Maresso, A. W. & Schneewind, O. Sortase as a Target of Anti-Infective Therapy. *Pharmacol. Rev.* **60**, 128–141 (2008).
124. Suree, N., Jung, M. E. & Clubb, R. T. Recent advances towards new anti-infective agents that inhibit cell surface protein anchoring in *Staphylococcus aureus* and other gram-positive pathogens. *Mini Rev. Med. Chem.* **7**, 991–1000 (2007).
125. Glasgow, J. E., Salit, M. L. & Cochran, J. R. In Vivo Site-Specific Protein Tagging with Diverse Amines Using an Engineered Sortase Variant. *J. Am. Chem. Soc.* **138**, 7496–7499 (2016).
126. Guimaraes, C. P. *et al.* Site-specific C-terminal and internal loop labeling of proteins using sortase-mediated reactions. *Nat. Protoc.* **8**, 1787–1799 (2013).
127. Sijbrandij, T., Cukkemane, N., Nazmi, K., Veerman, E. C. I. & Bikker, F. J. Sortase A as a Tool to Functionalize Surfaces. *Bioconjug. Chem.* **24**, 828–831 (2013).
128. Pallen, M. J., Lam, A. C., Antonio, M. & Dunbar, K. An embarrassment of sortases - a richness of substrates? *Trends Microbiol.* **9**, 97–102 (2001).
129. Clancy, K. W., Melvin, J. A. & McCafferty, D. G. Sortase Transpeptidases: Insights into Mechanism, Substrate Specificity and Inhibition. *Biopolymers* **94**, 385–396 (2010).

130. Naik, M. T. *et al.* Staphylococcus aureus Sortase A transpeptidase. Calcium promotes sorting signal binding by altering the mobility and structure of an active site loop. *J. Biol. Chem.* **281**, 1817–1826 (2006).
131. Ton-That, H., Liu, G., Mazmanian, S. K., Faull, K. F. & Schneewind, O. Purification and characterization of sortase, the transpeptidase that cleaves surface proteins of Staphylococcus aureus at the LPXTG motif. *Proc. Natl. Acad. Sci. U. S. A.* **96**, 12424–12429 (1999).
132. Frankel, B. A., Tong, Y., Bentley, M. L., Fitzgerald, M. C. & McCafferty, D. G. Mutational Analysis of Active Site Residues in the Staphylococcus aureus Transpeptidase SrtA. *Biochemistry* **46**, 7269–7278 (2007).
133. Zong, Y., Bice, T. W., Ton-That, H., Schneewind, O. & Narayana, S. V. L. Crystal Structures of Staphylococcus aureus Sortase A and Its Substrate Complex. *J. Biol. Chem.* **279**, 31383–31389 (2004).
134. Antos, J. M. *et al.* Site-Specific Protein Labeling via Sortase-Mediated Transpeptidation. *Curr. Protoc. Protein Sci.* **CHAPTER 15**, Unit-15.3 (2009).
135. Huang, X. *et al.* Kinetic Mechanism of Staphylococcus aureus Sortase SrtA. *Biochemistry* **42**, 11307–11315 (2003).
136. Frankel, B. A., Kruger, R. G., Robinson, D. E., Kelleher, N. L. & McCafferty, D. G. Staphylococcus aureus sortase transpeptidase SrtA: insight into the kinetic mechanism and evidence for a reverse protonation catalytic mechanism. *Biochemistry* **44**, 11188–11200 (2005).
137. Vocadlo, D. J., Wicki, J., Rupitz, K. & Withers, S. G. A case for reverse protonation: identification of Glu160 as an acid/base catalyst in Thermoanaerobacterium saccharolyticum beta-xylosidase and detailed kinetic analysis of a site-directed mutant. *Biochemistry* **41**, 9736–9746 (2002).
138. Mock, W. L. & Stanford, D. J. Arazoformyl dipeptide substrates for thermolysin. Confirmation of a reverse protonation catalytic mechanism. *Biochemistry* **35**, 7369–7377 (1996).
139. Race, P. R. *et al.* Crystal Structure of Streptococcus pyogenes Sortase A IMPLICATIONS FOR SORTASE MECHANISM. *J. Biol. Chem.* **284**, 6924–6933 (2009).
140. Ton-That, H., Mazmanian, S. K., Alksne, L. & Schneewind, O. Anchoring of surface proteins to the cell wall of Staphylococcus aureus. Cysteine 184 and histidine 120 of sortase form a thiolate-imidazolium ion pair for catalysis. *J. Biol. Chem.* **277**, 7447–7452 (2002).
141. Antos, J. M., Truttmann, M. C. & Ploegh, H. L. Recent Advances in Sortase-Catalyzed Ligation Methodology. *Curr. Opin. Struct. Biol.* **38**, 111–118 (2016).
142. Hirakawa, H., Ishikawa, S. & Nagamune, T. Design of Ca²⁺-independent Staphylococcus aureus sortase A mutants. *Biotechnol. Bioeng.* **109**, 2955–2961 (2012).
143. Hirakawa, H., Ishikawa, S. & Nagamune, T. Ca²⁺-independent sortase-A exhibits high selective protein ligation activity in the cytoplasm of Escherichia coli. *Biotechnol. J.* **10**, 1487–1492 (2015).
144. Dai, X., Böker, A. & Glebe, U. Broadening the scope of sortagging. *RSC Adv.* **9**, 4700–4721 (2019).
145. Popp, M. W., Dougan, S. K., Chuang, T.-Y., Spooner, E. & Ploegh, H. L. Sortase-catalyzed transformations that improve the properties of cytokines. *Proc. Natl. Acad. Sci. U. S. A.* **108**, 3169–3174 (2011).
146. Antos, J. M., Miller, G. M., Grotenbreg, G. M. & Ploegh, H. L. Lipid modification of proteins through sortase-catalyzed transpeptidation. *J. Am. Chem. Soc.* **130**, 16338–16343 (2008).
147. Williamson, D. J., Fascione, M. A., Webb, M. E. & Turnbull, W. B. Efficient N-Terminal Labeling of Proteins by Use of Sortase. *Angew. Chem. Int. Ed.* **51**, 9377–9380 (2012).

148. Popp, M. W., Artavanis-Tsakonas, K. & Ploegh, H. L. Substrate Filtering by the Active Site Crossover Loop in UCHL3 Revealed by Sortagging and Gain-of-function Mutations. *J. Biol. Chem.* **284**, 3593–3602 (2009).
149. Jiang, R., Weingart, J., Zhang, H., Ma, Y. & Sun, X.-L. End-point immobilization of recombinant thrombomodulin via sortase-mediated ligation. *Bioconjug. Chem.* **23**, 643–649 (2012).
150. Raeeszadeh-Sarmazdeh, M., Parthasarathy, R. & Boder, E. T. Site-specific immobilization of protein layers on gold surfaces via orthogonal sortases. *Colloids Surf. B Biointerfaces* **128**, 457–463 (2015).
151. Ta, H. T. *et al.* Enzymatic single-chain antibody tagging: a universal approach to targeted molecular imaging and cell homing in cardiovascular disease. *Circ. Res.* **109**, 365–373 (2011).
152. Hata, Y., Matsumoto, T., Tanaka, T. & Kondo, A. C-Terminal-oriented Immobilization of Enzymes Using Sortase A-mediated Technique. *Macromol. Biosci.* **15**, 1375–1380 (2015).
153. Nguyen, H. D., Phan, T. T. P. & Schumann, W. Analysis and application of *Bacillus subtilis* sortases to anchor recombinant proteins on the cell wall. *AMB Express* **1**, 22 (2011).
154. Azzarito, V., Long, K., Murphy, N. S. & Wilson, A. J. Inhibition of α -helix-mediated protein-protein interactions using designed molecules. *Nat. Chem.* **5**, 161–173 (2013).
155. Swee, L. K., Lourido, S., Bell, G. W., Ingram, J. R. & Ploegh, H. L. One-step enzymatic modification of the cell surface redirects cellular cytotoxicity and parasite tropism. *ACS Chem. Biol.* **10**, 460–465 (2015).
156. Phillips, K. A. *et al.* Ligand-Tuneable, Red-Emitting Iridium(III) Complexes for Efficient Triplet-Triplet Annihilation Upconversion Performance. *Chem. - Eur. J.* **24**, 8577–8588 (2018).
157. Langdon-Jones, E. E. *et al.* Using Substituted Cyclometalated Quinoxaline Ligands To Finely Tune the Luminescence Properties of Iridium(III) Complexes. *Inorg. Chem.* **52**, 448–456 (2013).
158. Mohammadi, B., Majnooni, M. B., Khatabi, P. M., Jalili, R. & Bahrami, G. 9-fluorenylmethyl chloroformate as a fluorescence-labeling reagent for derivatization of carboxylic acid moiety of sodium valproate using liquid chromatography/tandem mass spectrometry for binding characterization: a human pharmacokinetic study. *J. Chromatogr. B Analyt. Technol. Biomed. Life. Sci.* **880**, 12–18 (2012).
159. Sciuto, E. L. *et al.* Photo-physical characterization of fluorophore Ru(bpy)₃²⁺ for optical biosensing applications. *Sens. Bio-Sens. Res.* **6**, 67–71 (2015).
160. Guimaraes, C. P. *et al.* Site-specific C-terminal and internal loop labeling of proteins using sortase-mediated reactions. *Nat. Protoc.* **8**, 1787–1799 (2013).
161. Stoodley, P., Sauer, K., Davies, D. G. & Costerton, J. W. Biofilms as complex differentiated communities. *Annu. Rev. Microbiol.* **56**, 187–209 (2002).
162. Flemming, H.-C. *et al.* Biofilms: an emergent form of bacterial life. *Nat. Rev. Microbiol.* **14**, 563–575 (2016).
163. Wingender, J. & Flemming, H.-C. Biofilms in drinking water and their role as reservoir for pathogens. *Int. J. Hyg. Environ. Health* **214**, 417–423 (2011).
164. DeBenedictis, E. P., Liu, J. & Keten, S. Adhesion mechanisms of curli subunit CsgA to abiotic surfaces. *Sci. Adv.* **2**, e1600998 (2016).
165. Vogeleeer, P., Tremblay, Y. D. N., Mafu, A. A., Jacques, M. & Harel, J. Life on the outside: role of biofilms in environmental persistence of Shiga-toxin producing *Escherichia coli*. *Front. Microbiol.* **5**, (2014).
166. Flemming, H.-C. & Wingender, J. The biofilm matrix. *Nat. Rev. Microbiol.* **8**, 623–633 (2010).
167. Beloin, C., Roux, A. & Ghigo, J.-M. *Escherichia coli* biofilms. *Curr. Top. Microbiol. Immunol.* **322**, 249–289 (2008).

168. Jonas, K. *et al.* Roles of curli, cellulose and BapA in Salmonella biofilm morphology studied by atomic force microscopy. *Bmc Microbiol.* **7**, 70 (2007).
169. Otzen, D. Functional amyloid Turning swords into plowshares. *Prion* **4**, 256–264 (2010).
170. Kikuchi, T., Mizunoe, Y., Takade, A., Naito, S. & Yoshida, S. Curli Fibers Are Required for Development of Biofilm Architecture in Escherichia coli K-12 and Enhance Bacterial Adherence to Human Uroepithelial Cells. *Microbiol. Immunol.* **49**, 875–884 (2005).
171. Tian, P. *et al.* Structure of a Functional Amyloid Protein Subunit Computed Using Sequence Variation. *J. Am. Chem. Soc.* **137**, 22–25 (2015).
172. Robinson, L. S., Ashman, E. M., Hultgren, S. J. & Chapman, M. R. Secretion of curli fibre subunits is mediated by the outer membrane-localized CsgG protein. *Mol. Microbiol.* **59**, 870–881 (2006).
173. Dueholm, M. S. *et al.* Fibrillation of the major curli subunit CsgA under a wide range of conditions implies a robust design of aggregation. *Biochemistry* **50**, 8281–8290 (2011).
174. Wang, X., Smith, D. R., Jones, J. W. & Chapman, M. R. In vitro polymerization of a functional Escherichia coli amyloid protein. *J. Biol. Chem.* **282**, 3713–3719 (2007).
175. Wang, X. & Chapman, M. R. Sequence determinants of bacterial amyloid formation. *J. Mol. Biol.* **380**, 570–580 (2008).
176. Evans, M. L. *et al.* The Bacterial Curli System Possesses a Potent and Selective Inhibitor of Amyloid Formation. *Mol. Cell* **57**, 445–455 (2015).
177. Ogasawara, H., Yamamoto, K. & Ishihama, A. Role of the Biofilm Master Regulator CsgD in Cross-Regulation between Biofilm Formation and Flagellar Synthesis. *J. Bacteriol.* **193**, 2587–2597 (2011).
178. Brombacher, E., Baratto, A., Dorel, C. & Landini, P. Gene Expression Regulation by the Curli Activator CsgD Protein: Modulation of Cellulose Biosynthesis and Control of Negative Determinants for Microbial Adhesion. *J. Bacteriol.* **188**, 2027–2037 (2006).
179. Vidal, O. *et al.* Isolation of an Escherichia coli K-12 mutant strain able to form biofilms on inert surfaces: involvement of a new ompR allele that increases curli expression. *J. Bacteriol.* **180**, 2442–2449 (1998).
180. Evans, M. L. *et al.* The bacterial curli system possesses a potent and selective inhibitor of amyloid formation. *Mol. Cell* **57**, 445–455 (2015).
181. Chen, A. Y. *et al.* Synthesis and patterning of tunable multiscale materials with engineered cells. *Nat. Mater.* **13**, 515–523 (2014).
182. Rzhepishevskaya, O. *et al.* The surface charge of anti-bacterial coatings alters motility and biofilm architecture. *Biomater. Sci.* **1**, 589–602 (2013).
183. Ammar, Y., Swailes, D., Bridgens, B. & Chen, J. Influence of surface roughness on the initial formation of biofilm. *Surf. Coat. Technol.* **284**, 410–416 (2015).
184. Azeredo, J. *et al.* Critical review on biofilm methods. *Crit. Rev. Microbiol.* **43**, 313–351 (2017).
185. Koo, H., Allan, R. N., Howlin, R. P., Stoodley, P. & Hall-Stoodley, L. Targeting microbial biofilms: current and prospective therapeutic strategies. *Nat. Rev. Microbiol.* **15**, 740–755 (2017).
186. Djordjevic, D., Wiedmann, M. & McLandsborough, L. A. Microtiter plate assay for assessment of Listeria monocytogenes biofilm formation. *Appl. Environ. Microbiol.* **68**, 2950–2958 (2002).
187. McCoy, W. F., Bryers, J. D., Robbins, J. & Costerton, J. W. Observations of fouling biofilm formation. *Can. J. Microbiol.* **27**, 910–917 (1981).
188. Miles, A. A., Misra, S. S. & Irwin, J. O. The estimation of the bactericidal power of the blood. *J. Hyg. (Lond.)* **38**, 732–749 (1938).

189. Li, L., Mendis, N., Trigui, H., Oliver, J. D. & Faucher, S. P. The importance of the viable but non-culturable state in human bacterial pathogens. *Front. Microbiol.* **5**, 258 (2014).
190. Christensen, G. D. *et al.* Adherence of coagulase-negative staphylococci to plastic tissue culture plates: a quantitative model for the adherence of staphylococci to medical devices. *J. Clin. Microbiol.* **22**, 996–1006 (1985).
191. Fletcher, M. The effects of culture concentration and age, time, and temperature on bacterial attachment to polystyrene. *Can. J. Microbiol.* **23**, 1–6 (1977).
192. Guilbaud, M., Piveteau, P., Desvaux, M., Brisse, S. & Briandet, R. Exploring the diversity of *Listeria monocytogenes* biofilm architecture by high-throughput confocal laser scanning microscopy and the predominance of the honeycomb-like morphotype. *Appl. Environ. Microbiol.* **81**, 1813–1819 (2015).
193. Lawrence, J. R., Korber, D. R., Hoyle, B. D., Costerton, J. W. & Caldwell, D. E. Optical sectioning of microbial biofilms. *J. Bacteriol.* **173**, 6558–6567 (1991).
194. Nguyen, P. Q., Botyanszki, Z., Tay, P. K. R. & Joshi, N. S. Programmable biofilm-based materials from engineered curli nanofibres. *Nat. Commun.* **5**, ncomms5945 (2014).
195. Reichhardt, C. *et al.* Congo Red Interactions with Curli-Producing *E. coli* and Native Curli Amyloid Fibers. *PLOS ONE* **10**, e0140388 (2015).
196. Wood, P. J., Erfle, J. D. & Teather, R. M. Use of complex formation between Congo Red and polysaccharides in detection and assay of polysaccharide hydrolases. in *Methods in Enzymology* **160**, 59–74 (Academic Press, 1988).
197. Serra, D. O., Richter, A. M. & Hengge, R. Cellulose as an Architectural Element in Spatially Structured *Escherichia coli* Biofilms. *J. Bacteriol.* **195**, 5540–5554 (2013).
198. Liu, D. & Reeves, P. R. *Escherichia coli* K12 regains its O antigen. *Microbiol. Read. Engl.* **140 (Pt 1)**, 49–57 (1994).
199. Zogaj, X., Nimtz, M., Rohde, M., Bokranz, W. & Römling, U. The multicellular morphotypes of *Salmonella typhimurium* and *Escherichia coli* produce cellulose as the second component of the extracellular matrix. *Mol. Microbiol.* **39**, 1452–1463 (2001).
200. Casadaban, M. J. Transposition and fusion of the lac genes to selected promoters in *Escherichia coli* using bacteriophage lambda and Mu. *J. Mol. Biol.* **104**, 541–555 (1976).
201. Lecoeur, H. Nuclear Apoptosis Detection by Flow Cytometry: Influence of Endogenous Endonucleases. *Exp. Cell Res.* **277**, 1–14 (2002).
202. Hufnagel, D. A., DePas, W. H. & Chapman, M. R. The Biology of the *Escherichia coli* Extracellular Matrix. *Microbiol. Spectr.* **3**, (2015).
203. Laganenka, L., Colin, R. & Sourjik, V. Chemotaxis towards autoinducer 2 mediates autoaggregation in *Escherichia coli*. *Nat. Commun.* **7**, 12984 (2016).
204. Richter, A. M., Povolotsky, T. L., Wieler, L. H. & Hengge, R. Cyclic-di-GMP signalling and biofilm-related properties of the Shiga toxin-producing 2011 German outbreak *Escherichia coli* O104:H4. *EMBO Mol. Med.* **6**, 1622–1637 (2014).
205. Liu, H. & Naismith, J. H. An efficient one-step site-directed deletion, insertion, single and multiple-site plasmid mutagenesis protocol. *BMC Biotechnol.* **8**, 91 (2008).
206. Chart, H., Smith, H. R., Ragione, R. M. L. & Woodward, M. J. An investigation into the pathogenic properties of *Escherichia coli* strains BLR, BL21, DH5 α and EQ1. *J. Appl. Microbiol.* **89**, 1048–1058 (2000).
207. Chen, I., Dorr, B. M. & Liu, D. R. A general strategy for the evolution of bond-forming enzymes using yeast display. *Proc. Natl. Acad. Sci.* **108**, 11399–11404 (2011).

208. Venkatesh, S. & Lipper, R. A. Role of the development scientist in compound lead selection and optimization. *J. Pharm. Sci.* **89**, 145–154 (2000).
209. Lambert, B., Laugâa, P., Roques, B. P. & le Pecq, J. B. Cytotoxicity and SOS-inducing ability of ethidium and photoactivable analogs on *E. coli* ethidium-bromide-sensitive (Ebs) strains. *Mutat. Res.* **166**, 243–254 (1986).
210. Gianferrara, T. *et al.* Ruthenium–Porphyrin Conjugates with Cytotoxic and Phototoxic Antitumor Activity. *J. Med. Chem.* **53**, 4678–4690 (2010).
211. Rodrigues, A. D. & Lin, J. H. Screening of drug candidates for their drug–drug interaction potential. *Curr. Opin. Chem. Biol.* **5**, 396–401 (2001).
212. Perentesis, J. P., Miller, S. P. & Bodley, J. W. Protein toxin inhibitors of protein synthesis. *BioFactors Oxf. Engl.* **3**, 173–184 (1992).
213. Di, L. & Kerns, E. H. Profiling drug-like properties in discovery research. *Curr. Opin. Chem. Biol.* **7**, 402–408 (2003).
214. Moura, C., Mendes, F., Gano, L., Santos, I. & Paulo, A. Mono- and dicationic Re(I)/99mTc(I) tricarbonyl complexes for the targeting of energized mitochondria. *J. Inorg. Biochem.* **123**, 34–45 (2013).
215. Hallett, A. J. *et al.* Exploring the cellular uptake and localisation of phosphorescent rhenium fac-tricarbonyl metallosurfactants as a function of lipophilicity. *Dalton Trans.* **47**, 14241–14253 (2018).
216. Skiba, J. *et al.* Mitochondria Targeting with Luminescent Rhenium(I) Complexes. *Mol. J. Synth. Chem. Nat. Prod. Chem.* **22**, (2017).
217. Amoroso, A. J. *et al.* 3-Chloromethylpyridyl bipyridine fac-tricarbonyl rhenium: a thiol-reactive luminophore for fluorescence microscopy accumulates in mitochondria. *New J. Chem.* **32**, 1097–1102 (2008).
218. Balasingham, R. G., Thorp-Greenwood, F. L., Williams, C. F., Coogan, M. P. & Pope, S. J. A. Biologically Compatible, Phosphorescent Dimetallic Rhenium Complexes Linked through Functionalized Alkyl Chains: Syntheses, Spectroscopic Properties, and Applications in Imaging Microscopy. *Inorg. Chem.* **51**, 1419–1426 (2012).
219. Cheng, L. L. & Wilkie, D. Mitochondrial activity and cytotoxicity of vitamin a (retinol) in yeast and human cell cultures: Protective effect of antioxidants. *Biochem. Pharmacol.* **42**, 1237–1240 (1991).
220. Fernández-Moreira, V. *et al.* Uptake and localisation of rhenium fac-tricarbonyl polypyridyls in fluorescent cell imaging experiments. *Org. Biomol. Chem.* **8**, 3888–3901 (2010).
221. Alberto, R. *et al.* A Novel Organometallic Aqua Complex of Technetium for the Labeling of Biomolecules: Synthesis of [99mTc(OH₂)₃(CO)₃]⁺ from [99mTcO₄]⁻ in Aqueous Solution and Its Reaction with a Bifunctional Ligand. *J. Am. Chem. Soc.* **120**, 7987–7988 (1998).
222. Ferri, E. *et al.* Luminescent conjugates between dinuclear rhenium(I) complexes and peptide nucleic acids (PNA) for cell imaging and DNA targeting. *Chem. Commun.* **46**, 6255–6257 (2010).
223. Clède, S. *et al.* Influence of the Side-Chain Length on the Cellular Uptake and the Cytotoxicity of Rhenium Triscarbonyl Derivatives: A Bimodal Infrared and Luminescence Quantitative Study. *Chem. – Eur. J.* **20**, 8714–8722 (2014).
224. Murphy, M. P. Targeting lipophilic cations to mitochondria. *Biochim. Biophys. Acta* **1777**, 1028–1031 (2008).
225. Kadenbach, B., Ramzan, R., Moosdorf, R. & Vogt, S. The role of mitochondrial membrane potential in ischemic heart failure. *Mitochondrion* **11**, 700–706 (2011).
226. Ganitkevich, V., Reil, S., Schwethelm, B., Schroeter, T. & Benndorf, K. Dynamic responses of single cardiomyocytes to graded ischemia studied by oxygen clamp in on-chip picochambers. *Circ. Res.* **99**, 165–171 (2006).

227. Nigam, S. *et al.* Structurally optimised BODIPY derivatives for imaging of mitochondrial dysfunction in cancer and heart cells. *Chem. Commun.* **52**, 7114–7117 (2016).
228. Modica-Napolitano, J. S. & Aprille, J. R. Delocalized lipophilic cations selectively target the mitochondria of carcinoma cells. *Adv. Drug Deliv. Rev.* **49**, 63–70 (2001).
229. Zhou, Y. & Liu, S. ⁶⁴Cu-Labeled Phosphonium Cations as PET Radiotracers for Tumor Imaging. *Bioconjug. Chem.* **22**, 1459–1472 (2011).
230. Yan, X., Zhou, Y. & Liu, S. Optical imaging of tumors with copper-labeled rhodamine derivatives by targeting mitochondria. *Theranostics* **2**, 988–998 (2012).
231. Xavier, C., Pak, J.-K., Santos, I. & Alberto, R. Evaluation of two chelators for labelling a PNA monomer with the fac-[^{99m}Tc(CO)₃]⁺ moiety. *J. Organomet. Chem.* **692**, 1332–1339 (2007).
232. Anakok, O. SERRULATANES FROM EREMOPHILA NEGLECTA: THEIR SPECTRUM OF ANTIBACTERIAL ACTIVITY, CYTOTOXICITY AND MODE OF ACTION. (2010). doi:10.13140/RG.2.2.29383.60320